Borg, Annika Jasmin Eveliina, MSc

Mechanistic Insights into the Catalytic Pathways of SDR Enzymes

DOCTORAL THESIS

to achieve the university degree of

Doktor der Naturwissenschaften

submitted to

Graz University of Technology

Supervisor

Univ.-Prof. Dipl.-Ing. Dr.techn. Bernd Nidetzky

Institute of Biotechnology and Biochemical Engineering

Faculty of Technical Chemistry, Chemical and Process Engineering and Biotechnology

Graz, April 2021

AFFIDAVIT

I declare that I have authored this thesis independently, that I have not used other than the declared sources/resources, and that I have explicitly indicated all material which has been quoted either literally or by content from the sources used. The text document uploaded to TUGRAZonline is identical to the present doctoral thesis.

22.4.2021
Date

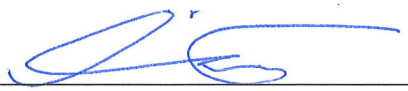
Signature

Acknowledgement

The journey of my PhD would not have been possible without the help and support of many people. First and foremost, I would like to express my sincerest gratitude to Prof. Dr. Bernd Nidetzky for giving me the opportunity to do my PhD in his group. I want to thank him for giving me the chance to work on several different, interesting projects and for having the freedom to pursue my ideas. I want to thank all the people who have collaborated/worked with me in different parts of my PhD. Special thank you goes to Dr. Alexander Dennig, who shared with me the first 3 years of my time at the TU. Alex, without you I would have never found my way to TU. I still remember the message where you advertised the open PhD position to me, and encouraged me to apply. You were always there when I needed you, and we had so much fun together, at the institute and outside the institute. You made me believe in myself even in the hardest of times, and I am really thankful for that. You taught me a lot, not only about work but also about myself. During the time in Graz you became one of my best friends. You, Christina and Tobi have been like a second family for me, and I want to thank you all for your unconditional support and for having me in your life. Prof. Dr. Andrea Mattevi, I would like to express my gratitude for the great and fruitful collaboration, which led to two excellent publications in JBC and Nature Catalysis. I would also like to thank the other people from the protein crystallographer team; Dr. Simone Savino, Prof. Dr. Claudia Binda, Dr. Luca Giacinto Iacovino and Francesca De Giorgi, thank you very much for the collaboration. Prof. Dr. Carme Rovira and Dr. Kshatresh Dutta Dubey, I would like to thank you for the joint effort on the high-level computational studies which helped us to get to Nature Catalysis. Carme, I would like to give special thanks to you for all the nice (work- and non-work-related) discussions and for being such a great host during my visit in Barcelona. I would also like to show my appreciation to Prof. Dr. Hansjörg Weber for all the NMR acquisitions that I have needed in the past years. I would like to give special thanks to Dr. Martin Pfeiffer, who has been an amazing colleague and friend over the years at TU. Martin, I am really thankful for all the help and support that I have received from you, for all the advice and discussions, and for the nice time that we have had both in the lab and outside the institute. I will never forget our conference trip to Toulouse and the hospital experience! I would like to express my deepest appreciation to Christian Rapp, who has been the best office mate and a wonderful friend during these years of my PhD. Christian, thank you for your unconditional support, for being there on the good and bad times. I would not be able to imagine accomplishing this PhD journey without you. I know that our friendship will last a lifetime and I am really thankful for that. I would also like to thank Klara Seelich for being a great office mate, and for all the nice chats we had together. I also want to express my gratitude to all the former and current members of the BIOTE team for creating a nice and friendly scientific environment. For the financial support I would like to thank Austrian Science Fund (FWF) and DK Molecular Enzymology. I would also like to give big thanks to all my friends and relatives who have walked with me through this path of PhD. I want to especially thank Ivana Drienovská for raising my curiosity about enzymes while supervising my Bachelor thesis in Groningen. Ivana, thank you for helping me to grow not only as a scientist but also as a person, and for all the support that made me to come this far where I am now. It was also great to share 2 years of time in Graz with you, and I want to thank you for the wonderful lifetime friendship. Ana Rioz, I would also like to give special thanks to you for being such a great friend since my very early days in

Groningen. You were the one who initially gave me the idea of coming to Graz, and I am forever thankful for that. Daria, Tim and Maya, I am deeply grateful for all the support that I have got from you during my PhD, and I am very thankful for the beautiful friendship that we have. Ilona, sinä ansaitset erityisen suuret kiitokset siitä, että olen saanut tämän väitöskirjani päätökseen. Ilman sinun tukeasi en olisi päässyt tähän pisteeseen, ja haluan kiittää sinua siitä että olet elämässäni. Olet maailman paras ystävä. Iskä, haluan kiittää sinua siitä, että olet aina uskonut minuun ja kasvattanut minut kiinnostuneeksi luonnontieteistä. Iskä ja äiskä, haluan kiittää teitä molempia kaikesta siitä mitä olette tehneet vuokseni, ja sen myötä mahdollistaneet elämäni ulkomailla. Haluan myös kiittää kaikkia muita sukulaisia ja ystäviä, jotka ovat olleet osa tätä matkaa.

Abstract

Carbohydrates are crucial for all forms of life, due to their essential roles as structural elements, energy source and signaling molecules. Synthesis and modification of carbohydrates is vital for every organism. Short-chain dehydrogenase/reductase (SDR) enzymes are active on nucleotide-activated sugars and catalyze a broad variety of multi-step nucleotide sugar interconversions. Uridine-5'-diphosphate (UDP)-glucuronic acid (UDP-GlcA) is an essential nucleotide sugar serving as a precursor for the biosynthesis of pivotal carbohydrates (e.g. galacturonic acid, xylose, apiose) for the plant cell wall development, and it is an intermediate in the biosynthesis of ascorbic acid. UDP-apiose/UDP-xylose synthase (UAXS) forms UDP-xylose and UDP-apiose from UDP-GlcA via a mechanism involving oxidation, ring-opening, rearrangement and reduction. The unusually complex reaction pathway is catalyzed by a single active site, where a glutamate residue (Glu141) plays a key role in initiating the sugar ring-opening via an aldol cleavage. A comprehensive mutagenesis and substrate analog study allowed to decipher the details of the enzymatic mechanism of UAXS. UDP-GlcA 4-epimerase (UGAepi) shares structural and substrate similarity with UAXS, catalyzing the interconversion of UDP-GlcA and UDP-galacturonic acid (UDP-GalA). UAXS, UGAepi and UDP-xylose synthase (UXS) utilize the same substrate (UDP-GlcA) and proceed via a common intermediate (UDP-4-keto-hexose uronic acid) to different products (UDP-xylose, UDP-apiose, UDP-GalA). The initial oxidation of UDP-GlcA to the labile keto-intermediate involves deprotonation at C4-OH of the sugar and abstraction of C4 hydride by NAD^+. UGAepi differs from UXS and UAXS in its ability to prevent decarboxylation of the β-keto acid intermediate. A comprehensive mechanistic and structural analysis of UGAepi from *Bacillus cereus* (BcUGAepi) allowed to propose a mechanism for this enzyme. Kinetic isotope effect studies together with the absence of enzyme-NADH at the steady state revealed the oxidation as a rate-limiting step of the reaction. UGAepis catalyze rotation of the UDP-4-keto-hexose uronic acid in the enzyme's active site in order to perform the reduction from the opposite face of the keto-moiety to yield both epimers. BcUGAepi is able to handle the labile keto-intermediate species without even a trace amount of decarboxylation by holding the carboxylate moiety in equatorial position disfavored for decarboxylation. In contrast, UXS promotes a ring pucker change resulting in axial carboxylate facilitating fast decarboxylation. UAXS utilizes stereo-electronic control to master the timing of the catalytic steps, by delaying decarboxylation with an initially equatorially oriented carboxylate and promoting ring pucker change to later facilitate decarboxylation. BcUGAepi takes advantage of a tight binding of the substrate's and product's carboxylate moiety to keep the equatorial positioning. The substrate complex employs a fine-tuned hydrogen bonding network around the carboxylate, while an arginine residue (Arg185) is responsible for the product complex by holding the carboxylate with ionic interactions. Mutating Arg185 to another amino acid results in decarboxylation and the epimerase activity is completely abolished in Arg185Ala and Arg185Asp variants. Substitution by histidine or lysine partially recovers the epimerase activity, producing an enzyme which has a dual function of an epimerase and primitive decarboxylase.

Zusammenfassung

Kohlenhydrate sind aufgrund ihrer Rolle als Energiequelle, sowie der als strukturelle Elemente und Signalmoleküle essenzielle Bausteine aller Lebensformen. Synthese und Modifikation von Kohlenhydraten ist daher unerlässlich für jeden Organismus. Short-Chain Dehydrogenase/Reduktase Enzyme weisen Aktivität mit nukleotidaktivierten Zuckern auf und katalysieren eine große Vielfalt mehrstufiger Umwandlungen derselbigen. Uridin-5'-diphosphat (UDP)-Glucuronsäure (UDP-GlcA) ist ein essenzieller Nukleotidzucker, welcher als Vorstufe zur Biosynthese von zentralen Kohlenhydraten wie Galacturonsäure, Xylose oder Apiose für die Entwicklung pflanzlicher Zellwände unabdingbar ist. UDP-Apiose/UDP-Xylose Synthase (UAXS) bildet mithilfe eines Mechanismus', welcher Oxidation, Ringöffnung, Umlagerung und Reduktion umfasst, sowohl UDP-Xylose als auch UDP-Apiose aus UDP-GlcA. Der ungewöhnlich komplexe Reaktionsweg wird durch ein einziges aktives Zentrum katalysiert, in welchem ein Glutamatrest (Glu141) eine Schlüsselrolle bei der Initiierung der Zuckerringöffnung mittels Aldolspaltung einnimmt. Eine umfassende Mutagenese- und Substratanalogastudie ermöglichte es, die Feinheiten der enzymatischen Reaktion von UAXS zu entschlüsseln. UDP-GlcA 4-Epimerase (UGAepi) zeigt strukturelle und substratbezogene Ähnlichkeit mit UAXS und katalysiert die Umwandlung von UDP-GlcA zu UDP-Galacturonsäure (UDP-GalA). UAXS, UGAepi und UDP-Xylose Synthase (UXS) verwenden dasselbe Substrat (UDP-GlcA), welches über ein gemeinsames Intermediat (UDP-4-keto-hexose Uronsäure) in verschiedene Produkte (UDP-Xylose, UDP-Apiose, UDP-GalA) umgesetzt werden kann. Die anfängliche Oxidation von UDP-GlcA zum labilen Ketointermediat involviert eine Deprotonierung an C4-OH des Zuckers und die Abstraktion des C4 Hydrids durch NAD^+. UGAepi unterscheidet sich von UXS und UAXS in seiner Fähigkeit, die Decarboxylierung des β-keto Säureintermediats zu verhindern. Durch eine ausführliche mechanistische und strukturelle Analyse von UGAepi aus *Bacillus cereus* (BcUGAepi) konnte ein großer Beitrag zur Aufklärung des Reaktionsmechanismus' des Enzyms erbracht werden. Studien zum kinetischen Isotopeneffekt in Kombination mit der Abwesenheit von enzymgebundenem NADH im Fließgleichgewicht zeigten die Oxidation als geschwindigkeitslimitierenden Schritt der Reaktion auf. UGAepis katalysieren die Rotation von UDP-4-keto-hexose Uronsäure im aktiven Zentrum des Enzyms, wodurch die Reduktion der Ketogruppe von beiden Seiten ermöglicht wird. BcUGAepi ist im Stande, das labile Ketointermediat ohne jegliche Decarboxylierung zu handhaben. Dies gelingt durch Fixierung der Carboxylatgruppe in äquatorialer Position. Im Gegensatz dazu katalysiert UXS eine Ringformänderung, welche zu einer axial orientierten Carboxylatgruppe führt und eine schnelle Decarboxylierung zur Folge hat. BcUGAepi fixiert die Carboxylatgruppe des Substrates und Produktes in äquatorialer Position. Der Substratkomplex wird durch ein feinabgestimmtes Wasserstoffbrückennetzwerk um die Carboxylatgruppe fixiert, während ein Argininrest (Arg185) die Carboxylatgruppe im Produktkomplex mittels ionischer Wechselwirkung in Position hält. Die Mutation von Arg185 zu anderen Aminosäuren resultiert in Decarboxylierung und dem gänzlichen Wegfall der Epimeraseaktivität in Arg185Ala und Arg185Asp Varianten. Substitution durch Histidin oder Lysin führt zu partieller Wiederherstellung der Epimeraseaktivität und einem Enzym mit dualer Funktion: Epimerase und primitive Decarboxylase.

Table of Contents

Deciphering the Enzymatic Mechanism of Sugar Ring Contraction in UDP-Apiose Biosynthesis

nature catalysis

ARTICLES

https://doi.org/10.1038/s41929-019-0382-8

Deciphering the enzymatic mechanism of sugar ring contraction in UDP-apiose biosynthesis

Simone Savino[1,2,7], Annika J. E. Borg[3,7], Alexander Dennig[2,3,7], Martin Pfeiffer[3], Francesca De Giorgi[1,3], Hansjörg Weber[4], Kshatresh Dutta Dubey[5], Carme Rovira[5,6], Andrea Mattevi[1*] and Bernd Nidetzky[2,3*]

The *C*-branched pentose sugar D-apiose is important for plant cell wall development. Its biosynthesis as urdine diphosphate-D-apiose (UDP-D-apiose) involves decarboxylation of the UDP-D-glucuronic acid precursor coupled with pyranosyl-to-furanosyl sugar ring contraction. This unusual multistep reaction is catalysed in a single active site by UDP-D-apiose/UDP-D-xylose synthase (UAXS). Here we decipher the UAXS catalytic mechanism on the basis of crystal structures of the enzyme (which is from *Arabidopsis thaliana*), molecular dynamics simulations that are expanded by hybrid quantum mechanics/molecular mechanics calculations and mutational mechanistic analyses. Our studies show how UAXS uniquely integrates a classical catalytic cycle of oxidation and reduction by a tightly bound nicotinamide co-enzyme with retroaldol/aldol chemistry for the sugar ring contraction. We further demonstrate that decarboxylation occurs only after the sugar ring opening and identify that the thiol group of Cys100 steers the sugar skeleton rearrangement by proton transfer to and from C3′. The mechanistic features of UAXS highlight the evolutionary expansion of the basic catalytic apparatus of short-chain dehydrogenases/reductases for functional versatility in sugar biosynthesis.

The *C*-branched pentofuranose D-apiose (3-*C*-(hydroxymethyl)-D-glycero-tetrose; **1b** in Fig. 1) is widely distributed in plants[1–3] and has also recently been found in bacteria[4]. In plants, apiose is present in pectin polysaccharides and certain glycosylated natural products[1]. By forming borate ester cross-links between polysaccharide chains, apiose residues are essential for cell wall development and stability[1,3,5,6]. The degradation of apiose-containing polysaccharides by human-gut microorganisms[7] and the biological routes of catabolism of the apiose monosaccharide[3] have recently attracted considerable attention. Chemical de novo synthesis of apiose was developed[8]; however, apiose is naturally synthesized as uridine diphosphate (UDP)-apiose (**1a**) from UDP-D-glucuronic acid (UDP-GlcA; **2**) by UDP-apiose/UDP-xylose synthases (UAXS; Fig. 1)[2,4,6,9,10]. The UAXS reaction is unusually challenging for just a single enzyme to perform. It involves decarboxylation coupled with sugar ring contraction to generate a five-membered ring furanosyl product[11–13]. The enzyme also produces a six-membered ring pyranosyl product UDP-xylose (**3**) in consistent ratios (typically about 1:1 at neutral pH)[6,13]. A plausible reaction path that is based on mechanistic studies spanning several decades has been proposed, as shown in Fig. 1 (refs. [6,9–19]). The relative timing of the catalytic steps has been recently elucidated from kinetic isotope effects on the enzymatic rates as well as on the distribution of **1a** and **3** (ref. [13]).

UDP-GlcA is first oxidized at C4′ by the tightly bound NAD^+. Subsequent deprotonation of the 2′-OH facilitates a C2′–C3′ aldol cleavage[11–13]. Decarboxylation thus occurs on the ring-opened oxidized substrate[13]. Rearrangement of the carbon skeleton yields either UDP-apiose aldehyde (**4**) or UDP-4-keto-xylose (**5**), whose reduction by NADH gives the respective furanosyl or pyranosyl products (**1a** and **3**, respectively). However, despite these extensive studies, it remains obscure how UAXS can incorporate such a complex mechanism and orchestrate multiple catalytic steps in a single active site.

The mechanistic complexity of UAXS becomes even more fascinating when viewed from an evolutionary perspective. The enzyme is classified as member of the sugar nucleotide epimerase/dehydratase subclass of the short-chain dehydrogenase/reductase superfamily (SDR)[20–22]. UAXS incorporates the distinctive SDR sequence signature (that is, a highly conserved Thr/Tyr/Lys motif) for catalytic oxidoreduction by NAD^+/NADH[23,23]. The catalytic roles of these residues are well described from studies of other SDRs and involve the use of Tyr as a Brønsted acid/base for reduction/oxidation[23,24]. Functional SDR homologues of UAXS (Supplementary Fig. 2) such as UDP-xylose synthase (UXS)[24–26] and UDP-GlcA dehydrogenase/decarboxylase (ArnA)[27,28] catalyse the decarboxylation of **2** to form **3** or **5**, respectively[28]; however, neither UXS nor ArnA promote the rearrangements that lead to sugar ring contraction[28], which is an activity specific of UAXS. By contrast to UAXS (Fig. 1), UXS and ArnA catalyse oxidative decarboxylation of **2** without opening the sugar ring. The core problem for this mechanistic inquiry is thus understanding how UAXS integrates the retroaldol/aldol rearrangement of the sugar-ring carbon skeleton with the established[11–13] SDR catalytic cycle of substrate oxidation, decarboxylation and reduction.

Here we report crystal structures of the ternary complexes of *Arabidopsis thaliana At*UAXS[6] (named UAXS in the following text for convenience) with NAD^+ and UDP (3.0 Å; resolution), and with NADH and **2** (3.5 Å resolution), respectively. We identify the

[1]Department of Biology and Biotechnology, University of Pavia, Pavia, Italy. [2]Austrian Centre of Industrial Biotechnology, Graz, Austria. [3]Institute of Biotechnology and Biochemical Engineering, Graz University of Technology, NAWI Graz, Graz, Austria. [4]Institute of Organic Chemistry, Graz University of Technology, NAWI Graz, Graz, Austria. [5]Organic Chemistry Section, Department of Inorganic and Organic Chemistry & Institute of Computational and Theoretical Chemistry (IQTCUB), University of Barcelona, Barcelona, Spain. [6]Catalan Institution for Advanced Studies (ICREA), Barcelona, Spain. [7]These authors contributed equally: Simone Savino, Annika J. E. Borg, Alexander Dennig. *e-mail: andrea.mattevi@unipv.it; bernd.nidetzky@tugraz.at

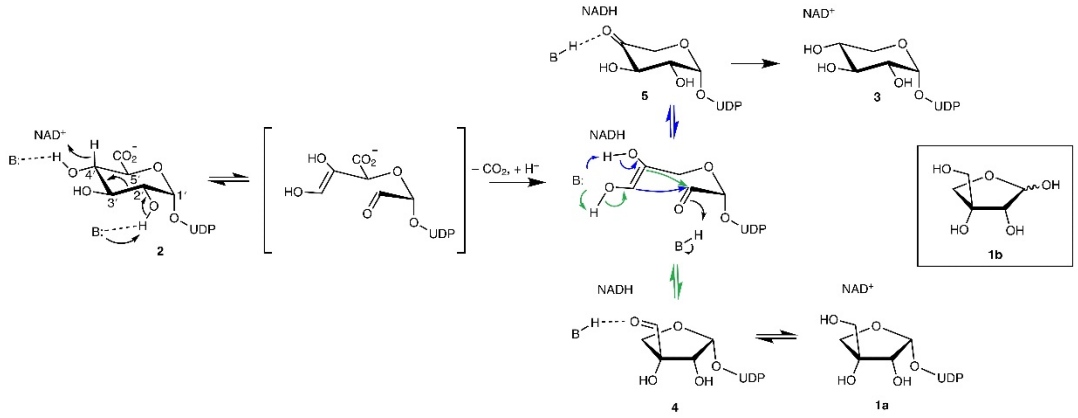

Fig. 1 | The proposed mechanism of UAXS. The substrate oxidation, aldol cleavage for ring opening, and decarboxylation steps are shown (a full representation is given in Supplementary Fig. 1). The green and blue arrows indicate the aldol reactions that lead to the ring-contracted furanosyl product and the pyranosyl product, respectively. B, enzyme base.

key catalytic elements of UAXS using structural evidence of the enzyme in combination with molecular dynamics (MD) simulations and hybrid quantum mechanics/molecular mechanics (QM/MM) calculations. Mutational analysis of the active-site interactions substantiates their proposed roles in catalysis. In particular, we find that pyranosyl ring distortion in the **2** substrate—away from the preferred $^4C_1$ chair conformation in solution to a relatively flexible skew-boat ($^1S_3$, $^1S_5$) or boat ($^{1,4}B$) conformation in the Michaelis complex—serves to precisely align the reactive groups of the substrate (4′-OH, C4′-H, 2′-OH) with the catalytic groups of the enzyme. Comparisons of UAXS with human UXS and ArnA reveal the remarkable catalytic subtlety that is involved in each enzyme to achieve conversion of **2** according to the corresponding individual reaction path (Fig. 1 and Supplementary Fig. 1). We show that UAXS uses only minimal extensions to the SDR core catalytic machinery to establish its unique catalytic functionality.

Results

The overall structure of UAXS features a highly conserved active-site architecture. We first determined the crystal structure of wild-type UAXS in complex with the NAD$^+$ co-enzyme and UDP (3.0 Å resolution; Supplementary Table 1 and Supplementary Figs. 3–8). The structure comprises a single polypeptide chain (residues 8–382) with a surface loop that could not be traced during modelling (residues 61–68). The protein is composed of ten α-helices and twelve β-strands (Fig. 2a). The asymmetric unit contains two protein subunits that are arranged into a homodimer, as reported for other UAXS enzymes in solution[19]. As with other dimeric SDRs[20–22], the inter-subunit interface is stabilized by hydrophobic interactions[30] between a pair of α-helices, forming a four-helical bundle and two elongated loops (Fig. 2a). The UAXS monomer is built of two domains: a large NAD$^+$-binding domain (residues 8–215, 263–292, 343–358) that is a modified version of the classical Rossmann fold and a considerably smaller UDP-GlcA-binding domain (residues 216–262, 293–342, 359–382). This two-domain folding topology is typical of SDRs and has high structural similarity with its closest functional homologues; namely, human UXS and ArnA[25,27,28]. Compared with human UXS (28% sequence identity and an overall root-mean squared deviation of 1.6 Å)[25], UAXS exhibits several elongated loops (residues 59–67, 147–65, 224–234, 310–321 and 326–336) and contains an additional helix (α3, residues 80–90) that is replaced by a loop in human UXS. An UAXS loop (residues 102–109) makes a larger turn around the active site than the equivalent loop of human UXS (residues 81–88), as shown in Supplementary Fig. 9.

The active site of UAXS is located in a cavity that is formed between the NAD$^+$- and UDP-GlcA-binding domains and is made up of seven highly conserved residues (Fig. 2a). The characteristic signature of an SDR catalytic centre is formed by Thr139, Tyr185 and Lys189 (the lysine is not shown in Fig. 2 but it is shown in Fig. 3)[20–22], whereas Tyr105, Glu141, Arg182 and Arg341 are distinct features of the UAXS/UXS/ArnA group of enzymes. As in human UXS[24–26,28] and ArnA[27,30], the interaction between Glu141 and Arg341 fastens together two long loops (residues 128–173 and 332–345), thus closing the active site (Supplementary Fig. 10). Sequence changes that distinguish the UAXS active site from the active sites of human UXS (Fig. 2b) and ArnA (Supplementary Fig. 11) are Cys100 and Cys140, which are Ala or Ser in the two other enzymes[25,30]. This sequence conservation is matched by highly similar ligand-binding modes, as revealed by the comparison of our structure (wild-type UAXS in complex with NAD$^+$ and UDP) with the structures of human UXS[28] (Fig. 2b) and substrate-bound ArnA[30] (Supplementary Fig. 11). Specifically, NAD$^+$ is buried deeply in the protein (Fig. 2a), which is consistent with the observation that the co-enzyme is tightly bound by UAXS. Biochemical data show that UAXS retains one co-enzyme/protein monomer throughout purification. Between 30% and 80% of the bound co-enzyme in UAXS was isolated as NADH (Supplementary Fig. 12); however, incubation of the enzyme in the presence of NAD$^+$ results in a complete exchange for the oxidized form of the co-enzyme (Supplementary Fig. 13). Binding of the reduced form of the co-enzyme is probably due to recombinant (over)production. Other SDR enzymes that—like UAXS—contain tightly bound NAD$^+$ or NADP$^+$ (for example, epimerases, dehydratases, decarboxylases) show a similar effect, with the portion of reduced co-enzyme greatly varying dependent on the enzyme and the conditions used[31,32].

The structural basis of catalysis by UAXS. Cocrystallization or soaking of wild-type UAXS with **2** proved unfruitful. The electron density in the area that was supposedly occupied by the substrate's α-glucuronyl moiety showed discontinuity from the density of UDP, probably due to a phosphate from the crystallization solution;

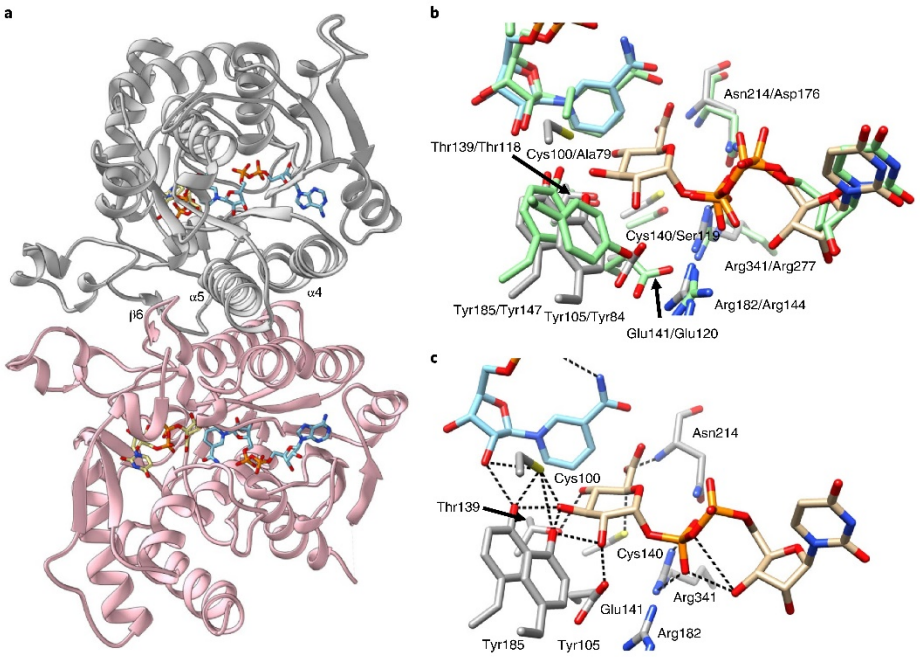

Fig. 2 | Crystallographic analysis of the three-dimensional structure of UAXS from *Arabidopsis thaliana*. a, The UAXS subunit features the typical SDR fold. The enzyme is a functional dimer, with chain A shown in grey and chain B shown in pink. The dimer interface of UAXS is composed of helices α4 (residues 109–129) and α5 (residues 181–202). There are more dimer contacts from strand β6 (residues 170–179) and from an extended loop. NAD^+ and **2** are represented by cyan and beige carbons, respectively. Red, oxygen; blue, nitrogen; orange, phosphorus; yellow, sulfur. **b**, A structural comparison/overlay of the active sites of UAXS and human UXS is shown (PDB: 2B69; light-green carbon atoms). Most of the residues are conserved and have similar conformations. The main changes are replacements of Cys100 and Cys140 in UAXS with Ala79 and Ser119 in human UXS (Supplementary Fig. 2). **c**, A model for the UAXS Michaelis complex (NAD^+:UDP-GlcA:enzyme) was built by combining the ligands from two different structures: the wild-type enzyme bound to NAD^+ and UDP (Supplementary Fig. 7), and the C100A mutant bound to NADH and UDP-GlcA (Supplementary Fig. 8). Enzyme residues, UDP-GlcA and NAD^+ are represented by light-grey, beige and cyan carbon atoms, respectively. Cys100 was modelled in a rotameric conformation that is suitable to interact with the 3′OH of the sugar substrate. Possible hydrogen-bond interactions between the labelled residues and the ligands are shown as black dashed lines.

however, by using a lower activity UAXS variant (C100A; Table 1) and by undergoing cocrystallization with NADH, we obtained a structure with well-defined electron density for the complete molecule of **2**, which is bound to the enzyme (Supplementary Fig. 8). Although clear electron density was found for the remaining part of the bound co-enzyme, the nicotinamide ring in this structure could not be traced. Ala100 is in a position that could also accommodate the Cys100 of wild-type UAXS (Fig. 2c and Supplementary Fig. 8). The residues surrounding NAD^+ and **2** in the C100A variant structure have the same conformation as in wild-type UAXS (Supplementary Fig. 14). We therefore combined the two structures to obtain a model of the NAD^+:UDP-GlcA:enzyme ternary complex (Fig. 2c). We validated the resulting enzyme complex through comparison with ArnA, for which a complex structure with **2** has been reported (PDB: 1Z7E)[30]. The structures of ArnA and UAXS share 37% residue identity and have a root-mean squared deviation of the atomic positions of 1.2 Å. Most importantly, **2** accommodates almost identically in the two structures, as shown in Supplementary Fig. 11.

The substrate positioning for catalysis in the Michaelis complex of UAXS. With the support of the crystallographic data, we performed MD simulations with GLYCAM06[33] that were combined with hybrid QM/MM calculations to further examine the positioning of the **2** in the active site of UAXS. Molecular dynamics simulations have previously aided the identification of probable substrate positioning for catalysis in human UXS[25]; 600 ns MD simulations in two replicas of the NAD^+:UDP-GlcA:enzyme complex were initially carried out with Tyr185 in the protonated or unprotonated forms. The pK_a of the homologous tyrosine in related SDRs (epimerase, dehydratase)[32,34] is around 6.5, making it necessary to consider both of the protonation states of Tyr185. Only with unprotonated Tyr185 did we identify conformations that were plausibly catalytic; that is, (1) they showed proper arrangement of substrate and NAD^+ for hydride transfer and (2) had the conserved SDR catalytic dyad positioned for the required deprotonation of the 4′-OH (Tyr185, Thr139; Fig. 3). A representative snapshot from each MD trajectory was further optimized using hybrid QM/MM calculations at the density functional theory level of theory (Fig. 3a). Thorough analysis of the MD trajectories for the Tyr185-deprotonated enzyme revealed considerable flexibility in the active-site interactions of bound **2** (Supplementary Videos 1 and 2). This flexibility arises due to seemingly coordinated, atomic motions of the active-site residues, NAD^+ and the substrate, and it involves substan-

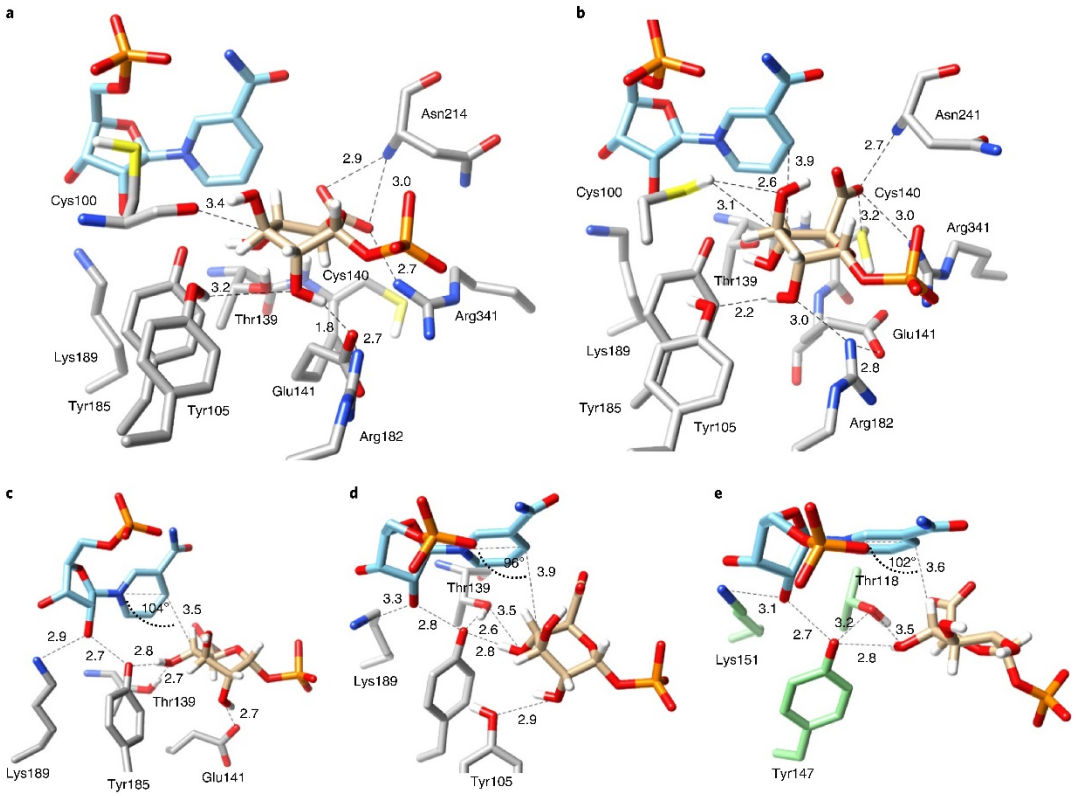

Fig. 3 | The positioning of the UDP-GlcA substrate for catalytic oxidation and ring opening at the active site of UAXS, as revealed by QM/MM calculations. The QM/MM calculations were performed on representative snapshots selected from the MD simulations. **a**, A close-up of the structure and key interactions for the proposed Michaelis complex; the ternary NAD^+:UDP-GlcA:enzyme complex is from replica 1 (Supplementary Video 1). The pyranosyl ring of GlcA adopts a $^1S_5$ conformation. **b**, A close-up of the structure and key interactions for an alternative ternary complex that is prominently present in MD simulations from replica 2 (Supplementary Video 2). The pyranosyl ring of GlcA adopts a $^1C_4$ conformation. **c**,**d**, More close ups (taken from panels **a** (**c**) and **b** (**d**)) that highlight the catalytic interactions for the oxidation of the C4′ alcohol group (via hydride transfer to NAD^+ and proton transfer to Tyr185) and sugar ring opening (via deprotonation of the 2′-hydroxy group). Note that the orientations from panels **a** and **b** were adapted for better viewing. **e**, A modelled Michaelis complex of human UXS with bound **2** and NAD^+ (ref. [25]).

tial rearrangements in the sugar ring conformation, as shown in detailed maps of the puckering geometries that are adopted along the full MD trajectories (Supplementary Fig. 15).

In replica 1, the pyranosyl ring of UDP-GlcA is distorted from the preferred $^4C_1$ chair conformation in solution to either skew-boat ($^1S_3$, $^1S_5$) or boat ($^{1,4}B$) conformations. The ring-flipped $^1C_4$ conformation is present to a minor extent (Supplementary Fig. 15a). The nicotinamide C4 is above the substrate C4′, with a distance (3.5 Å) and angle (104° relative to the nicotinamide ring C4–N1 axis) that are well set for hydride transfer (Fig. 3,a; Supplementary Video 1). The 4′-OH is oriented by hydrogen bonds with Tyr185 and Thr139. The polarity of these hydrogen bonds indicates proton abstraction to the phenolate of Tyr185. The catalytic function of the tyrosine–threonine dyad in alcohol oxidation is analogous to other SDR enzymes[22,23,25,32,34], as visible from the comparison with the proposed Michaelis complex of human UXS that was obtained from a previous study (Fig. 3e)[25]. The substrate 2′-OH is hydrogen-bonded to Glu141 whereas the 5′-carboxylate is oriented equatorially and interacts with Arg341 and Asn214 (main chain NH). Furthermore, the C5′ of **2** is close to Cys140, which is a good candidate to play a role in the obligatory proton uptake to the C5′ during decarboxylation (Supplementary Fig. 1). An alternative snapshot from replica 1 has the Cys140 side chain oriented toward the C5′ (Supplementary Fig. 16a).

The other prominent enzyme complex that was obtained from the MD simulations (replica 2) features the pyranosyl ring of **2** in a $^1C_4$ chair conformation (Supplementary Fig. 15b) with the carboxylate oriented axially. The sugar remains reasonably positioned for hydride transfer (with a C4′–C4 distance of 3.9 Å; and an angle of 96° relative to the nicotinamide ring C4–N1 axis) and the 4′-OH retains the characteristic hydrogen bond with the Thr139–Tyr185 dyad (Fig. 3,b and Supplementary Video 2). The substrate sugar–protein interactions are further enriched by hydrogen bonds between the 2′-OH and Tyr105 (Fig. 3d), and the direct contacts of the C3′ and C5′ atoms with the side chains of Cys100 and Cys140, respectively (Supplementary Fig. 16b). Moreover, in a representative portion of the simulated structures (~30%), a water molecule that is coordinated by Glu141 is placed close to the C5′, thus establishing a proton conduit (Supplementary Fig. 16c).

Table 1 | Activity and selectivity of wild-type UAXS and variant enzymes for the conversion of 2

Enzyme	k_{cat}[a] (min^{-1})	1a (%)	3 (%)	5[b] (%)	1 (%)
Wild-type	0.49	59	26	8	7
Y185F	0	n.a.	n.a.	n.a.	n.a.
Y105F	0.05	18	41	32	9
Y105A	0.13	0	50	50	0
T139V	3×10^{-3}	0	0	100	0
C100A	0.12	18	61	15	6
C100S	0.09	0	21	79	0
C140S	0.07	29	26	35	10
C140A	0.11	15	33	52	0
C100A/C140S	0.23	27	32	33	8
E141A	3×10^{-3}	0	0	100[b]	0

[a]Activity (k_{cat}) was measured by HPLC–UV as the depletion of substrate in H_2O at pH 7.0 (Supplementary Figs. 17–32). Selectivity for product formation was determined by ^{1}H-NMR in D_2O at pD 7.0 (Supplementary Figs. 33–35). Reaction conditions: 50 mM potassium phosphate buffer; 30 °C; 2 mM substrate; 0.1 mM NAD^+ (1.0 mM for T139V and E141A variants). An appropriate enzyme concentration between 0.5 and 14.3 mg ml^{-1} was used. Note that there was no solvent isotope effect on the k_{cat} (see Supplementary Fig. 36). Data are from multiple determinations and have relative s.d. of less than 10% (except Y105F, 20%; see Supplementary Figs. 17–32). [b]22 mg ml^{-1} enzyme added for ^{1}H-NMR measurement. n.a., not applicable.

The analysis of the MD trajectories and the QM/MM optimized models collectively highlight several features that are relevant for catalysis (Fig. 1 and Supplementary Fig. 1). The pyranosyl ring of UDP-GlcA can adopt multiple conformations that deviate from the $^4C_1$ chair conformation and yet retain an acceptable geometry for hydride transfer to the NAD^+. The carboxylate at C5′ can be equatorially (replica 1) or axially (replica 2) oriented. The change in orientation from axial to equatorial can be catalytically relevant by modulating the reactivity of the C5′ carboxylate for decarboxylation. Glu141 and Tyr105 are the hydrogen bond partners for the 2′-OH of the substrate and may thereby be involved in ring opening. Cys140 is consistently found in proximity to C5′ and is positioned well to protonate the C5′ in the decarboxylation step (possibly together with the nearby waters and side chains). Cys100 adopts flexible conformations with its side chain pointing out of and into the active site (Fig. 3,a, respectively). In the 'in' conformation, its thiol group points towards the sugar C3′ atom in a position that is suited for subsequent proton transfer to and from C3′.

Probing the catalytic roles by mutagenesis. The residues that were suggested to have a role in enzymatic catalysis from the structural and computational studies were first probed by site-directed mutagenesis (Table 1). Our strategy was to target residues that are (1) part of the conserved SDR catalytic core (Tyr185–Thr139 dyad)[20–22], (2) characteristic of the UAXS/UXS/ArnA subgroup of enzymes (Tyr105, Glu141)[25,30] and (3) specifically present only in the UAXS active site (Cys100, Cys140) (Fig. 2,b). The C100A–C140S variant was made with the aim of creating a UXS/ArnA-like active site in UAXS (Fig. 2 and Supplementary Figs. 2 and 11). The activities of the purified enzymes were initially measured with an HPLC–UV-based substrate depletion assay as summarized in Table 1 (Supplementary Figs. 17–32). The Y185F protein was inactive, which is in agreement with a role in acid/base catalysis of Tyr185, as generally observed in the SDR enzymes[20–23]. The T139V variant retained a very low level of activity, which is consistent with an auxiliary[25] yet highly relevant function for the original threonine (Supplementary Figs. 22 and 25). The E141A variant also showed very low activity (Supplementary Fig. 32), which is in accordance with the suggestion that Glu141 has a role in forming the reactive UAXS–substrate complex and stabilizing the active-site conformation (Fig. 3,a; Supplementary Fig. 10). All of the other variants (C100A, C100S, Y105F, Y105A, C140A, C140S, C100A/C140S) exhibited two- to ninefold lower activities than the wild-type enzyme (Table 1).

The active variants were subjected to NMR experiments to determine the distributions of **1a**, **3** and **5** that can be generated by UAXS following the conversion of **2** (Table 1 and Fig. 1)[19]. Spontaneous decomposition of **1a** gives the cyclic 1,2-apiosyl-phosphate (**1**, Supplementary Fig. 1), which we also measured (Supplementary Fig. 33)[13,19]. Furthermore, NMR was employed for the detection of reaction intermediates that were accumulated before or after decarboxylation (Supplementary Figs. 34 and 35)[19]. Wild-type UAXS was found to have clear preference for **1a**, which is produced in 2.5-fold excess over **3** with minimal leakage of intermediates (8% of **5**). This reactivity pattern was found to be altered in all studied variants, which were indiscriminate (C140S) regarding the formation of **1a** and **3** or exhibited an 'inverted' (C100A, Y105F, C140A, C100A/C140S) preference for the xylose over the apiose product (Table 1 and Supplementary Figs. 34 and 35). The C100S and Y105A variants produced no **1a** and are mechanistically very insightful because their reactions may no longer involve ring opening. Moreover, all of the variants featured enhanced accumulation of intermediate **5**, which was the only detectable product for the minimally active T139V and E141A variants. Accumulation of intermediate **4** was not detected in any variant. The trend common to all of the variants was therefore a reduced or abolished capacity to produce a ring-contracted apiose product.

Incorporation of solvent deuterium into UDP-xylose C3′. The mechanistic proposal for UAXS (Supplementary Fig. 1) entails a proton transfer to and from the C3′ of the ring-opened reaction intermediates before and after the decarboxylation, respectively. From its position in the enzyme structure and the outcome of the mutagenesis experiments, Cys100 was the prime residue candidate to catalyse these proton transfers (Figs. 2c and 3,a). To assess the role of Cys100, we analysed the C100A and C100S variants along with wild-type UAXS and measured the incorporation of solvent deuterium into the C3′ of **3**, which is released during the conversion of **2** by these enzymes (Fig. 4 and Supplementary Fig. 37 and 38). It was found in a previous study[13] (and confirmed here for different pH conditions) that wild-type UAXS does not promote deuterium incorporation from the solvent at C3′ (Fig. 4a); however, as shown in Fig. 4b, we considered that the C100A variant might promote deuterium incorporation in the case where water is substituted for the supposed proton transfer function of the original thiol side chain of Cys100. The **3** formed by the C100A variant indeed showed H/D exchange at the C3′ (Fig. 4c). The degree of deuterium labelling was large, with only traces of proton remaining at C3′ (Fig. 4c). A role of Cys100 in proton transfer to the C3′ (Fig. 4b) was strongly supported from these results. The C100S variant, by contrast, did not incorporate solvent deuterium into the C3′ of **3** and **5**, as shown in Fig. 4d. This finding, together with the evidence that ring-contracted apiosyl product cannot be formed by the C100S variant (Table 1), suggests that this variant proceeds in oxidative decarboxylation such as in human UXS, without ring opening. The pK_a (~13) of serine is much larger than that of cysteine (~8.5) and it does not allow Ser100 to catalyse proton transfer analogously as the Cys100.

UAXS reaction uncoupled from the decarboxylation. The post decarboxylation steps that lead to rearrangement of the five-carbon skeleton to yield **5** and **4** have so far eluded detailed characterization. Several studies[6,12,35] including our own (data not shown) indicate that **3** is not detectably converted to **1a**, which is too unstable for isolation in relevant/required amounts and purity[36], prohibiting product interconversion in the other direction (**1a** to **3**). (Note that we considered purification of **1a** in the presence of organic amines, such as trimethylamine, that seem to be somewhat stabilizing[36];

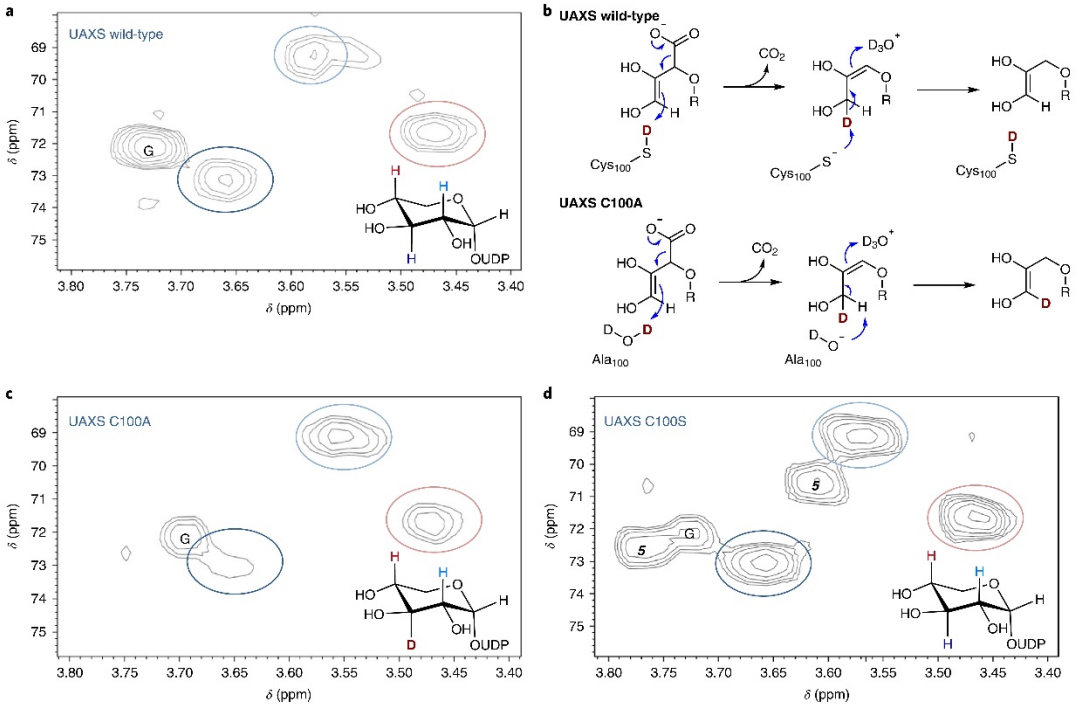

Fig. 4 | Deuterium incorporation at C3′ during the conversion of 2 by the wild-type, C100A and C100S forms of UAXS. a,**c**,**d**, The results of the heteronuclear single quantum coherence experiments are shown, analysing **3** that was isolated from the reactions of UAXS wild-type (**a**), C100A variant (**c**) and C100S variant (**d**) in D_2O (pD 7.0). The relevant hydrogens at carbons 2′, 3′ and 4′ are coloured and are indicated in the spectra with correspondingly coloured circles. G represents the signal derived from traces of glycerol, whereas **5** represents the signals derived from **5** (C3–H at ~3.78 ppm; C2–H at ~3.61 ppm). **b**, The protonation and deprotonation events during the decarboxylation, which lead to deuterium incorporation at C3′ in the reaction of the C100A variant but not in the reaction of the wild-type enzyme, are shown. Note that the C5′ in **3** is partly deuterated (50%) from the solvent in all of the enzymatic reactions, as expected from the proposed mechanism shown in **b**.

however, our attempt failed after the last step of removing the amine by size-exclusion chromatography. The isolated **1a** rapidly decomposed in water). Liu and co-workers[12] demonstrated that a chemically stable phosphonate analogue of **1a** obtains the corresponding UDP-xylose analogue enzymatically. The actual turnover product is cyclic xylose 1,2-phosphonate (and UMP), which, however, renders the overall reaction irreversible. Using the C-terminal decarboxylase fragment of ArnA (Supplementary Fig. 39)[27,28], we established a new protocol for the synthesis of **5** in excellent yields (≥90%) as the sole product of the conversion of **2** in the presence of NAD^+ (Fig. 5a and Supplementary Fig. 40 and 41). By means of a highly sensitive (herein developed) HPLC–UV assay, we could thereby show that **5** is not a substrate for ring rearrangement by UAXS (Fig. 5,b and Supplementary Figs. 42–45). No **1a** was formed from **5**; rather, **5** was gradually converted into **3** in the presence of externally added NADH (Fig. 5b). The reduction of **5** by both wild-type UAXS and the C100S variant features a kinetic behaviour similar to that seen for the same reaction catalysed by human UXS (Fig. 5c and Supplementary Fig. 45). The reaction time course characteristically involves an initial 'burst' of **3** release, with the product amount corresponding to the molar equivalent of enzyme-NADH present in the reaction (Fig. 5c and Supplementary Fig. 44). The burst rate (~1–3 min^{-1}) is consistent with the k_{cat} for the full enzymatic reaction starting from **2** (Table 1).

The requirement for co-enzyme exchange (NAD^+ to NADH) to continue the reduction of **5** explains the appearance of a second, slower phase in the reaction time course (Fig. 5c). In addition, we found that reduction of **5** in D_2O does not involve deuterium incorporation at C3′ (Supplementary Fig. 46). These results demonstrate that **5** is a substrate for reduction, but not for aldol/retroaldol rearrangement, by UAXS (Fig. 1). Formation of **5** is therefore a quasi-irreversible step of the enzymatic reaction path, providing strong support to the mechanistic notion of a sugar ring opening that precedes the decarboxylation[13].

Discussion

We propose a detailed catalytic mechanism for the enzymatic reaction of UAXS on the basis of the evidence presented (Fig. 6). We assign functions to the main active-site residues in each step of the catalytic conversion. The proposed mechanism involves a largely conserved exploitation of the enzyme's SDR catalytic machinery for NAD-dependent oxidoreduction (Fig. 6a)[20–23,25]. The enzyme affords catalysis of retroaldol/aldol rearrangement for sugar ring opening/contraction[11–13] due to a strategic residue substitution that introduces two cysteines into the active site (Fig. 2, Fig. 3a). Following the initial 'activation' of the substrate by oxidation at C4′, which is facilitated by Tyr185 as the catalytic base (Fig. 6a), the characteristic steps of ring opening and decarboxylation would be promoted by

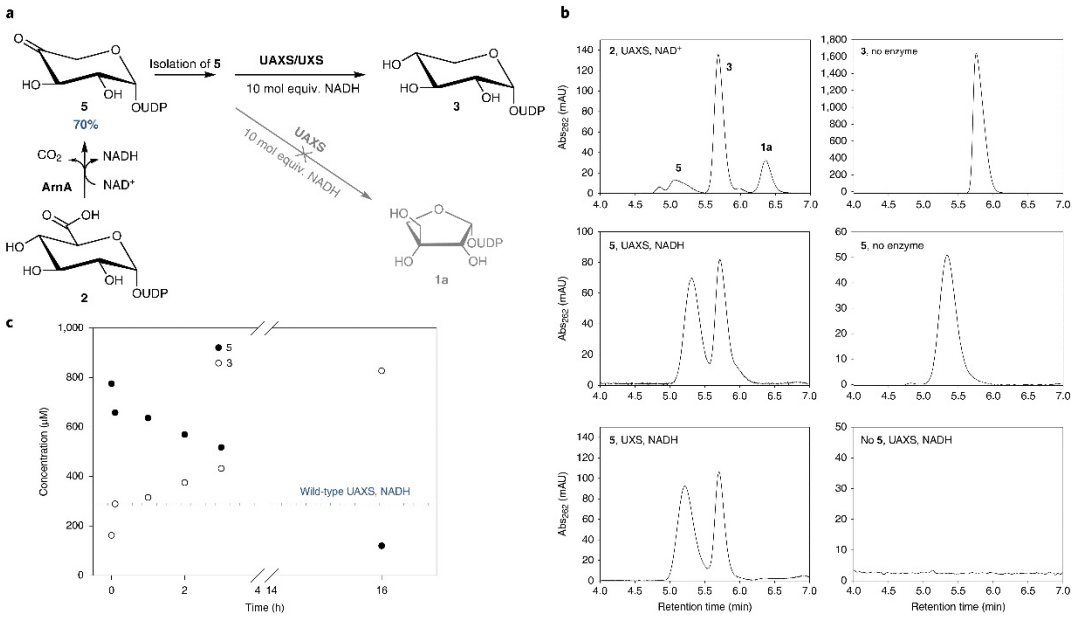

Fig. 5 | The reaction of UAXS with 5 to study ring opening and reduction by the enzyme. a, The different steps of the experiment are shown: **5** was synthesized from **2** using the enzyme ArnA, isolated compound **5** was then subjected to conversion by UAXS in the presence of excess NADH. As a reference, the reaction was also performed with UXS. **b**, The HPLC traces from the conversions of **5** with wild-type UAXS and human UXS, as well as the most relevant controls, are shown. **c**, A time course for the reduction of **5** by wild-type UAXS is shown. The blue dashed line indicates the concentration of enzyme-bound NADH in UAXS (here approximately 60% of 412 μM enzyme).

concerted general acid–general base catalysis. The sugar ring puckering ($^1S_3$, $^{1,4}B$, $^1S_5$) that is observed in replica 1 represents a plausible model of the reactant complex. In this conformation, the carboxylate at C5′ is equatorially oriented to delay the decarboxylation that characteristically follows aldol cleavage in UAXS. There thus seems to be chemical rationale for UAXS (in contrast to UXS) to favour an equatorial orientation of the carboxylate at C5′ (Fig. 3a).

Aldol cleavage of C2′–C3′ requires the catalytic deprotonation of the C2′–OH group (Fig. 6a)[11–13]. Molecular dynamics simulation and QM/MM calculations reveal that Glu141 and Tyr105 are well positioned to fulfil that role. Specifically, the structure of replica 1 suggests that Glu141 is directly responsible for this catalytic step whereas Tyr105 might form a conduit for proton release and/or modulate the pK_a of Glu141 (Fig. 3a and Supplementary Video 1). Mutagenesis data support the proposed function of these residues as the E141A variant shows only trace activity and is completely devoid of UDP-apiose formation whereas the Y105F enzyme is impaired in the ability to form **1a** (Table 1). Precise structural positioning for proper functional interplay between the catalytic residues that promote C4′ alcohol oxidation and the ensuing aldol cleavage seems to be essential for the UAXS type of reactivity. This is illustrated by the Y105A variant, which retains ~27% of wild-type activity for the conversion of **2** but shows complete disruption in the formation of **1a** (Table 1). The effect probably arises from the loss of aromatic stacking of Tyr105, which seems to help the positioning of Tyr185 in the wild-type enzyme (Fig. 2,b) to enable the reaction via ring opening.

In the next catalytic step, protonation of C3′ stabilizes the ring-opened oxidized substrate by preventing reclosure and promotes its decarboxylation (Fig. 6a). Our results identify Cys100 as the critical determinant for this step of the UAXS reaction. The C100S variant is unable to produce any apiose product and our isotope labelling experiments suggest that it reacts through the UXS path without ring opening. The apiose-producing activity of the C100A variant necessitates that proton uptake to C3′ occurs from the solvent. The keto–enol tautomerization steps before and after the decarboxylation involve reversible proton transfers to and from C3′ (Fig. 6a) that can lead to the observed deuterium incorporation at C3′ in the reaction of the C100A variant. In the wild-type enzyme, where Cys100 is present, the proton transfers seem to be selective in that only the previously transferred hydrogen (or deuterium) is reabstracted from the C3′ and no isotope exchange is observed. Finally, the distinct use of the highly conserved Glu141 by UAXS in catalysis to aldol cleavage emphasizes the requirement for an alternative residue (Cys140) that manages the proton transfer to C5′ during decarboxylation. Mechanistic explanation is thus provided for why UAXS has uniquely adopted the readily deprotonatable cysteine at position 140 where UXS and ArnA have a serine.

The space vacated by the release of the carboxylic group provides room for the rearrangement of the ring-open structure, which leads to closure and formation of the five-membered apiose ring (Fig. 6c). Evidence that **5** is not a substrate for retroaldol/aldol reaction by the enzyme suggests that the ring closure that leads to the formation of **5** is a largely spontaneous reaction. This step would therefore seem to primarily require selectivity control from the enzyme—rather than catalytic facilitation—to promote rearrangement of the five-carbon skeleton into **4**. The prime residue candidate for steering the ring closure is Tyr185 because it interacts with the reactive hydroxyl/carbonyl groups in the substrate (Fig. 6c); Glu141 might participate in proton uptake to the C2′ oxygen from the solvent, employing the

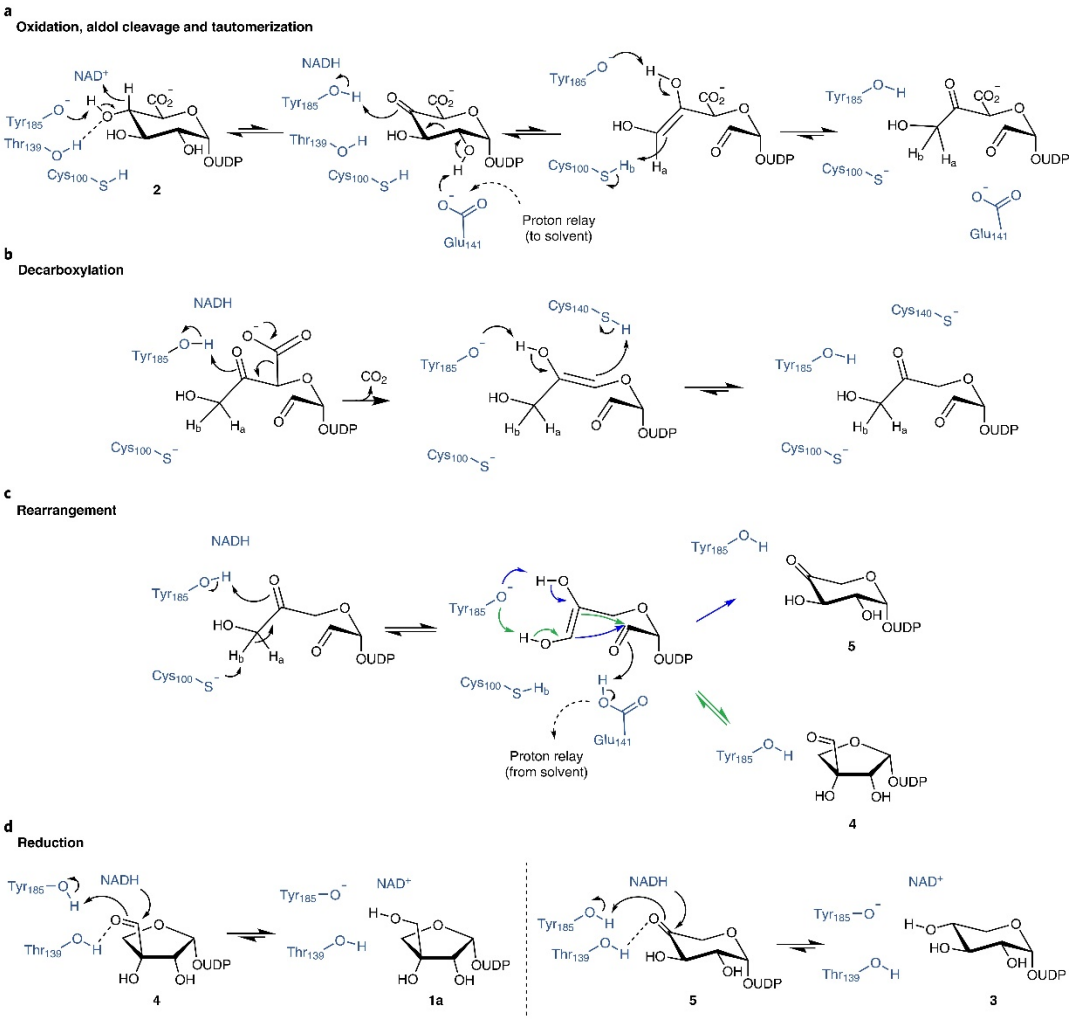

Fig. 6 | The proposed enzymatic mechanism of UAXS. a–d, The proposed oxidation, aldol cleavage and tautomerization (**a**), decarboxylation (**b**), rearrangement (**c**) and reduction (**d**) steps are shown. The proton transferred to and from C3′ by Cys100 is indicated as H_3 in **a**–**c**. The ring closure that gives **5** in **c** is not detectably reversible. The reductions in **d** are indicated to be reversible in principle; however, oxidation of **3** by UAXS was not detectable[11,12].

proton conduit identified in the protein structure (Supplementary Fig. 47). The final reductions of **4** to **1a** and **5** to **3** probably involve Tyr185 as the catalytic proton donor (Fig. 6d).

In conclusion, the mechanistic proposal builds on deepened understanding of how the core catalytic apparatus of SDRs was expanded in UAXS to incorporate catalysis to sugar ring opening/contraction as a unique functionality of this enzyme. Our findings also reveal distinct catalytic strategies that are employed by UAXS and UXS to achieve conversion of **2** according to the corresponding individual reaction path. Each enzyme seems to have found its own way of exploiting a specific substrate conformation to promote catalysis. Although UXS utilizes the distortion in sugar ring puckering to drive the oxidative decarboxylation from pyranosyl substrate[25], UAXS positions **2** to enable C2′–C3′ aldol cleavage coupled with alcohol oxidation at C4′. UAXS adds a genuinely new dimension to SDR catalytic principles to extend the functional diversity of this important enzyme superfamily.

Methods

The methods used are summarized in full detail in the Supplementary Information. See the Supplementary Methods and Supplementary Figs. 3–5 and 39 for enzyme production and purification. Protein crystallography and structure determination are reported in Supplementary Methods, Supplementary Table 1, and Supplementary Figs. 6–11 and 14. The MD simulation experiments and QM/MM calculations are available in the Supplementary Methods and Supplementary Figs. 15, 16 and 47. Kinetic analysis of enzymes is reported in the Supplementary Methods and is presented graphically in Supplementary Figs. 23–32. See the Supplementary Methods, and Supplementary Figs. 17–22, 33–37 and 40–46 for product analysis by HPLC and NMR.

Reporting Summary. Further information on research design is available in the Nature Research Reporting Summary linked to this article.

Data availability

Coordinates and structure factors have been deposited with the Protein Data Bank with accession codes 6H0N and 6H0P. All other data are available from the authors on reasonable request.

Received: 11 July 2018; Accepted: 10 October 2019;
Published online: 25 November 2019

References

1. Picmanova, M. & Moller, B. L. Apiose: one of nature's witty games. *Glycobiology* **26**, 430–442 (2016).
2. Smith, J. et al. Functional characterization of UDP-apiose synthases from bryophytes and green algae provides insight into the appearance of apiose-containing glycans during plant evolution. *J. Biol. Chem.* **291**, 21434–21447 (2016).
3. Carter, M. S. et al. Functional assignment of multiple catabolic pathways for D-apiose. *Nat. Chem. Biol.* **14**, 696–705 (2018).
4. Smith, J. A. & Bar-Peled, M. Synthesis of UDP-apiose in bacteria: the marine phototroph *Geminicoccus roseus* and the plant pathogen *Xanthomonas pisi*. *PLoS One* **12**, e0184953 (2017).
5. Matsunaga, T. et al. Occurrence of the primary cell wall polysaccharide rhamnogalacturonan II in pteridophytes, lycophytes, and bryophytes. Implications for the evolution of vascular plants. *Plant Physiol.* **134**, 339–351 (2004).
6. Molhoj, M., Verma, R. & Reiter, W. D. The biosynthesis of the branched-chain sugar D-apiose in plants: functional cloning and characterization of a UDP-D-apiose/UDP-D-xylose synthase from *Arabidopsis*. *Plant J.* **35**, 693–703 (2003).
7. Ndeh, D. et al. Complex pectin metabolism by gut bacteria reveals novel catalytic functions. *Nature* **544**, 65–70 (2017).
8. Kim, M., Kang, S. & Rhee, Y. H. De novo synthesis of furanose sugars: catalytic asymmetric synthesis of apiose and apiose-containing oligosaccharides. *Angew. Chem. Int. Ed.* **55**, 9733–9737 (2016).
9. Picken, J. M. & Mendicino, J. The biosynthesis of D-apiose in *Lemna minor*. *J. Biol. Chem.* **242**, 1629–1634 (1967).
10. Sandermann, H. Jr., Tisue, G. T. & Grisebach, H. Biosynthesis of D-apiose. IV. Formation of UDP-apiose from UDP-D-glucuronic acid in cell-free extracts of parsley (*Apium petroselinum* L.) and *Lemna minor*. *Biochim. Biophys. Acta* **165**, 550–552 (1968).
11. Choi, S. H., Ruszczycky, M. W., Zhang, H. & Liu, H. W. A fluoro analogue of UDP-α-D-glucuronic acid is an inhibitor of UDP-α-D-apiose/UDP-α-D-xylose synthase. *Chem. Commun.* **47**, 10130–10132 (2011).
12. Choi, S. H. et al. Analysis of UDP-D-apiose/UDP-D-xylose synthase-catalyzed conversion of UDP-D-apiose phosphonate to UDP-D-xylose phosphonate: implications for a retroaldol-aldol mechanism. *J. Am. Chem. Soc.* **134**, 13946–13949 (2012).
13. Eixelsberger, T. et al. Isotope probing of the UDP-apiose/UDP-xylose synthase reaction: evidence of a mechanism via a coupled oxidation and aldol cleavage. *Angew. Chem. Int. Ed.* **56**, 2503–2507 (2017).
14. Mendicino, J. & Abouissa, H. Conversion of UDP-D-glucuronic acid to UDP-D-apiose and UDP-D-xylose by an enzyme isolated from *Lemna minor*. *Biochim. Biophys. Acta* **364**, 159–172 (1974).
15. Kelleher, W. J. & Grisebach, H. Hydride transfer in the biosynthesis of uridine diphospho-apiose from uridine diphospho-D-glucuronic acid with an enzyme preparation of *Lemna minor*. *Eur. J. Biochem.* **23**, 136–142 (1971).
16. Baron, D. & Grisebach, H. Further studies on the mechanism of action of UDP-apiose/UDP-xylose synthase from cell cultures of parsley. *FEBS J.* **38**, 153–159 (1973).
17. Gebb, C., Baron, D. & Grisebach, H. Spectroscopic evidence for the formation of a 4-keto intermediate in the UDP-apiose/UDP-xylose synthase reaction. *Eur. J. Biochem.* **54**, 493–498 (1975).
18. Kelleher, W. J., Baron, D., Ortmann, R. & Grisebach, H. Proof for the origin of the branch hydroxymethyl carbon of D-apiose from carbon 3 of D-glucuronic acid. *FEBS Lett* **22**, 203–204 (1972).
19. Guyett, P., Glushka, J., Gu, X. & Bar-Peled, M. Real-time NMR monitoring of intermediates and labile products of the bifunctional enzyme UDP-apiose/UDP-xylose synthase. *Carbohydr. Res.* **344**, 1072–1078 (2009).
20. Persson, B. et al. The SDR (short-chain dehydrogenase/reductase and related enzymes) nomenclature initiative. *Chem. Biol. Interact.* **178**, 94–98 (2009).
21. Kavanagh, K. L., Jornvall, H., Persson, B. & Oppermann, U. Medium- and short-chain dehydrogenase/reductase gene and protein families: the SDR superfamily: functional and structural diversity within a family of metabolic and regulatory enzymes. *Cell. Mol. Life Sci.* **65**, 3895–3906 (2008).
22. Jornvall, H. et al. Short-chain dehydrogenases/reductases (SDR). *Biochemistry* **34**, 6003–6013 (1995).
23. Filling, C. et al. Critical residues for structure and catalysis in short-chain dehydrogenases/reductases. *J. Biol. Chem.* **277**, 25677–25684 (2002).
24. Thibodeaux, C. J., Melancon, C. E. & Liu, H. W. Natural-product sugar biosynthesis and enzymatic glycodiversification. *Angew. Chem. Int. Ed.* **47**, 9814–9859 (2008).
25. Eixelsberger, T. et al. Structure and mechanism of human UDP-xylose synthase: evidence for a promoting role of sugar ring distortion in a three-step catalytic conversion of UDP-glucuronic acid. *J. Biol. Chem.* **287**, 31349–31358 (2012).
26. Bar-Peled, M., Griffith, C. L. & Doering, T. L. Functional cloning and characterization of a UDP-glucuronic acid decarboxylase: the pathogenic fungus *Cryptococcus neoformans* elucidates UDP-xylose synthesis. *Proc. Natl Acad. Sci. USA.* **98**, 12003–12008 (2001).
27. Gatzeva-Topalova, P. Z., May, A. P. & Sousa, M. C. Crystal structure of *Escherichia coli* ArnA (PmrI) decarboxylase domain. A key enzyme for lipid A modification with 4-amino-4-deoxy-L-arabinose and polymyxin resistance. *Biochemistry* **43**, 13370–13379 (2004).
28. Polizzi, S. J. et al. Human UDP-α-D-xylose synthase and *Escherichia coli* ArnA conserve a conformational shunt that controls whether xylose or 4-keto-xylose is produced. *Biochemistry* **51**, 8844–8855 (2012).
29. Matern, U. & Grisebach, H. UDP-apiose/UDP-xylose synthase. Subunit composition and binding studies. *Eur. J. Biochem.* **74**, 303–312 (1977).
30. Gatzeva-Topalova, P. Z., May, A. P. & Sousa, M. C. Structure and mechanism of ArnA: conformational change implies ordered dehydrogenase mechanism in key enzyme for polymyxin resistance. *Structure* **13**, 929–942 (2005).
31. Pfeiffer, M. et al. A parsimonious mechanism of sugar dehydration by human GDP-mannose-4,6-dehydratase. *ACS Catal.* **9**, 2962–2968 (2019).
32. Gerratana, B., Cleland, W. W. & Frey, P. A. Mechanistic roles of Thr134, Tyr160, and Lys 164 in the reaction catalyzed by dTDP-glucose 4,6-dehydratase. *Biochemistry* **40**, 9187–9195 (2001).
33. Kirschner, K. N. et al. GLYCAM06: a generalizable biomolecular force field. Carbohydrates. *J. Comput. Chem.* **29**, 622–655 (2008).
34. Berger, E. et al. Acid-base catalysis by UDP-galactose 4-epimerase: correlations of kinetically measured acid dissociation constants with thermodynamic values for tyrosine 149. *Biochemistry* **40**, 6699–6705 (2001).
35. Baron, D. & Grisebach, H. Further studies on mechanism of action of UDP-apiose/UDP-xylose synthase from cell-cultures of parsley. *Eur. J. Biochem.* **38**, 153–159 (1973).
36. Fujimori, T. et al. Practical preparation of UDP-apiose and its applications for studying apiosyltransferase. *Carbohydr. Res.* **477**, 20–25 (2019).

Acknowledgements

The contributions of P. Scudieri (enzyme characterization), A. Lepak (UDP-apiose HPLC assay) and J. Coines (analysis of MD trajectories) are gratefully acknowledged. This work was supported by the Federal Ministry of Science, Research and Economy (BMWFW), the Federal Ministry of Traffic, Innovation and Technology (bmvit), the Styrian Business Promotion Agency SFG, the Standortagentur Tirol, and the Government of Lower Austrian and Business Agency Vienna through the COMET-funding programme managed by the Austrian Research Promotion Agency FFG. Funding from the Austrian Science Funds (FWF; I-3247 to B.N. and A.J.E.B.) and by the Italian Ministry of Education, University and Research (MIUR) (Dipartimenti di Eccellenza Program (2018–2022)—Department of Biology and Biotechnology 'L. Spallanzani' University of Pavia) is acknowledged.

Author contributions

S.S. performed protein crystallization and determined the structures. K.D.D., M.P. and C.R. performed MD simulations and QM calculations, and, with A.J.E.B., analysed the data. A.D., with F. de G. and A.J.E.B., designed enzyme variants and performed biochemical characterization. A.D., A.J.E.B. and H.W. performed the NMR analyses. A.J.E.B. performed substrate synthesis and product isolation. A.J.E.B. and A.D. performed the mechanistic analyses. B.N. and A.M. designed and supervised the research. The manuscript was written with contributions from all authors. B.N., A.D., A.M. S.S. and A.J.E.B. wrote the paper.

Competing interests

The authors declare no competing interests.

Additional information

Supplementary information is available for this paper at https://doi.org/10.1038/s41929-019-0382-8.

Correspondence and requests for materials should be addressed to A.M. or B.N.

Reprints and permissions information is available at www.nature.com/reprints.

Publisher's note Springer Nature remains neutral with regard to jurisdictional claims in published maps and institutional affiliations.

nature catalysis

SUPPLEMENTARY INFORMATION

https://doi.org/10.1038/s41929-019-0382-8

In the format provided by the authors and unedited.

Deciphering the enzymatic mechanism of sugar ring contraction in UDP-apiose biosynthesis

Simone Savino[1,2,7], Annika J. E. Borg[3,7], Alexander Dennig[2,3,7], Martin Pfeiffer[3], Francesca De Giorgi[1,3], Hansjörg Weber[4], Kshatresh Dutta Dubey[5], Carme Rovira[5,6], Andrea Mattevi[1*] and Bernd Nidetzky[2,3*]

[1]Department of Biology and Biotechnology, University of Pavia, Pavia, Italy. [2]Austrian Centre of Industrial Biotechnology, Graz, Austria. [3]Institute of Biotechnology and Biochemical Engineering, Graz University of Technology, NAWI Graz, Graz, Austria. [4]Institute of Organic Chemistry, Graz University of Technology, NAWI Graz, Graz, Austria. [5]Organic Chemistry Section, Department of Inorganic and Organic Chemistry & Institute of Computational and Theoretical Chemistry (IQTCUB), University of Barcelona, Barcelona, Spain. [6]Catalan Institution for Advanced Studies (ICREA), Barcelona, Spain. [7]These authors contributed equally: Simone Savino, Annika J. E. Borg, Alexander Dennig. *e-mail: andrea.mattevi@unipv.it; bernd.nidetzky@tugraz.at

SUPPLEMENTARY INFORMATION

Deciphering the enzymatic mechanism of sugar ring contraction in UDP-apiose biosynthesis

Simone Savino[a,b]§, Annika J. E. Borg[c]§, Alexander Dennig[b,c]§, Martin Pfeiffer[c], Francesca de Giorgi[a,c], Hansjörg Weber[d], Kshatresh Dutta Dubey[e], Carme Rovira[e,f], Andrea Mattevi[a,b]*, and Bernd Nidetzky[b,c]*

[a] Department of Biology and Biotechnology, University of Pavia, Via Ferrata 1, 27100, Pavia, Italy

[b] Austrian Centre of Industrial Biotechnology, Petersgasse 14, 8010 Graz, Austria

[c] Institute of Biotechnology and Biochemical Engineering, Graz University of Technology, NAWI Graz, Petersgasse 12, 8010 Graz, Austria

[d] Institute of Organic Chemistry, Graz University of Technology, NAWI Graz, Stremayrgasse 9, 8010 Graz, Austria

[e] Department of Inorganic and Organic Chemistry (Organic Chemistry Section) & Institute of Computational and Theoretical Chemistry (IQTCUB), University of Barcelona, Martí i Franquès 1, 08028 Barcelona, Spain

[f] Catalan Institution for Advanced Studies (ICREA), Passeig Lluís Companys 23, 08010 Barcelona.

* Corresponding authors (B.N., bernd.nidetzky@tugraz.at; A.M., andrea.mattevi@unipv.it)

§ Equally contributing first authors

Table of Contents

Supplementary Methods

Chemicals, enzymes and strains

Uridine monophosphate (UMP, 98% purity) was from Carbosynth (Compton, UK). Uridine diphosphate (UDP) and UDP-D-glucuronic acid (UDP-GlcA (**2**); >98% purity) was from Sigma-Aldrich (Vienna, Austria). NAD^+ (>98% purity) was from Roth (Karlsruhe, Germany). Deuterium

oxide (99.96% ^{2}H) was from Euriso-Top (Saint-Aubin Cedex, France). Polyethylene glycols in various lengths (200, 300, 400, 1000, 4000, 6000 and 8000) and ammonium sulphate were from Sigma-Aldrich. Protease inhibitors (leupeptin and pepstatin-A), DNase, PMSF (protease inhibitor), and lysozyme were also from Sigma-Aldrich. All other reagents and chemicals were of highest available purity. For plasmid DNA isolation the GeneJET Plasmid Miniprep Kit (Thermo Scientific; Waltham, MA, USA) was used. DpnI and Q5® High-Fidelity DNA polymerase were from New England Biolabs (Frankfurt am Main, Germany). Oligonucleotide primers were from Sigma-Aldrich. Sparse matrix and systematic screening kits for crystallization of UAXS were from Molecular Dimensions (Newmarket, Suffolk, UK), Qiagen (Hilden, Germany) and Jena Bioscience (Jena, Germany).

Expression and purification of UAXS for biochemical characterization

UAXS (cloned into pET26 vector) was expressed as N-terminally histidine tagged protein in *E. coli* BL21 (DE3) cells.[1] For this, cells were grown in lysogeny broth media (37 °C, 120 rpm; 50 µg/mL kanamycin) until reaching an OD_{600} of 0.6. Then IPTG (250 µM) was added followed by incubation of cells for 24 h (120 rpm, 18 °C). Disruption of cells and purification of UAXS via His-tag affinity chromatography (GE Healthcare 5 mL His trap column; loaded with Cu^{2+} instead of Ni^{2+}) was done as described elsewhere in detail.[1] Fractions containing pure protein (confirmed by SDS-PAGE; see Supplementary Figure 3) were pooled and concentrated to a volume of 200 to 300 µL using a Vivaspin Turbo 30 kDa cut-off centrifugation tube (Sartorius, Göttingen, Germany; 4000 × g, 4 °C). For removal of imidazole, 5 mL storage buffer (50 mM potassium phosphate buffer, pH 7.0; 5% (v/v) glycerol; 1 mM dithiothreitol) were added followed by centrifugation until reaching a volume of 200 to 300 µL. The washing step was repeated three times. For in-situ ^{1}H-NMR analysis of enzymatic reactions, the storage buffer was prepared in D_2O (pD 7.0). For long-term storage, purified enzymes were frozen in liquid N_2 and stored at -20 °C until further use. The protein concentration of purified UAXS was determined by UV spectroscopy (λ = 280 nm) on a DeNovix DS-11+ micro volume spectrophotometer (DeNovix, Wilmington, DE, USA). The molar extinction coefficient of 48360 $M^{-1}cm^{-1}$ and a molecular mass of 44703 Da were used for calculating the UAXS concentration.[1]

Expression and purification of UAXS for crystallization experiments

Expression of UAXS was done as described above using the identical *E. coli* strain and plasmid. Transformed cells were centrifuged (4000 x g for 15 minutes, 4 °C) and stored as pellet at -20°C. For purification of UAXS, cells were re-suspended in buffer A (20 mM Tris-HCl; pH 7.5; 50 mM NaCl) containing protease inhibitors (leupeptin and pepstatin-A; 10 µg/mL each), DNase (1

mg/mL), PMSF (2 mM), and lysozyme (10 µg/mL). Cells were disrupted by sonication and solid particles removed by centrifugation (70000 x g for 45 minutes, 4 °C). Clear supernatants were collected, pooled, and filtered through a 0.45 µM syringe filter before loading on a 5 mL His trap excel column (GE Healthcare). Prior to loading the protein, the column was connected to a single wavelength ÄKTA system (GE Healthcare) and equilibrated with buffer A. The filtered lysate was loaded onto the His trap column while collecting the flow through. Unbound *E. coli* proteins were removed by washing the column with 5 column volumes buffer A. Elution of UAXS was achieved at 50% buffer B (buffer A containing 400 mM imidazole). Dispensed 0.5 mL fractions were collected and samples were analysed by SDS-PAGE to determine purity. A single, abundant band at the expected molecular mass of 45 kDa was found in correspondence of the elution peak. Fractions containing pure UAXS were pooled and concentrated by centrifugation in 30 kDa cut-off Amicon centrifugal filter units (Merck Millipore, Darmstadt, Germany). The concentrated UAXS protein was loaded on a Superdex 200 Increase 10/300 size exclusion column (GE Healthcare). A single sharp peak obtained by size exclusion chromatography indicated a unique oligomeric state of UAXS as dimer (Supplementary Figure 5), making the sample suitable for crystallization experiments.

Crystallization and X-ray diffraction analysis of UAXS

Crystallization plates (Swissci, Molecular Dimensions for robot dispensing; Cryschem (Hampton Research, Aliso Viejo, CA, USA) for handmade conditions) were prepared containing 10 to 100 mg/mL purified UAXS protein. The experiments were reproduced multiple times without ligands or by adding 1 to 2 mM NAD^+ and/or 1 to 2 mM UDP. Systematic handmade screens of varying concentrations and varying types of polyethylene glycols and $(NH_4)_2SO_4$ were dispensed in sitting and hanging drop configurations. Further, crystallization screening kits (sparse matrix and systematic) were tested, dispensing them manually in hanging drop or with a Douglas Instruments Oryx 8 robot in 96-wells plates. The only positive hit yielding diffracting protein crystals was found in well D10 of Qiagen Classic Suite, composed of 0.8 M sodium phosphate, 0.8 M potassium phosphate, and 0.1 M sodium-HEPES (all pH 7.5). Initial crystals grew when supplementing 1 mM NAD^+ and 1 mM UDP to a 25 mg/mL protein solution. The obtained transparent crystals appeared as regularly shaped hexagonal based prisms (Supplementary Figure 6). Crystals were found to be reproducible in an identical handmade reservoir condition. Under those conditions, crystals could be grown also in absence of NAD^+ and UDP. The crystal structure of C100A variant was obtained under identical conditions in co-crystallization experiments with UDP-GlcA (**2**) (2 mM) and NADH (2 mM). The crystals were harvested and cryo-cooled in their respective crystallization solution added with 20% v/v glycerol, followed by X-ray diffraction analysis at the SLS facility (Villigen,

Switzerland) or ESRF (Grenoble, France). Diffracting crystals were displaying low anisotropy and, after XDS indexing[2], space group was found to be $P3_221$ (number 154 of International Tables of Crystallography) with defined cell parameters (a = 146.03 Å; b = 146.03 Å; c = 132.85 Å; $\alpha = 90°$; $\beta = 90°$; $\gamma = 120°$). Data were scaled using the Aimless program from CCP4 suite[3] and molecular replacement was performed with Phaser-MR[4] using a 29% sequence-identity model (PDB entry: 3SLG) trimmed with Chainsaw.[5] A Phenix Autobuild run[6] was performed to trace the main chain followed by a Fem run[7] to improve map density. At this point manual tracing of sidechains and poorly traced surface loops was performed using Coot[8] alternated to *REFMAC*5 cycles[9]. Non-crystallographic symmetry (NCS) was applied, taking advantage of the dimeric arrangement in the unit cell; translation-libration-screw-rotation (TLS) was also used. Molprobity[10] was used for model validation.

Molecular dynamics (MD) simulations and Quantum Mechanical/Molecular Mechanical (QM/MM) calculations

System Setup: Molecular Dynamics (MD) simulations were performed with the Amber 18 GPU code[11], using the Amber ff14SB force field for the protein, TIP3P model[12] for water and ions and GLYCAM06[13] for the UDP-GlcA substrate. Established force field parameters from the Amber database were used for the NAD^+ cofactor (http://research.bmh.manchester.ac.uk/bryce/amber/). Of the two UAXS-chains present in the experimental structures, chain A had no gaps or unresolved loops and was therefore used to generate a dimer by aligning two copies of chain A using UCSF Chimera.[14] The resulting dimer was protonated using Leap module of Amber18 and used as input for PROPKA (version 3.1) to ensure that all ionizable amino acids were correctly protonated and all His, Asn and Gln residues had their most probable orientations, respectively. The conserved Tyr185, which in other enzymes of this superfamily functions as catalytic acid-base[15], was simulated in the deprotonated or protonated state. MODELLER[16] was used to generate atom coordinates for missing side-chains of the protein. Since the nicotinamide of NAD^+ in the original structure of the C100A variant was only partially resolved, the missing coordinates were modelled by aligning each chain with the experimental structure of human UXS (PDB: 2B69)[15], which contains the complete structure of NAD^+. The resulting protein dimer including two copies of NAD^+ and UDP-GlcA (**2**) (Michaelis complex; Figure 2a,c) was placed into a truncated octahedral solvation box of water molecules extending to 10 Å from the protein surface, and then the complex was neutralized with Na^+ ions.

MD simulations: After proper parameterizations and setup, the resulting structure was minimized (5000 steps of steepest descent and 10000 steps of conjugate gradient) to remove poor contacts and

allow the system to relax. Afterwards, the system was gently annealed from 10 to 300 K under the isothermal (NVT) ensemble for 50 ps with a weak restraint of 5 kcal mol^{-1} $Å^{-2}$ applied on protein and ligands, while keeping water and ions relaxed. Subsequently, one ns of density equilibration in the isothermal-isobaric (NPT) ensemble at a target temperature of 300 K and a target pressure of 1.0 atm was performed. The Langevin thermostat[17] and the Barendsen barostat[18] with collision frequency of 2 ps, a pressure relaxation time of 1 ps with a weak restraint of 1 kcal mol^{-1} $Å^{-2}$ were used with a time step of 2 fs. It should be noted that the 1 ns of density equilibration is not identical with conformational equilibration, but rather a weakly restrained MD simulation, in which the system is slowly relaxed to achieve a uniform density after heating dynamics under periodic boundary conditions. Thereafter, we removed all of the restraints applied during heating and density dynamics and further equilibrated the system. Two replicas were considered. In each one, we equilibrated the system for ~3 ns to get a well-settled pressure and temperature for conformational and chemical analysis. The hydrogen bonds were constrained using SHAKE[19] while Particle Mesh Ewald[20] was used to treat the long rang electrostatic interactions in all simulations, with a cut off distance of 12 Å for the van der Waals interactions. Long-time scale MD production simulations were performed for 0.6 μs (300 ns for each replica). Analysis of the sugar ring conformations and the RMSD evolution along the simulation is provided in Supplementary Figure 15 (see below). All analyses of the trajectories were done with Cpptraj Module of the Amber MD package.[11]

QM/MM calculations: Two representative snapshots of active-site conformation were chosen from the MD trajectories and QM/MM (quantum mechanics/molecular mechanics) optimization was performed on those.[21] For QM/MM calculations, a snapshot from the most persistent conformation from each replica was taken. To find the most frequent conformation in each replica, we first performed a population analysis and subsequently, by visual inspection of the most populated trajectories, a conformation was chosen with suitable substrate-enzyme interactions for catalysis. NAD^+, GlcA, the phosphate group of UDP and protein residues (Cys100, Tyr105, Thr139, Glu141, Tyr185) were kept in the QM region. All other protein residues and water molecules were kept in the MM region. All atoms within 8 Å of GlcA were treated as active residues and their effect due to polarization on the QM atoms were considered in the QM/MM calculations. All QM/MM calculations were performed using ChemShell,[22,23] combining Turbomole[24] for the QM part and DL_POLY[25] for the MM part. The electronic embedding scheme was used to account for the polarizing effect of the enzyme environment on the QM region. The link atom model for the frontier covalent bonds on the QM and MM interfaces was applied to treat the QM/MM boundary. In QM/MM geometry optimizations, the QM region was treated by the hybrid B3LYP functional with

def2-SVP as basis set. The same force-fields as in the MD simulations previously described were employed throughout this study to describe the atoms of the MM region.

Detection and quantification of NADH in UAXS preparations

NADH fluorescence measurements were performed in a Hellma fluorescence cuvette (80 µL sample volume; Suprasil quartz, 3×3 mm light path) placed in a Hitachi F-4500 (Tokyo, Japan) fluorescence spectrophotometer (excitation slit: 5 nm, emission slit: 5 nm). NADH was quantified via its specific fluorescence using excitation wavelength (λ_{Ex}) of 340 nm and emission wavelength (λ_{Em}) of 460 nm, respectively. Defined concentrations of NADH (2.5 to 25 µM) were prepared in double distilled water and directly used for measurements. NADH bound in purified wild-type UAXS was determined by denaturation of the enzyme (10 µL, 19.6 and 23.5 µM) in methanol (90 µL) at 30 °C for 3 h. Solids were removed by centrifugation (16000 × g, 60 min, 4 °C). The supernatant was collected, and the fluorescence emission of the free cofactor measured as described above. The occupancy of NADH in UAXS was calculated in % based on the concentration of released NADH (in µM) divided by the total protein concentration (in µM) applied to the experiment (Supplementary Figure 12). To determine the possible exchange of NADH by NAD^+ in the active site of wild-type UAXS, 1.3 µM of purified enzyme was incubated in presence of 100 µM NAD^+ in potassium phosphate buffer (50 mM, pH 7). The decrease of the fluorescence emission signal (i.e. cofactor exchange from NADH to NAD^+; protein bound NADH has a higher quantum yield than free/unbound NADH[26]) was followed as described above (Supplementary Figure 12). In order to reduce the enzyme-bound NAD^+, UAXS (20 mg/mL, 412 µM) was incubated with $NaBH_4$ (300 mM final concentration). $NaBH_4$ was added in five steps (60 mM each) every 1 h and the final mixture was incubated at 37 °C for 16 h. The enzyme solution was transferred into a centrifugation filter tube (Vivaspin 500, 10 kDa cut-off) and washed five times (centrifugation at 16000 × g, 4 °C) thoroughly with buffer (25 mM Tris-HCl pH 7.0; 1 mM dithiothreitol) to remove residual $NaBH_4$. A sample of 12.5 µl was taken and the enzyme denatured by incubating it in methanol (75% (v/v) final concentration), followed by centrifugation (16000 x g, 4 °C, 1 h) to remove the solid residues. The supernatant was analyzed on a HPLC-UV system (see details for HPLC analysis below). The amount of released NADH was calculated based on a calibration curve for free NADH (Supplementary Figure 42). The efficiency of the reduction was confirmed by comparing the NADH content after $NaBH_4$ reduction to the NADH content of the same amount of denatured UAXS before reduction. Representative HPLC chromatograms before and after reduction are shown in Supplementary Figure 43.

Site-directed mutagenesis

Site-directed mutagenesis was performed using a modified version of the QuikChange protocol and Q5 DNA polymerase for DNA amplification. PCRs were performed in 50 µL reaction volume according to supplier's recommendation using 40 ng of plasmid DNA as template and 0.2 µM forward primer or reverse primer, respectively. The DNA oligonucleotide primers used are shown below. The underlined nucleotides highlight the mutations introduced by PCR.

Name	Mutation	DNA primer sequence (5'-3')
C100A_Fw	C100A	CAATCTGGCGGCCATTGCTACGCCTGCTGATTATAAC
C100A_Rv	C100A	GTTATAATCAGCAGGCGTAGCAATGGCCGCCAGATTG
C100S_Fw	C100S	CAATCTGGCTGCAATTAGCACGCCTGCTGATTATAAC
C100S_Rv	C100S	GTTATAATCAGCAGGCGTGCTAATTGCAGCCAGATTG
Y105F_Fw	Y105F	CATTTGTACGCCTGCTGATTTTAACACCCGTCCGCTGGAC
Y105F_Rv	Y105F	GTCCAGCGGACGGGTGTTAAAATCAGCAGGCGTACAAATG
Y105A_Fw	Y105A	CATTTGTACGCCTGCTGATGCTAACACCCGTCCGCTGGAC
Y105A_Rv	Y105A	GTCCAGCGGACGGGTGTTAGCATCAGCAGGCGTACAAATG
T139V_Fw	T139V	GATCCATTTTTCCGTGTGTGTGAAGTGTACGGC
T139V_Rv	T139V	GCCGTACACTTCACACACGGAAAAATGGATC
C140S_Fw	C140S	CATTTTTCCACCAGCGAAGTGTACGGC
C140S_Rv	C140S	GCCGTACACTTCGCTGGTGGAAAAATG
C140A_Fw	C140A	CATTTTTCCACCGCTGAAGTGTACGGC
C140A_Rv	C140A	GCCGTACACTTCAGCGGTGGAAAAATG
Y185F_Fw	Y185F	CAGCGTTGGTCTTTTGCATGTGCTAAAC
Y185F_Rv	Y185F	GTTTAGCACATGCAAAAGACCAACGCTG
E141A_Fw	E141A	CATTTTTCCACCTGTGCAGTGTACGGCAAAACGATTGGTTC
E141A_Rv	E141A	CACTGCACAGGTGGAAAAATGGATCAGGCGTTTGTTGTTTTCACTGC

First, three cycles of linear PCR amplification were done with separate forward and reverse primers (initial denaturation: 1 min/94°C; 3 cycles amplification: 30 sec/94°C for denaturation, 30 sec/55°C for primer annealing and 15 min/72°C extension; final extension: 72°C/10 min). Both reaction solutions were mixed (combining forward/reverse primers) and the PCR program was restarted for 15 cycles of exponential DNA amplification (initial denaturation: 1 min/94°C; 3 cycles amplification: 30 sec/94°C for denaturation, 30 sec/55°C for primer annealing and 6 min/72°C extension; final extension: 72°C/10 min). PCR products were separated by agarose gel electrophoresis and visualized by DNA staining. Residual template DNA was removed by addition of 2 U DpnI and following the recommended procedure by the supplier. Without further purification, PCR products were transformed via heat-shock into chemical competent *E. coli* Top 10 cells (New England Biolabs, Frankfurt am Main, Germany). Plasmid DNA was extracted and

sequenced with T7prom/T7term primers provided by LGC Genomics (Berlin, Germany) to verify mutations. Correct constructs were transformed into *E. coli* BL21 cells followed by expression of UAXS as described above.

Product analysis by HPLC

Reaction samples were analyzed by reversed phase HPLC-UV (λ = 262 nm) on a Shimadzu Prominence HPLC system (Shimadzu, Korneuburg, Austria). Separation was achieved on a Kinetex C18 analytical HPLC column (5 µm; 4.6 × 50 mm; Phenomenex, Aschaffenburg, Germany) using isocratic elution (35 °C; flow rate of 2 mL/min; 5 µL injection volume; mobile phase: 87.5% 40 mM tetra-n-butylammonium bromide in 20 mM potassium phosphate buffer (pH 5.9) and 12.5% acetonitrile). Separation of UDP-xylose (**3**) and UDP-apiose (**1a**) is not possible under the described conditions.[1,27] Therefore, the formation of UDP-apiose (**1a**) can be referred to the release of UMP (formed during decomposition of UDP-apiose).[1,27] Authentic standards of UMP and UDP-GlcA (**2**) were used as analytical references (Supplementary Figures 17, 18). UMP is a known decomposition product derived from self-cyclization of instable UDP-apiose.[28] An optimized protocol for HPLC-UV detection of UDP-apiose (**1a**) is described below in the section describing the conversion of UDP-4-keto-xylose (**5**) with UAXS and human UXS.

Kinetic characterization of enzymatic conversion of UDP-GlcA

Enzymatic rates (k_{cat}) were measured for wild-type UAXS and all generated variants. We used purified human UXS to generate UDP-xylose (**3**) as analytical reference (Supplementary Figure 19).[1,29] The reaction mixtures contained (if not stated otherwise) 2 mM UDP-GlcA (**2**), 100 µM NAD^+ and 14 mg/mL enzyme (except: wild-type UAXS and C100S/C140A variant, 2 mg/mL; C100S variant, 7 mg/mL; Y105A variant, 3.5 mg/mL) in a final reaction volume of 1 mL potassium phosphate buffer (pH 7.0, 50 mM). Reactions with the T139V variant contained 0.5 mM UDP-GlcA (**2**), 1.0 mM NAD^+ and 3.3 mg/mL enzyme. In all cases, UDP-GlcA (**2**) was added to initiate the reaction followed by incubation at 30 °C (no agitation). In order to stop the reaction at defined time points, 50 µL reaction sample were taken and mixed with equal volume of a 50% acetonitrile. Samples were incubated for at least one hour on ice, to allow denaturation of the protein. Insoluble compounds were removed by centrifugation (16000 × g, 15 min, 4 °C). Depletion of UDP-GlcA (**2**) over time was used to calculate enzyme activity (k_{cat}) (see Supplementary Figures 23-32). Initial rates were obtained from the linear part of the time course, as shown in Supplementary Figures 23-32. The k_{cat} was calculated from the initial rate, recorded in nmol/(min mg protein), with the appropriate molecular mass of the functional enzyme monomer (wild-type UAXS: 44703 g/mol).

The activity of wild-type UAXS for conversion of UDP-GlcA (**2**) was further recorded in D_2O (Supplementary Figure 36). Therefore, purified wild-type UAXS was re-buffered against phosphate buffer prepared in D_2O (50 mM potassium phosphate; pD 7.0) containing 1 mM DTT, 1% glycerol (w/v). The enzyme (2 mg/mL, 44.7 µM), NAD^+ (100 µM) and UDP-GlcA (**2**) (1 mM) were mixed together in the corresponding buffers (prepared in H_2O or D_2O; pH/pD 7.0) followed by incubation at 30 °C for 2 h. Samples were taken at defined time points and the reaction was quenched by addition of methanol (50%). After centrifugation the supernatant was collected and analyzed by HPLC.

^{1}H-NMR analysis of enzymatic reactions

Enzyme selectivity was determined by ^{1}H-NMR analysis (Supplementary Figures 33-35). For this, all reagents including UAXS were prepared using exclusively D_2O as solvent. The reaction mixtures contained 2 mM UDP-GlcA (**2**), 100 µM NAD^+, 2 mg/mL purified UAXS in a final volume of 700 µL of potassium phosphate buffer (50 mM; pD 7.0). UDP-GlcA (**2**) conversions were carried out for 24 h at 30°C. Samples were centrifuged (15 min, 4 °C, 16000 g) and 700 µL filled into NMR tubes followed by measurement in a Varian INOVA 500-MHz NMR spectrometer (Agilent Technologies, Santa Clara, California, USA). The VNMRJ 2.2D software was used for all measurements. ^{1}H-NMR spectra (499.98 MHz) were recorded on a 5 mm indirect detection PFG-probe with pre-saturation of the water signal by a shaped pulse. The following standard pre-saturation sequence was performed: 2 s relaxation delay; 90° proton pulse; 2.048 s acquisition time; 8 kHz spectral width; number of points 32 k. Signals from anomeric C1 of the sugar were used for integration and quantification of products (percentage of each proton signal relative to the sum of all C1 proton signals in a sample) in order to determine selectivity of wild-type UAXS and mutants. ACD/NMR Processor Academic (Edition 12.0, Advanced Chemistry Development Inc., Toronto, CA) was used for evaluation of spectra.

Synthesis and isolation of UDP-xylose (3) from deuterium wash-in experiments

For preparative isolation of UDP-xylose (**3**), 2 mM UDP-GlcA (**2**) were converted in total volume of 9 ml buffer prepared in D_2O (50 mM potassium phosphate, pD 7.0). The reactions were started by adding 100 µM NAD^+ and enzyme (2 mg/ml for wild-type UAXS or 5 mg/ml in case of variants C100A and C100S). All reactions were carried out overnight at 30°C (no agitation) until no further substrate depletion was detectable by HPLC. Residual enzyme was removed by centrifugal filtration (4000 x g, 4 °C) using a 10 kDa cut-off centrifugation tube. For purification, the flow-through was loaded at 2 mL/min flowrate via a 10 ml sample loop onto an ÄKTA FPLC system (GE Healthcare) connected to a 125 ml Toyopearl SuperQ-650M anion exchange column (GE

Healthcare) equilibrated with 20 mM sodium acetate solution (pH 4.3). Flow-rates between 3 and 5 mL/min were used during the purification process depending on back pressure of the column. After washing the column with 250 mL NaOAc (20 mM), compounds were eluted with a step-wise gradient of 1 M sodium acetate buffer (pH 4.3). The following elution steps were used during compound purification: 150 mL of 200 mM NaOAc, 250 mL of 350 mM NaOAc, 150 mL of 500 mM NaOAc, 330 mL of 1 M NaOAc. After eluting all compounds, the column was re-equilibrated in 20 mM NaOAc. Fractions containing the desired products were identified by UV absorption (λ = 254 nm). A representative chromatogram from the ion-exchange purification is shown in Supplementary Figure 37. The fractions containing UDP-xylose (**3**) (confirmed by HPLC) were combined and concentrated under reduced pressure (40 °C) to a final volume of 5 to 10 mL using a Laborota 4000 rotary evaporator (Heidolph, Schwabach, Germany). At next NaOAc was removed by size-exclusion chromatography. Therefore, the concentrated sample was loaded via a 5 mL sample loop onto an ÄKTA FPLC system connected to a Superdex G-10 column (GE Healthcare). Filtered and deionized water was used as mobile phase and elution of UDP-xylose (**3**) was detected by UV absorption (λ = 254 nm). A representative ÄKTA chromatogram from the desalting step is shown in Supplementary Figure 38. The fractions containing UDP-xylose (**3**) were combined and concentrated under reduced pressure (40 °C) to a final volume of approximately 20 mL. Desalted UDP-xylose (**3**) was frozen in liquid N_2 and residual H_2O was removed by lyophilization (Christ Alpha 1-4 lyophilizer, B. Braun Biotech International, Melsungen, Germany), yielding the nucleotide sugar (>95% pure) as white powder. The product was re-dissolved in D_2O (700 µL) prior to NMR analysis.

Enzymatic synthesis and isolation of UDP-4-keto-xylose

UDP-4-keto-xylose (**5**) was synthesized by converting UDP-GlcA (**2**) with the C-terminal subunit of ArnA from *E. coli*.[30] The enzyme was obtained as synthetic gene and expressed in *E. coli* BL21 (DE3). After affinity chromatography utilizing a C-terminal Strep-tag, the protein was obtained in >90% purity (Supplementary Figure 39). The obtained protein was re-buffered (25 mM Tris-HCl pH 8.0 and 1 mM DTT) and stored at -20 °C. The reaction for synthesis of UDP-4-keto-xylose (**5**) contained 2 mM UDP-GlcA (**2**), 2 mM NAD^+ and 5 mg/mL purified ArnA. The sample was incubated for 5 min at 30 °C (no agitation; 70% conversion, >99% selectivity for **5**). Longer reaction times resulted in significant formation of the unwanted side product UDP-xylose (**3**).[31] The conversion of UDP-GlcA (**2**) was constantly followed by HPLC-UV (see Supplementary Figure 40). When reaching the highest amount of UDP-4-keto-xylose (**5**) ArnA was removed from the mixture by centrifugal filtration (Vivaspin Turbo centrifugal filter tube, 30 kDa cut-off). The desired product was separated from the other components by anion exchange and size-exclusion

chromatography using ÄKTA FPLC system (see above purification of UDP-Xyl).[15] The purity and structure of UDP-4-keto-xylose (**5**) was confirmed by ^{1}H-NMR (Supplementary Figure 41).

Conversion of UDP-4-keto-xylose (5) with UAXS and UXS

The UDP-4-keto-xylose (**5**) (1 mM) and NADH (10 mM) were dissolved in KPi buffer (50 mM, pH 7.0). The reaction was started by addition of the respective SDR catalyst (20 mg/mL wild-type UAXS (reduced or non-reduced), 15 mg/mL C100S variant or 5 mg/mL human UXS) followed by incubation at 30 °C (no agitation). The reaction was quenched with methanol (75% (v/v) final concentration) at desired time points and the precipitated enzyme was removed by centrifugation (16000 x g, 4 °C, 30 min) prior to HPLC analysis. The products were separated on a Kinetex C18 column (5 µm, 100 Å, 150 x 4.6 mm) using 3% methanol and 97% tetra-n-butylammonium bromide (TBAB) buffer (40 mM, 20 mM KPi, pH 5.9) as mobile phase. UDP-sugars and NAD(H) were detected via UV absorbance at 262 nm. Examples of representative HPLC chromatograms for wild-type UAXS, C100S variant and human UXS are shown in Supplementary Figure 45. Wild-type UAXS showed similar activity and behavior for conversion of UDP-4-keto-xylose (**5**) using either reduced (0.06 mU/mg) or non-reduced (0.055 mU/mg) enzyme. For deuterium wash-in experiments, UDP-4-keto-xylose (**5**) (2 mM) and NADH (10 mM) were dissolved in KPi buffer (50 mM, pD 7.0). All solutions and UAXS were prepared using D_2O as bulk solvent as stated above. The reaction was started by addition of UAXS (11 mg/mL in case of wild-type UAXS; 3.8 mg/mL in case of C100A variant). The reactions were run for 6 h followed by removal of enzymes centrifugal filtration (Vivaspin 500, 10 kDa cut-off). Clear supernatants were collected, frozen in liquid N_2 and freeze-dried overnight. Solid residues were dissolved in D_2O (600 µL) and used for NMR (HSQC) analysis.

Supporting Tables and Figures

Supplementary Table 1: Crystallographic table for structures of wild-type UAXS in complex with UDP and NAD^+ and the C100A variant in complex with UDP-GlcA (**2**) and NADH, respectively.[a]

	Wild-type, PDB: 6H0N	C100A, PDB: 6H0P
Resolution range	49.1 - 3.0 (3.2 - 3.0)	48.4 - 3.5 (3.8 - 3.5)
Space group	$P3_221$	$P3_221$
Unit cell (Å), (°)	146.0 146.0 132.8 90 90 120	144.6 144.6 130.5 90 90 120
Total reflections	143316 (20101)	173716 (38422)
Unique reflections	32264 (4488)	20833 (4867)
Multiplicity	4.4 (4.5)	8.3 (7.9)
Completeness (%)	98.9 (95.4)	99.8 (99.2)
Mean I/sigma (I)	9.2 (1.0)	13.1 (1.9)
R-merge (%)	0.146 (1.291)	0.151 (1.138)
CC1/2[b]	0.992 (0.378)	0.998 (0.844)
R-work (%)	0.207 (0.369)	0.200 (0.360)
R-free	0.253 (0.377)	0.243 (0.317)
Number of non-hydrogen atoms	6009	5870
Protein	5848	5723
Ligands	138	147
Waters	23	-
RMS (bonds) (Å)	0.013	0.013
RMS (angles) (°)	1.82	1.91

Ramachandran favoured (%)	94.44	91.85
Ramachandran allowed (%)	4.75	7.34
Ramachandran outliers (%)	0.81	0.82
Average B-factor	77.85	125.51
Macromolecules	80.35	131.0
NAD^+/NADH	74.30	125.8
UDP/ UDP-GlcA	70.00	124.1

[a] Statistics for the highest-resolution shell are shown in parentheses

[b] A cut-off criterion for resolution limits was applied on the basis of the mean intensity correlation coefficient of half-subsets of each dataset

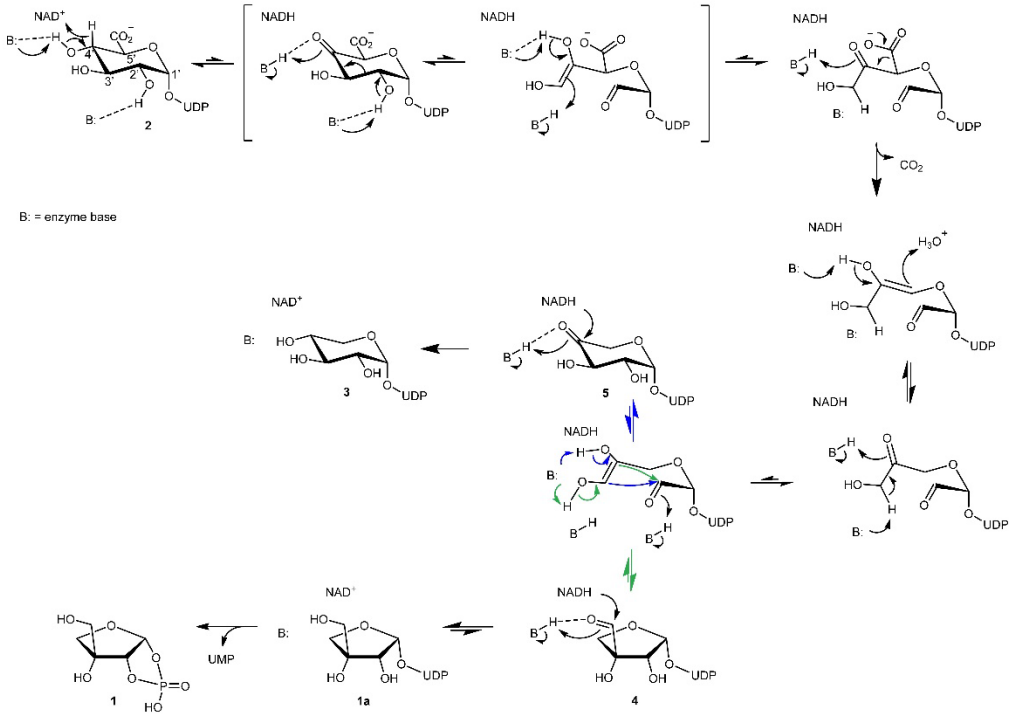

Supplementary Figure 1. Proposed mechanism of UAXS based on evidence from earlier studies. The steps of substrate oxidation, aldol cleavage for ring opening, and decarboxylation are shown in full detail here (see Figure 1 of main text). Kinetic and mechanistic studies of UAXS[1] suggest that substrate oxidation and aldol cleavage are strongly coupled steps of the reaction but it is not known how UAXS promotes the multi-step catalytic conversion of UDP-GlcA (**2**). The reaction of UXS (UDP-xylose synthase) does not involve ring opening. Like the UAXS reaction, it proceeds via an initial oxidation of UDP-GlcA (**2**) at the C4'. Decarboxylation of the incipient UDP-4-keto-GlcA leads to UDP-4-keto-xylose (**5**) which is reduced to UDP-xylose (**3**). **1** = α-D-apiofuranosyl-1,2-cyclic phosphate; **1a** = UDP-apiose; **2** = UDP-GlcA; **3** = UDP-xylose; **5** = UDP-4-keto-xylose.

[Uniprot accession number of UAXS: Q9ZUY6]

```
>sp|Q9ZUY6|AXS1_ARATH  UDP-D-apiose/UDP-D-xylose  synthase  1  OS=Arabidopsis
thaliana GN=AXS1 PE=1 SV=1
MANGANRVDLDGKPIQPLTICMIGAGGFIGSHLCEKLLTETPHKVLALDVYNDKIKHLLEPDTVEWSGRIQFHRINIKHD
SRLEGLVKMADLIINLAAICTPADYNTRPLDTIYSNFIDALPVVKYCSENNKRLIHFSTCEVYGKTIGSFLPKDHPLRDD
PAFYVLKEDISPCIFGSIEKQRWSYACAKQLIERLVYAEGAENGLEFTIVRPFNWIGPRMDFIPGIDGPSEGVPRVLACF
SNNLLRREPLKLVDGGESQRTFVYINDAIEAVLLMIENPERANGHIFNVGNPNNEVTVRQLAEMMTEVYAKVSGEGAIES
PTVDVSSKEFYGEGYDDSDKRIPDMTIINRQLGWNPKTSLWDLLESTLTYQHRTYAEAVKKATSKPVAS

sp|Q9M0B6|GAE1_ARATH      QVR-----------TSAQIHRSGGISVLVTGATGFVGSHVSLALRKRGDGV-VGLDNFNN  122
sp|Q8NBZ7|UXS1_HUMAN      KIRDLEKSFTQKYPPVKFLSEKDRKRILITGGAGFVGSHLTDKLMMDGHEVTVVDNFFTG  124
sp|Q9ZUY6|AXS1_ARATH      ----MANG--ANR-VDLDGKPIQPLTICMIGAGGFIGSHLCEKLLTETPHKVLALDVYN-  52
sp|P77398|ARNA_ECOLI      TLG-LVQG--SRLNSQPACTARRRTRVLILGVNGFIGNHLTERLLREDHYEVYGLDIGS-  350
                                                 : : *  **:*.*:   *          :  .

sp|Q9M0B6|GAE1_ARATH      YYDPSLKRARRSLLSSRGIFVVEGDLNDAKLLAKLFD-----VVAFTHVMHLAAQAGVRY  177
sp|Q8NBZ7|UXS1_HUMAN      RK-----RNVEHWIGHENFELI-----------NHDVVEPLYIEVDQIYHLASPASPPN  167
sp|Q9ZUY6|AXS1_ARATH      -------DKIKHLLEPDTVEW-SGRIQFHRINIKHDSRLEGLVKMADLIINLAAICTPAD  104
sp|P77398|ARNA_ECOLI      -------DAISRFLNHPHFHFVEGDISI------HSEWIEYHVKKCDVVLPLVAIATPIE  397
                                  :    .               .          :  *.: .

sp|Q9M0B6|GAE1_ARATH      ALENPQSYVHSNIAGLVNLLEICKAANPQPAIVWASSSSVYGLNEKVPFSESD-------  230
sp|Q8NBZ7|UXS1_HUMAN      YMYNPIKTLKTNTIGTLNMLGLAKRVG--ARLLLASTSEVYGDPEVH------PQSED--  217
sp|Q9ZUY6|AXS1_ARATH      YNTRPLDTIYSNFIDALPVVKYCSENN--KRLIHFSTCEVYGKTIGSFLPKDHPLRDDPA  162
sp|P77398|ARNA_ECOLI      YTRNPLRVFELDFEENLRIIRYCVKYR--KRIIFPSTSEVYGMCSDKYFDE---------  446
                             .*   .  :    : ::  .        ::  *:..***

sp|Q9M0B6|GAE1_ARATH      ----------------RTDQPASLYAATKKAGEEITHTYNHIYGLAITGLRFFTVYGPWG  274
sp|Q8NBZ7|UXS1_HUMAN      -----------YWGHVNPIGPRACYDEGKRVAETMCYAYMKQEGVEVRVARIFNTFGPRM  266
sp|Q9ZUY6|AXS1_ARATH      FYVLKEDISPCIFGSI--EKQRWSYACAKQLIERLVYAEGAENGLEFTIVRPFNWIGPRM  220
sp|P77398|ARNA_ECOLI      ------DHSNLIVGPV--NKPRWIYSVSKQLLDRVIWAYGEKEGLQFTLFRPFNWMGPRL  498
                                        *   *:  : :  :     *: .   * *.  **
```

Supplementary Figure 2. Amino acid sequence alignment of UDP-GlcA (**2**) converting enzymes. (Top) The complete sequences of UAXS1 from *Arabidopsis thaliana* (Uniprot: Q9M0B6) used for this study. (Bottom) Sequence alignment shows partial sequences of epimerase GAE1 from *Arabidopsis thaliana* (Uniprot: Q9M0B6), UXS1 from *Homo sapiens* (Uniprot: Q8NBZ7), UAXS1 from *Arabidopsis thaliana* (Uniprot: Q9M0B6; this study) and ArnA from *E. coli* (Uniprot: P77398). Yellow highlighted amino acids correspond to active site residues targeted in UAXS for mutagenesis in this study as well as consensus amino acids in GAE1, UXS1, ArnA and UAXS1 (C100 and C140). Numbers indicate amino acid positions in the respective protein sequence.

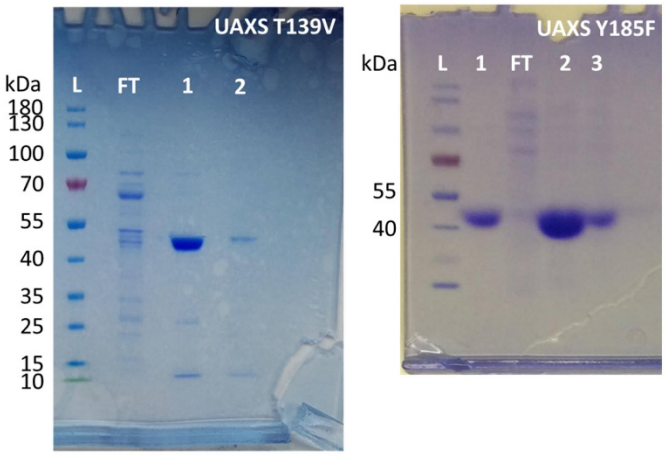

Supplementary Figure 3. Enzyme purification documented by SDS-PAGE, shown for variants T139V and Y185F. The wild-type UAXS and other variants yielded soluble protein with similar purity and quantity. L, molecular mass markers; FT, flow through during sample loading on His trap column; other lanes: protein after purification loaded in different quantities.

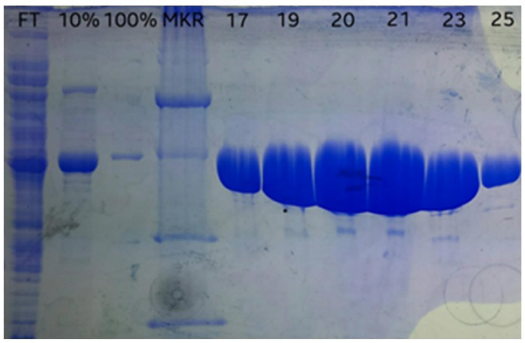

Supplementary Figure 4. SDS polyacrylamide gel showing purified wild-type UAXS used for crystallization experiments. From left to right: FT, flow through during sample loading on His trap column; 10% and 100%, wash steps with 10% and 100% buffer B, containing 400 mM imidazole; MKR, molecular mass marker; 17-25, fractions containing purified UAXS (elution with 50% buffer B).

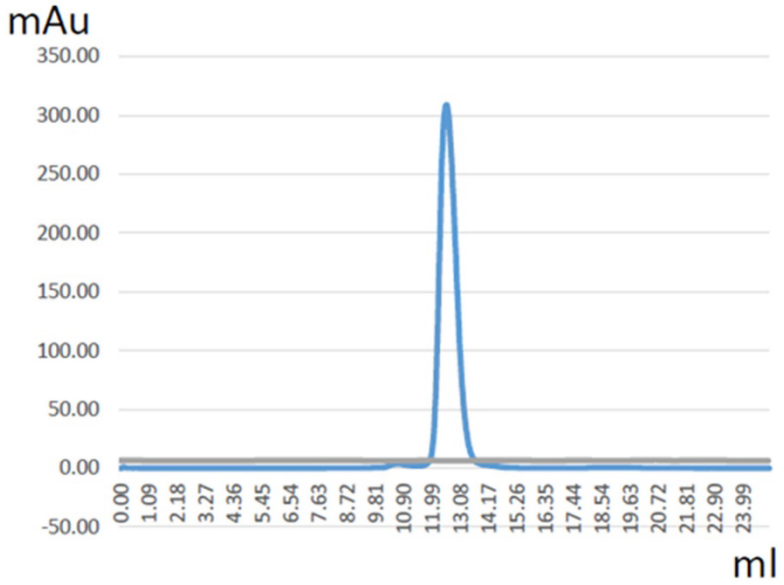

Supplementary Figure 5. Absorbance trace from size exclusion chromatography performed with purified wild-type UAXS. A single monodispersed peak consistent with a 90 kDa object (dimeric UAXS; 12 to 14 mL) is eluted from the column.

17

Supplementary Figure 6. Crystals of wild-type UAXS in a 4 μL sitting drop.

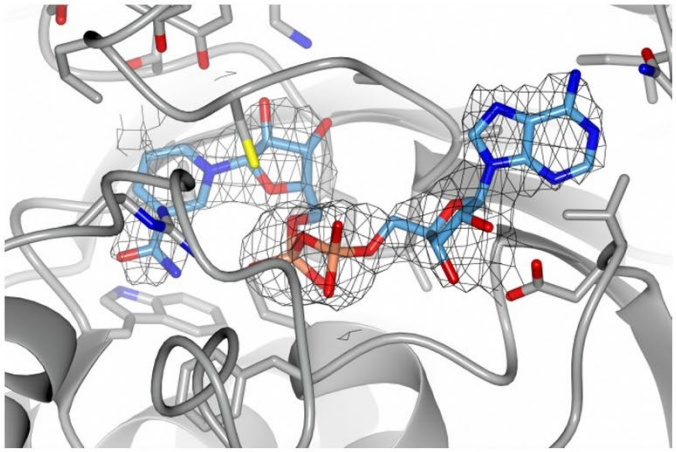

Supplementary Figure 7. The final weighted 2Fo-Fc electron density map with fully traced NAD^+ in wild-type UAXS. The contour level is 1.2 σ.

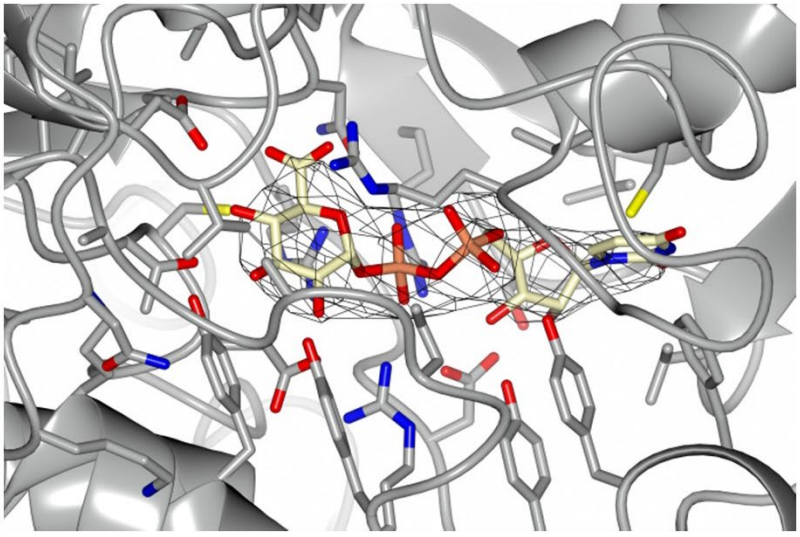

Supplementary Figure 8. The final weighted 2Fo-Fc electron density map for UDP-GlcA (**2**) within the structure of C100A variant co-crystallized with NADH and UDP-GlcA (**2**). The contour level is 1.2 σ.

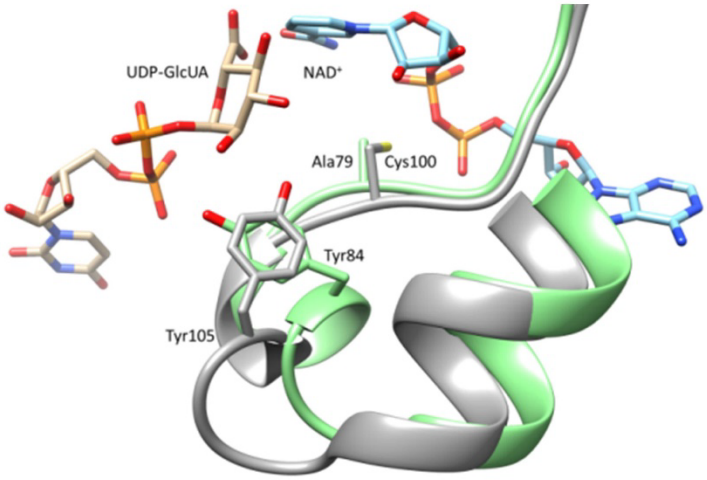

Supplementary Figure 9. Comparison of the loop proximal to the active site of UAXS (amino acid residues 97-115) and human UXS (amino acid residues 76-94; PDB: 2B69). In human UXS (light green ribbon)[22], the shorter loop results in Tyr84 pointing away from the active site (distance between the Tyr84-OH and the C2'-OH and C3'-OH is 3.1 and 5.5 Å, respectively), while in UAXS (grey ribbon) Tyr105-OH point towards the C2'-OH and C3'-OH of UDP-GlcA (**2**) with distances of 3.0 and 3.4 Å, respectively. The UAXS model was generated by combining two experimental structures (wild-type UAXS and C100A variant).

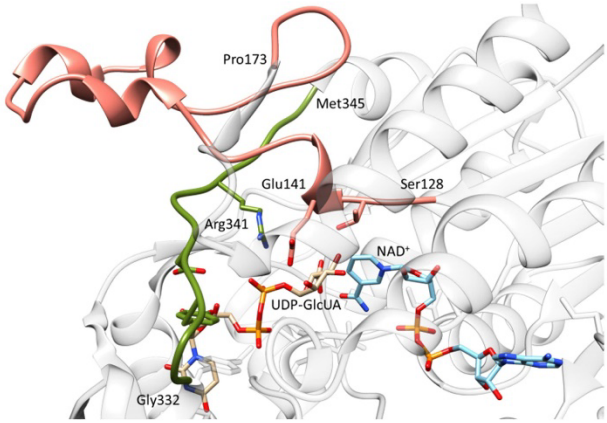

Supplementary Figure 10. Crystal structure of UAXS highlighting loops harbouring Glu141 (salmon ribbon, amino acid residues 128-173) and Arg341 (olive ribbon, amino acid residues 332-345).

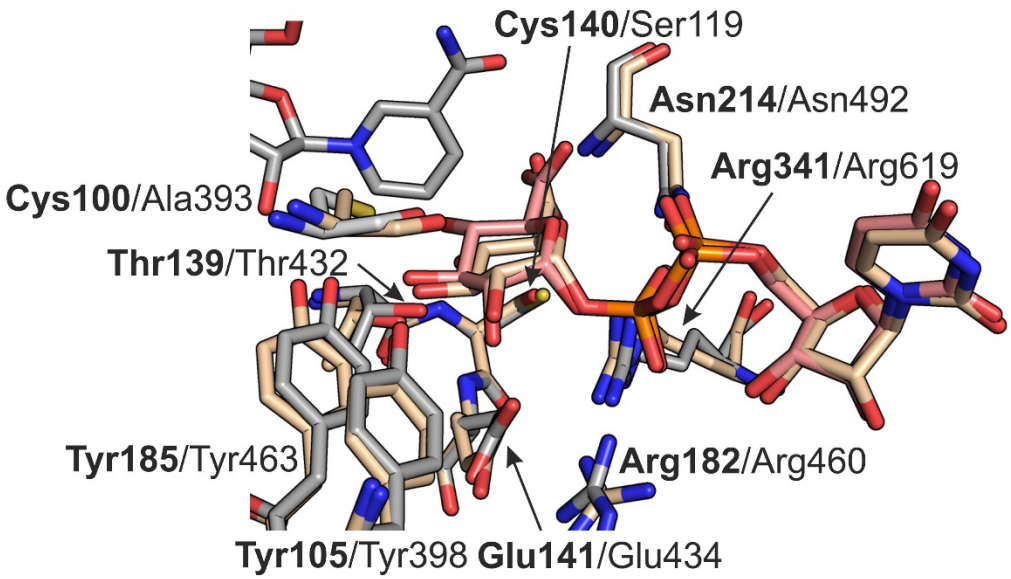

Supplementary Figure 11. Structural comparison of the active sites of wild-type UAXS (grey carbon atoms) in complex with UDP-GlcA (**2**) and NAD^+ and ArnA in complex with UDP-GlcA (**2**) (PDB entry 1Z7E; beige carbon atoms).[32] For comparison, the UAXS structure also contains the glucuronyl moiety of UDP-GlcA (**2**) in the conformation observed in the structure of the C100A variant (Supplementary Figure 8). The major differences in the active site are residues Cys100 and Cys140 of UAXS as compared to Ala393 and Ser119 of ArnA.

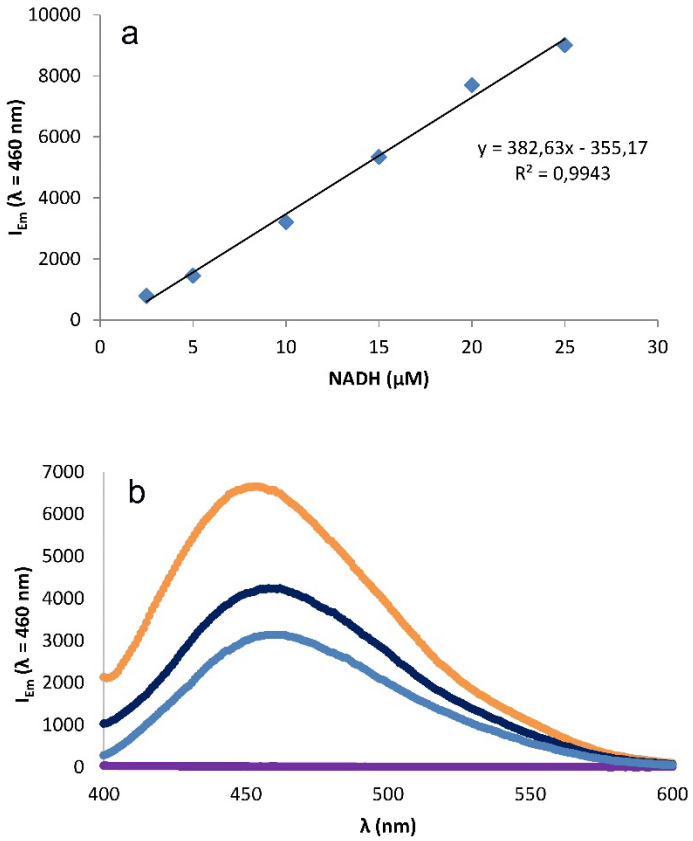

Supplementary Figure 12. NAD(H) binding to UAXS. The top panel (**a**) shows the calibration for NADH fluorescence. Standard solutions (80 μL each) of NADH were prepared in double distilled water and the fluorescence emission intensity was measured with λ_{Ex} at 340 nm and λ_{Em} at 460 nm. The bottom panel (**b**) shows the fluorescence emission spectra of released NADH from two independently purified UAXS preparations. Batch 1 (orange line): 18.3 μM NADH was released from 23.5 μM of UAXS (78% occupancy by NADH). Batch 2 (dark blue line): 12.0 μM NADH was released from 19.6 μM of UAXS (61% occupancy by NADH). Standard solution of 10 μM NADH in methanol (light blue line) was used as a reference. Purple line: storage buffer used in experiments with UAXS.

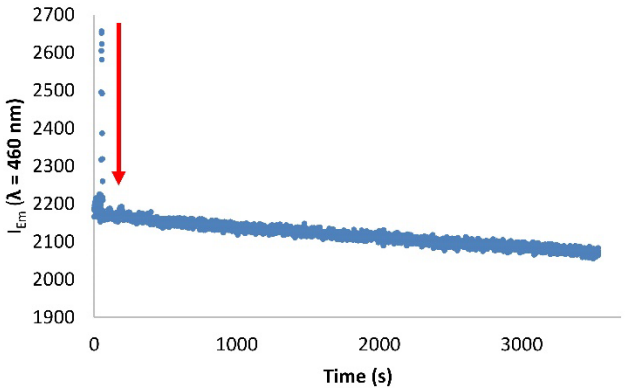

Supplementary Figure 13. Exchange of NADH by NAD^+ in the active site of wild-type UAXS. Note that there is a small spectral difference between the free and bound form of NADH.[26] NADH exists in (at least) two forms: a free state (unbound) with low quantum yield and a protein bound state, where the quantum yield can be substantially higher. The red arrow indicates the rapid drop in emission directly after addition of NAD^+ to the sample.

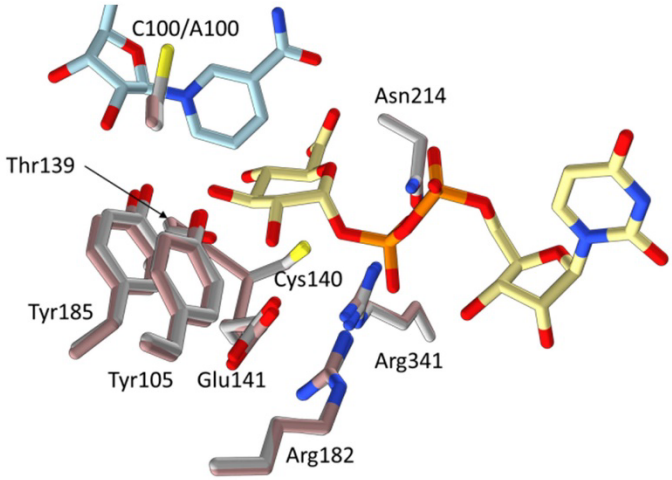

Supplementary Figure 14. Superposition of active-site residues of wild-type UAXS (light grey carbon atoms) and C100A variant (light brown carbon atoms).

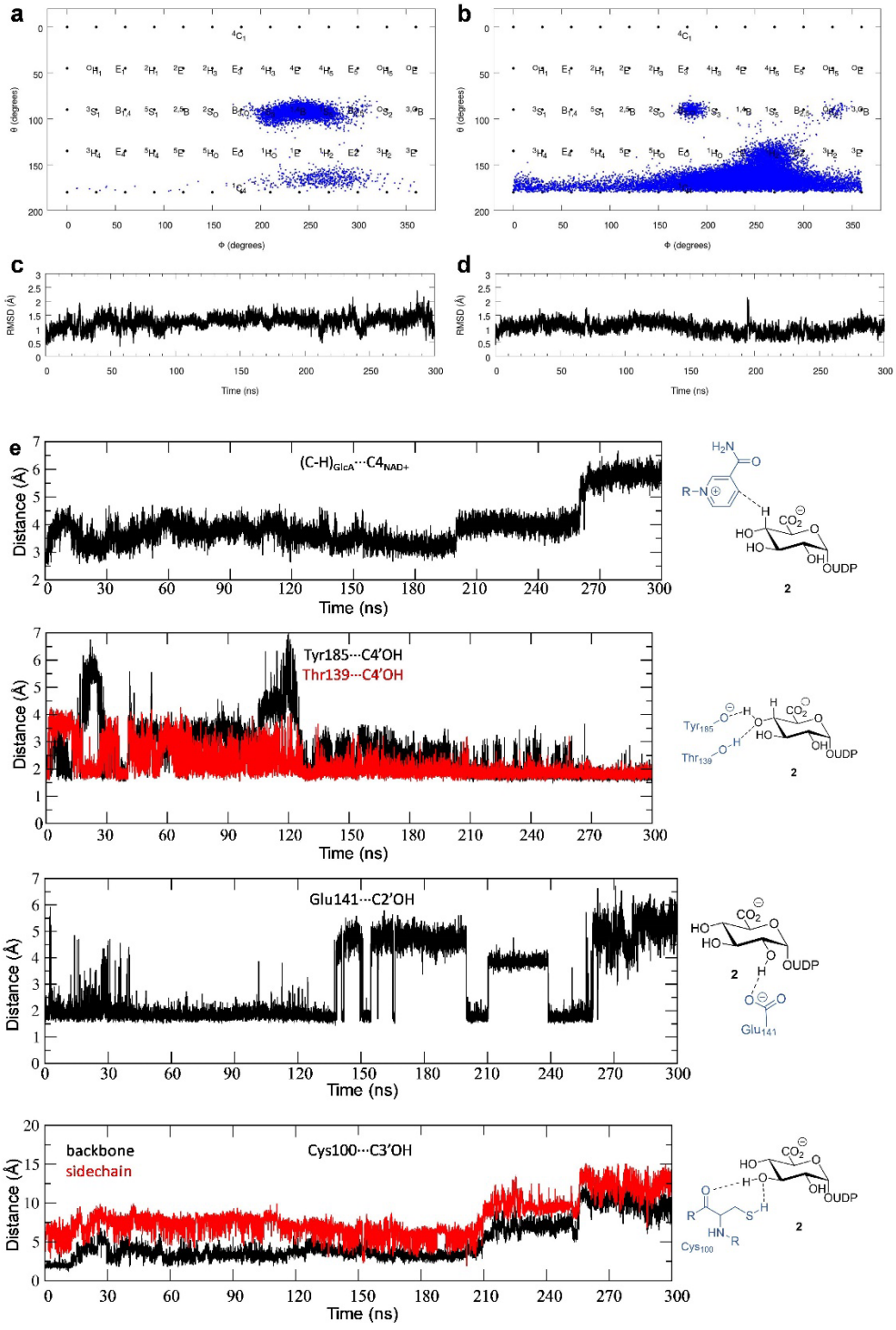
a
b
θ (degrees)
Φ (degrees)
c
d
RMSD (Å)
Time (ns)
e
(C-H)GlcA···C4NAD+
Distance (Å)
Time (ns)
Tyr185···C4'OH
Thr139···C4'OH
Glu141···C2'OH
backbone
sidechain
Cys100···C3'OH
OUDP
2

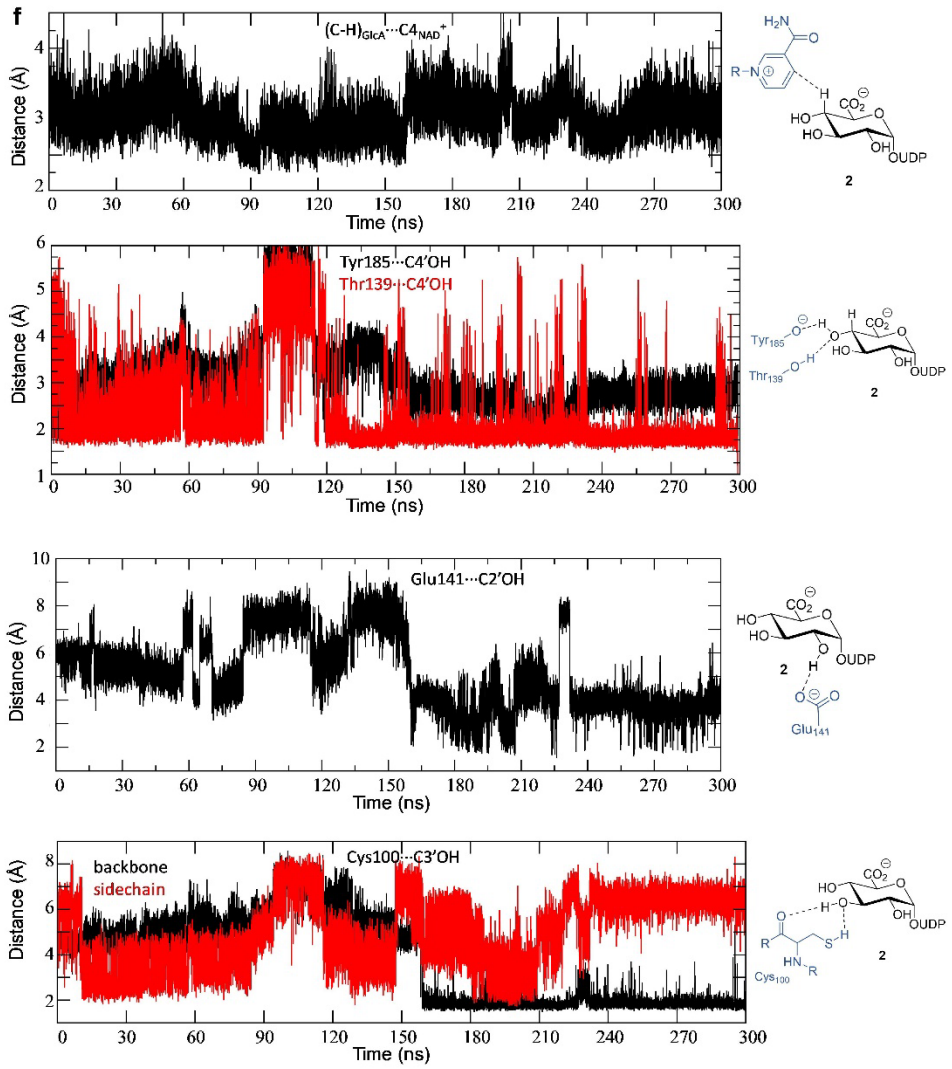

Supplementary Figure 15. Maps of the ring puckering geometries and representation of the root mean square displacement (RMSD) of the protein backbone with respect to the initial structure and selected distances along the MD simulations. Panels (**a**), (**c**) and (**e**) show data from Replica 1. Panels (**b**), (**d**) and (**f**) show data from Replica 2. The distance plots for Cys100 are shown to highlight the conformational flexibility of this residue and its proximity to the C3/C3OH of substrate. However, note: Cys100 is not involved in the initial steps of oxidation and ring opening.

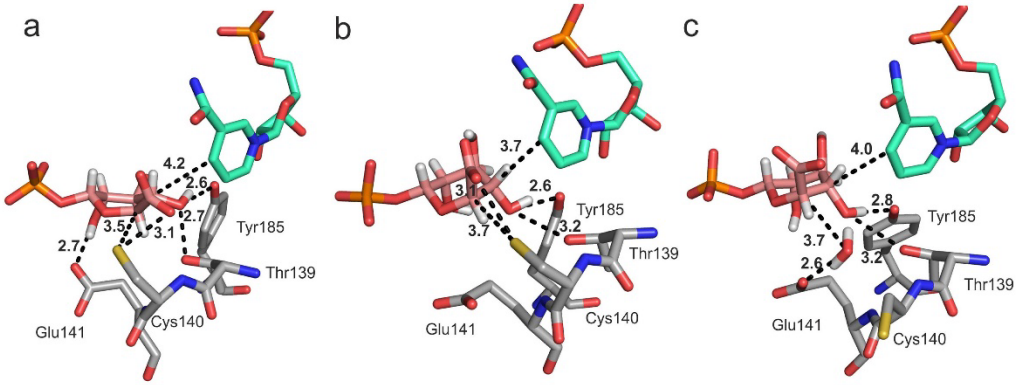

Supplementary Figure 16. Results of MD simulation suggest a possible role of Cys140 in the obligatory proton uptake to substrate C5' in the decarboxylation step of the UAXS reaction. The panels **a** - **c** show representative snapshots from the trajectories of the MD simulations (panel **a**, Replica 1; panels **b** and **c**, Replica 2). The side chain of Cys140 is generally quite flexible in the MD simulations. (**a**) An enzyme-substrate complex from Replica 1 that has Glu141 interacting with the 2'-OH and Cys140 placed close to the C5' of UDP-GlcA (**2**). The Cys140 would thus be positioned for stereospecific (*Si* side) protonation of the C5' from below the sugar ring. Note: due to side chain flexibility, the position of Cys140 is slightly different from that in Figure 3a of the main text. The results show that Cys140 could easily adopt a conformation suitable for proton transfer during the decarboxylation. (**b**) An enzyme-substrate complex from Replica 2 that has Cys140 positioned side-on of the sugar ring. Although the side chain of Cys140 points toward the C5', it is not in a position suitable for proton transfer. Glu141 is not interacting with the 2'-OH. (**c**) An enzyme-substrate complex from Replica 2 that would establish an UXS-like[15] proton conduit to the C5'. This proton conduit involves a Glu141-coordinated water that is placed below the sugar ring for stereospecific protonation. The analogous arrangement of groups (involving the homologous glutamate residue) is observed in human UXS.[15]

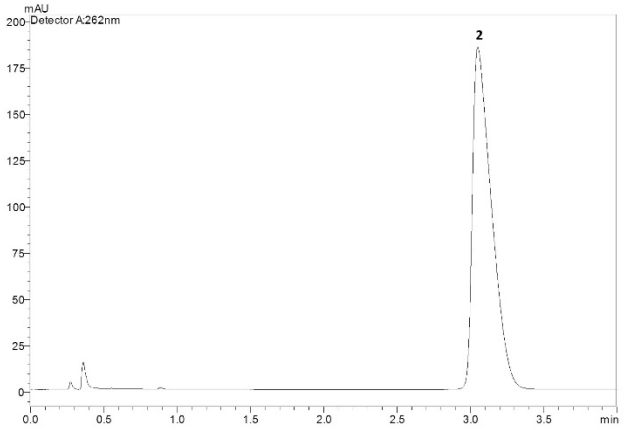

Supplementary Figure 17. HPLC trace for commercial standard of UDP-GlcA (**2**). The sample contained no enzyme (negative control).

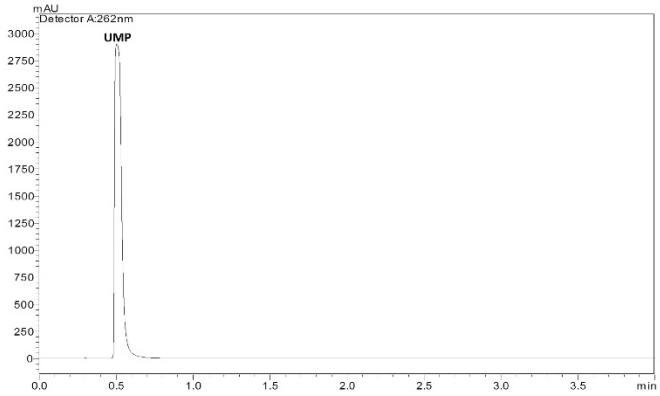

Supplementary Figure 18. HPLC trace for commercial standard of UMP. The sample contained no enzyme.

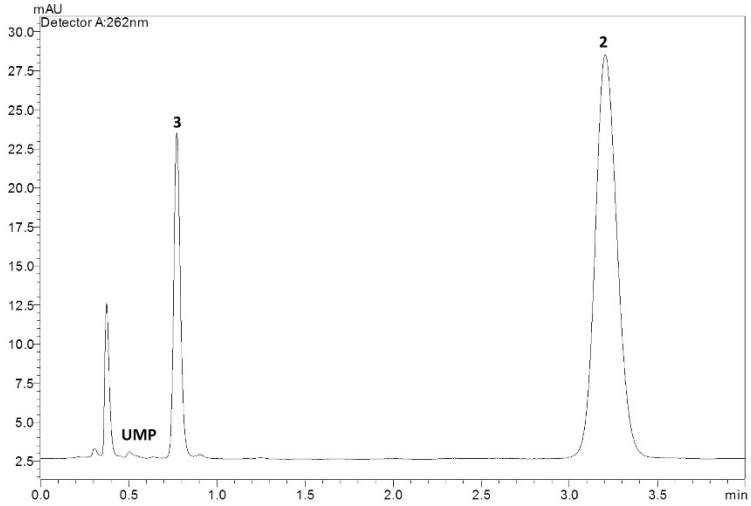

Supplementary Figure 19. HPLC trace for conversion of UDP-GlcA (**2**) by human UXS. **3** = UDP-xylose.

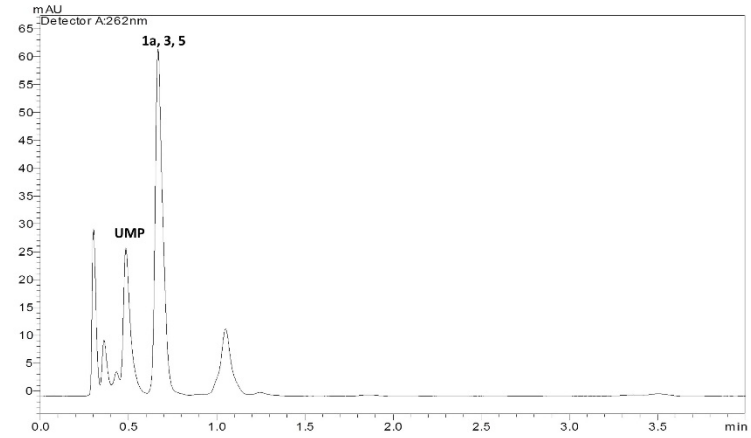

Supplementary Figure 20. HPLC trace showing conversion of UDP-GlcA (**2**) by wild-type UAXS. **1a** = UDP-apiose; **3** = UDP-xylose; **5** = UDP-4-keto-xylose. Products cannot be separated efficiently using HPLC under the described conditions. The peak at ~1 min corresponds to UDP.

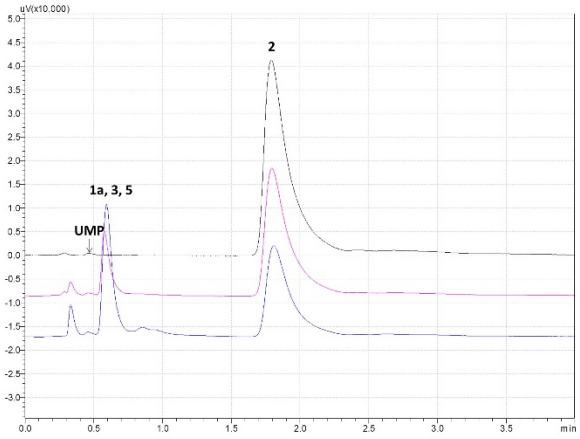

Supplementary Figure 21. Representative conversion of UDP-GlcA (**2**) by Y105F variant. Black lane = no enzyme. Pink lane = human UXS. Blue lane = Y105F variant. **1a** = UDP-apiose; **2** = UDP-GlcA; **3** = UDP-xylose; **5** = UDP-4-keto-xylose. Products cannot be separated efficiently using HPLC under the described conditions. Retention times were shifted slightly due to minor changes in mobile phase composition, flow-rate, and HPLC column performance. Reference compounds (UMP, UDP-GlcA, **2**) and control reactions (UDP-GlcA (**2**) conversion with wild-type UAXS and human UXS) were injected to ensure reliable assignment of products.

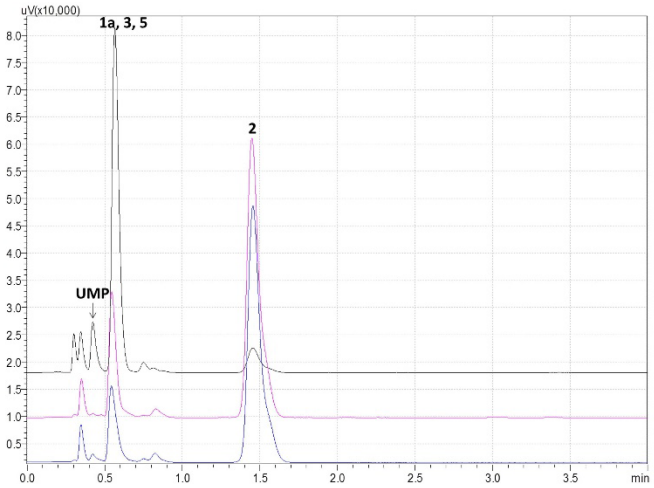

Supplementary Figure 22. HPLC traces for conversion of UDP-GlcA (**2**) by T139V variant. Black lane: UAXS pH 7.0; Pink lane: T139V variant (reaction at pH 7.0); Blue lane: T139V variant (reaction at pH 8.5). **1a** = UDP-apiose; **2** = UDP-GlcA; **3** = UDP-xylose; **5** = UDP-4-keto-xylose. Products cannot be separated efficiently using HPLC under the described conditions. Retention times were shifted slightly due to minor changes in mobile phase composition, flow-rate, and HPLC column performance. Reference compounds (UMP, UDP-GlcA (**2**)) and control reactions (UDP-GlcA (**2**) conversion with wild-type UAXS and human UXS) were injected to ensure reliable assignment of products.

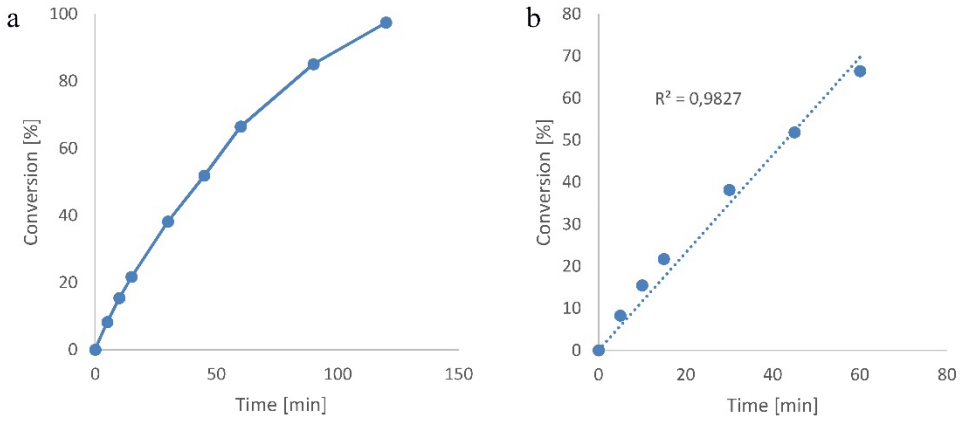

Supplementary Figure 23. Time course for conversion of 2 mM UDP-GlcA (**2**) by wild-type UAXS (2 mg/mL). (**a**) Full time course recorded in the experiment. (**b**) Part of the time course used for initial rate determination. The data shown are averages from two independent replicates. The initial rate determined from linear fit of the data in panel b was 11 nmol/(min mg protein). This value is used to calculate a k_{cat} of 0.49 (± 0.02) min^{-1}.

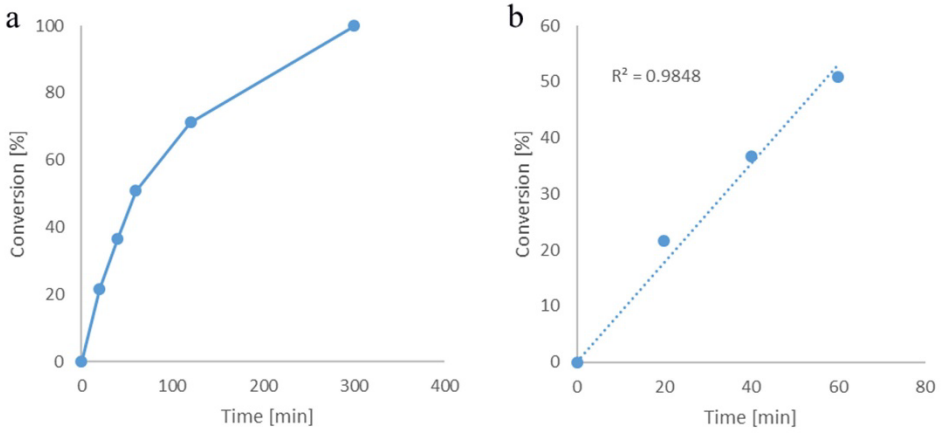

Supplementary Figure 24. Time course for conversion of 2 mM UDP-GlcA (**2**) by Y105F variant (14.3 mg/mL). (**a**) Full time course recorded in the experiment. (**b**) Part of the time course used for initial rate determination. The data shown are averages from two independent replicates. The initial rate determined from linear fit of the data in panel b was 1.2 nmol/(min mg protein). This value is used to calculate a k_{cat} of 0.053 (± 0.017) min^{-1}.

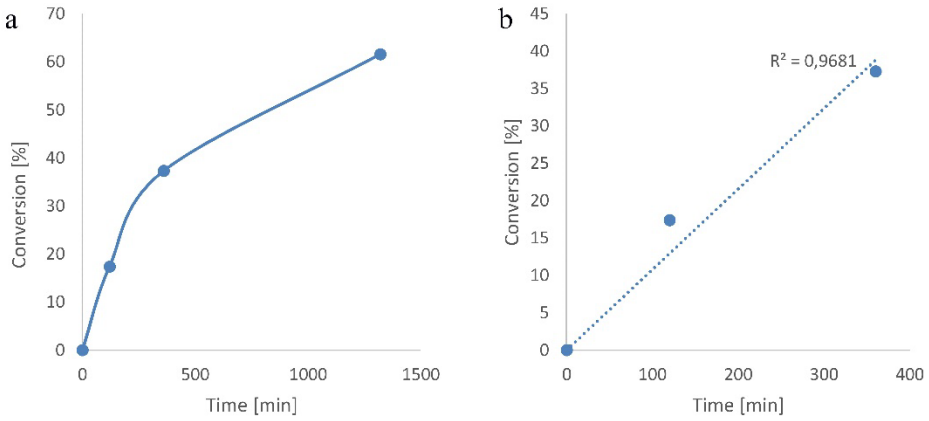

Supplementary Figure 25. Time course for conversion of 0.5 mM UDP-GlcA (**2**) by T139V variant (3.3 mg/mL). Due to the very low activity and the suppressed reduction activity of this variant, 1 mM NAD^+ were supplemented to the reaction. (**a**) Full time course recorded in the experiment. (**b**) Part of the time course used for initial rate determination. The data shown are averages from two independent replicates. The initial rate determined from linear fit of the data in panel b was 6.6×10^{-5} nmol/(min mg protein). This value is used to calculate a k_{cat} of 3×10^{-3} ($\pm$ 9.6×10^{-5}) min^{-1}.

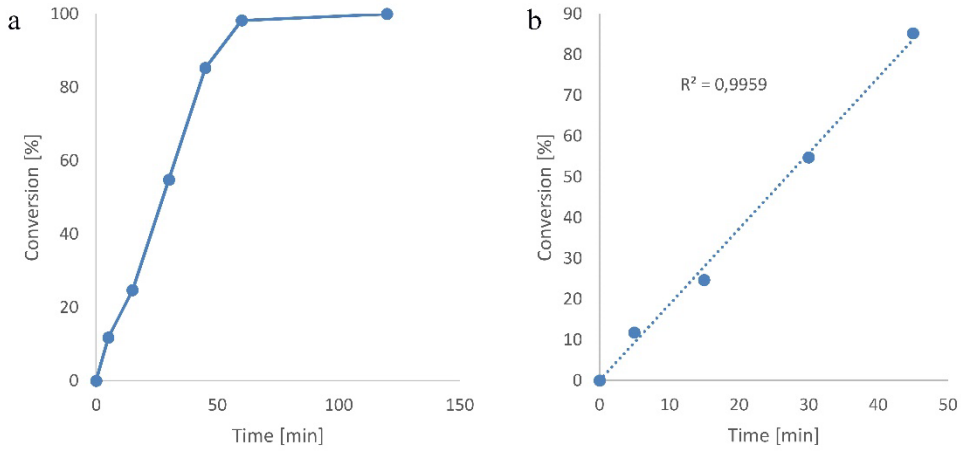

Supplementary Figure 26. Time course for conversion of 2 mM UDP-GlcA (**2**) by C100A variant (14.3 mg/mL). (**a**) Full time course recorded in the experiment. (**b**) Part of the time course used for initial rate determination. The data shown are averages from two independent replicates. The initial rate determined from linear fit of the data in panel b was 2.6 nmol/(min mg protein). This value is used to calculate a k_{cat} of 0.12 ($\pm$ 4.9 $\times$ 10^{-4}) min^{-1}.

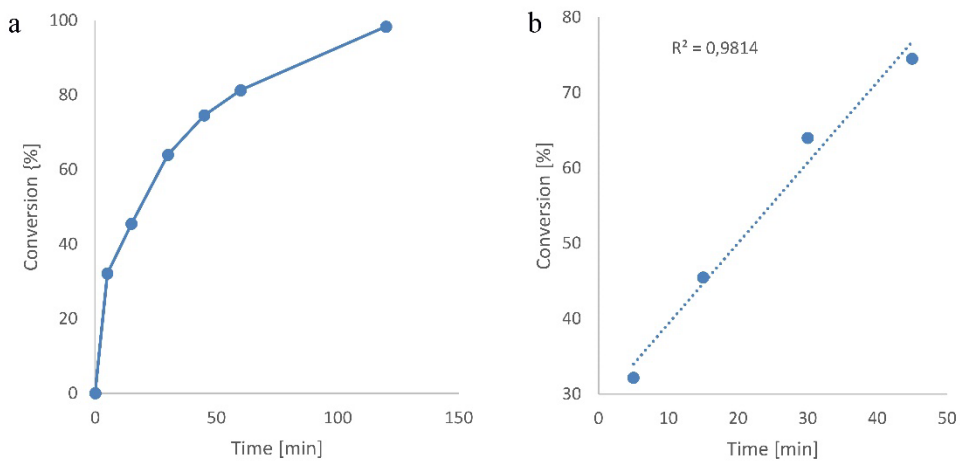

Supplementary Figure 27. Time course for conversion of 2 mM UDP-GlcA (**2**) by C140S variant (14.3 mg/mL). (**a**) Full time course recorded in the experiment. (**b**) Part of the time course used for initial rate determination. The data shown are averages from two independent replicates. The initial rate determined from linear fit of the data in panel b was 1.5 nmol/(min mg protein). This value is used to calculate a k_{cat} of 0.07 ($\pm$ 1.2 $\times$ 10^{-3}) min^{-1}.

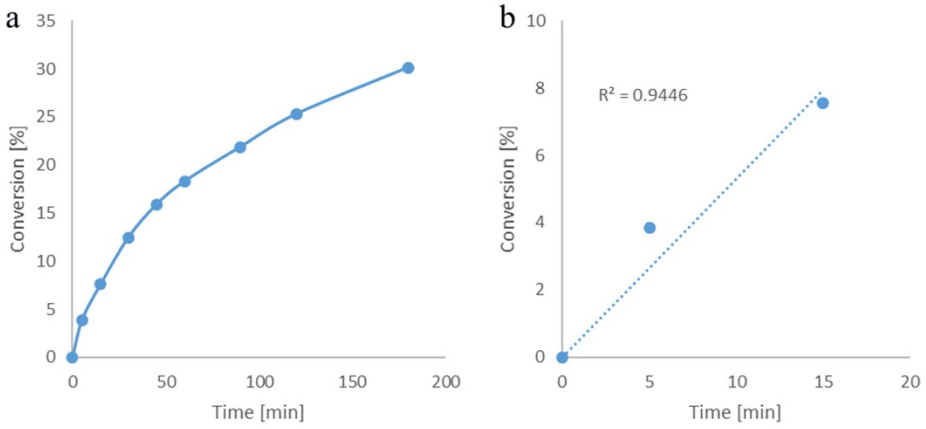

Supplementary Figure 28. Time course for conversion of 2 mM UDP-GlcA (**2**) by C100A/C140S variant (2 mg/mL). (**a**) Full time course recorded in the experiment. (**b**) Part of the time course used for initial rate determination. The data shown are averages from two independent replicates. The initial rate determined from linear fit of the data in panel b was 5 nmol/(min mg protein). This value is used to calculate a k_{cat} of 0.23 (± 0.01) min^{-1}.

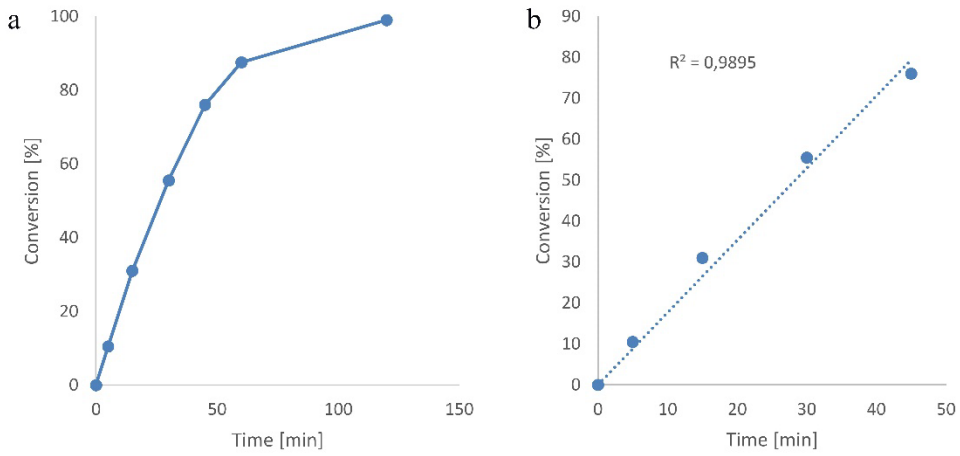

Supplementary Figure 29. Time course for conversion of 2 mM UDP-GlcA (**2**) by C140A variant (14.3 mg/mL). (**a**) Full time course recorded in the experiment. (**b**) Part of the time course used for initial rate determination. The data shown are averages from two independent replicates. The initial rate determined from linear fit of the data in panel b was 2.4 nmol/(min mg protein). This value is used to calculate a k_{cat} of 0.11 ($\pm$ 1.1 $\times$ 10^{-3}) min^{-1}.

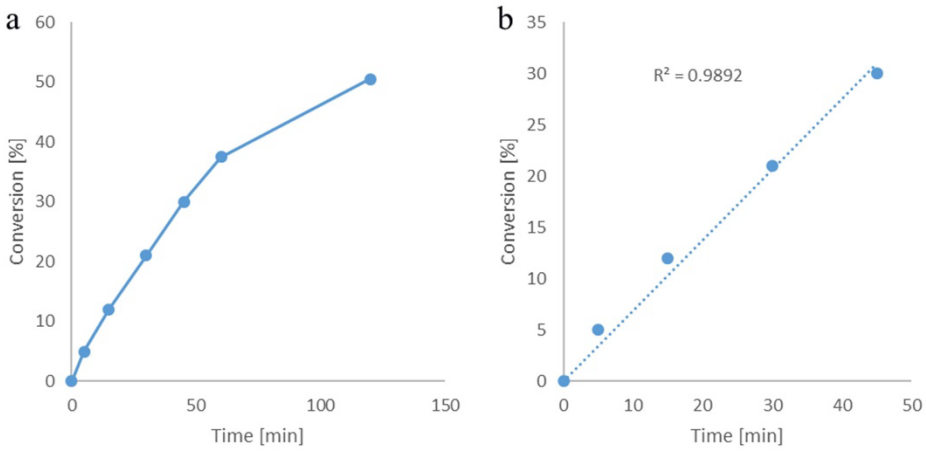

Supplementary Figure 30. Time course for conversion of 2 mM UDP-GlcA (**2**) by C100S variant (7 mg/mL). (**a**) Full time course recorded in the experiment. (**b**) Part of the time course used for initial rate determination. The data shown are averages from two independent replicates. The initial rate determined from linear fit of the data in panel b was 1.9 nmol/(min mg protein). This value is used to calculate a k_{cat} of 0.09 ($\pm$ 9.2 $\times$ 10^{-4}) min^{-1}.

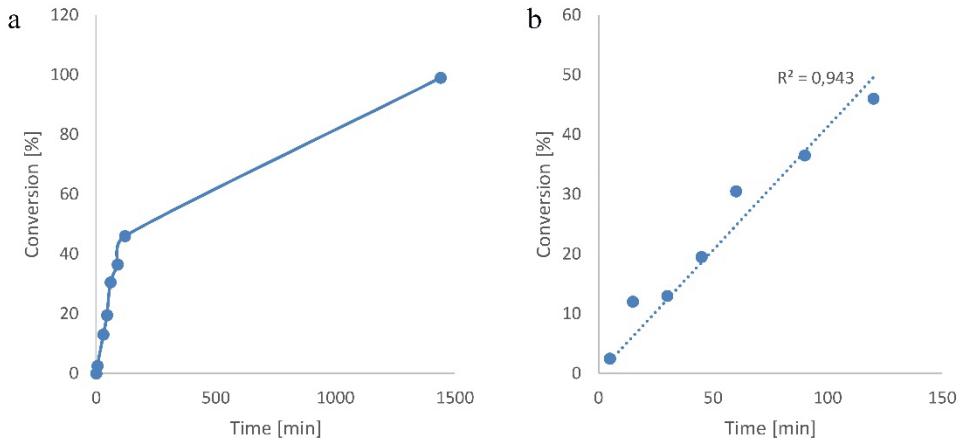

Supplementary Figure 31. Time course for conversion of 2 mM UDP-GlcA (**2**) by Y105A variant (3.5 mg/mL). (**a**) Full time course recorded in the experiment. (**b**) Part of the time course used for initial rate determination. The data shown are averages from two independent replicates. The initial rate determined from linear fit of the data in panel b was 2.9 nmol/(min mg protein). This value is used to calculate a k_{cat} of 0.13 ($\pm$ 7.4 $\times$ 10^{-3}) min^{-1}.

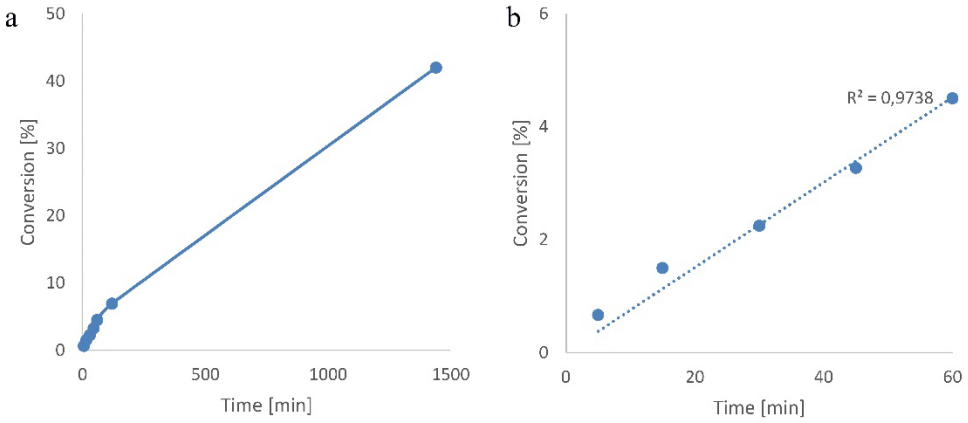

Supplementary Figure 32. Time course for conversion of 2 mM UDP-GlcA (**2**) by E141A variant (14.8 mg/mL). (**a**) Full time course recorded in the experiment. (**b**) Part of the time course used for initial rate determination. The data shown are averages from two independent replicates. The initial rate determined from linear fit of the data in panel b was 6.6×10^{-5} nmol/(min mg protein). This value is used to calculate a k_{cat} of 3.0×10^{-3} ($\pm$ 7.8×10^{-5}) min^{-1}.

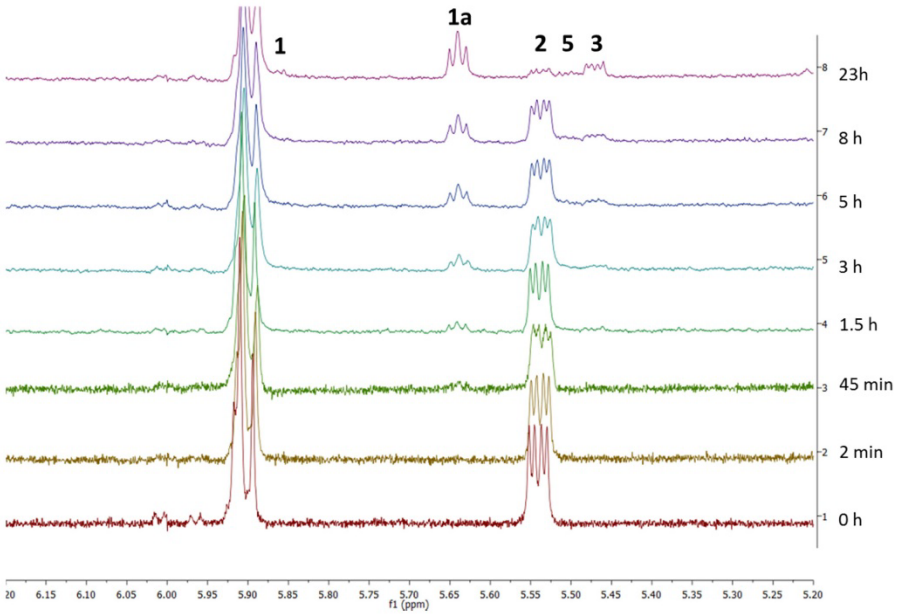

Supplementary Figure 33. ^{1}H-NMR time course for conversion of 2 mM UDP-GlcA (**2**) by wild-type UAXS (2 mg/mL). **1** = α-D-apiofuranosyl-1,2-cyclic phosphate; **1a** = UDP-apiose; **2** = UDP-GlcA; **3** = UDP-xylose; **5** = UDP-4-keto-xylose.

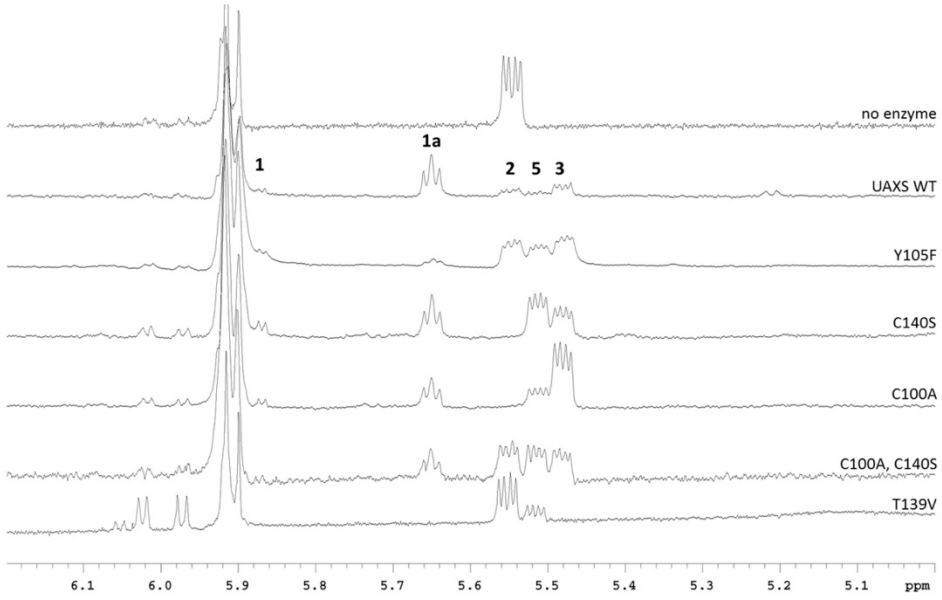

Supplementary Figure 34. Alignment of ^{1}H-NMR signals from conversion of 2 mM UDP-GlcA (**2**) with wild-type UAXS and enzyme variants generated by site-directed mutagenesis. As control, a reaction without enzyme is shown (lane 1). **1** = α-D-apiofuranosyl-1,2-cyclic phosphate; **1a** = UDP-apiose; **2** = UDP-GlcA; **3** = UDP-xylose; **5** = UDP-4-keto-xylose. The doublets around 6 ppm are signals from the uracil moiety of UMP and UDP.

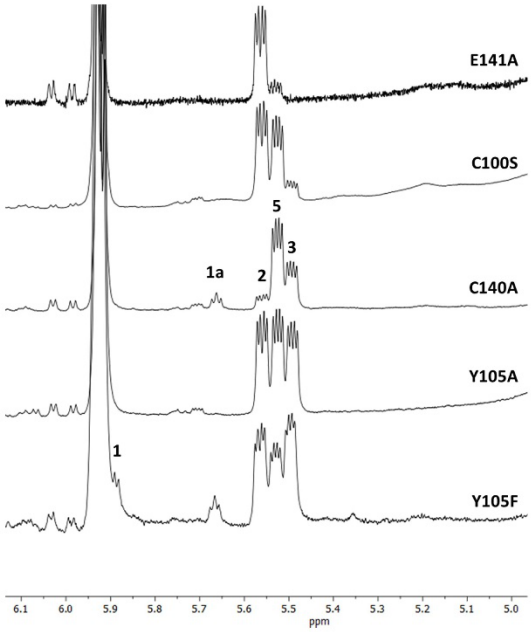

Supplementary Figure 35. Alignment of ^{1}H-NMR signals from conversion of 2 mM UDP-GlcA (**2**) with enzyme variants generated by site-directed mutagenesis. **1** = α-D-apiofuranosyl-1,2-cyclic phosphate; **1a** = UDP-apiose; **2** = UDP-GlcA; **3** = UDP-xylose; **5** = UDP-4-keto-xylose.

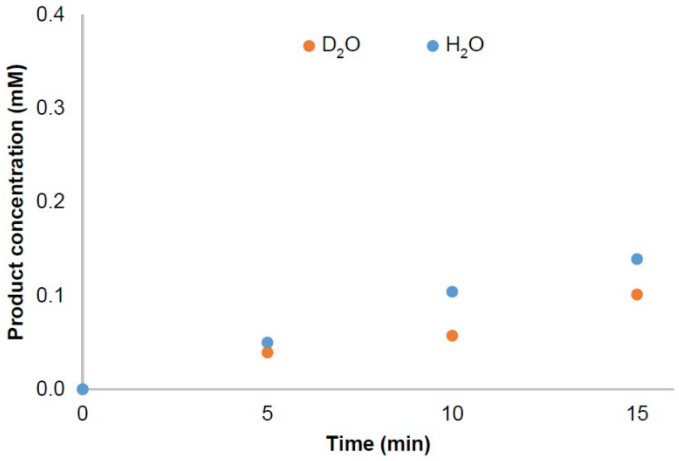

Supplementary Figure 36. Time course for conversion of 1 mM UDP-GlcA (**2**) by wild-type UAXS (2 mg/mL) using D_2O or H_2O as bulk solvent. Reactions were performed in duplicates. Linear fits of the data give a specific activity of 4.7 nmol/(min mg protein) in H_2O and 3.2 nmol/(min mg protein) in D_2O, respectively.

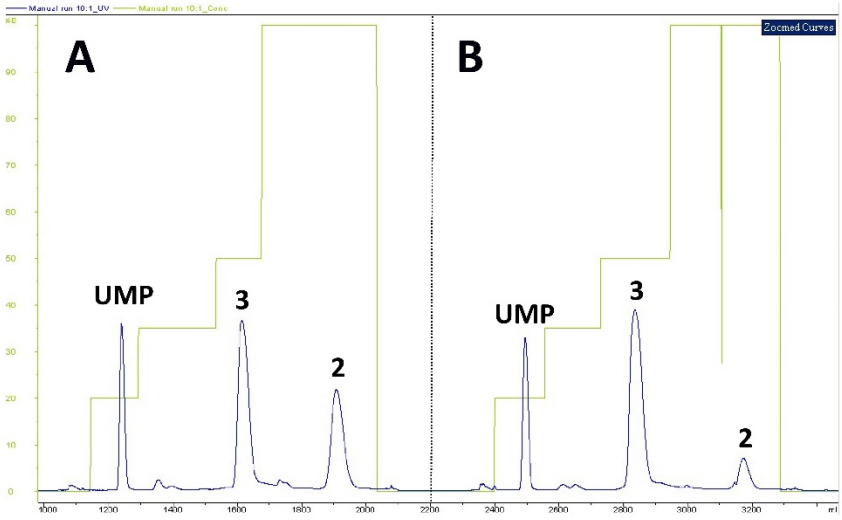

Supplementary Figure 37. Chromatogram recorded during the isolation of UDP-xylose (**3**) from conversions of UDP-GlcA (**2**) by C100S (A) and C100A (B) performed in D_2O (deuterium wash-in experiment). Blue line = UV signal. Green line = salt gradient used for elution. UMP = uridine monophosphate.

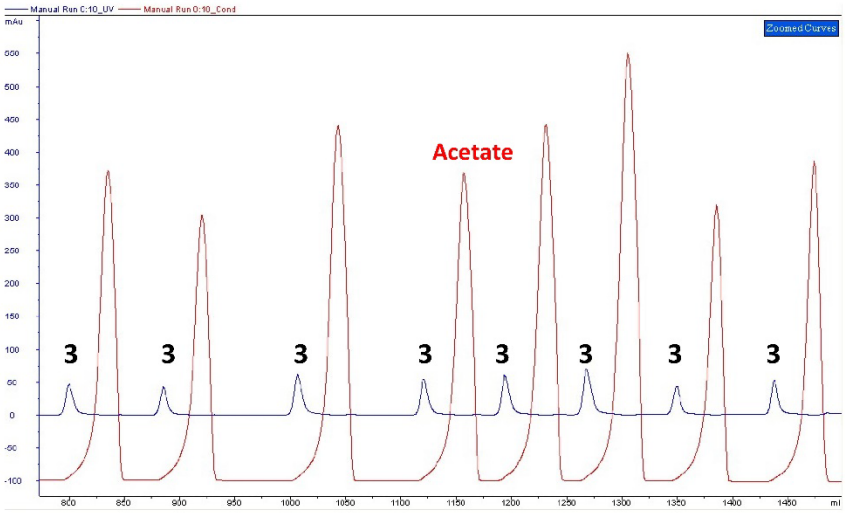

Supplementary Figure 38. Chromatogram recorded during the desalting of isolated UDP-xylose (**3**). Blue line = UV signal. Red line = conductivity signal of acetate.

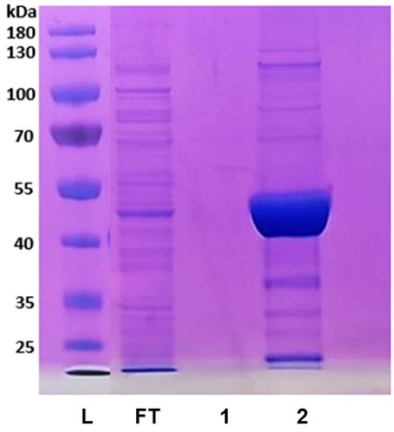

Supplementary Figure 39. SDS polyacrylamide gel showing the Strep-tag purified C-terminal domain of ArnA. From left to right: L, molecular mass marker; FT, flow through during sample loading; 1, washing fraction; 2, elution fraction containing purified ArnA (molecular mass = 43 kDa).[30,31]

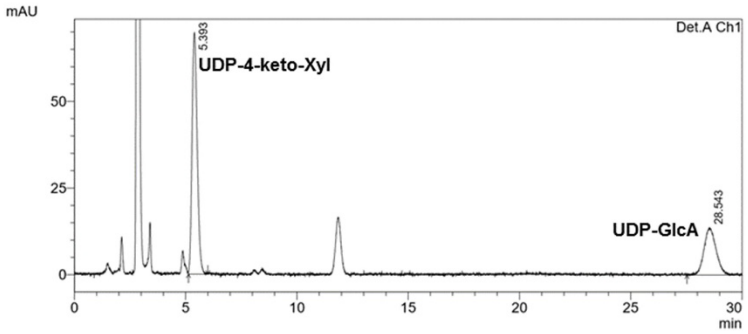

Supplementary Figure 40. HPLC chromatogram of the ArnA reaction mixture after 5 min. The peaks corresponding to the desired product UDP-4-keto-xylose (**5**, here named UDP-4-keto-Xyl) and residual substrate (UDP-GlcA, **2**) are labelled accordingly. The reaction for synthesis of UDP-4-keto-xylose (**5**) contained 2 mM UDP-GlcA (**2**), 2 mM NAD^+, and 5 mg/mL purified ArnA. The sample was incubated for 5 min at 30 °C (no agitation; 70% conversion, >99% selectivity for **5**).

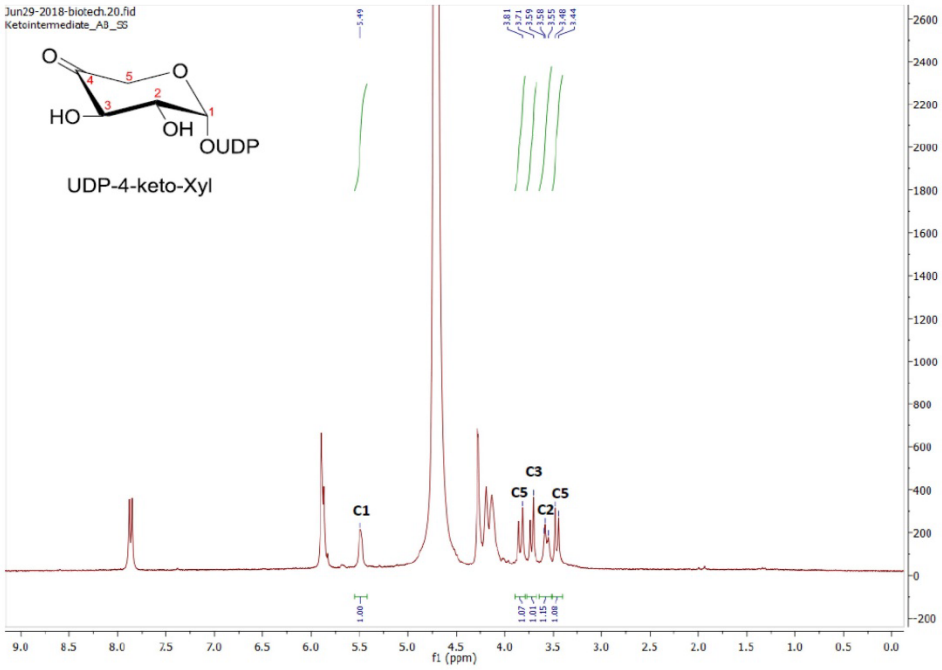

Supplementary Figure 41. ^{1}H-NMR spectrum (300 MHz, deuterium oxide) of isolated UDP-4-keto-xylose (**5**). Signals from the protons attached to respective carbons (C1-C5) in the pyranose ring are labelled accordingly. δ 5.49 (dd, J = 6.8, 3.5 Hz, 1H), 3.83 (d, J = 12.1 Hz, 1H), 3.72 (d, J = 9.9 Hz, 1H), 3.57 (dd, J = 8.1, 5.0 Hz, 1H), 3.46 (d, J = 12.2 Hz, 1H).

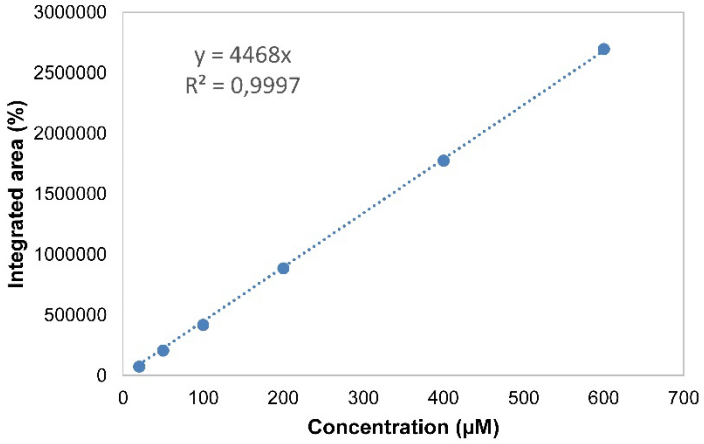

Supplementary Figure 42. Calibration curve for free NADH. Data points were recorded by HPLC-UV.

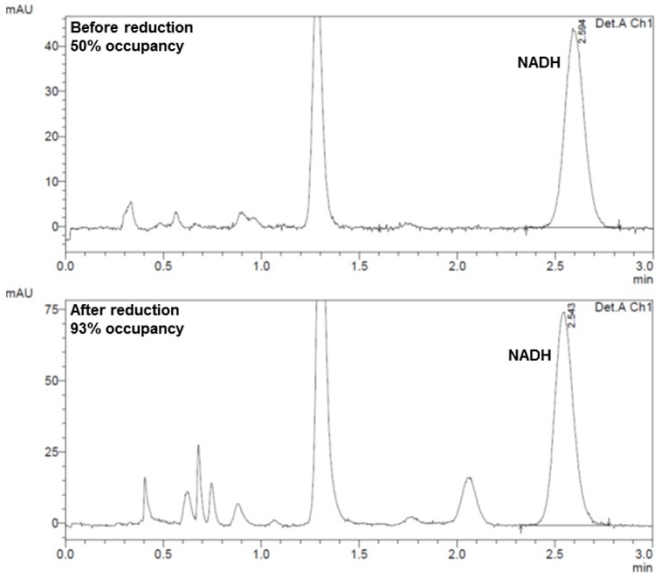

Supplementary Figure 43. HPLC traces from the chemical ($NaBH_4$) reduction of NAD^+ bound to purified wild-type UAXS. The top panel shows a HPLC chromatogram of the as-isolated enzyme with 50% occupancy by NADH. The bottom panel shows NADH released from the active site (93% occupancy with NADH) after the reduction with $NaBH_4$.

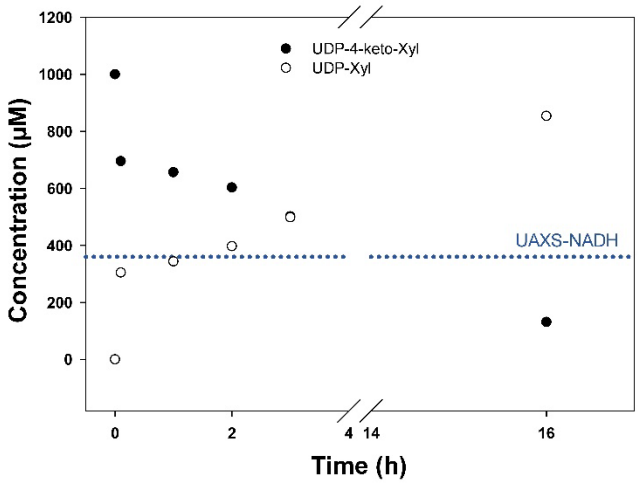

Supplementary Figure 44. Time course for the conversion of 1 mM UDP-4-keto-xylose (**5**) with chemically reduced UAXS (20 mg/mL; NADH content >90%) and excess of NADH (10 mM). The blue dotted line indicates the concentration of enzyme-bound NADH in UAXS.

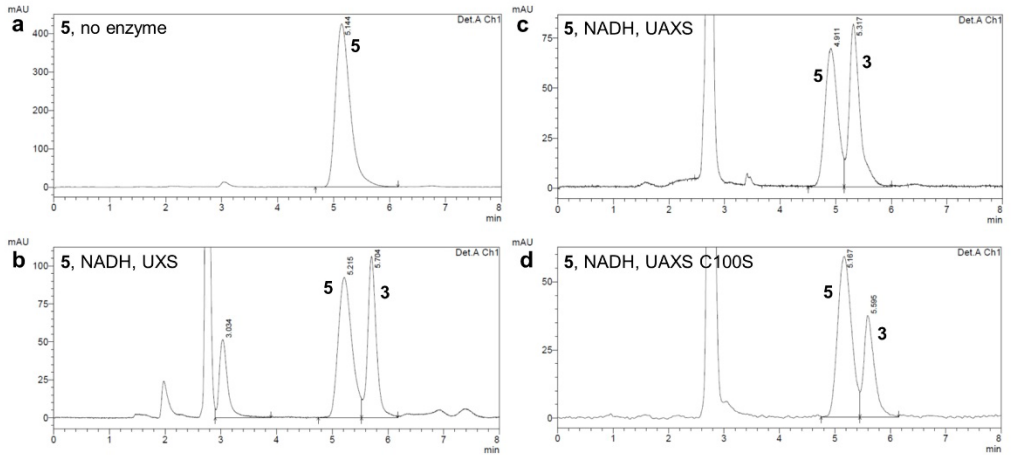

Supplementary Figure 45. Additional HPLC traces for UDP-4-keto-xylose (**5**) conversions with wild-type UAXS, human UXS, and C100S variant. **a**. Control without enzyme. **b**. Reaction of 1 mM UDP-4-keto-xylose (**5**) with human UXS (5 mg/mL) and 10 mM NADH recorded after 180 min. **c**. Reaction of 1 mM UDP-4-keto-xylose (**5**) with wild-type UAXS (20 mg/mL) and 10 mM NADH recorded after 180 min. **d**. Reaction of 1 mM UDP-4-keto-xylose (**5**) with C100S variant (15 mg/mL) and 10 mM NADH recorded after 30 min.

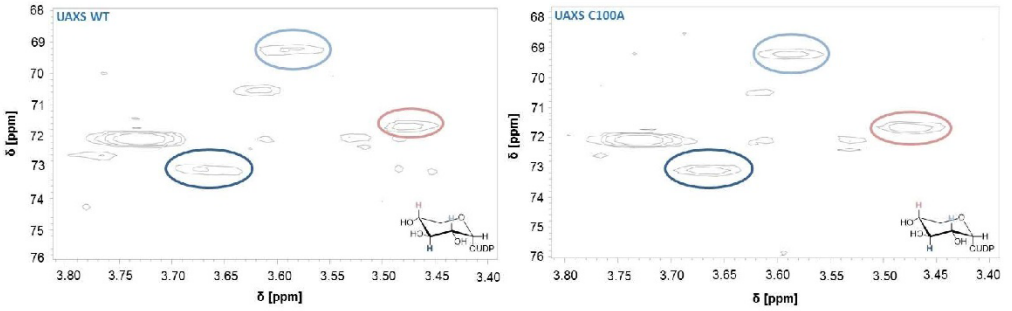

Supplementary Figure 46. Deuterium wash-in experiment to study potential ring-opening during reduction of UDP-4-keto-xylose (**5**) to UDP-xylose (**3**) using wild-type UAXS (left panel) and C100A variant (right panel). Results show snapshots of heteronuclear single quantum coherence (HSQC) experiments analyzing proton signals from UDP-xylose (**3**). Relevant hydrogens at carbons 2-4 are labelled with colored circles.

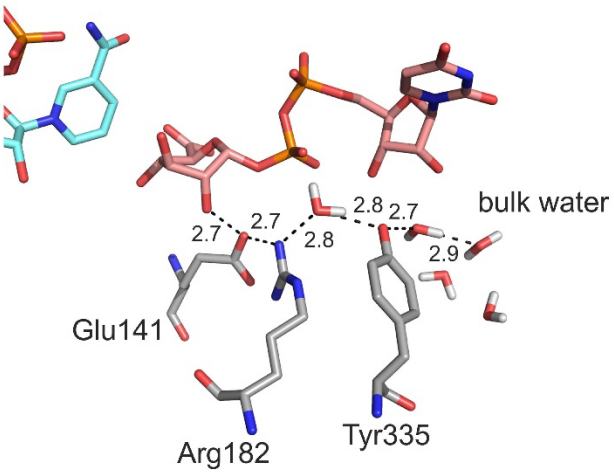

Supplementary Figure 47. A possible proton relay in the active site of UAXS is shown. The proton relay connects the C2'-OH of UDP-GlcA (**2**) to bulk solvent via UAXS residues Glu141 and Arg182, and Tyr335. The figure was prepared based on the Michaelis complex shown in Figure 3a,c of the main text.

Supplementary References

1 Eixelsberger, T. *et al.* Isotope probing of the UDP-apiose/UDP-xylose synthase reaction: Evidence of a mechanism via a coupled oxidation and aldol cleavage. *Angew. Chem. Int. Ed. Engl.* **56,** 2503-2507, (2017).

2 Kabsch, W. Xds. *Acta Crystallogr., Sect. D: Biol. Crystallogr.* **66,** 125-132, (2010).

3 Winn, M. D. *et al.* Overview of the CCP4 suite and current developments. *Acta Crystallogr., Sect. D: Biol. Crystallogr.* **67,** 235-242, (2011).

4 McCoy, A. J. *et al.* Phaser crystallographic software. *J. Appl. Crystallogr.* **40,** 658-674, (2007).

5 Stein, N. CHAINSAW: A program for mutating pdb files used as templates in molecular replacement. *J. Appl. Crystallogr.* **41,** 641-643, (2008).

6 Adams, P. D. *et al.* PHENIX: a comprehensive Python-based system for macromolecular structure solution. *Acta Crystallogr., Sect. D: Biol. Crystallogr.* **66,** 213-221, (2010).

7 Afonine, P. V. *et al.* FEM: feature-enhanced map. *Acta Crystallogr., Sect. D: Biol. Crystallogr.* **71,** 646-666, (2015).

8 Emsley, P. & Cowtan, K. Coot: Model-building tools for molecular graphics. *Acta Crystallogr., Sect. D: Biol. Crystallogr.* **60,** 2126-2132, (2004).

9 Dodson, E. J., Murshudov, G. N. & Vagin, A. A. Description of program using maximum likelihood residual for macromolecular refinement, illustrated by several examples. *Acta Crystallogr., Sect. A: Found. Adv.* **52,** C85-C85, (1996).

10 Chen, V. B. *et al.* MolProbity: all-atom structure validation for macromolecular crystallography. *Acta Crystallogr., Sect. D: Biol. Crystallogr.* **66,** 12-21, (2010).

11 Salomon-Ferrer, R. *et al.* Routine microsecond molecular dynamics simulations with AMBER on GPUs. 2. Explicit solvent particle mesh Ewald. *J. Chem. Theory Comput.* **9,** 3878-3888, (2013).

12 Jorgensen, W. L. *et al.* Comparison of simple potential functions for simulating liquid water. *J. Chem. Phys.* **79,** 926-935, (1983).

13 Kirschner, K. N. *et al.* GLYCAM06: A generalizable Biomolecular force field. Carbohydrates. *J. Comput. Chem.* **29,** 622-655, (2008).

14 Pettersen, E. F. *et al.* UCSF chimera - A visualization system for exploratory research and analysis. *J. Comput. Chem.* **25,** 1605-1612, (2004).

15 Eixelsberger, T. *et al.* Structure and mechanism of human UDP-xylose synthase: Evidence for a promoting role of sugar ring distortion in a three-step catalytic conversion of UDP-glucuronic acid. *J. Biol. Chem.* **287,** 31349-31358, (2012).

16 Fiser, A., Do, R. K. G. & Sali, A. Modeling of loops in protein structures. *Protein Sci.* **9,** 1753-1773, (2000).

17 Izaguirre, J. A., Catarello, D. P., Wozniak, J. M. & Skeel, R. D. Langevin stabilization of molecular dynamics. *J. Chem. Phys.* **114,** 2090-2098, (2001).

18 Berendsen, H. J. C. *et al.* Molecular-dynamics with coupling to an external bath. *J. Chem. Phys.* **81,** 3684-3690, (1984).

19 Ryckaert, J. P., Ciccotti, G. & Berendsen, H. J. C. Numerical-integration of cartesian equations of motion of a system with constraints - Molecular-dynamics of n-alkanes. *J. Comput. Phys.* **23,** 327-341, (1977).

20 Darden, T., York, D. & Pedersen, L. Particle mesh Ewald - an N.Log(N) method for Ewald sums in large systems. *J. Chem. Phys.* **98,** 10089-10092, (1993).

21 Warshel, A. & Levitt, M. Theoretical studies of enzymic reactions - Dielectric, electrostatic and steric stabilization of carbonium-ion in reaction of lysozyme. *J. Mol. Biol.* **103,** 227-249, (1976).

22 Sherwood, P. *et al.* QUASI: A general purpose implementation of the QM/MM approach and its application to problems in catalysis. *J. Mol. Struct.: THEOCHEM* **632,** 1-28, (2003).

23 Metz, S. *et al.* ChemShell-a modular software package for QM/MM simulations. *Wiley Interdiscip. Rev.: Comput. Mol. Sci.* **4,** 101-110, (2014).

24 Ahlrichs, R. *et al.* Electronic-structure calculations on workstation computers - the program system turbomole. *Chem. Phys. Lett.* **162,** 165-169, (1989).

25 Smith, W. & Forester, T. R. DL_POLY_2.0: A general-purpose parallel molecular dynamics simulation package. *J. Mol. Graphics* **14,** 136-141, (1996).

26 Ma, N., Digman, M. A., Malacrida, L. & Gratton, E. Measurements of absolute concentrations of NADH in cells using the phasor FLIM method. *Biomed. Opt. Express* **7,** 2441-2452, (2016).

27 Guyett, P., Glushka, J., Gu, X. G. & Bar-Peled, M. Real-time NMR monitoring of intermediates and labile products of the bifunctional enzyme UDP-apiose/UDP-xylose synthase. *Carbohyd. Res.* **344,** 1072-1078, (2009).

28 Fujimori, T. *et al.* Practical preparation of UDP-apiose and its applications for studying apiosyltransferase. *Carbohydr. Res.* **477,** 20-25, (2019).

29 Eixelsberger, T. & Nidetzky, B. Enzymatic redox cascade for one-pot synthesis of uridine 5'-diphosphate xylose from uridine 5'-diphosphate glucose. *Adv. Synth. Catal.* **356,** 3575-3584, (2014).

30 Gatzeva-Topalova, P. Z., May, A. P. & Sousa, M. C. Crystal structure of *Escherichia coli* ArnA (PmrI) decarboxylase domain. A key enzyme for lipid A modification with 4-amino-4-deoxy-L-arabinose and polymyxin resistance. *Biochemistry* **43,** 13370-13379, (2004).

31 Polizzi, S. J. *et al.* Human UDP-alpha-D-xylose synthase and *Escherichia coli* ArnA conserve a conformational shunt that controls whether xylose or 4-keto-xylose is produced. *Biochemistry* **51,** 8844-8855, (2012).

32 Gatzeva-Topalova, P. Z., May, A. P. & Sousa, M. C. Structure and mechanism of ArnA: Conformational change implies ordered dehydrogenase mechanism in key enzyme for polymyxin resistance. *Structure* **13,** 929-942, (2005).

Supplementary Videos and Data Sets

Supporting Video S1: Motions of the UAXS active site during MD simulations (Replica 1). Representative fragment (1 ns; 100 frames of 1 ps/frame) taken from the trajectory of the MD simulation (total MD simulation for 300 ns) of the proposed Michaelis complex (*Glu141 interacting with the C2'OH for ring-opening aldol cleavage*). The simulation started from the UAXS complex containing NAD^+ and UDP-GlcA. Tyr185 was deprotonated. In the shown video, hydrogen atoms were omitted for clarity, except those involved in relevant hydrogen bonding interactions of UAXS and UDP-GlcA (here: Glu141 and C2'OH; Tyr185 and C4'OH; Thr139 and C4'OH). Interactions of the aforementioned amino acid residues with UDP-GlcA are drawn as dashed lines from the H atom to the corresponding heteroatom. Dashed lines are only shown when the distance is <2.5 Å. The distance (in Å) between the C4'H of UDP-GlcA and C4 of NAD^+ is constantly measured and visualized (dashed line and distance in number) throughout the simulation.

Supporting Video S2: Motions of the UAXS active site during MD simulations (Replica 2). Representative fragment (1 ns; 100 frames of 1 ps/frame) taken from the trajectory of the MD simulation (total MD simulation for 300 ns) showing an alternative (UXS-like) UAXS complex in which the interaction of Glu141 with the C2'OH is lacking. The second replica was chosen according to the heat and density relaxations from the first simulation. In the shown video, hydrogen atoms were omitted for clarity, except those involved in relevant hydrogen bonding interactions of UAXS and UDP-GlcA (here: Tyr105 and C2'OH; Tyr185 and C4'OH; Thr139 and C4'OH). Interactions of the aforementioned amino acid residues with UDP-GlcA are drawn as dashed lines from the H atom to the corresponding heteroatom. Dashed lines are only shown when the distance is <2.5 Å. The distance (in Å) between the C4'H of UDP-GlcA and C4 of NAD^+ is constantly measured and visualized (dashed line and distance in number) throughout the simulation.

Supplementary data for computational work. The supplementary data from computational work contains ten coordinate files. The details of these files are as below:

1. The file 'initial-coordinate-rep1.pdb' represents the initial coordinate for the Replica 1. Since we have performed two different replicas with different initial velocities, initial coordinates for replica 1 and replica 2 are the same.

2. The file 'initial-coordinate-rep2.pdb' represents the initial coordinate for the Replica 2. Initial coordinates for replica 2 is similar to replica 1.

3. The file 'final-coordinate-rep1.pdb' represents the final coordinates after 300 ns of MD simulations for replica 1.

4. The file 'final-coordinate-rep2.pdb' represents the final coordinates after 300 ns of MD simulations for replica 2.

5. The file 'RC-OPT-QM-region-rep1.xyz' is the QM/MM optimized geometry of the QM-region of the QM/MM calculation in the XYZ file format for a snapshot taken from the MD of replica 1.

6. The file 'RC-OPT-QM-region-rep2.xyz' is the QM/MM optimized geometry of the QM-region of the QM/MM calculation in the XYZ file format, the snapshot is taken from the MD for replica 2.

7. The file 'RC-OPT-rep1-QMMM.pdb' is the QM/MM optimized geometry of the entire complex including the QM and MM region from the QM/MM calculation in the XYZ file format, the snapshot was taken from the MD of replica 1.

8. The file 'RC-OPT-rep2-QMMM.pdb' is the QM/MM optimized geometry of the entire complex including the QM and MM region of the QM/MM calculation in the XYZ file format, the snapshot was taken from the MD of replica 2.

9. The file 'snap-populated-replica1.pdb' is a snapshot from replica 1 used for QM/MM calculations, it represents the Michaelis complex before QM/MM optimization.

10. The file 'snap-populated-replica2.pdb' is a snapshot from replica 2 used for QM/MM calculations, it represents the complex before QM/MM optimization.

Mechanistic Characterization of UDP-Glucuronic Acid 4-Epimerase

The FEBS Journal

FEBS PRESS science publishing by scientists

Mechanistic characterization of UDP-glucuronic acid 4-epimerase

Annika J. E. Borg[1], Alexander Dennig[1,2], Hansjörg Weber[3] and Bernd Nidetzky[1,2]

1 Institute of Biotechnology and Biochemical Engineering, Graz University of Technology, NAWI Graz, Austria
2 Austrian Centre of Industrial Biotechnology, Graz, Austria
3 Institute of Organic Chemistry, Graz University of Technology, NAWI Graz, Austria

Keywords
decarboxylase; epimerase; kinetic isotope effect; short-chain dehydrogenase/reductase; UDP-glucuronic acid

Correspondence
B. Nidetzky, Institute of Biotechnology and Biochemical Engineering, Graz University of Technology, Petersgasse 12, 8010 Graz, Austria
Tel: +43 316 873 8400
E-mail: bernd.nidetzky@tugraz.at

(Received 6 March 2020, revised 22 June 2020, accepted 6 July 2020)

doi:10.1111/febs.15478

UDP-glucuronic acid (UDP-GlcA) is a central precursor in sugar nucleotide biosynthesis and common substrate for C4-epimerases and decarboxylases releasing UDP-galacturonic acid (UDP-GalA) and UDP-pentose products, respectively. Despite the different reactions catalyzed, the enzymes are believed to share mechanistic analogy rooted in their joint membership to the short-chain dehydrogenase/reductase (SDR) protein superfamily: Oxidation at the substrate C4 by enzyme-bound NAD^+ initiates the catalytic pathway. Here, we present mechanistic characterization of the C4-epimerization of UDP-GlcA, which in comparison with the corresponding decarboxylation has been largely unexplored. The UDP-GlcA 4-epimerase from *Bacillus cereus* functions as a homodimer and contains one NAD^+/subunit (k_{cat} = 0.25 ± 0.01 s^{-1}). The epimerization of UDP-GlcA proceeds via hydride transfer from and to the substrate's C4 while retaining the enzyme-bound cofactor in its oxidized form (≥ 97%) at steady state and without trace of decarboxylation. The k_{cat} for UDP-GlcA conversion shows a kinetic isotope effect of 2.0 (±0.1) derived from substrate deuteration at C4. The proposed enzymatic mechanism involves a transient UDP-4-keto-hexose-uronic acid intermediate whose formation is rate-limiting overall, and is governed by a conformational step before hydride abstraction from UDP-GlcA. Precise positioning of the substrate in a kinetically slow binding step may be important for the epimerase to establish stereo-electronic constraints in which decarboxylation of the labile β-keto acid species is prevented effectively. Mutagenesis and pH studies implicate the conserved Tyr149 as the catalytic base for substrate oxidation and show its involvement in the substrate positioning step. Collectively, this study suggests that based on overall mechanistic analogy, stereo-electronic control may be a distinguishing feature of catalysis by SDR-type epimerases and decarboxylases active on UDP-GlcA.

Introduction

Uridine 5′-diphosphate α-D-glucuronic acid (UDP-GlcA) is a central intermediate at the cross-roads of diverse metabolisms, including the biosynthesis of essential monosaccharides (e.g., D-xylose) [1] and polysaccharides (e.g., pectin, alginate) [2], the biosynthesis of secondary metabolites [3], and detoxification [4,5]. In plants and microorganisms, UDP-GlcA is the immediate precursor of three important monosaccharides (D-galacturonic acid, D-xylose, and D-apiose) required in cell wall polysaccharide biosynthesis [6,7]. Besides their importance in cell biology, the sugar nucleotide syntheses from UDP-GlcA are of

Abbreviations
KIE, kinetic isotope effect; SDR, short-chain dehydrogenase/reductase; UGAepi, UDP-glucuronic acid 4-epimerase.

considerable interest for mechanistic enzyme research. Three enzymes (UDP-GlcA epimerase, UGAepi, ECnonbreakingspace5.1.3.6; UDP-xylose synthase, UXS, ECnonbreakingspace4.1.1.35; and UDP-apiose/xylose synthase, UAXS, ECnonbreakingspace4.1.1.) share a common substrate in order to form distinct products from it [8–10]. The enzymes are evolutionary related by common membership to the short-chain dehydrogenase/reductase (SDR) protein superfamily [11]. All belong to the extended subclass of SDRs that are distinct from the canonical SDR type in having NAD^+ coenzyme tightly bound to their structure [11–13]. Common feature of their mechanism appears to be a transient UDP-4-keto-hexose-uronic acid intermediate which is formed by proton abstraction from C4-OH together with hydride transfer to enzyme-NAD^+ [13–19]. At this stage, the catalytic paths of the individual enzymes diverge (Fig. 1) [11]. Remarkably, only UGAepi avoids decarboxylation of UDP-GlcA. Further, the enzyme is able to catalyze re-addition of the hydride at the equatorial position of the C4 to achieve the D-glucose to D-galactose switch in stereochemistry [20]. Little is known about determinants of the finely tuned reactivity in each of these enzymes. While the reactions of UDP-xylose synthase (UXS) and UDP-apiose/xylose synthase (UAXS) have been characterized mechanistically [13,17,21], the one of UDP-GlcA epimerase (UGAepi) is yet unexplored for direct evidence in support of the central claims of enzymatic mechanism.

A transient UDP-4-keto-hexose-uronic acid species in the UGAepi reaction is currently supported solely by inference to the UXS and UDP-galactose 4-epimerase (GALE) reactions [13,16,22]. GALE, active on UDP-glucose (UDP-Glc), is mechanistically the best-characterized member of the extended SDR family. GALE promotes a 180°-degree rotation of the formed 4-ketopyranose intermediate around the phosphate backbone, therefore offering the opposite face of the sugar for reduction by NADH [16,23]. A similar rotation has been assumed, although not shown, to be involved in UGAepi reactions as well [22]. The central role of a highly conserved Tyr as the catalytic base for initiating the oxidation at C4 of the sugar has been proposed for UGAepi, based on the similarity to the GALE reaction [22,24,25]. UGAepi has been described from plants and bacteria in studies spanning several decades, with reported difficulties in recombinant production [10,20,22,26–28]. The enzymes were often found to be quite unstable in isolated form, thus complicating their detailed characterization.

Here, we report the identification of a new UGAepi from *Bacillus cereus HuA2-4* (BcUGAepi). The enzyme was conveniently produced in *Escherichia coli* (30 $mg \cdot L^{-1}$) and proved quite robust during isolation, storage, and use. Thus, it was a practical candidate for the proposed mechanistic study. We performed here a comprehensive biochemical and steady-state kinetic analysis of the enzyme. We developed efficient enzymatic syntheses of UDP-GalA and UDP-4-[^{2}H]-GlcA as substrate for the reverse reaction of the epimerase and as mechanistic probe, respectively. Using UDP-4-[^{2}H]-GlcA and *in situ* real-time monitoring of the reaction by proton NMR, we demonstrated that the overall net epimerization involves two stereospecific steps of hydride transfer, from and to the sugar C4, and proceeds without loss of deuterium label from the substrate in the product. We further used site-directed mutagenesis, kinetic isotope effects, and pH studies to obtain deepened insight into the enzyme mechanism.

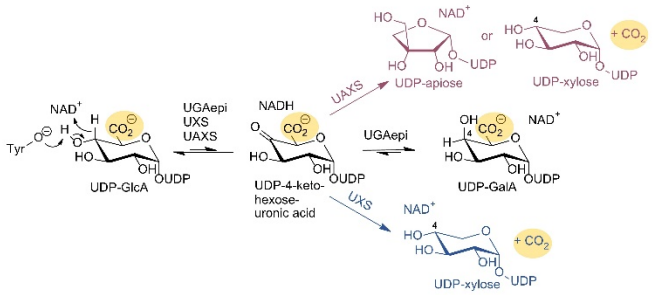

Fig. 1. Simplified reaction pathways for UDP-apiose/xylose synthase (UAXS), UDP-xylose synthase (UXS), and UDP-glucuronic acid 4-epimerase (UGAepi). The routes leading to decarboxylation are highlighted in red (UAXS) and blue (UXS), and position of CO_2 is assigned with a yellow circle. Orientation of the C4-hydroxyl group in the products is equatorial in case of UDP-xylose (UAXS, UXS) and axial in UDP-GalA (UGAepi). UDP-GlcA, uridine diphosphate glucuronic acid; UDP-GalA, uridine diphosphate galacturonic acid.

We provide evidence supporting catalytic reaction via a transient UDP-4-keto-hexose-uronic acid intermediate. Reduction in the intermediate is considerably faster than its formation. A kinetic isomerization of the enzyme–substrate complex before the hydride abstraction from UDP-GlcA is rate-limiting. The isomerization step arguably reflects a slow protein conformational change in which the reactive groups on substrate and NAD^+ are aligned with the catalytic groups on the enzyme. Based on structural comparisons and mechanistic considerations, we put forth the idea that stereo-electronic control is crucial in the epimerase reaction to protect the labile β-keto acid species from undergoing decarboxylation. Our study thus shows basic mechanistic analogy between SDR-type epimerases (UGAepi) and decarboxylases (UXS, AXS) active on UDP-GlcA and proposes essential features of their mechanistic distinction.

Results

Identification and biochemical characterization of a new UGAepi

BLAST search against the known microbial UGAepis revealed an uncharacterized protein (UniProt: J8BY31_BACCE) in *Bacillus cereus HuA2-4* that was annotated as UDP-glucose 4-epimerase. Since the protein was similar to already known UGAepi enzymes, we wished to examine its reactivity. Protein harboring C-terminal Strep-tag (referred to as BcUGAepi throughout) was conveniently obtained from standard *E. coli* culture in a yield of ~30 mg purified protein per L (Fig. S1). We showed with gel filtration that the isolated protein was a homodimer of ~37-kDa subunits (Figs S2 and S3). Absorbance spectrum indicated the presence of a protein-bound nicotinamide cofactor, as expected (Fig. S4). Using sensitive HPLC assay for detection (Fig. S5), we identified the cofactor as NAD, not NADP. We determined that the NAD was mainly oxidized (NAD^+). NADH was also present, the content varying slightly ($4.3 \pm 1.1\%$; $N = 3$) dependent on the enzyme batch used (Fig. S5). The protein was stable during storage (−20°C; ≥52 weeks) and under all assay conditions (pH 7.6; 23 °C) used later.

We then offered sugar nucleotides (1 mM; UDP-Glc, UDP-GlcA, UDP-Xyl) as substrates of the putative epimerase (2 μM) and monitored their conversion with HPLC. UDP-Glc and UDP-Xyl were not reactive above the detection limit (~5 μM), irrespective of the addition of NAD^+ (up to 1 mM) to the reaction. UDP-GlcA was a substrate, and it was converted into a single product detectable by HPLC (Fig. 2A). Using authentic standard of UDP-GalA synthesized according to herein developed procedure (see later), we confirmed the identity of the product and thus demonstrated the enzymatic reactivity as epimerization at C4 of UDP-GlcA.

We show in Fig. 2B the results of time-course study of conversion of UDP-GlcA. The reaction proceeded to equilibrium whose position (K_{eq} = [UDP-GalA]/[UDP-GlcA]) we determined as 2.0 ± 0.1 ($N = 10$). We also showed that NAD^+ (0–1000 μM) had no effect on the reaction rate nor on the equilibrium position (Fig. S6), indicating that the cofactor is tightly bound to the enzyme during the recombinant expression. A specific activity for UDP-GlcA epimerization of 0.6 $U \cdot mg^{-1}$ was calculated from the data. The enzyme activity was unaffected by pH in the range 7.0–9.0. It increased with temperature up to 37 °C (Fig. S7). However, to avoid convoluted effects of temperature on enzyme and sugar nucleotide stability, we chose 23 °C for further experiments. Besides demonstrating the enzymatic reactivity, our results also illuminate the substrate specificity of the epimerase, showing that a carboxylate group at C5 of the UDP-sugar is required for enzymatic function.

We further used proton NMR to monitor the epimerization directly from the enzymatic reaction mixture in D_2O solvent (pD 7.6). The conversion of UDP-GlcA into UDP-GalA was conveniently recorded from the change in the corresponding anomeric proton signals, as shown in Fig. 2C. The equilibrium ratio of UDP-GalA and UDP-GlcA was ~2, consistent with the results obtained in H_2O. The NMR data confirmed the results from HPLC analysis that UDP-GalA was the sole product of the enzymatic reaction. Release of an intermediate, or of a potential side product resulting from adventitious decarboxylation, was ruled out at level of approximately the enzyme molarity used (~5 μM; HPLC).

Enzymatic synthesis of UDP-GalA and UDP-4-[^{2}H]-GlcA

To characterize UGAepi kinetically, we required UDP-GalA as enzyme substrate for the reverse direction of reaction. We considered previous protocol that had obtained UDP-GalA from commercial α-galacturonic acid 1-phosphate, using enzymatic reaction with UTP [29]. Since α-galacturonic acid 1-phosphate is no longer offered, we attempted its synthesis by anomeric phosphorylation of GalA but were unsuccessful for lack of a suited kinase. In our hands, the GalA kinase [30] suffered from poor stability in its isolated form and showed insufficient activity with GalA. We considered isolation of UDP-GalA from an epimerase

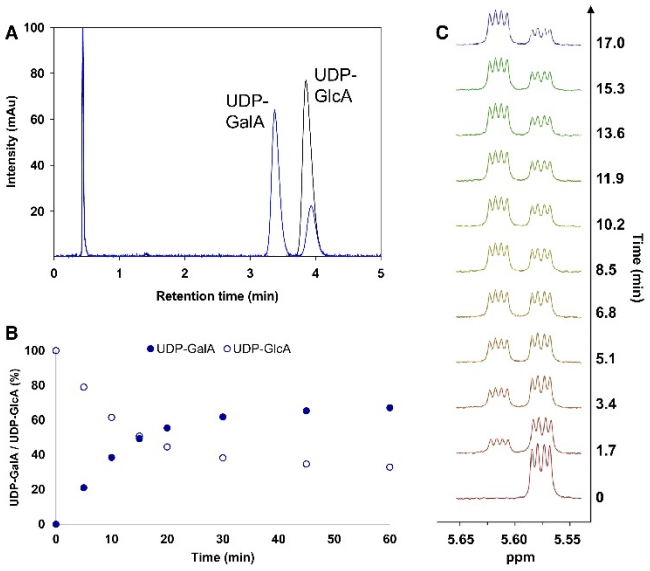

Fig. 2. Analysis of the reaction of BcUGAepi. (A) Achiral HPLC analysis of the reaction mixture of BcUGAepi with UDP-GlcA as substrate (sample at equilibrium state) is shown in blue. HPLC chromatogram of a control reaction (without enzyme) is shown in black. (B) Time course of BcUGAepi reaction with UDP-GlcA as a substrate. The reaction mixture contained 1 mM UDP-GlcA, 100 μM NAD^+, and 2 μM (0.07 mg·mL^{-1}) purified recombinant BcUGAepi in sodium phosphate buffer (50 mM Na_2HPO_4, 100 mM NaCl, pH 7.6). (C) Snapshot of *in situ* ^{1}H-NMR of the BcUGAepi reaction (in D_2O) with UDP-GlcA as a substrate (0–16.8 min). Signals from the anomeric proton of UDP-GlcA (5.57 ppm) and UDP-GalA (5.62 ppm) are shown. UDP-GlcA, uridine diphosphate glucuronic acid; UDP-GalA, uridine diphosphate galacturonic acid.

reaction mixture at equilibrium; however, preparative HPLC separation of UDP-GalA from UDP-GlcA proved impractical due to the low yield (~1 mg) obtained. We improved on the isolation efficiency by exploiting the enzyme ArnA for selective conversion of UDP-4-ketoxylose (UDP-β-L-threo-pentopyranosid-4-ulose; (Scheme S1) [31,32]. The ArnA does not utilize UDP-GalA within limits of detection. The UDP-GalA is conveniently separated from UDP-4-keto-xylose, thus enabling its isolation in high purity (≥ 98%) and in amounts of 10–50 mg (Figs S8 and S9). The identity of UDP-GalA was confirmed by HPLC and NMR (Figs S10 and S11).

The UDP-4-[^{2}H]-GlcA was prepared as mechanistic probe to analyze hydrogen transfer steps of the overall C4 epimerization of UDP-GlcA. The synthetic route was effective that reported earlier [33,34], except that regeneration of NAD^+ for twofold oxidation of UDP-glucose was done using the pyruvate/L-lactate dehydrogenase system [35]. This seemingly small change in procedure was, however, crucial to enhance the efficiency of the key oxidative step catalyzed by UDP-glucose dehydrogenase (Scheme S2). The efficient NAD^+ regeneration system also allowed higher substrate concentration (up to 30 mM) while retaining full conversion to the desired product. UDP-4-[^{2}H]-GlcA was obtained in high purity (≥ 99.5%) and in amounts of 40–50 mg (Figs S12 and S13). The yield from 4-[^{2}H]-glucose was ~50%. The identity of UDP-4-[^{2}H]-GlcA was confirmed by HPLC and NMR (Figs S14 and S15). The [^{2}H] content at C4 was 99% or greater.

Kinetic characterization of UGAepi

Initial rates of C4 epimerization were recorded using UDP-GlcA and UDP-GalA as the substrate. Time courses of substrate consumption were linear in the early phase of the reaction (Fig. 2b, Fig. S16), and there was a closed balance between substrate utilized and product formed at all conditions used. Kinetic parameters (k_{cat}, K_m) were obtained from nonlinear fits of regular hyperbolic dependencies of the initial rate upon the substrate concentration, as shown in Fig. S17. The K_m was 0.36 ± 0.02 mM for UDP-GlcA and 0.89 ± 0.13 mM for UDP-GalA. The k_{cat} was 0.25 ± 0.01 s^{-1} for UDP-GlcA and 0.32 ± 0.02 for s^{-1} for UDP-GalA. The catalytic efficiencies (k_{cat}/K_m) for forward (0.71 mM^{-1}·s^{-1}) epimerization and reverse (0.35 mM^{-1} s^{-1}) epimerization are used to calculate the K_{eq} from the Haldane relationship for the reaction [36]. The kinetically determined K_{eq} of 2.0 is in excellent agreement with the equilibrium constant measured directly. Kinetic parameters for the forward epimerization agree between this epimerase and other such enzymes of microbial and plant origin [20,22,26,27]. However, this is the first full kinetic study of a UDP-GlcA 4-epimerase at steady state.

pH studies of wild-type enzyme and Y149F variant

The canonical active site of SDR enzymes involves an invariant tyrosine whose canonical role in catalysis is that of a general base to facilitate alcohol oxidation by NAD^+ [11]. Sequence comparison with the well-studied UDP-Gal 4-epimerase revealed Tyr149 as the candidate residue in UGAepi (Fig. S18). We used replacement with phenylalanine to disrupt the catalytic functionality of the original tyrosine. The purified Y149F variant (Fig. S19) contained protein-bound NAD^+ as the wild-type enzyme. As anticipated from the proposed role of Tyr149 in catalysis, the Y149F variant was highly impaired in epimerase activity that was about 1.2×10^3-fold lower than the wild-type activity (Fig. S20). Nonetheless, the Y149F variant converted UDP-GlcA into UDP-GalA without trace formation of side products (e.g., due to decarboxylation) or intermediates. Note: we rigorously excluded contamination by the wild-type enzyme during purification of the Y149F variant (see Materials and methods). In addition, the triplet codon exchange (TAC → TTC) used for mutagenesis made translational errors during incorporation of Phe149 into the Y149F variant extremely unlikely [37–40]. Generally, removal of base catalytic assistance to the reaction does not, by necessity, lead to a complete loss of activity in the variant enzyme. Other factors effective in catalysis (e.g., positioning) might suffice to reduce the energetic barrier such that reaction can still occur at a detectable rate [41]. To further address the question of acid–base catalysis in UGAepi, we carried out pH studies with wild-type enzyme and Y149F variant. Results are shown in Fig. 3.

The pH dependence of the wild-type enzyme was sigmoidal with low and high levels of activity (k_{cat}) at low and high pH, respectively. Model for a mechanism with a single ionizable group that must be unprotonated for enzyme activity was used to fit the data [42]. An apparent pK_a of 5.90 (±0.05) was calculated. The Y149F variant was inactive at pH 6.5 or lower. Activity was found at pH ~7 and the logarithmic k_{cat} increased linearly with pH, showing a slope of 0.85 (±0.07). These results suggested that the Y149F variant might exploit alternative forms of base catalysis, perhaps from H_2O/OH^- or from another enzyme residue, as proposed for an analogous tyrosine-to-phenylalanine variant of GALE [24,43]. They provide strong evidence in support of a catalytic base function of Tyr^{149} in the wild-type UGAepi.

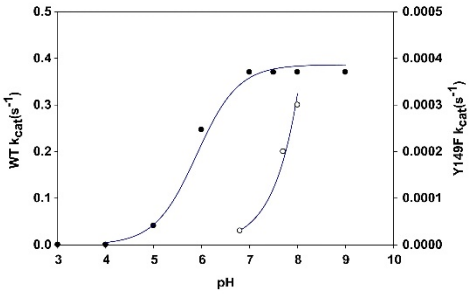

Fig. 3. Apparent k_{cat} values for the BcUGAepi reaction with UDP-GlcA dependent on pH. Symbols show the data, and the solid line is the corresponding fit. Closed circles correspond to wild-type and open circles to Y149F variant of BcUGAepi.

Isotope-labeling studies and kinetic isotope effects

To explore the epimerization mechanism used by the enzyme, we analyzed with *in situ* NMR the conversion of UDP-4-[^{2}H]-GlcA catalyzed by wild-type UGAepi. We show in Fig. S21 that deuterium label at the C4 of substrate was retained completely at the C4 of UDP-GalA product. The overall epimerization is thus shown to consist of two stereospecific steps of hydrogen transfer: abstraction (to NAD^+) of the axial C4 hydrogen/deuterium in the D-*gluco* configuration and transfer back to C4 (from NADH) in an equatorial position to establish the D-*galacto* configuration. The reaction proceeds through a transient UDP-4-keto-hexose-uronic acid intermediate that is not released from the enzyme.

Having determined that epimerization involves cleavage and formation of C4-H bond, we analyzed the effect of deuterium labeling at C4 on the enzymatic reaction rates of wild-type UGAepi and Y149F variant. We showed that the apparent k_{cat} for the wild-type reaction with UDP-4-[^{2}H]-GlcA was 2.0 (±0.1)-fold ($N = 5$) slower than the k_{cat} for the corresponding reaction with unlabeled substrate (prepared identically as the isotopically labeled one). This demonstrates that the reaction is subject to a normal primary kinetic isotope effect (KIE). The KIE ($= {k_{cat}}^H/{k_{cat}}^D$) was independent of pH in the range 6.0–9.5. At pH 5.0, the KIE was 3.5 (±0.3). The corresponding KIE for reaction of the Y149F variant was dependent on pH and increased from a value of 1.17 (±0.01) at pH 7.0 to higher values of 2.39 (±0.09) at pH 8.0 and 3.53 (±0.02) at pH 9.0.

The relative rates of the enzymatic half-reactions leading to and from the UDP-4-keto-hexose-uronic acid intermediate determine the reduced-state portion of the nicotinamide cofactor at steady state. Absorbance and fluorescence are useful to detect the enzyme-bound NADH, but the data are challenging to quantify. We therefore measured directly with a rapid-

quenching HPLC assay the relative NADH content in the wild-type enzyme while reacting with UDP-GlcA or UDP-4-[^{2}H]-GlcA. The NADH content normalized on the total amount of cofactor present was 0.014 and 0.016 in reactions with unlabeled and labeled substrates, respectively (Figs S22 and S23). It was not different within limits of error from the relative NADH content in the enzyme as isolated (0.031) (Fig. S5).

Discussion

Functional annotation of UDP-GlcA epimerases

Phylogenetic analysis places UDP-GlcA epimerases into a distinct subgroup within the sugar nucleotide epimerase family of SDR enzymes (Fig. S24). The UDP-pyranose 4-epimerases (GALE, UDP-GlcNAc 4-epimerase) [44–46] and CDP-D-paratose 2-epimerases [47,48] constitute further subgroups of that family. The UDP-GlcA epimerases are separated from UDP-GlcA decarboxylases (UXS, UAXS, ArnA) that represent a different SDR family. They are also clearly separated from two-site sugar nucleotide epimerases such as GDP-D-mannose 3,5-epimerase (Fig. S24) [49] as well as from sugar nucleotide dehydratases (not shown). The UDP-GlcA epimerases are further subdivided according to phylogenetic origin and specificity. Besides the main 4-epimerase found in plant and bacterial subgroups, a second bacterial subgroup additionally contains 5-epimerase that converts UDP-GlcA into UDP-L-IdoA [50]. However, a recent computational analysis suggested that these 5-epimerases might in fact all be UDP-GlcA 4-epimerases [51]. Studies of UGAepi substrate specificity show that the C5 carboxylate group of UDP-GlcA is essential for substrate-binding recognition and/or catalysis. UDP-Glc, UDP-Gal, UDP-GlcNAc, and UDP-Xyl are often not accepted as substrates by UGAepis [20,26,27] or give strongly decreased activity [22].

Although basic functional attributes are assignable from the sequence-based categorization, specific correlations between molecular structure and enzymatic reactivity remain elusive in the absence of detailed mechanistic–kinetic analysis. Except for the Tyr/Ser/Lys catalytic triad of residues that are universally conserved, the residues involved in sugar binding are highly variable. There is effectively very little conservation in UGAepi of the relevant sugar-binding residues of UDP-pyranose 4-epimerases [45,52], as presented with an example of GALE in Fig. S25. The epimerase and the decarboxylase reaction both face the challenge of having to combine specificity in substrate recognition with flexibility in the positioning of the respective 4-keto intermediate (Fig. 1). Each mechanism additionally requires that the different chemical steps of the enzymatic reaction are precisely coordinated with at least one physical step of reorientation/repositioning of the 4-keto intermediate. Particular task of UGAepi is to handle the highly reactive UDP-4-keto-hexose-uronic acid species for epimerization which in the corresponding decarboxylases is immediately taken further to the UDP-4-keto-pentulose intermediate via decarboxylation [13,14,17]. Only little can be inferred from the well-characterized epimerases (GALE) and UDP-GlcA decarboxylases (UXS, AXS) as to the particular catalytic strategy employed by UGAepi, thus necessitating the current study.

Kinetic properties of UGAepi

Despite their overall structural similarity and mechanistic analogy, UGAepi and GALE show interesting differences in the observable kinetic behavior. The proposed reaction pathway for UGAepi is shown in Fig. 4.

This pathway may be largely identical with that of GALE [46] but differs from it in respect to the kinetic significance of the reductive half-reaction, leading from the 4-keto intermediate to the D-*galacto* configured product. The GALE reaction with UDP-glucose was shown to involve 19% enzyme-NADH of total enzyme, hence enzyme-bound 4-keto intermediate, at the steady state [53,54]. This indicates that both half-reactions of the GALE mechanism proceed at rates of the same magnitude order. The absence of enzyme-NADH in the UGAepi reaction with UDP-GlcA shows that effectively no 4-keto intermediate is accumulated on the enzyme at the steady state.

Two kinetic scenarios are consistent with enzyme-NADH below detection in the catalytic reaction: (a) The overall sequence of steps leading to enzyme-NADH is rate-limiting. (b) Release of the UDP-GalA product from enzyme-NAD^+ is rate-limiting. The KIE of 2.0 is in accordance with the first scenario, while it refutes the second for which no isotope effect (KIE = 1) is expected. UGAepi reaction with hydride transfer to NAD^+ as the rate-limiting step is expected to show a sizeable KIE on k_{cat} ($\geq$ 3.5), substantially larger than the one observed [55–57]. Plausible explanation is that the enzymatic mechanism involves a slow physical step, most likely a conformational rearrangement of the enzyme/NAD^+/UDP-GlcA complex (Fig. 4), that precedes the hydride transfer step; this physical step suppresses the intrinsic KIE on the hydride transfer step to the one effectively measurable in k_{cat}. The proposed precatalytic step is further supported by evidence from pH studies of wild-type enzyme and

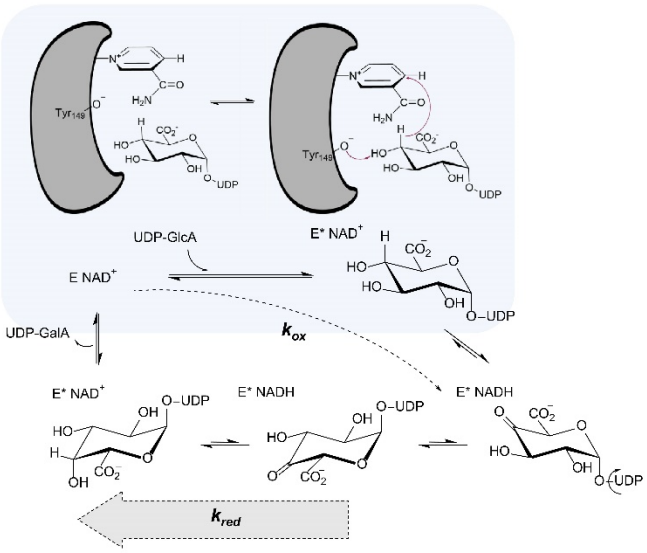

Fig. 4. Proposed kinetic mechanism of UGAepi. The first step is the binding of uridine diphosphate glucuronic acid (UDP-GlcA) into the free enzyme (E-NAD$^+$) including a slow conformational change (highlighted with gray background) in the enzyme to E*-NAD$^+$. Hydride transfer from C4-H to NAD$^+$ yields E*-NADH and UDP-4-keto-hexose-uronic acid as a reaction intermediate. This 4-keto intermediate rotates around the phosphate backbone of the substrate positioning the opposite face of the 4-keto group toward NADH. Hydride transfer from NADH yields the product uridine diphosphate galacturonic acid (UDP-GalA) which is released from the enzyme regenerating E-NAD$^+$. The flux through the reduction (k_{red}) of the 4-keto intermediate to UDP-GalA is considerably higher than the net flux through the steps involved in the oxidation (k_{ox}), which the thickness of arrows should illustrate. One can estimate that, for just 3% or less of total enzyme accumulated as enzyme-NADH at the steady state when UDP-GlcA is saturating, the flux from enzyme-NADH to give enzyme-NAD$^+$ (k_{red}) must exceed by two magnitude orders ($\geq$ 30-fold) and the net flux from enzyme-NAD$^+$ to enzyme-NADH (k_{ox}). The portion of enzyme-NADH is given by the relationship $k_{ox}/(k_{red} + k_{ox})$.

Y149F variant. At low pH, where the k_{cat} of wild-type UGAepi decreases, the KIE increases to a value of 3.5 (pH 5.0). This result suggests that the hydride transfer step of the enzymatic mechanism requires a group of enzyme/NAD$^+$/UDP-GlcA to be unprotonated and therefore is dependent upon the pH. It further suggests that an additional pH-independent step (the proposed conformational rearrangement) partly limits the k_{cat} at the pH optimum. The effect of substitution of Tyr149 by Phe on the pH dependencies of the k_{cat} and its associated KIE suggests that Tyr149 is part of the ionizable molecular group (apparent pK_a = 5.9) critical for the hydride transfer; the tyrosine is also involved in the precatalytic physical step whose probable role is to align precisely the reactive groups in enzyme/NAD$^+$/UDP-GlcA complex (Fig. 4). By analogy with the reaction of GALE, the conformational rearrangement can also be important to increase the redox potential of the enzyme-bound NAD$^+$ through favorable change in electrostatic environment [58,59]. We note furthermore that pH studies of GALE have also pointed to an unusually low pK_a (= 6.9) for the catalytic tyrosine [43].

UGAepi: stereo-electronic control for catalytic epimerization under prevention of decarboxylation

How then does UGAepi prevent decarboxylation of the labile β-keto acid moiety of the transient 4-keto intermediate? The combined evidence from kinetic analysis and structural comparison (discussed below) suggests an important role for stereo-electronic control in enzyme catalysis to the epimerization of UDP-GlcA (for general case, see ref. 60). Using structure-based, multiple sequence alignment (Fig. 5A), we show that residues involved in binding of the substrate's carboxylate group differ between UGAepis and UDP-GlcA decarboxylases (UXS, UAXS, ArnA). Crystal structure of MoeE5 [28] provides the essential structural basis

for UGAepi, and a homology model of BcUGAepi shows excellent agreement with the experimental template (Fig. 5B). In UGAepi, the substrate carboxylate is embedded in a hydrogen bond network of four coordinating residues, namely Thr126, Ser127, Ser128, and Thr178 (main chain). In the decarboxylases (UAXS, Fig. 5C; UXS, Fig. S26a; ArnA, Fig. S26b), the carboxylate group appears to be more loosely bound. The overall structure of the binding pocket is changed to provide fewer interactions (compare Fig. 5C to Fig. 5B); a binding residue (Ser128) of the epimerase is replaced by an acidic residue (Glu; Fig. 5a), known from earlier studies of UXS and UAXS to play an important role in the decarboxylase catalytic mechanism. In the epimerase, the threonine from the SDR catalytic triad (Thr126 in BcUGAepi) is in hydrogen bond distance to both the C5 carboxylate and the reactive 4-hydroxy group of the substrate. By way of comparison (Fig. S27), the 6-OH of UDP-Glc in *E. coli* GALE has just two coordinating residues (Asn179 and Tyr299) and is oriented away from Ser124 (the positional/functional homologue of Thr126 in BcUGAepi). The unique substrate-binding mode in UGAepi gives rise to the suggestion that the carboxylate of UDP-GlcA not only serves as a recognition site for binding, but it can also have an immediate involvement in substrate positioning for the catalytic event.

Analyzing the epimerase-bound conformation of UDP-GlcA in more detail, we notice that the pyranose moiety adopts an undistorted $^4C_1$ ring pucker and has the carboxylate group in a perfectly equatorial position, as shown in Fig. 6A. Based on stereo-electronic considerations [61–64], decarboxylation of the 4-keto intermediate would be optimal with the carboxylate group-oriented axially, for the dihedral angle between the C = O bond of the ketone and the C5-C6 bond could thus approach the ideal ~90°. It follows that, by maintaining the dihedral angle at close to ~0° due to the equatorial carboxylate, the epimerase might constrain its catalytic reaction so as to minimize decarboxylation. To achieve this, the epimerase has to limit sugar ring distortion in its active site, which is noteworthy in light of chemical studies showing that distortion from chair conformation influences the reactivity of 2-oxocyclohexane carboxylic acid isomers for decarboxylation in solution [61,62]. The appealing idea of differential stereo-electronic control in epimerase and decarboxylase reactions receives additional support from mechanistic studies of UXS and UAXS. In UXS, as revealed by molecular dynamics simulations, the enzyme-bound UDP-GlcA features a binding energy-driven sugar ring distortion ($^4C_1 \rightarrow B_{O,3}$) that forces the carboxylate group into an almost fully axial position (Fig. 6B) [13]. Thus, the UXS Michaelis complex provides optimal stereo-electronic conditions for immediate decarboxylation subsequent to the oxidation at C4. The UAXS reaction exploits substrate oxidation at C4 to promote retro-aldol ring opening between C2 and C3, and the decarboxylation happens only after the ring opening has occurred [17]. Stereo-electronic conditions in the active site of UAXS meet requirements for the particular timing of the catalytic steps in the enzymatic conversion. The Michaelis complex involves a largely undistorted UDP-GlcA substrate that has the carboxylate in a closely equatorial position (Fig. 6C). As suggested from molecular dynamics simulation, the ring-opened conformation of the 4-keto intermediate will only change later during the reaction to move the carboxylate into a quasi-axial position suitable for decarboxylation [17]. The special importance of stereo-electronic control for 4-keto intermediate protection in the UGAepi reaction is emphasized by the catalytic behavior of active-site variants of UXS and UAXS which despite showing only trace activity lack the ability to uncouple substrate oxidation at the C4 from decarboxylation at C5 [13,14,17].

Central task of catalysis by SDR-type epimerases is to position their keto intermediates flexibly for non-stereospecific reduction. Studies of GALE show that the requirement can be realized through a relatively weak binding of the intermediate's sugar moiety, compared with binding of its UDP moiety [25]. Therefore, mechanistic conundrum posed for UGAepi is to establish proper balance between stereo-electronic control, due to a relatively more constrained substrate binding compared with GALE (compare Fig. 5B and Fig. S27), and free rotation of the 4-keto-hexose intermediate. It can be significant, therefore, that in terms of their k_{cat} the known UGAepis (this work, 0.25 s^{-1}; *B. cereus* isozyme, 3.2 s^{-1}, [20]; *Arabidopsis thaliana*, 24 s^{-1}, [27]) are much slower enzymes than GALE (760 s^{-1}, [24]). Added binding interactions with the UDP-sugar substrate in UGAepi compared with GALE may be responsible for the slowing down of the catalytic reaction. Figure 4 shows the particular distribution of fluxes across the reaction pathway of BcUGAepi. The conformational restraint imposed by the enzyme on the rate of 4-keto intermediate formation (which also limits the k_{cat}) might reflect the structural requirements of the active site to implement the proposed stereo-electronic control. Rotation of the 4-keto-hexose-uronic acid intermediate bound to enzyme-NADH is part of the sequence of microscopic steps involved in the reduction of the 4-keto intermediate to UDP-GalA (k_{red} in Fig. 4). Although considerably faster than the enzyme's k_{cat}, the rotation step in BcUGAepi could still be appreciably slower than the

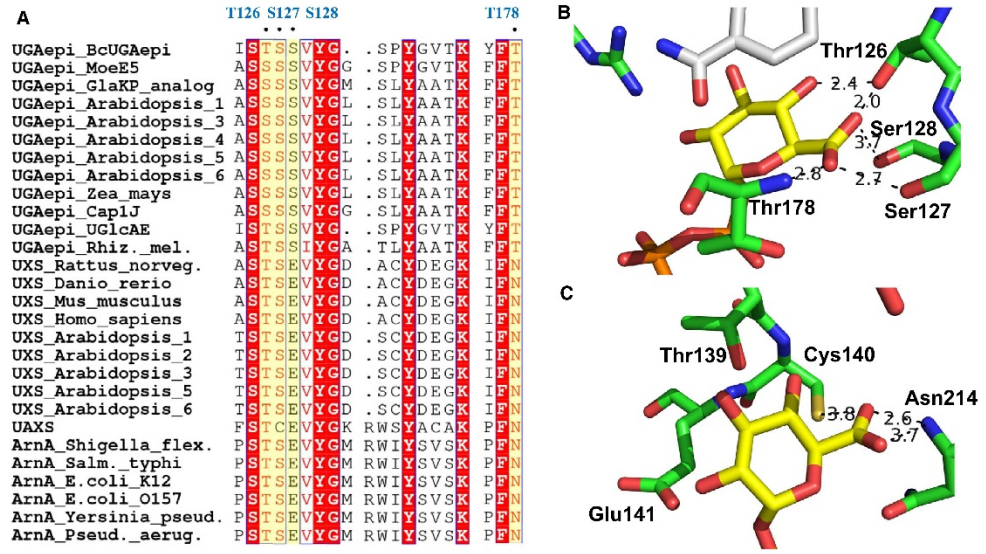

Fig. 5. Structural comparison of UDP-glucuronic acid 4-epimerases (UGAepis) and SDR-type decarboxylases active on UDP-GlcA. ArnA, UDP-glucuronic acid decarboxylase; UXS, UDP-xylose synthase; UAXS, UDP-apiose/xylose synthase. (A) Partial multiple sequence alignment (aligned with Clustal Omega and visualized with ESPript). The epimerase residues involved in binding of the carboxylate group of UDP-GlcA are highlighted in yellow, and the corresponding residues of BcUGAepi are labeled in blue at the top of the alignment. UniProt entries: UGAepi_BcUGAepi (J8BY31), UGAepi_MoeE5 (A0A003), UGAepi_GlaKP_analog (Q9RP53), UGAepi_Arabidopsis_1 (Q9M0B6), UGAepi_Arabidopsis_3 (O81312), UGAepi_Arabidopsis_4 (O22141), UGAepi_Arabidopsis_5 (Q9STI6), UGAepi_Arabidopsis_6 (Q9LIS3), UGAepi_Zea_mays (Q304Y2), UGAepi_Cap1J (P96481), UGAepi_UGlcAE (A7GQD3), UGAepi_Rhiz._mel. (O54067), UXS_Rattus_norveg. (Q5PQX0), UXS_Danio_rerio (Q6GMI9), UXS_Mus_musculus (Q91XL3), UXS_Homo_sapiens (Q8NBZ7), UXS_Arabidopsis_1 (Q8VZC0), UXS_Arabidopsis_2 (Q9LZI2), UXS_Arabidopsis_3 (Q9FIE8), UXS_Arabidopsis_5 (Q9SN95), UXS_Arabidopsis_6 (O9ZV36), UAXS (Q9ZUY6), ArnA_Shigella_flex. (Q83QT8), ArnA_Salm._typhi (O52325), ArnA_E.coli_K12 (P77398), ArnA_E.coli_O157 (Q8XDZ3), ArnA_Yersinia_pseud. (Q93PD8), and ArnA_Pseud._aerug. (Q9HY63). (B) Active-site close up of BcUGAepi modeled with YASARA from the experimental UDP-GlcA complex structure of the epimerase MoeE5 [28]. (C) Active-site close up of the UDP-GlcA complex structure of *Arabidopsis thaliana* UAXS (C100A variant; PDB: 6H0P), showing the relevant residues from the alignment. PyMOL was used to generate the structures.

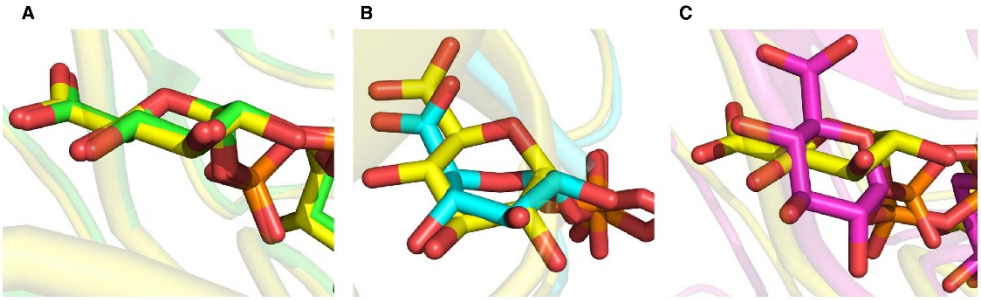

Fig. 6. PyMOL representation of the position of the C5 carboxylate group of UDP-GlcA bound to UGAepi, UXS, and UAXS. The yellow carbon atoms show BcUGAepi (modeled). (A) Overlay of the structures of MoeE5 (green; PDB: 6KV9) and BcUGAepi (modeled). The carboxylate group is equatorial. (B) Overlay of the structures of UXS (cyan; PDB: 2B69, sugar modeled into the active site [13]) and BcUGAepi. The axially oriented carboxylate can be seen in the structure of UXS. (C) Overlay of the structures of UAXS (pink; PDB: 6H0P) and BcUGAepi, showing the nearly equatorial carboxylate group in UAXS.

analogous rotation step is in GALE. To keep a tight 'grip' on the equatorial C5 carboxylate group during a comparably slow rotation may be important for BcUGAepi to retain stereo-electronic control during conversion of the 4-keto intermediate into UDP-GalA.

In summary, this study provides biochemical foundation for enzymatic C4 epimerization in UDP-GlcA. The proposed catalytic mechanism involves a transient UDP-4-keto-hexose-uronic acid intermediate whose formation and conversion via hydride transfer to and from enzyme-bound nicotinamide coenzyme are facilitated by Tyr149 acting as the general base/acid, respectively. While largely analogous to the GALE mechanism in its base features, the UGAepi mechanism is special in requiring the handling of a highly decarboxylation-prone 4-keto intermediate. Our study suggests stereo-electronic control as the catalytic strategy developed by UDP-GlcA 4-epimerase to achieve this task. Precisely orchestrated structural dynamics will be essential in their implementation. Importantly, stereo-electronic control provides an essential mechanistic distinction between UDP-GlcA 4-epimerase and SDR-type decarboxylases using UDP-GlcA as the substrate.

Materials and methods

Materials

The synthetic genes of BcUGAepi and ArnA were ordered in pET17b expression vector (pET17b_BcUGAepi; pET17b_ArnA) from GenScript (Piscataway, NJ, USA). Uridine monophosphate (UMP, 98% purity) was from Carbosynth (Compton, UK). Uridine diphosphate (UDP), UDP-D-glucuronic acid (UDP-GlcA; > 98% purity), and sodium pyruvate was from Sigma-Aldrich (Vienna, Austria). NAD^+ (> 98% purity) was from Roth (Karlsruhe, Germany). Deuterium oxide (99.96% ^2H) was from Euriso-Top (Saint-Aubin Cedex, France). All other reagents and chemicals were of highest available purity. For plasmid DNA isolation, the GeneJET Plasmid Miniprep Kit (Thermo Scientific, Waltham, MA, USA) was used. DpnI and Q5® High-Fidelity DNA polymerase were from New England Biolabs (Frankfurt am Main, Germany). Hexokinase and D-lactate dehydrogenase were from Megazyme (Vienna, Austria). All other enzymes were prepared in-house. Oligonucleotide primers were from Sigma-Aldrich. *E. coli* NEB5α competent cells were from New England Biolabs. *E. coli* Lemo21 (DE3) cells were prepared in-house.

Enzymes

The site-directed substitution Tyr149 by Phe was introduced by a modified QuikChange protocol (see Supporting information for details). Both BcUGAepi wild-type and Y149F variants were produced by expression in *E. coli* Lemo21 (DE3) cells that harbored the pET17b expression vector containing the gene of interest. The proteins were purified utilizing the C-terminal Strep-tag, and the size and purity of the proteins were confirmed by SDS/PAGE. For purification of the Y149F variant, new Strep-tag columns were used to avoid any possible contamination by the wild-type enzyme. Full details of the expression and purification conditions used are given in the Supporting information. ArnA was obtained by expression in *E. coli* BL21 (DE3) harboring the pET17b_ArnA vector using the same expression and purification procedure as for BcUGAepi.

Human UDP-glucose 6-dehydrogenase (hUGDH) was expressed in *E. coli* Rosetta 2 (DE3) cells harboring the vector pBEN_SGC_hUGDH [65]. Inorganic pyrophosphatase (iPPase) was produced by expression in *E. coli* BL21 (DE3) cells carrying pET-STREP3_iPPase vector. UDP-glucose pyrophosphorylase (UGPase) was expressed in *E. coli* BL21 (DE3) Gold cells harboring pET30_UGPase plasmid. hUGDH and iPPase were purified by affinity chromatography using Strep-tag following the same procedure as for BcUGAepi, and UGPase was isolated by His-tag purification (see the Supporting information for details). The activity of iPPase was determined as described in the literature [66], and the activity measurement of UGPase is described in the Supporting information.

Substrate synthesis

UDP-α-D-galacturonic acid

The reaction mixture (20 mL) contained 4.6 mM UDP-GlcA (60 mg, 0.09 mmol), 1 mM NAD^+ (13.3 mg, 0.02 mmol), and 2.7 μM BcUGAepi (0.1 mg·mL^{-1}, 2 mg) in buffer (50 mM Na_2HPO_4, 100 mM NaCl, pH 7.6). Incubation was at 30 °C until UDP-GalA and UDP-GlcA were present at the equilibrium ratio of 2:1, respectively, confirmed by HPLC. BcUGAepi was removed by ultrafiltration (Vivaspin Turbo centrifugal filter tube, 30 kDa cutoff). The remaining UDP-GlcA was converted to UDP-α-D-4-keto-xylose (Scheme S1) by adding the following components into the reaction mixture: 10 mM sodium pyruvate (22 mg, 0.2 mmol), 20 U·mL^{-1} LDH (400 U), and 4.7 μM ArnA (0.2 mg mL^{-1}, 2.8 mg). The reaction mixture was incubated at 30 °C for 16 h until all UDP-GlcA was consumed. ArnA and LDH were removed from the mixture by ultrafiltration (30 kDa cutoff).

UDP-α-D-4-^{2}H-glucuronic acid

The synthesis strategy is indicated in Scheme S2. The reaction mixture (37 mL) contained 15 mM 4-^{2}H-α-D-glucose (100 mg, 0.55 mmol), 50 mM uridine 5′-triphosphate (UTP, 716.5 mg, 1.3 mmol), 5 mM $MgCl_2$ (17.6 mg, 0.18 mmol), 0.13% (w/v) bovine serum albumin (BSA, 48.1 mg), and 10 μM α-D-glucose 1,6-bisphosphate dissolved in 50 mM Tris/HCl buffer (pH 7.5). Hexokinase (13.8 U·mL^{-1}, 510.6 U),

6.8 U·mL^{-1} phosphoglucomutase (251.6 U), 0.2 mg·mL^{-1} UGPase (7.4 mg), and 0.077 mg·mL^{-1} iPPase (2.8 mg) were added, and the reaction mixture was incubated at 30 °C for 20 h. After confirming the completeness of the reaction on HPLC, the final oxidation step toward UDP-4-^{2}H-GlcA was initiated by the addition of 2 mM NAD^+ (49 mg, 0.074 mmol), 40 mM sodium pyruvate (163 mg, 1.48 mmol), 20 U·mL^{-1} LDH (740 U), and 1.23 mg·mL^{-1} hUGDH (45.5 mg), and the reaction was incubated at 37 °C for 24 h. The enzymes were removed with Vivaspin Turbo centrifugal filter tubes (10 kDa cutoff, Sartorius) prior to column purification of the nucleotide sugar.

Product isolation

Both UDP-α-D-galacturonic acid and UDP-α-D-4-^{2}H-glucuronic acid were isolated by two-column chromatographic purification steps. First, the desired product was separated from the other components using ÄKTA FPLC system (GE Healthcare, Vienna, Austria) connected to a 125 mL TOYOPEARL SuperQ-650M anion exchange column (GE Healthcare) and a 10 mL sample loop. 20 mM sodium acetate solution (pH 4.3) was used as binding buffer. Compounds bound to the column were eluted with a step-wise gradient of 1 M sodium acetate buffer at pH 4.3; see SI for details. Fractions containing the desired product were detected via UV absorption (λ = 254 nm), identified by HPLC, and combined prior to concentrating under reduced pressure on a Laborota 4000 rotary evaporator (Heidolph, Schwabach, Germany) at 40 °C to a final volume of approximately 5–10 mL. NaOAc was removed from the concentrated product preparation using an ÄKTA FPLC connected to Superdex G-10 size-exclusion column (GE Healthcare) and 5 mL sample loop. The product was detected based on its UV absorption at 254 nm and eluted with deionized water. The product-containing fractions were combined and concentrated under reduced pressure at 40 °C to a final volume of approximately 20 mL. Residual H_2O was removed by lyophilization (Christ Alpha 1-4 Lyophilizer, B. Braun Biotech International, Melsungen, Germany), and the pure nucleotide sugar obtained as white powder. The purity and identity of UDP-α-D-galacturonic acid and UDP-α-D-4-^{2}H-glucuronic acid were determined on HPLC and ^{1}H-NMR.

Determination of enzyme-bound coenzyme

The dimeric oligomeric state of BcUGAepi wild-type was determined by gel filtration chromatography (see Supporting information for details).

Enzyme-bound NAD^+/ NADH

For studying the occupancy of BcUGAepi by NADH, the enzyme (50 µL, 18 mg·mL^{-1}) was denatured by incubating with 50 µL of methanol for 3 h at room temperature. The enzyme precipitation was removed by centrifugation (16 100 ***g***, 80 min, 4 °C) and the supernatant analyzed on HPLC. The amount of released NADH was calculated based on a calibration curve (Fig. S22), where defined concentrations of NADH were prepared in double-distilled water and directly used for measurements. UV absorbance at 262 nm was used for the detection of NAD^+ and NADH. The occupancy of NADH in BcUGAepi was calculated in % from the concentration of released NADH (in µM) divided by the total protein concentration (in µM) used in the experiment.

Rapid-quench procedure to analyze enzyme-bound NADH from reaction

Reaction mixture containing 1 mM UDP-GlcA or UDP-4-^{2}H-GlcA and 1 µM (0.035 mg·mL^{-1}) of purified BcUGAepi was prepared in 10 mL of sodium phosphate buffer (50 mM Na_2HPO_4, 100 mM NaCl, pH 7.6). The reaction was run for 2 min at 23 °C, and afterward, 10 mL of ice-cold phosphate buffer (50 mM Na_2HPO_4, 100 mM NaCl, pH 1.3) was added to decrease the pH of the reaction mixture to 4.4 and terminate the enzymatic activity, while retaining the enzyme soluble. The reaction mixture was immediately transferred into an ice-cold Vivaspin Turbo centrifugal filter tube (30 kDa cutoff) and centrifuged at 0 °C (2880 g) until 19 mL of the mixture had flowed through the filter. The flow-through was analyzed on HPLC, and the enzyme was washed twice with 5 mL of ice-cold phosphate buffer (50 mM Na_2HPO_4, 100 mM NaCl, pH 4.4). The flow-through from each washing step was analyzed on HPLC to confirm that the UDP-GlcA/UDP-GalA ratio remained unchanged over the washing procedure. The enzyme was concentrated up to the final volume of 50 µL and denatured with 50 µL of MeOH as described in the section 'Enzyme-bound NAD^+/ NADH'. The NADH released from the active site of BcUGAepi was detected on HPLC. As a control for the stability of NADH, the same procedure was performed for NADH standard solution to confirm that the coenzyme was not degrading during the denaturation experiment.

BcUGAepi activity assays

Standard BcUGAepi reaction mixtures (250 µL final volume) contained 1 mM UDP-GlcA, 100 µM NAD^+, and 2 µM (0.07 mg·mL^{-1}) purified recombinant BcUGAepi (135 µM/ 5 mg·mL^{-1} for variant Y149F) in sodium phosphate buffer (50 mM Na_2HPO_4, 100 mM NaCl, pH 7.6). The reactions were incubated at 23 °C, quenched with methanol (50% (v/v) final concentration) at desired time points, and the precipitated enzyme removed by centrifugation (16 100 ***g***, 4 °C, 30 min) prior to HPLC analysis. The initial rates were determined from the linear part of the time course by dividing the slope of the linear regression (mM·min^{-1}) by the enzyme

concentration ($mg \cdot mL^{-1}$) giving the initial rate in μmol per (min mg protein). The apparent k_{cat} values (s^{-1}) were calculated from the initial rate with the molecular mass of the functional enzyme monomer (wild-type BcUGAepi: 37 003 $g \cdot mol^{-1}$; Y149 variant: 36 987 $g \cdot mol^{-1}$). For the temperature optimum study, the reactions were performed under standard conditions but in varying temperatures. For NAD^+ concentration study, the reactions were carried out under standard conditions except that lower enzyme concentration (1 μM, 0.037 $mg \cdot mL^{-1}$) was used.

For the determination of the kinetic parameters, BcUGAepi (2 μM, 0.07 $mg \cdot mL^{-1}$) was mixed with NAD^+ (50 μM) in 50 mM Na_2HPO_4 buffer (containing 100 mM NaCl, pH 7.6). Varying concentrations of substrate (UDP-GlcA/UDP-GalA) were added into the 100 μL reaction mixture at room temperature, and the reactions were quenched after 10-min incubation time with 25% (v/v) acetonitrile and heated up to 95 °C for 5 min. Each reaction was carried out in duplicate. After centrifugation (16 100 ***g***, 4 °C, 30 min), the samples were analyzed on HPLC and the initial rates were plotted against the substrate concentration used. The kinetic parameters were calculated with SigmaPlot 10.0 based on fitting to the Michaelis–Menten kinetic model. The k_{cat} is based on the molarity of the enzyme subunit.

In situ ^{1}H NMR

For *in situ* NMR experiments, the reaction was carried out in D_2O buffer (50 mM K_2HPO_4/KH_2PO_4) titrated to pD 7.6, where pD corresponds to the reading of pH meter + 0.4. The reaction mixture contained 2.7 mM UDP-GlcA (or UDP-4-^{2}H-GlcA), 91 μM NAD^+, and 2.4 μM (0.09 $mg \cdot mL^{-1}$) purified recombinant BcUGAepi. The acquisition was carried out on a Varian INOVA 500-MHz NMR spectrometer (Agilent Technologies, Santa Clara, CA, USA) every 30 s from the enzyme addition. The VNMRJ 2.2D software was used for the measurements. ^{1}H-NMR spectra (499.98 MHz) were recorded on a 5-mm indirect detection PFG probe with presaturation of the water signal by a shaped pulse. The spectra were analyzed using MestReNova 16.0 (Mestrelab Research, S.L., Santiago de Compostela, Spain).

pH studies and kinetic isotope effects

All the experiments were performed with 1 mM UDP-GlcA. No significant increase in activity was observed if higher substrate concentration was used.

pH studies

For pH optimum studies (at 23 °C), the reaction buffer (50 mM Na_2HPO_4, 100 mM NaCl) was prepared in desired pH values (pH 3–9) and BcUGAepi wild-type was confirmed as stable over this pH range. The pH was adjusted either with 5 mM NaOH or with 10% HCl. UDP-GlcA (1 mM), NAD^+ (100 μM) and BcUGAepi (2 μM, 0.07 $mg \cdot mL^{-1}$) were mixed with the buffer, and samples were taken for HPLC analysis at defined time points from 0 to 150 min.

The initial rates (s^{-1}) were calculated at each pH value and plotted against the pH. The data for the BcUGAepi wild-type were fitted to an Eqn (1) where $\log k_{cat}$ increases with a slope of + 1 below pK and is level above pK. [42]

$$\log k_{cat} = \log\left[\frac{C}{1 + [H^+]/K}\right] \quad (1)$$

where C is the pH-independent value of k_{cat}, $[H^+]$ is the proton concentration, and K is a proton dissociation constant.

For Y149F variant, the data were fitted using standard linear regression.

Kinetic isotope effect measurements

For kinetic isotope effect measurements, BcUGAepi concentration of 0.037 $mg \cdot mL^{-1}$ (1 μM) was used and the reactions (30 μL final volume) were performed in quintuplicates for both UDP-GlcA and 4-^{2}H-UDP-GlcA (1 mM). The substrate concentration used was saturating. The KIE reaction mixtures were quenched (incubation in 50% (v/v) methanol at 90 °C for 5 min) after 5 min and analyzed on HPLC. Initial reaction rates (V) were calculated from the linear dependence of the product formed and time used. The KIE was calculated from the ratio of the reaction rates (effectively, k_{cat}) for the unlabeled and deuterium-labeled substrate ($KIE = V_{unlabeled}/V_{labeled}$).

Analytics

HPLC

The sugar nucleotides and NAD^+/NADH were separated with Shimadzu Prominence HPLC-UV system (Shimadzu, Korneuburg, Austria) on a Kinetex C18 column (5 μm, 100 Å, 50 × 4.6 mm) using an isocratic method with 5% acetonitrile and 95% tetrabutylammonium bromide buffer (40 mM TBAB, 20 mM K_2HPO_4/KH_2PO_4, pH 5.9) as mobile phase. UDP-sugars, NAD^+, and NADH were detected by UV at 262 nm wavelength. The amount of UDP-GlcA/UDP-GalA formed was determined based on the relative integrated peak areas and referred to a calibration curve of a commercial standard of UDP-GlcA.

NMR

The purity and identity of the synthesized compounds were determined by ^{1}H NMR. All the acquisitions were carried out in D_2O on a Varian INOVA 500-MHz NMR spectrometer (Agilent Technologies).

Acknowledgements

Financial support from the Austrian Science Fund FWF (project number: I 3247) is gratefully acknowledged. The authors thank Dr Mario Klimacek and Dr Manuel Eibinger for assistance in fitting the pH and kinetic data.

Conflict of interest

The authors declare no conflict of interest.

Author contributions

The experimental work included in this paper has been performed by AJEB and HW performed the NMR analyses. AD contributed in designing the synthesis route for UDP-GalA. BN designed and supervised the research. BN and AJEB wrote the paper.

References

1 Freeze HH, Hart GW & Schaar RL (2017) Glycosylation precursors. In Essentials of Glycobiology (Varki A, Cummings RD, Esko JD, Stanley P, Hart GW, Aebi M, Darvill AG, Kinoshita T, Packer NH, Prestegard JH, Schnaar RL & Seeberger PH, eds), 3rd edn. Cold Spring Harbor Laboratory Press, Cold Spring Harbor, NY. 1–25.

2 Bethke G, Thao A, Xiong G, Li B, Soltis NE, Hatsugai N, Hillmer RA, Katagiri F, Kliebenstein DJ, Pauly M *et al.* (2015) Pectin biosynthesis is critical for cell wall integrity and immunity in *Arabidopsis thaliana*. *Plant Cell* **28**, 537–556.

3 Bowles D, Lim EK, Poppenberger B & Vaistij FE (2006) Glycosyltransferases of lipophilic small molecules. *Annu Rev Plant Biol* **57**, 567–597.

4 Ritter JK (2000) Roles of glucuronidation and UDP-glucuronosyltransferases in xenobiotic bioactivation reactions. *Chem Biol Interact* **129**, 171–193.

5 Bhagavan NV & Ha CE (2015) Carbohydrate metabolism II. In Essentials of Medical Biochemistry, pp. 205–225. San Diego: Elsevier.

6 Reiter WD (2008) Biochemical genetics of nucleotide sugar interconversion reactions. *Curr Opin Plant Biol* **11**, 236–243.

7 Reboul R, Geserick C, Pabst M, Frey B, Wittmann D, Lütz-Meindl U, Léonard R & Tenhaken R (2011) Down-regulation of UDP-glucuronic acid biosynthesis leads to swollen plant cell walls and severe developmental defects associated with changes in pectic polysaccharides. *J Biol Chem* **286**, 39982–39992.

8 Kelleher WJ & Grisebach H (1971) Hydride transfer in the biosynthesis of uridine diphospho-apiose from uridine diphospho-D-glucuronic acid with an enzyme preparation of *Lemna minor*. *Eur J Biochem* **23**, 136–142.

9 Moriarity JL, Hurt KJ, Resnick AC, Storm PB, Laroy W, Schnaar RL & Snyder SH (2002) UDP-glucuronate decarboxylase, a key enzyme in proteoglycan synthesis: cloning, characterization and localization. *J Biol Chem* **277**, 16968–16975.

10 Neufeld EF, Feingold DS & Hassid WZ (1958) Enzymatic conversion of uridine diphosphate D-glucuronic acid to uridine diphosphate galacturonic acid, uridine diphosphate xylose and uridine diphosphate arabinose. *J Am Chem Soc* **80**, 4430–4431.

11 Kavanagh KL, Jçrnvall H, Persson B & Oppermann U (2008) The SDR superfamily: functional and structural diversity within a family of metabolic and regulatory enzymes. *Cell Mol Life Sci* **65**, 3895–3906.

12 Liu Y, Vanhooke JL & Frey PA (1996) UDP-galactose 4-epimerase: NAD^+ content and a charge-transfer band associated with the substrate-induced conformational transition. *Biochemistry* **35**, 7615–7620.

13 Eixelsberger T, Sykora S, Egger S, Brunsteiner M, Kavanagh KL, Oppermann U, Brecker L & Nidetzky B (2012) Structure and mechanism of human UDP-xylose Synthase. *J Biol Chem* **287**, 31349–31358.

14 Gatzeva-Topalova PZ, May AP & Sousa MC (2005) Structure and mechanism of ArnA: conformational change implies ordered dehydrogenase mechanism in key enzyme for polymyxin resistance. *Structure* **13**, 929–942.

15 Allard STM, Giraud MF & Naismith JH (2001) Epimerases: structure, function and mechanism. *Cell Mol Life Sci* **58**, 1650–1665.

16 Thoden JB, Henderson JM, Fridovich-Keil JL & Holden HM (2002) Structural analysis of the Y299C mutant of *Escherichia coli* UDP-galactose 4-epimerase. Teaching an old dog new tricks. *J Biol Chem* **277**, 27528–27534.

17 Savino S, Borg AJE, Dennig A, Pfeiffer M, de Giorgi F, Weber H, Dubey KD, Rovira C, Mattevi A & Nidetzky B (2019) Deciphering the enzymatic mechanism of sugar ring contraction in UDP-apiose biosynthesis. *Nat Catal* **2**, 1115–1123.

18 Thibodeaux CJ, Melancon CE & Liu HW (2007) Unusual sugar biosynthesis and natural product glycodiversification. *Nature* **446**, 1008–1016.

19 Samuel J & Tanner ME (2002) Mechanistic aspects of enzymatic carbohydrate epimerization. *Nat Prod Rep* **16**, 261–77.

20 Broach B, Gu X & Bar-Peled M (2012) Biosynthesis of UDP-glucuronic acid and UDP-galacturonic acid in *Bacillus cereus* subsp. cytotoxis NVH 391–98. *FEBS J* **279**, 100–112.

21 Eixelsberger T, Horvat D, Gutmann A, Weber H & Nidetzky B (2017) Isotope probing of the UDP-apiose/UDP-xylose synthase reaction: evidence of a mechanism

via a coupled oxidation and aldol cleavage. *Angew Chemie Int Ed* **56**, 2503–2507.
22 Frirdich E & Whitfield C (2005) Characterization of GlaKP, a UDP-galacturonic acid C4-epimerase from *Klebsiella pneumoniae* with extended substrate specificity. *J Bacteriol* **187**, 4104–4115.
23 Thoden JB, Wohlers TM, Fridovich-Keil JL & Holden HM (2001) Human UDP-galactose 4-epimerase. Accommodation of UDP-*N*-acetylglucosamine within the active site. *J Biol Chem* **276**, 15131–15136.
24 Liu Y, Thoden JB, Kim J, Berger E, Gulick AM, Ruzicka FJ, Holden HM & Frey PA (1997) Mechanistic roles of tyrosine 149 and serine 124 in UDP-galactose 4-epimerase from *Escherichia coli*. *Biochemistry* **36**, 10675–10684.
25 Frey PA & Hegeman AD (2013) Chemical and stereochemical actions of UDP–Galactose 4-epimerase. *Acc Chem Res* **46**, 1417–1426.
26 Muñoz R, López R, de Frutos M & García E (1999) First molecular characterization of a uridine diphosphate galacturonate 4-epimerase: an enzyme required for capsular biosynthesis in *Streptococcus pneumoniae* type 1. *Mol Microbiol* **31**, 703–713.
27 Gu X & Bar-Peled M (2004) The biosynthesis of UDP-galacturonic acid in plants. Functional cloning and characterization of *Arabidopsis* UDP-D-glucuronic acid 4-epimerase. *Plant Physiol* **136**, 4256–4264.
28 Sun H, Ko T-P, Liu W, Liu W, Zheng Y, Chen C-C & Guo R-T (2020) Structure of an antibiotic-synthesizing UDP-glucuronate 4-epimerase MocE5 in complex with substrate. *Biochem Biophys Res Commun* **521**, 31–36.
29 Ohashi T, Cramer N, Ishimizu T & Hase S (2006) Preparation of UDP-galacturonic acid using UDP-sugar pyrophosphorylase. *Anal Biochem* **352**, 182–187.
30 Yang T, Bar-Peled L, Gebhart L, Lee SG & Bar-Peled M (2009) Identification of galacturonic acid-1-phosphate kinase, a new member of the GHMP kinase superfamily in plants, and comparison with galactose-1-phosphate kinase. *J Biol Chem* **284**, 21526–21535.
31 Polizzi SJ, Walsh RM Jr, Peeples WB, Lim J-M, Wells L & Wood ZA (2012) Human UDP-α-D-xylose synthase and *Escherichia coli* ArnA conserve a conformational shunt that controls whether xylose or 4-keto-xylose is produced. *Biochemistry* **51**, 8844–8855.
32 Gatzeva-Topalova PZ, May AP & Sousa MC (2004) Crystal structure of *Escherichia coli* ArnA (PmrI) decarboxylase domain. A key enzyme for lipid A modification with 4-amino-4-deoxy-L-arabinose and polymyxin resistance. *Biochemistry* **43**, 13370–13379.
33 Ma X & Stöckigt J (2001) High yielding one-pot enzyme-catalyzed synthesis of UDP-glucose in gram scales. *Carbohydr Res* **333**, 159–163.
34 Eixelsberger T & Nidetzky B (2014) Enzymatic redox cascade for one-pot synthesis of uridine 5′-diphosphate xylose from uridine 5′-diphosphate glucose. *Adv Synth Catal* **356**, 3575–3584.
35 Toone EJ, Simon ES & Whitesides GM (1991) Enzymatic synthesis of uridine 5′-diphosphoglucuronic acid on a gram scale. *J Org Chem* **56**, 5603–5606.
36 Segel IH (1993) Enzyme Kinetics: Behavior and Analysis of Rapid Equilibrium and Steady-State Enzyme Systems. Wiley, New York, NY.
37 Johansson M, Zhang J & Ehrenberg M (2012) Genetic code translation displays a linear trade-off between efficiency and accuracy of tRNA selection. *Proc Natl Acad Sci USA* **109**, 131–136.
38 Ogle JM, Brodersen DE, Clemons WM Jr, Tarry MJ, Carter AP & Ramakrishnan V (2001) Recognition of cognate transfer RNA by the 30S ribosomal subunit. *Science* **292**, 897–902.
39 Ogle JM & Ramakrishnan V (2005) Structural insides into translational fidelity. *Annu Rev Biochem* **74**, 129–177.
40 Ou X, Cao J, Cheng A, Peppelenbosch MP & Pan Q (2019) Errors in translational decoding: tRNA wobbling or misincorporation? *PLOS Genet* **15**, e1008017.
41 Jencks WP (2006) Binding energy, specificity, and enzymic catalysis: the circe effect. In Advances in Enzymology and Related Areas of Molecular Biology, Vol. **43**, pp. 219–410. Hoboken: Wiley Blackwell.
42 Krahulec S, Armao GC, Bubner P, Klimacek M & Nidetzky B (2009) Polyol-specific long-chain dehydrogenases/reductases of mannitol metabolism in *Aspergillus fumigatus*: Biochemical characterization and pH studies of mannitol 2-dehydrogenase and mannitol-1-phosphate 5-dehydrogenase. *Chem Biol Interact* **178**, 274–282.
43 Berger E, Arabshahi A, Wei Y, Schilling JF & Frey PA (2001) Acid-base catalysis by UDP-galactose 4-epimerase: correlations of kinetically measured acid dissociation constants with thermodynamic values for tyrosine 149. *Biochemistry* **40**, 6699–6705.
44 Ishiyama N, Creuzenet C, Lam JS & Berghuis AM (2004) Crystal structure of WbpP, a genuine UDP-N-acetylglucosamine 4-epimerase from *Pseudomonas aeruginosa*: substrate specificity in UDP-hexose 4-epimerases. *J Biol Chem* **279**, 22635–22642.
45 Nam YW, Nishimoto M, Arakawa T, Kitaoka M & Fushinobu S (2019) Structural basis for broad substrate specificity of UDP-glucose 4-epimerase in the human milk oligosaccharide catabolic pathway of *Bifidobacterium longum*. *Sci Rep* **9**, 11081.
46 Frey PA & Hegeman AD (2013) Chemical and stereochemical actions of UDP–galactose 4-epimerase. *Acc Chem Res* **46**, 1417–1426.
47 Koropatkin NM, Liu HW & Holden HM (2003) High resolution X-ray structure of tyvelose epimerase from *Salmonella typhi*. *J Biol Chem* **278**, 20874–20881.

48 Hallis TM, Zhao Z & Liu HW (2000) New insights into the mechanism of CDP-D-tyvelose 2-epimerase: an enzyme-catalyzing epimerization at an unactivated stereocenter. *J Am Chem Soc* **122**, 10493–10503.
49 Major LL, Wolucka BA & Naismith JH (2005) Structure and function of GDP-mannose-3′,5′-epimerase: an enzyme which performs three chemical reactions at the same active site. *J Am Chem Soc* **127**, 18309–18320.
50 Jacobson B & Davidson EA (1963) UDP-D-glucuronic acid-5-epimerase and UDP-N-acetylglucosamine-4-epimerase of rabbit skin. *Biochim Biophys Acta* **73**, 145–151.
51 Gevaert O, Van Overtveldt S, Da Costa M, Beerens K & Desmet T (2020) Novel insights into the existence of the putative UDP-glucuronate 5-epimerase specificity. *Catal* **10**, 222.
52 Thoden JB, Frey PA & Holden HM (1996) Molecular structure of the NADH/UDP-glucose abortive complex of UDP-galactose 4-epimerase from *Escherichia coli*: implications for the catalytic mechanism. *Biochemistry* **35**, 5137–5134.
53 Maitra US, Gaunt MA & Ankel H (1974) The mechanism of uridine diphosphate-sugar-4-epimerase reactions. Isotope discrimination with 4-tritiated substrates. *J Biol Chem* **249**, 3075–3078.
54 Wilson DB & Hogness DS (1964) The enzymes of the galactose operon in *Escherichia coli*. I. Purification and characterization of uridine diphosphogalactose 4-epimerase. *J Biol Chem* **239**, 2469–2481.
55 Hermes JD & Cleland WW (1984) Evidence from multiple isotope effect determinations for coupled hydrogen motion and tunneling in the reaction catalyzed by glucose-6-phosphate dehydrogenase. *J Am Chem Soc* **106**, 7263–7264.
56 Cook PF (1991) Enzyme Mechanism from Isotope Effects, pp. 203–230. Boca Raton: CRC Press.
57 Kohen A & Limbach HH (2006) Isotope effects in chemistry and biology, pp. 811–830. Boca Raton: CRC Press.
58 Burke JR & Frey PA (1993) The importance of binding energy in catalysis of hydride transfer by UDP-galactose 4-epimerase: a carbon-13 and nitrogen-15 NMR and kinetic study. *Biochemistry* **32**, 13220–13230.
59 Swanson BA & Frea PA (1993) Identification of lysine 153 as a functionally important residue in UDP-galactose 4-epimerase from *Escherichia coli*. *Biochemistry* **32**, 13231–13236.
60 Gorenstein DG (1987) Stereoelectronic effects in biomolecules. *Chem Rev* **97**, 1047–1077.
61 Kayser RH, Brault M, Pollack RM, Bantia S & Sadoff SF (1983) Kinetics of decarboxylation of the two epimers of 5-tert-butyl-1-methyl-2-oxocyclohexanecarboxlic acid: lack of stereoelectronic control in beta-keto acid decarboxylation. *J Org Chem* **48**, 4497–4502.
62 Pollack RM (1989) Stereoelectronic control in the reactions of ketones and their enol(ate)s. *Tetrahedron* **45**, 4913–4938.
63 Silverman RB (2002) The Organic Chemistry of Enzyme-Catalyzed Reactions, pp. 364–367. Amsterdam: Elsevier.
64 Fortner KC & Shair MD (2007) Stereoelectronic effects dictate mechanistic dichotomy between Cu(II)-catalyzed and enzyme-catalyzed reactions of malonic acid half thioesters. *J Am Chem Soc* **129**, 1032–1033.
65 Eixelsberger T, Brecker L & Nidetzky B (2012) Catalytic mechanism of human UDP-glucose 6-dehydrogenase: in situ proton NMR studies reveal that the C-5 hydrogen of UDP-glucose is not exchanged with bulk water during the enzymatic reaction. *Carbohydr Res* **356**, 209–214.
66 Pfeiffer M, Bulfon D, Weber H & Nidetzky B (2016) A kinase-independent one-pot multienzyme cascade for an expedient synthesis of guanosine 5′-diphospho-D-mannose. *Adv Synth Catal* **358**, 3809–3816.

Supporting information

Additional supporting information may be found online in the Supporting Information section at the end of the article.

Fig. S1. Results of SDS-PAGE of purified BcUGAepi (~37 kDa).

Fig. S2. Calibration curve for HiLoad 16/60 Superdex 200 gel filtration column prepared with gel filtration standard mixture #1511901.

Fig. S3. Gel filtration chromatogram of BcUGAepi detected by UV absorbance at 280 nm.

Fig. S4. Absorbance spectrum of wild-type BcUGAepi indicating the presence of a protein-bound nicotinamide cofactor (260 nm, 340 nm).

Fig. S5. HPLC chromatograms of NAD^+, $NADP^+$ and NADH standards (a-c) and supernatant of denatured BcUGAepi showing the cofactor content (d).

Fig. S6. Influence of NAD+ concentration (0–1000 μM) on the catalytic activity of BcUGAepi with UDP-GlcA.

Fig. S7. Catalytic activity of BcUGAepi in the reaction with UDP-GlcA at different temperatures.

Fig. S8. Anion exchange chromatogram recorded during the purification of UDP-α-D-galacturonic acid (UDP-GalA).

Fig. S9. Chromatogram recorded during the desalting step of UDP-α-D-galacturonic acid.

Fig. S10. HPLC chromatogram of purified and desalted UDP-α-D-galacturonic acid. The purity of> 98% was obtained.

Fig. S11. ^1H NMR spectrum (500 MHz, D_2O) of purified and desalted UDP-α-D-galacturonic acid, δ

5.62 ppm (dd, 1H), 4.41 ppm (s, 1H), 4.23 ppm (m, 1H), 3.92 ppm (dd, 1H), 3.75 ppm (dd, 1H).

Fig. S12. Chromatogram recorded during the purification of UDP-α-D-4-^{2}H-glucuronic acid.

Fig. S13. Chromatogram recorded during the desalting of UDP-α-D-4-^{2}H-glucuronic acid.

Fig. S14. HPLC chromatogram of purified and desalted UDP-α-D-4-2H-glucuronic acid. The purity of> 99% was obtained.

Fig. S15. ^{1}H NMR spectrum (500 MHz, D_2O) of purified and desalted UDP-α-D-4-^{2}H-glucuronic acid, δ 5.58 ppm (dd, 1H), 4.17 ppm (d, 1H), 3.74 ppm (d, 1H), 3.55 ppm (dd, 1H).

Fig. S16. Time course of BcUGAepi reaction with UDP-GalA as a substrate.

Fig. S17. Michaelis-Menten kinetics of the forward (a. UDP-GlcA → UDP-GalA) and reverse (b. UDP-GalA → UDP-GlcA) reaction catalyzed by BcUGAepi.

Fig. S18. Multiple sequence alignment (prepared with Clustal Omega) of UDP-galactose 4-epimerases (GALEs) and BcUGAepi.

Fig. S19. Results of SDS-PAGE of purified BcUGAepi _Y149F (~37 kDa).

Fig. S20. Time course of BcUGAepi_Y149F catalyzed reaction with UDP-GlcA as a substrate.

Fig. S21. *In situ* NMR experiments with BcUGAepi.

Fig. S22. NADH calibration curve on HPLC.

Fig. S23. HPLC chromatograms from denaturation experiments of BcUGAepi reacted with UDP-GlcA and UDP-4-[^{2}H]-GlcA.

Fig. S24. Phylogenetic analysis of SDRs active on sugar nucleotides.

Fig. S25. (a) A part of a sequence alignment (aligned with Clustal Omega and visualized with ESPript [4]) of UGAepis and GALEs. The residues responsible for glucose binding in GALE [5,6] and the corresponding residues in UGAepis are highlighted in yellow. The amino acids involved in binding of glucose in *E. coli* GALE (structure in panel b) are labelled in red (below the alignment) and the corresponding amino acids in BcUGAepi in blue (above the alignment). UniProt entries: UGAepi BcUGApi (J8BY31), UGAepi UGlcAE (A7GQD3), UGAepi MoeE5 (A0A003), UGAepi Arabidopsis_1 (Q9M0B6), UGAepi Zea mays (Q304Y2), UGAepi Cap1J (P96481), UGAepi GlaKP analog (Q9RP53), GALE E.coli K12 (P09147), GALE Homo sapiens (Q14376), GALE Neiss. gonorr. (Q05026), GALE Salm. typhi (Q56093) and GALE Yersinia pestis (Q9F7D4). (b) Close-up structure of the active site of GALE (generated with PyMOL) showing the positioning of the conserved glucose-binding interactions. Residues (light green) responsible for recognition of the sugar moiety: Tyr149, Lys84, Ser124, Asn179, Asn199. Yellow and grey carbon atoms correspond to UDP-Glc and NADH, respectively. PDB: 1XEL.

Fig. S26. (a) Interactions with the carboxylate moiety of UDP-GlcA (yellow carbons) in the active site of UXS (cyan carbons; PDB: 2B69, sugar modeled into the active site) [7]. (b) Interactions with the carboxylate group in the active site of ArnA (peach carbons; PDB: 1Z7E) [8]. The structures were generated with PyMOL.

Fig. S27. Residues (Asn179 and Tyr299) on the active site of GALE (green carbons; PDB: 1XEL) responsible for binding the 6-OH group of UDP-Glc (yellow carbons).

Scheme S1. NAD^{+} dependent oxidative decarboxylation of UDP-α-D-glucuronic acid yielding UDP-4-keto-α-D-xylose (and CO_2) catalyzed by *E. coli* enzyme ArnA.

Scheme S2. One-pot synthesis of UDP-α-d-4-2H-glucuronic acid with lactate dehydrogenase-based regeneration system of NAD+.

FEBS PRESS
science publishing by scientists
WILEY
The FEBS Journal
www.febsjournal.org

Mechanistic characterization of UDP-glucuronic acid 4-epimerase

Annika J. E. Borg, Alexander Dennig, Hansjörg Weber and Bernd Nidetzky

DOI: 10.1111/febs.15478

SUPPLEMENTARY INFORMATION

Mechanistic characterization of UDP-glucuronic acid 4-epimerase

Annika J. E. Borg[a], Alexander Dennig[a,b], Hansjörg Weber[c] and Bernd Nidetzky[a,b]*

[a] Institute of Biotechnology and Biochemical Engineering, Graz University of Technology, NAWI Graz, Petersgasse 12, 8010 Graz, Austria

[b] Austrian Centre of Industrial Biotechnology, Petersgasse 14, 8010 Graz, Austria

[c] Institute of Organic Chemistry, Graz University of Technology, NAWI Graz, Stremayrgasse 9, 8010 Graz, Austria

* Corresponding author (B.N., bernd.nidetzky@tugraz.at)

DNA sequence of BcUGAepi

ATGAAAATATTAGTAACAGGAGCTGCAGGGTTTATAGGATCACACCTATGTCAAGCGCTGCTGAAG
AACAGCGCGTACCACGTGGTTGGCATTGACCACTTTATTGGTCCGACCCCGGCGACCCTGAAAACC
GGCAACATCCAGAGCCTGGAACTGAACAGCCGTTTCCAATTTATTCGTGAGGACATCCTGAACACC
GATCTGAGCAAACTGCTGCAGGACATTGATGTGGTTTATCATCTGGCGGCGATCCCGGGCGTTCGT
ACCAGCTGGGGCAAGGATTTCCAACCGTATGTGACCAACAACATTATGGTTACCCAGCAACTGCTG
GAAGCGTGCAAGCACATCAAACTGGACAAGTTTATCCACATTAGCACCAGCAGCGTGTACGGCGA
GAAGAGCGGTGCGGTTAGCGAAGATCTGCTGCCGATCCCGCTGAGCCCGTACGGCGTGACCAAAC
TGAGCGGTGAACACCTGTGCCACGTTTATCACAAGAACTTCCACATCCCGATTGTGATCCTGCGTTA
CTTTACCGTTTATGGTCCGCGTCAGCGTCCGGACATGGCGTTCCACCGTCTGATTAAACAAATGCTG
GAGGATAAGCCGCTGACCATCTTCGGTGACGGCACCCAGACCCGTGATTTTACCTATATTGACGAT
TGCATCCGTGGCACCGTGGCGGCGCTGGAAACCAAGAAGAACATCATTGGTGAAGTTATTAACATC
GGTGGCAAAGAGCAAGCGAGCATTCTGGACATCATTAGCATGCTGGAAAAAATCAGCGGCAAGAG
CGCGACCAAAAACTTCCTGAAGAGCGTGCCGGGCGAGCCGAAACAGACCTGGGCGGATATTAGCA
AGGCGAGCACCCTGCTGCAATACAGCCCGACCGTTAGCCTGAGCGATGGCCTGGAGGCGGAATAC
GATTATATCAAACAGCTGTATAAGGGTGACGCGGCGTGGAGCCACCCGCAATTTGAGAAGTAA

Amino acid sequence of BcUGAepi

M K I L V T G A A G F I G S H L C Q A L L K N S A Y H V V G I D H F I G P T P A T L K T G N
I Q S L E L N S R F Q F I R E D I L N T D L S K L L Q D I D V V Y H L A A I P G V R T S W G K
D F Q P Y V T N N I M V T Q Q L L E A C K H I K L D K F I H I S T S S V Y G E K S G A V S E
D L L P I P L S P Y G V T K L S G E H L C H V Y H K N F H I P I V I L R Y F T V Y G P R Q R P
D M A F H R L I K Q M L E D K P L T I F G D G T Q T R D F T Y I D D C I R G T V A A L E T K
K N I I G E V I N I G G K E Q A S I L D I I S M L E K I S G K S A T K N F L K S V P G E P K Q T
W A D I S K A S T L L Q Y S P T V S L S D G L E A E Y D Y I K Q L Y K G D A A W S H P Q F
E K **Stop**

Strep-tag

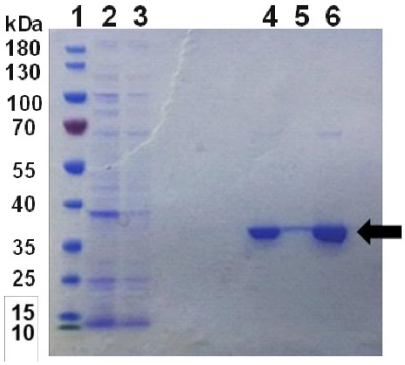

Figure S1. Results of SDS-PAGE of purified BcUGAepi (~37 kDa). Lane 1: molecular mass ladder, lane 2 and 3: flow through fractions from purification, lane 4 and 5: elution fractions from purification, lane 6: concentrated protein sample. Qualitatively identical results were obtained in multiple experiements (N = 10) that included enzyme production, purification and analysis by SDS PAGE as shown.

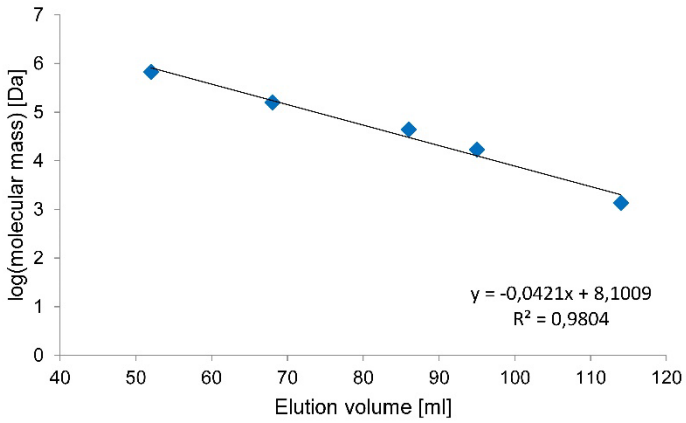

Figure S2. Calibration curve for HiLoad 16/60 Superdex 200 gel filtration column prepared with gel filtration standard mixture #1511901. The logarithm of the molecular masses of thyroglobulin (670000 Da), bovine γ-globulin (158000 Da), chicken ovalbumin (44000 Da), equine myoglobin (17000 Da) and vitamin B12 (1350 Da) is plotted against their elution volumes.

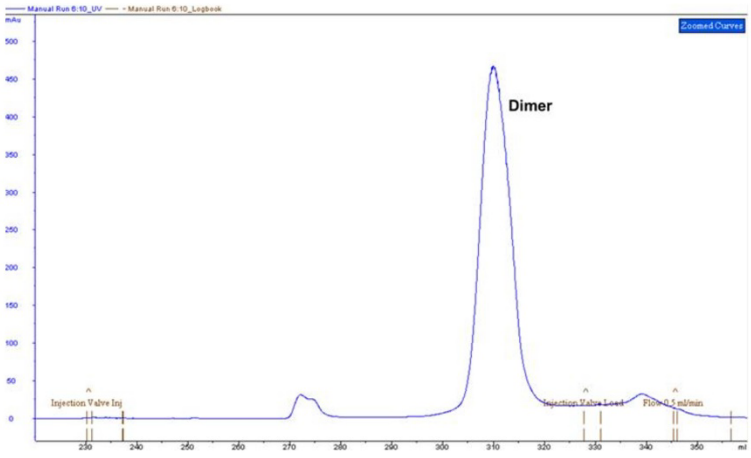

Figure S3. Gel filtration chromatogram of BcUGAepi detected by UV absorbance at 280 nm. The peak corresponding to the apparent molecular mass of BcUGAepi dimer (elution volume 80 ml) is labelled.

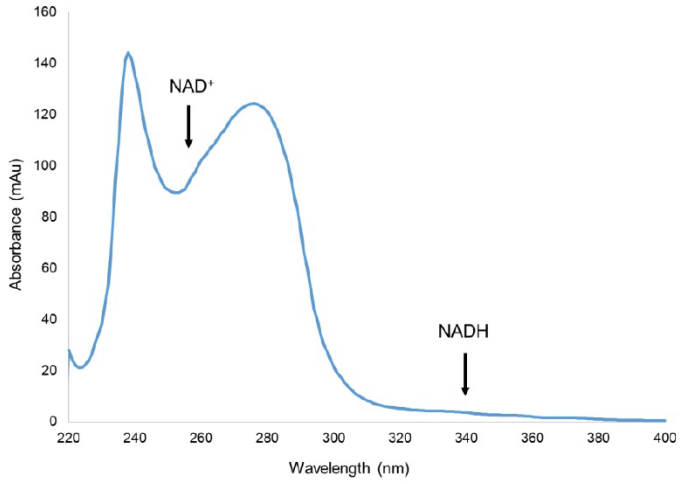

Figure S4. Absorbance spectrum of wild-type BcUGAepi indicating the presence of a protein-bound nicotinamide cofactor (260 nm, 340 nm).

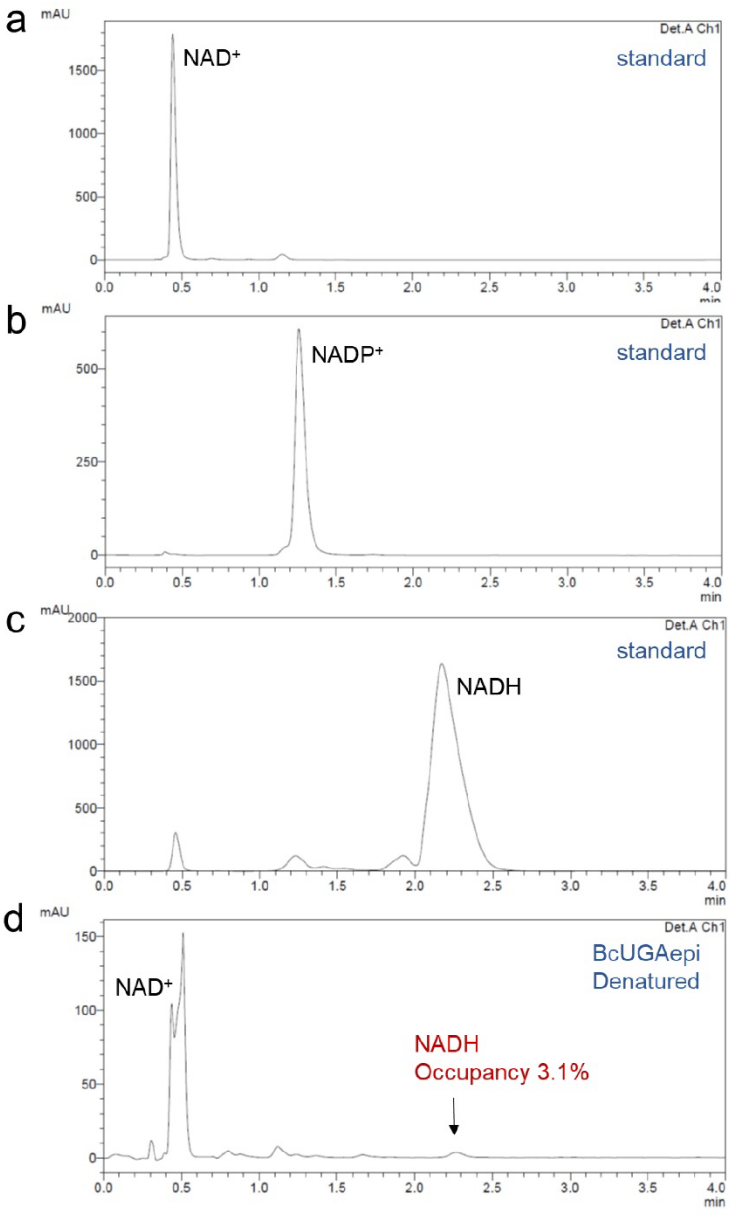

Figure S5. HPLC chromatograms of NAD^+, $NADP^+$ and NADH standards (**a-c**) and supernatant of denatured BcUGAepi showing the cofactor content (**d**).

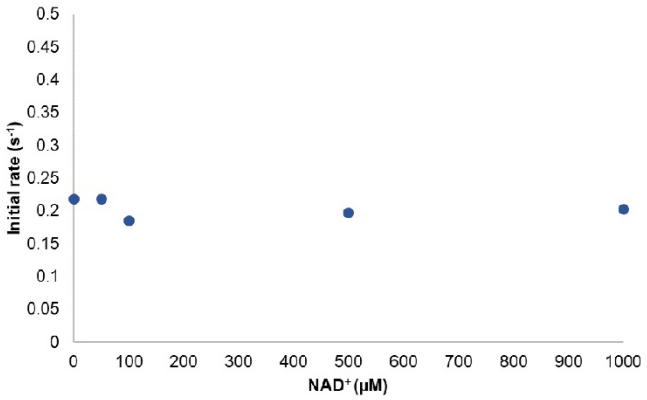

Figure S6. Influence of NAD^+ concentration (0-1000 µM) on the catalytic activity of BcUGAepi with UDP-GlcA. The reactions were performed with 1 mM UDP-GlcA and 1 µM (0.035 mg/ml) purified recombinant BcUGAepi in sodium phosphate buffer (50 mM Na_2HPO_4, 100 mM NaCl, pH 7.6) in final volume of 250 µl. The initial rates (s^{-1}) were plotted against the concentration of NAD^+.

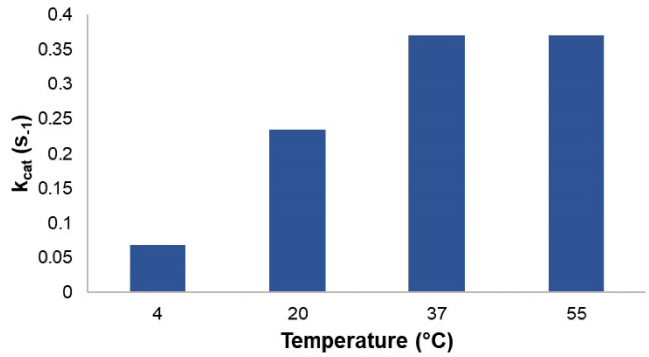

Figure S7. Catalytic activity of BcUGAepi in the reaction with UDP-GlcA at different temperatures. The reactions were performed with 1 mM UDP-GlcA, 100 µM NAD^+ and 2 µM (0.07 mg/ml) purified recombinant BcUGAepi in sodium phosphate buffer (50 mM Na_2HPO_4, 100 mM NaCl, pH 7.6) in final volume of 250 µl. The initial velocities (s^{-1}) were plotted against the temperature.

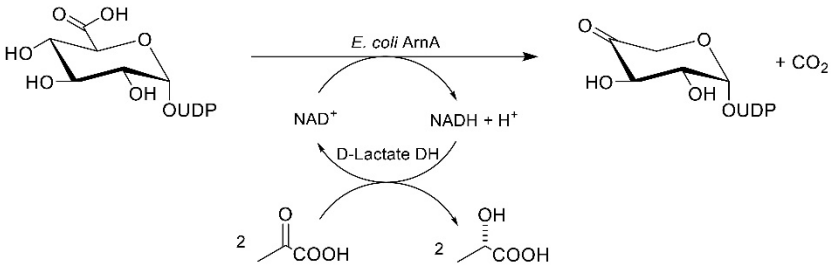

Scheme S1. NAD^+ dependent oxidative decarboxylation of UDP-α-D-glucuronic acid yielding UDP-4-keto-α-D-xylose (and CO_2) catalyzed by *E. coli* enzyme ArnA. Sodium pyruvate (10 mM), 20 U/ml D-lactate dehydrogenase (DH) and 4.7 μM ArnA (0.2 mg/ml) were added into the BcUGAepi reaction mixture and incubated at 30 °C for 16 h until all UDP-GlcA was consumed. UDP = uridine-5'-diphosphate.

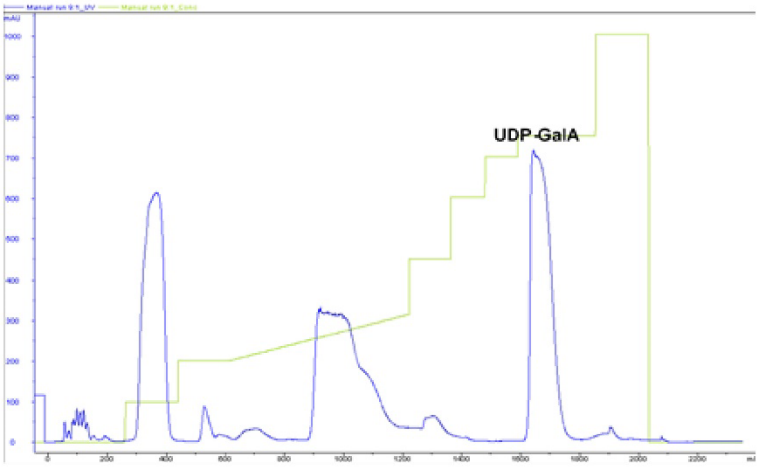

Figure S8. Anion exchange chromatogram recorded during the purification of UDP-α-D-galacturonic acid (UDP-GalA). The UV signal (blue line, 280 nm) of the desired product is labelled as UDP-GalA, the green line corresponds to the salt gradient used for elution. UDP = uridine-5'-diphosphate.

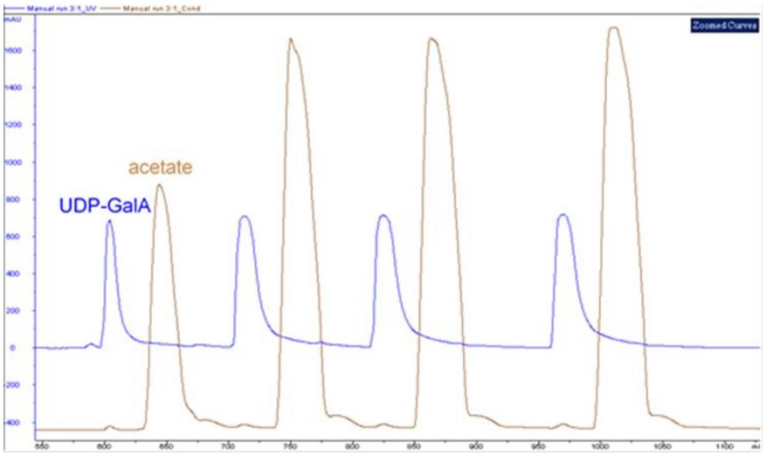

Figure S9. Chromatogram recorded during the desalting step of UDP-α-D-galacturonic acid. The blue line corresponds to the UV-signal of the desired product (at 280 nm), the brown line corresponds to the conductivity signal of acetate.

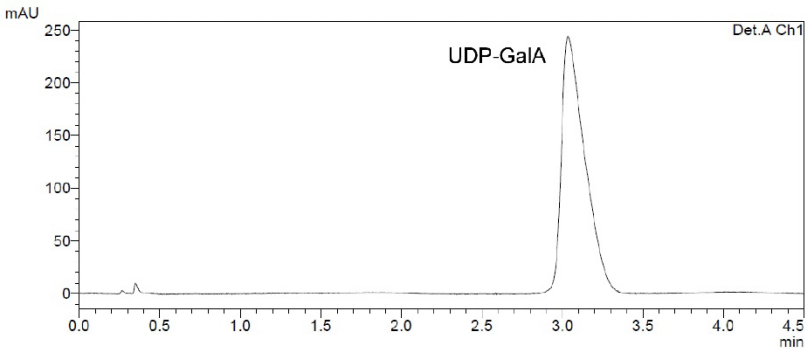

Figure S10. HPLC chromatogram of purified and desalted UDP-α-D-galacturonic acid. The purity of >98% was obtained.

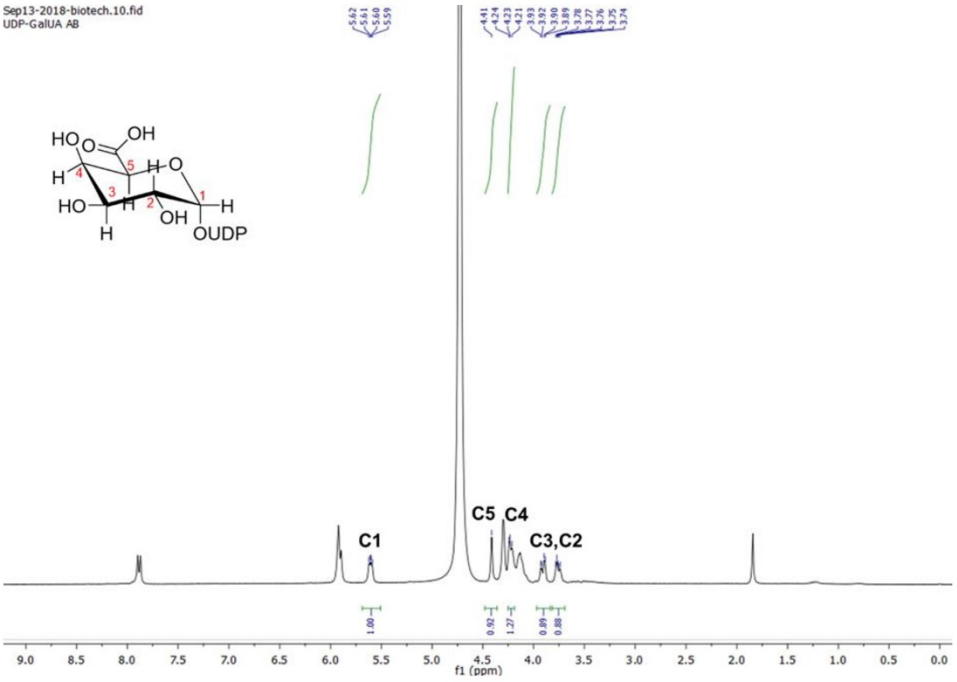

Figure S11. ^{1}H NMR spectrum (500 MHz, D_2O) of purified and desalted UDP-α-D-galacturonic acid, δ 5.62 ppm (dd, 1H), 4.41 ppm (s, 1H), 4.23 ppm (m, 1H), 3.92 ppm (dd, 1H), 3.75 ppm (dd, 1H). The chemical shifts are well in agreement with the values described in literature [1].

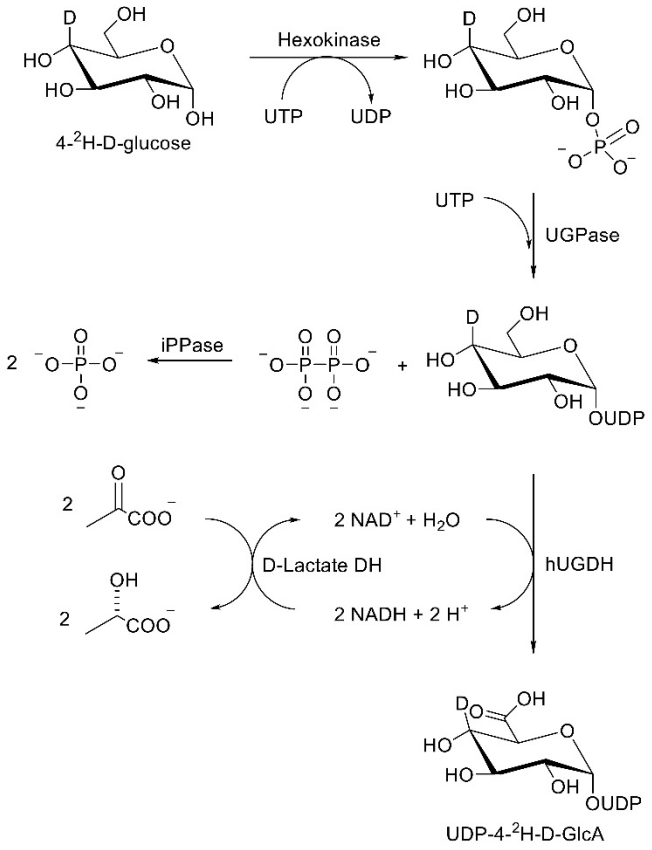

Scheme S2. One-pot synthesis of UDP-α-D-4-^{2}H-glucuronic acid with lactate dehydrogenase-based regeneration system of NAD^{+}. UTP = uridine-5'-triphosphate, UDP = uridine-5'-diphosphate, UGPase = UDP-glucose pyrophosphorylase, iPPase = inorganic pyrophosphatase, hUGDH = human UDP-glucose 6-dehydrogenase, D-lactate DH = D-lactate dehydrogenase.

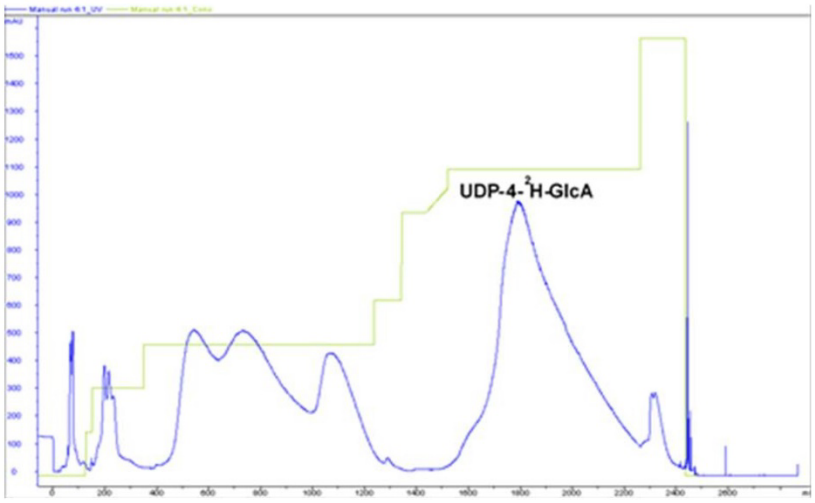

Figure S12. Chromatogram recorded during the purification of UDP-α-D-4-^{2}H-glucuronic acid. The UV peak of the desired product (blue line, 280 nm) is labelled as UDP- 4-^{2}H-GlcA, the green line corresponds to the salt gradient used for elution.

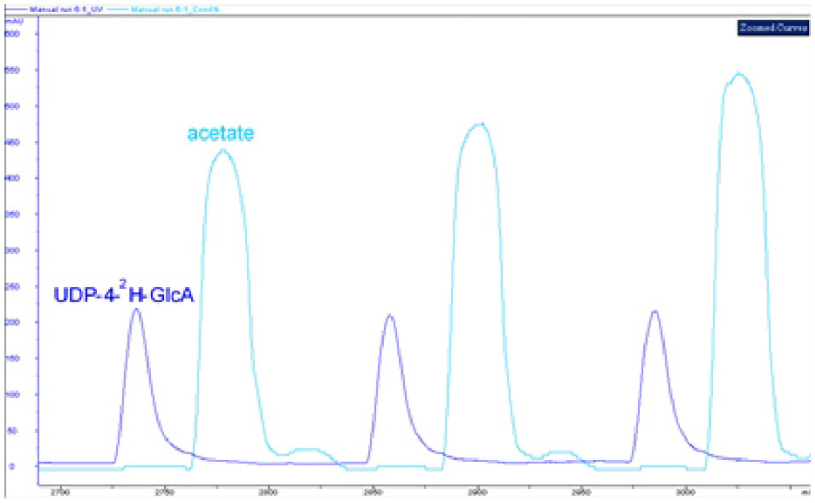

Figure S13. Chromatogram recorded during the desalting of UDP-α-D-4-^{2}H-glucuronic acid. The dark blue line corresponds to the UV-signal of the desired product (at 280 nm), the light blue line shows the conductivity signal of acetate.

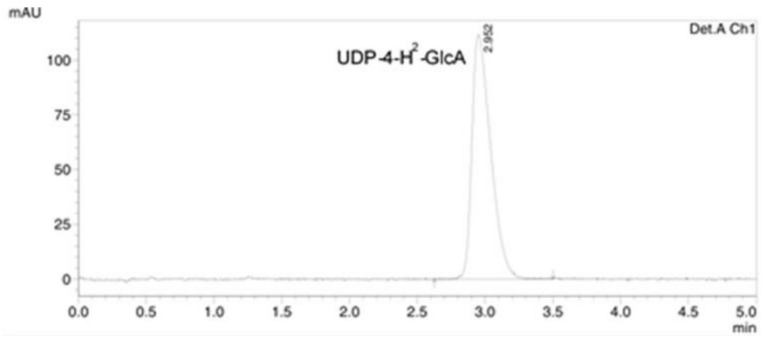

Figure S14. HPLC chromatogram of purified and desalted UDP-α-D-4-^{2}H-glucuronic acid. The purity of >99% was obtained.

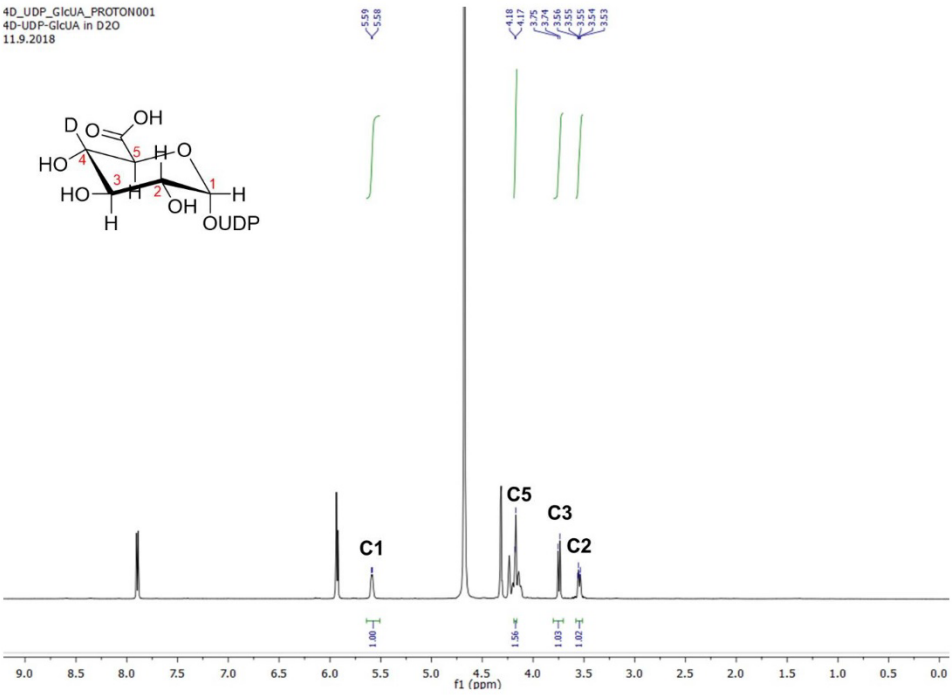

Figure S15. ^{1}H NMR spectrum (500 MHz, D_2O) of purified and desalted UDP-α-D-4-^{2}H-glucuronic acid, δ 5.58 ppm (dd, 1H), 4.17 ppm (d, 1H), 3.74 ppm (d, 1H), 3.55 ppm (dd, 1H).

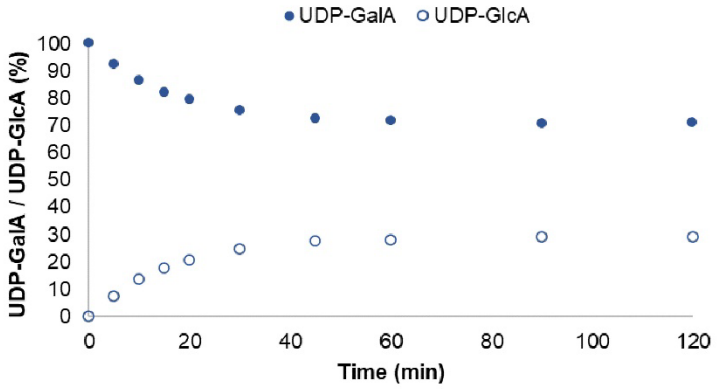

Figure S16. Time course of BcUGAepi reaction with UDP-GalA as a substrate. The reaction mixture contained 1 mM UDP-GalA, 100 µM NAD^+ and 2 µM (0.07 mg/ml) purified recombinant BcUGAepi in sodium phosphate buffer (50 mM Na_2HPO_4, 100 mM NaCl, pH 7.6) in final volume of 250 µl.

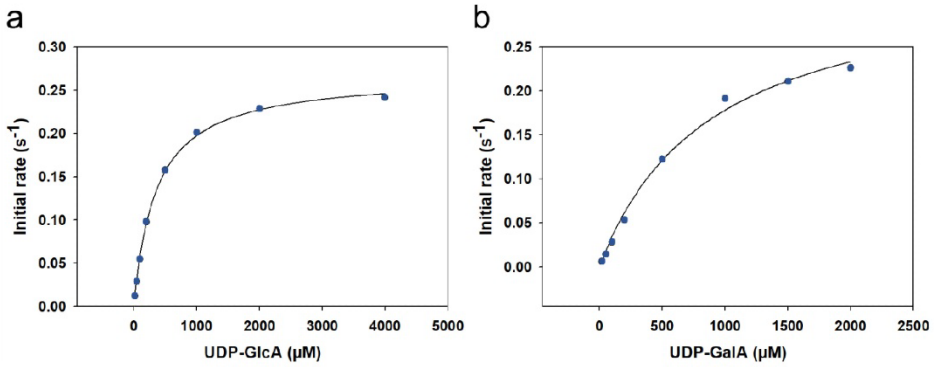

Figure S17. Michaelis-Menten kinetics of the forward (**a.** UDP-GlcA → UDP-GalA) and reverse (**b.** UDP-GalA → UDP-GlcA) reaction catalyzed by BcUGAepi. The reactions contained 2 µM (0.07 mg/ml) BcUGAepi, 50 µM NAD^+ and varying concentration of substrate in sodium phosphate buffer (50 mM Na_2HPO_4, 100 mM NaCl, pH 7.6) in final volume of 50 µl. Each reaction was performed in triplicate and the data was fitted according to the standard Michaelis-Menten kinetic model.

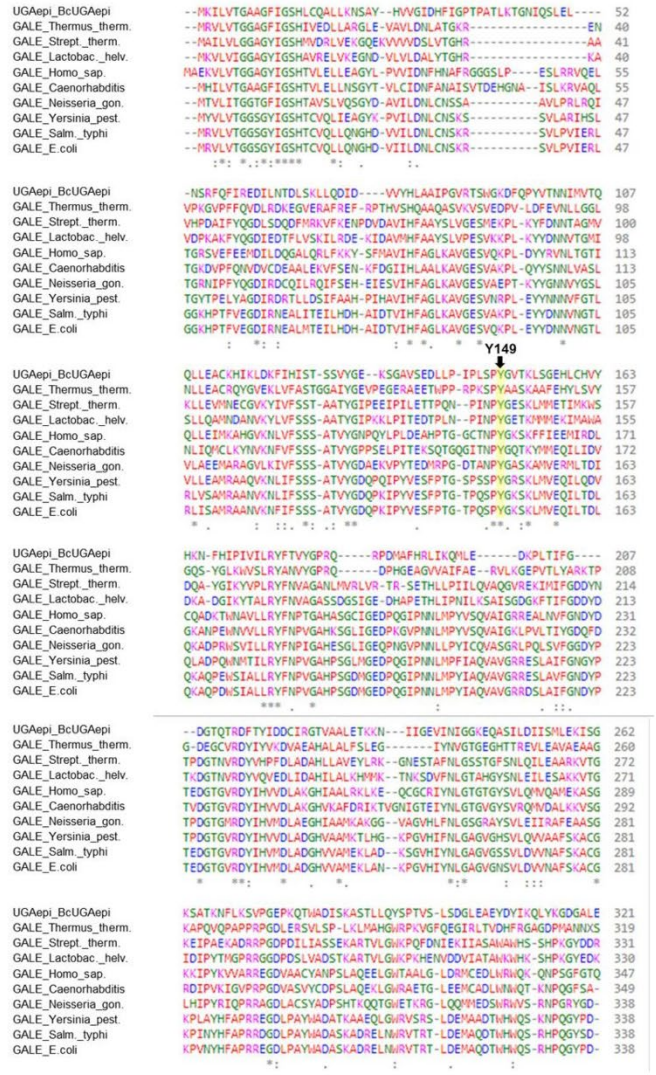

Figure S18. Multiple sequence alignment (prepared with Clustal Omega) of UDP-galactose 4-epimerases (GALEs) and BcUGAepi. Position of the catalytic tyrosine (Tyr149 in BcUGAepi) is highlighted in yellow. UniProt entries: UGAepi_BcUGApi (J8BY31), GALE_Thermus_therm. (Q5SKQ2), GALE_Strept._therm. (P21977), GALE_Lactobac._helv. (Q7WTB1), GALE_Homo_sap. (Q14376), GALE_Caenorhabditis (Q564Q1), GALE_Neisseria_gon. (Q05026), GALE_Yersinia_pest. (Q9F7D4), GALE_Salm._typhi (Q56093) and GALE_E.coli (P09147).

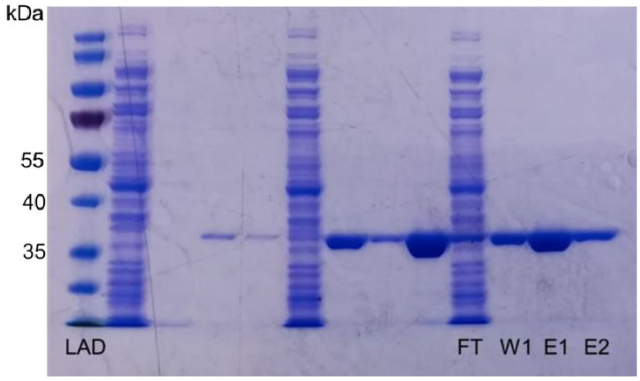

Figure S19. Results of SDS-PAGE of purified BcUGAepi _Y149F (~37 kDa). LAD: molecular mass ladder, FT: flow through (unbound protein), W1: washing fraction from purification, lane E1 and E2: elution fractions from purification. Qualitatively identical results were obtained in multiple experiements (N =3) that included enzyme production, purification and analysis by SDS PAGE as shown.

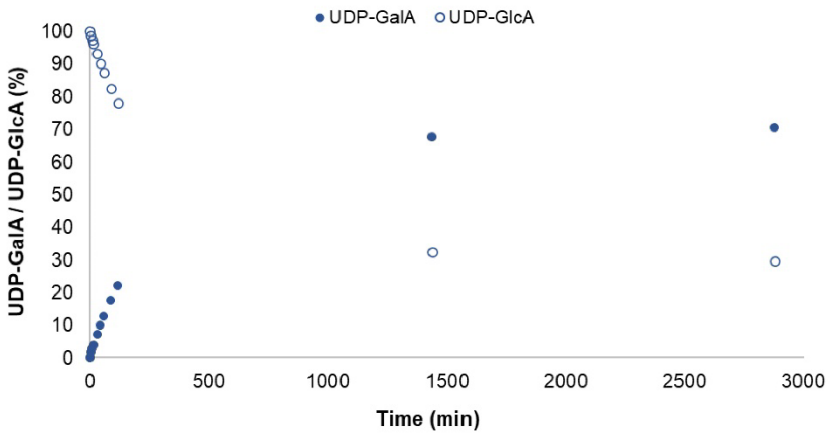

Figure S20. Time course of BcUGAepi_Y149F catalyzed reaction with UDP-GlcA as a substrate. The reaction was performed with 1 mM UDP-GlcA, 100 µM NAD^+ and 135 µM (5 mg/ml) purified recombinant BcUGAepi_Y149F in sodium phosphate buffer (50 mM Na_2HPO_4, 100 mM NaCl, pH 7.6) in final volume of 250 µl. The activity of Y149F variant (0.5 mU/mg) was calculated from the initial velocity (linear part) of the time course.

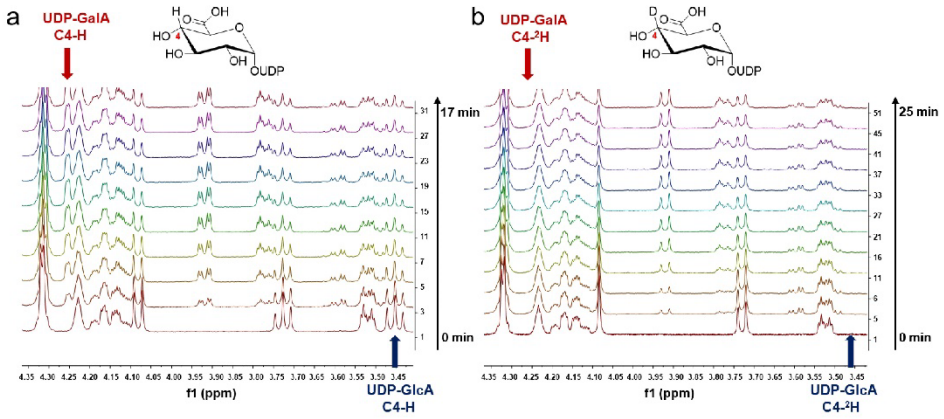

Figure S21. In situ NMR experiments with BcUGAepi. The x-axis shows the chemical shift in ppm and the y-axis the number of the acquisition (only selected spectra are shown for clarity). The direction of the reaction (left: from 0 min in spectrum 1 to 17 min in spectrum 31; right: from 0 min in spectrum 1 to 25 min in spectrum 51) is indicated with an arrow. **a.** Conversion of UDP-GlcA with BcUGAepi. **b.** Conversion of UDP-4-^{2}H-GlcA with BcUGAepi. The missing signals for the C4-H of UDP-GlcA and UDP-GalA are due to the incorporation of deuterium at C4.

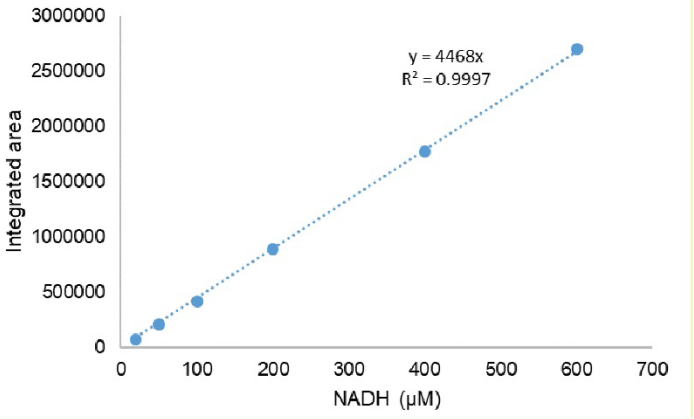

Figure S22. NADH calibration curve on HPLC. The integrated peak areas from HPLC are plotted against the concentration of NADH standards.

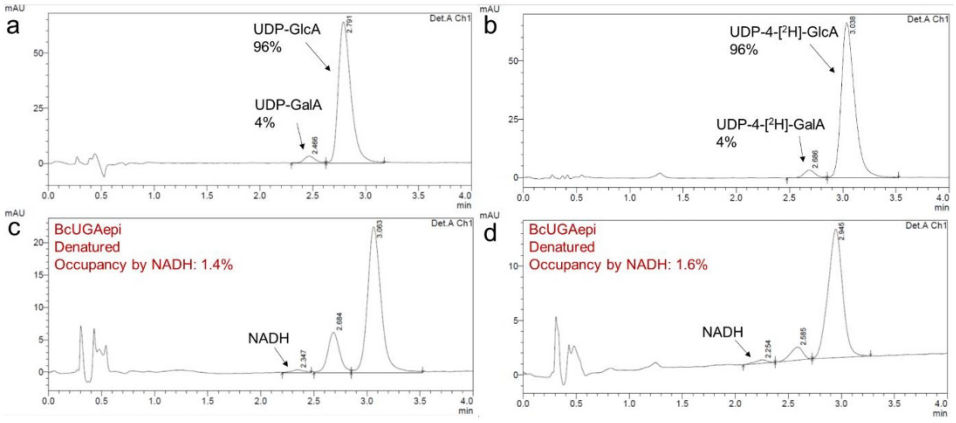

Figure S23. HPLC chromatograms from denaturation experiments of BcUGAepi reacted with UDP-GlcA and UDP-4-[^{2}H]-GlcA. **a,b.** Reaction mixture with UDP-GlcA (**a**) or UDP-4-[^{2}H]-GlcA (**b**) as a substrate at the point where the reaction was stopped and the enzyme filtered out. **c,d.** HPLC chromatograms of the supernatant from the denatured BcUGAepi from reaction a (**c**) and b (**d**).

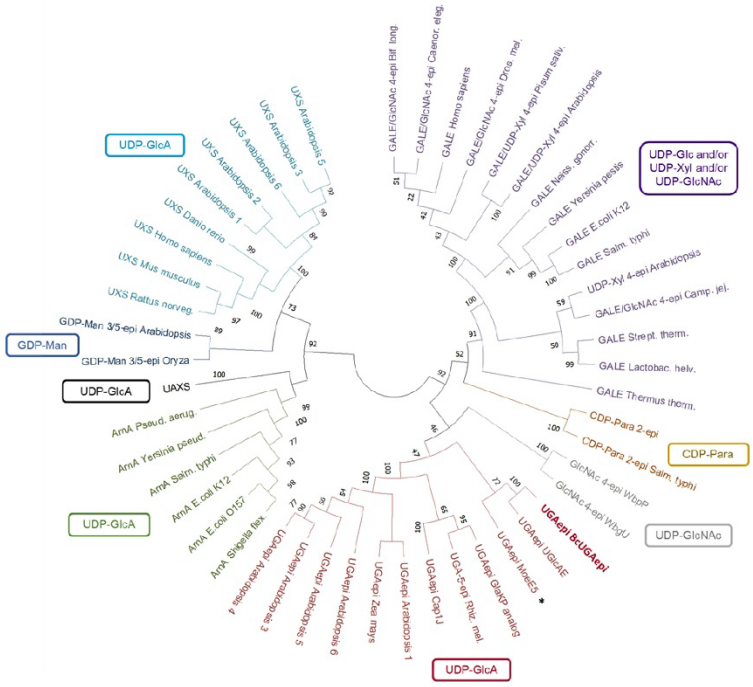

Figure S24. Phylogenetic analysis of SDRs active on sugar nucleotides. Color coding is used to highlight the subgroups of enzymes and their corresponding substrates. The UGAepi with expanded substrate specificity is marked with an asterisk and BcUGAepi is highlighted in bold. The evolutionary history was determined by using the Maximum Likelihood method and Poisson Correction model [2]. The tree with the highest log likelihood is shown and the percentage of trees in which the associated taxa clustered together is shown next to the branches. Initial tree(s) for the heuristic search were obtained automatically by applying Neighbor-Join and BioNJ algorithms to a matrix of pairwise distances estimated using a JTT model, and then selecting the topology with superior log likelihood value. There were a total of 621 positions in the final dataset. Evolutionary analyses were conducted in Mega X [3]. GDP-Man = Guanosine diphosphate mannose, CDP-Para = Cytidine diphosphate paratose, UDP-Glc = Uridine diphosphate glucose, UDP-Xyl = Uridine diphosphate xylose, UDP-GlcNAc = Uridine diphosphate N-acetylglucosamine, UXS = UDP-xylose synthase, UAXS = UDP-apiose/xylose synthase, UGAepi = UDP-glucuronic acid 4-epimerase.

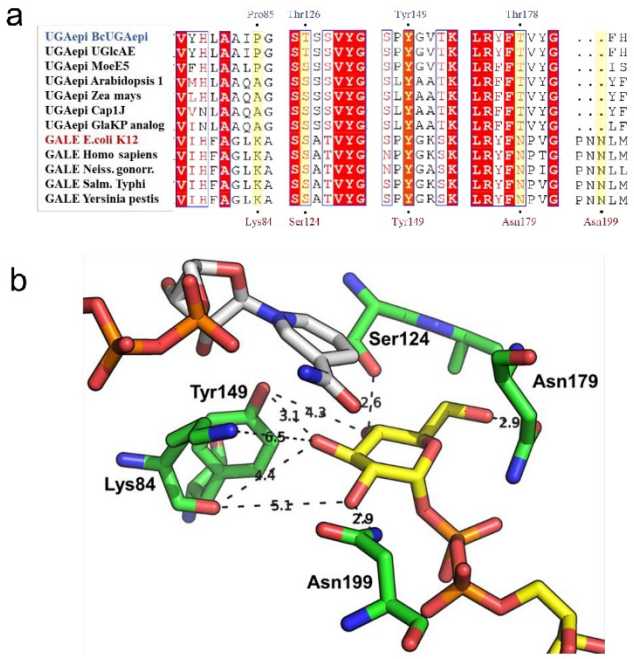

Figure S25. a. A part of a sequence alignment (aligned with Clustal Omega and visualized with ESPript [4]) of UGAepis and GALEs. The residues responsible for glucose binding in GALE [5,6] and the corresponding residues in UGAepis are highlighted in yellow. The amino acids involved in binding of glucose in *E. coli* GALE (structure in panel b) are labelled in red (below the alignment) and the corresponding amino acids in BcUGAepi in blue (above the alignment). UniProt entries: UGAepi BcUGApi (J8BY31), UGAepi UGlcAE (A7GQD3), UGAepi MoeE5 (A0A003), UGAepi Arabidopsis_1 (Q9M0B6), UGAepi Zea mays (Q304Y2), UGAepi Cap1J (P96481), UGAepi GlaKP analog (Q9RP53), GALE E.coli K12 (P09147), GALE Homo sapiens (Q14376), GALE Neiss. gonorr. (Q05026), GALE Salm. typhi (Q56093) and GALE Yersinia pestis (Q9F7D4). **b.** Close-up structure of the active site of GALE (generated with PyMOL) showing the positioning of the conserved glucose-binding interactions. Residues (light green) responsible for recognition of the sugar moiety: Tyr149, Lys84, Ser124, Asn179, Asn199. Yellow and grey carbon atoms correspond to UDP-Glc and NADH, respectively. PDB: 1XEL.

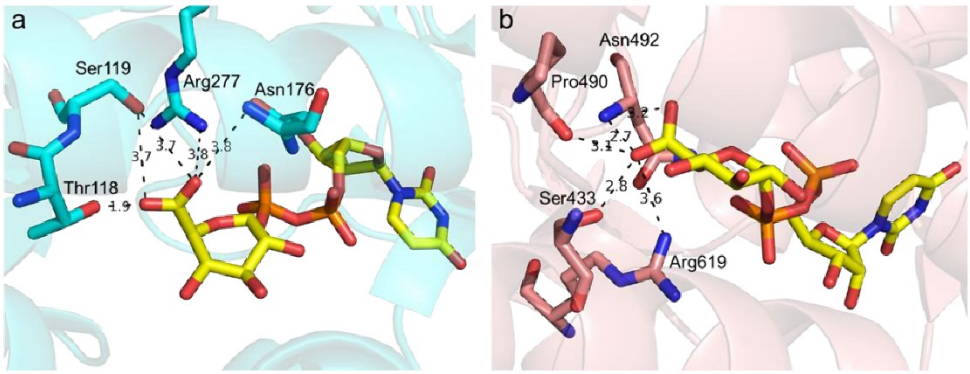

Figure S26. a. Interactions with the carboxylate moiety of UDP-GlcA (yellow carbons) in the active site of UXS (cyan carbons; PDB: 2B69, sugar modeled into the active site) [7]. **b.** Interactions with the carboxylate group in the active site of ArnA (peach carbons; PDB: 1Z7E) [8]. The structures were generated with PyMOL.

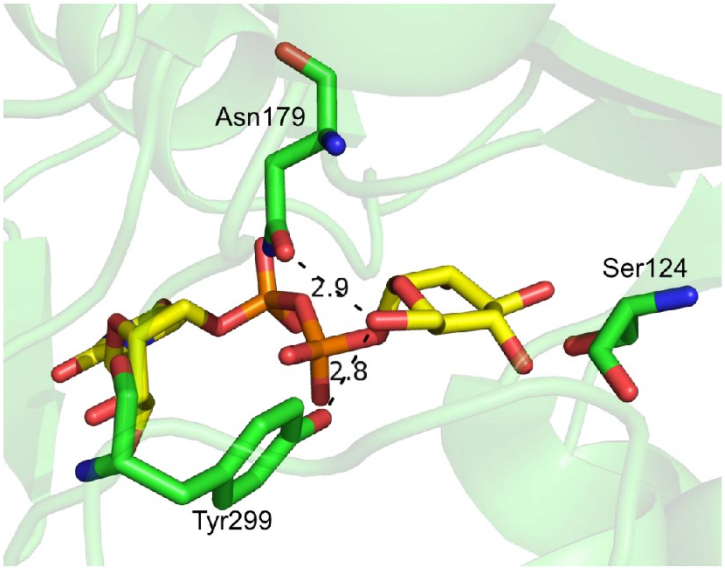

Figure S27. Residues (Asn179 and Tyr299) on the active site of GALE (green carbons; PDB: 1XEL) responsible for binding the 6-OH group of UDP-Glc (yellow carbons). Ser124 (Thr126 in BcUGAepi) is positioned away from 6-OH [5]. PyMOL was used to generate the structure.

Experimental procedures (addition to the main text)

Site-directed mutagenesis

BcUGAepi_Y149F variant was prepared using a modified QuikChange protocol. PCRs were carried out in the reaction volume of 50 µl using 20 ng of plasmid DNA as template and 0.2 µM of forward or reverse primer. Q5 DNA polymerase was used for DNA amplification. The sequences of DNA oligonucleotide primers used for the mutagenesis in BcUGAepi are shown below. The underlined nucleotides highlight the Y149F mutation introduced by PCR.

Name	Mutation	DNA primer sequence (5'-3')
Y149F_fw	Y149F	GATCCCGCTGTCCCCGTTCGGCGTGACCAAACTG
Y149F_rv	Y149F	CAGTTTGGTCACGCCGAACGGGGACAGCGGGATC

First, three cycles of linear PCR amplification were performed with separate forward and reverse primers (initial denaturation: 30 sec/98 °C; 3 cycles amplification: 10 sec/98 °C for denaturation, 15 sec/55 °C for primer annealing and 6 min/72 °C extension; final extension: 5 min/72 °C). The reaction mixtures were combined to mix the forward and reverse primer solutions, divided again into two mixtures of 50 µl (for better heat transfer) and the PCR program was restarted for 15 cycles of exponential DNA amplification (initial denaturation: 30 sec/98 °C; 3 cycles amplification: 10 sec/98 °C for denaturation, 15 sec/55 °C for primer annealing and 6 min/72 °C extension; final extension: 5 min/72 °C). Residual template DNA was removed by addition of 10 U DpnI and incubation at 37 °C for 16 h. DpnI was inactivated by incubating at 80 °C for 20 min, the mixtures were centrifuged and the PCR products analyzed by agarose gel electrophoresis and visualized by DNA staining. The PCR products were directly transformed into chemically competent *E. coli* NEB5α cells (New England Biolabs). Plasmid DNA was extracted and sequenced with T7prom/T7term primers provided by LGC Genomics (Berlin, Germany) to confirm the mutations. The correct construct was transformed into *E. coli* Lemo21(DE3) cells followed by expression of BcUGAepi as described below.

Expression and purification of BcUGAepi

The synthetic vector pET17b_BcUGAepi was ordered from GenScript (USA) and transformed into chemically competent *E. coli* Lemo21(DE3) cells. BcUGAepi was ordered as a codon optimized gene for optimal expression in *E. coli* and with C-terminal Strep-tag for protein purification (sequence given in the beginning of SI). The cells harboring pET17b_BcUGAepi (or pET17b_BcUGAepi_Y149F) were grown in 10 ml of LB medium (50 μg/ml ampicillin and 35 μg/ml chloramphenicol) at 37 °C for 16 h. From the preculture 2 ml was used to inoculate fresh LB medium (250 ml) supplemented with ampicillin (50 μg/ml) and chloramphenicol (35 μg/ml) and the cells were grown at 37 °C and 120 rpm. After the cell density (OD_{600}) of 0.8 was reached, isopropyl β-D-thiogalactoside (0.2 mM) was added to the culture media to induce gene expression. The cells were incubated at 18 °C and 120 rpm for 20 h. The cells were harvested by centrifugation (2800 g, 4 °C, 20 min), the pellet resuspended in 10 ml of Strep-tag loading buffer (100 mM Tris, 150 mM NaCl, pH 8) and the suspension was stored overnight at -20 °C prior to cell lysis. The cells were disrupted by sonication (pulse 2 sec on, 5 sec off, 70% amplitude, 5 min) and centrifuged (16100 g) at 4 °C for 45 min. The supernatant was collected and filtered (0.45 μm) prior to loading onto the StrepTrap™ HP column (5 ml resin, GE Healthcare Life Sciences) pre-equilibrated with the loading buffer (100 mM Tris, 150 mM NaCl, pH 8). The Strep-tagged protein was eluted with elution buffer (100 mM Tris, 150 mM NaCl, 2.5 mM D-desthiobiotin, pH 8) and re-buffered against reaction buffer (50 mM Na_2HPO_4, 100 mM NaCl, pH 7.6) containing 10% glycerol using Vivaspin filter tubes (30 kDa cut-off). After buffer exchange, the protein was divided into aliquots, flash frozen in liquid nitrogen, and stored at -20 °C. Protein concentration was determined based on the absorption at 280 nm on a Nanodrop spectrophotometer. Size and purity of the protein were confirmed by SDS-PAGE.

Purification and activity assay of UGPase

UGPase was purified by affinity chromatography using a HisTrap 5 ml Ni^{2+} column. The binding buffer was 20 mM imidazole, 100 mM Tris, 50 mM NaCl, pH 7 and the protein was eluted with a buffer containing 400 mM imidazole, 100 mM Tris, 50 mM NaCl, pH 7. Activity was measured in 50 mM Tris-HCl buffer (pH 7.5) supplemented with 5 mM $MgCl_2$, 15 mM UTP, 0.13% (w/v) BSA, 5 mM glucose 1-phosphate and traces of glucose 1,6-bisphosphate. The reactions were started by addition of UGPase in various concentrations (0.064 mg/ml, 0.16 mg/ml, 0.32 mg/ml and 0.64 mg/ml). Samples were taken (0, 5, 10, 15, 30, 60 min) and the reaction quenched by addition of acetonitrile up to 25% (v/v) final concentration prior to HPLC analysis. The increasing concentration of UDP-glucose was plotted against time and the specific activity of UGPase was calculated from the slope of a linear fit to that curve by using equation 1, where k is the slope and c_{enzyme} corresponds to the enzyme concentration.

$$Specific\ activity\left[\frac{U}{mg}\right] = \frac{k[mmol/(min \times l)]}{c_{enzyme}[mg/ml]} \quad (1)$$

One unit of UGPase activity is defined as the amount of enzyme producing 1 µmol of UDP-glucose from UTP and glucose 1-phosphate per minute.

Anion exchange chromatography of sugar nucleotides

UDP-α-D-galacturonic acid

A step-wise gradient of 1 M sodium acetate buffer (pH 4.3) was used to elute the compounds bound to the column. The steps were: 270 ml of 20 mM NaOAc, 160 ml of 100 mM NaOAc, 170 ml of 200 mM NaOAc, 620 ml of NaOAc from 200 to 300 mM with gradient for 140 min, 160 ml of 450 mM NaOAc, 140 ml of 600 mM NaOAc, 140 ml of 700 mM NaOAc, 250 ml of 800 mM NaOAc, 200 ml of 1000 mM NaOAc, 300 ml of 20 mM NaOAc.

UDP-α-D-4-^{2}H-glucuronic acid

During the anion exchange chromatography following flow settings were used: 120 ml of 20 mM NaOAc, 220 ml of 200 mM NaOAc, 900 ml of 300 mM NaOAc, 100 ml of 400 mM NaOAc, 100 ml of 600 mM NaOAc, 120 ml of NaOAc from 600 to 670 mM with gradient for 30 min, 680 ml of 700 mM NaOAc, 200 ml of 1000 mM NaOAc, 200 ml of 20 mM NaOAc.

Oligomeric state of BcUGAepi

For determining the oligomeric state of BcUGAepi, gel filtration was performed with an ÄKTA FPLC connected to HiLoad 16/6 Superdex 200 prep grade column (GE Healthcare) and 1 ml sample loop. The protein was eluted with 150 mM K_2HPO_4 buffer (pH 7.6) (Figure S3) and the apparent molecular mass was calculated from a calibration curve (Figure S2) which was prepared with gel filtration standard mixture #1511901 (Bio-Rad).

References

1. Gu X & Bar-Peled M (2004) The biosynthesis of UDP-galacturonic acid in plants. Functional cloning and characterization of *Arabidopsis* UDP-D-glucuronic acid 4-epimerase. *Plant Physiol* 136, 4256–64.
2. Zuckerkandl E & Pauling L (1965) Evolutionary divergence and convergence in proteins in *Evolving Genes and Proteins* pp. 97–166. Elsevier.
3. Kumar S, Stecher G, Li M, Knyaz C & Tamura K (2018) MEGA X: Molecular evolutionary genetics analysis across computing platforms. *Mol Biol Evol* 35, 1547–1549.
4. Robert X & Gouet P (2014) Deciphering key features in protein structures with the new ENDscript server. *Nucleic Acids Res* 42, W320–324.
5. Thoden JB, Frey PA & Holden HM (1996) Molecular structure of the NADH/UDP-glucose abortive complex of UDP-galactose 4-epimerase from *Escherichia coli*: Implications for the catalytic mechanism. *Biochemistry* 35, 5137–5134.
6. Nam YW, Nishimoto M, Arakawa T, Kitaoka M & Fushinobu S (2019) Structural basis for broad substrate specificity of UDP-glucose 4-epimerase in the human milk oligosaccharide catabolic pathway of *Bifidobacterium longum*. *Sci Rep* 9, 11081.
7. Eixelsberger T *et al.* (2012) Structure and mechanism of human UDP-xylose synthase. *J Biol Chem* 287, 31349–31358.
8. Gatzeva-Topalova PZ, May AP & Sousa MC (2005) Structure and mechanism of ArnA: conformational change implies ordered dehydrogenase mechanism in key enzyme for polymyxin resistance. *Structure* 13, 929–942.

Crystallographic Snapshots of UDP-Glucuronic Acid 4-Epimerase Ligand Binding, Rotation and Reduction

JBC ARTICLE

Crystallographic snapshots of UDP-glucuronic acid 4-epimerase ligand binding, rotation, and reduction

Received for publication, June 8, 2020, and in revised form, July 10, 2020 Published, Papers in Press, July 13, 2020, DOI 10.1074/jbc.RA120.014692

Luca Giacinto Iacovino[1], Simone Savino[2], Annika J. E. Borg[2], Claudia Binda[1], Bernd Nidetzky[2,3,*], and Andrea Mattevi[1,*]

From the [1]Department of Biology and Biotechnology "Lazzaro Spallanzani", University of Pavia, Pavia, Italy, the [2]Institute of Biotechnology and Biochemical Engineering, Graz University of Technology, NAWI Graz, Graz, Austria, and the [3]Austrian Centre of Industrial Biotechnology, Graz, Austria

Edited by Ruma Banerjee

UDP-glucuronic acid is converted to UDP-galacturonic acid en route to a variety of sugar-containing metabolites. This reaction is performed by a NAD^+-dependent epimerase belonging to the short-chain dehydrogenase/reductase family. We present several high-resolution crystal structures of the UDP-glucuronic acid epimerase from *Bacillus cereus*. The geometry of the substrate-NAD^+ interactions is finely arranged to promote hydride transfer. The exquisite complementarity between glucuronic acid and its binding site is highlighted by the observation that the unligated cavity is occupied by a cluster of ordered waters whose positions overlap the polar groups of the sugar substrate. Co-crystallization experiments led to a structure where substrate- and product-bound enzymes coexist within the same crystal. This equilibrium structure reveals the basis for a "swing and flip" rotation of the pro-chiral 4-keto-hexose-uronic acid intermediate that results from glucuronic acid oxidation, placing the C4′ atom in position for receiving a hydride ion on the opposite side of the sugar ring. The product-bound active site is almost identical to that of the substrate-bound structure and satisfies all hydrogen-bonding requirements of the ligand. The structure of the apoenzyme together with the kinetic isotope effect and mutagenesis experiments further outlines a few flexible loops that exist in discrete conformations, imparting structural malleability required for ligand rotation while avoiding leakage of the catalytic intermediate and/or side reactions. These data highlight the double nature of the enzymatic mechanism: the active site features a high degree of precision in substrate recognition combined with the flexibility required for intermediate rotation.

Nucleotide sugars are high-energy donor molecules that fulfill many roles, including contributing to cellular and tissue structural integrity (1–3), acting as molecular recognition markers for xenobiotic detoxification (4–6), and providing scaffolds for drug development (7). Among these metabolites, UDP-glucuronic acid (UDP-GlcA) represents a very versatile compound that undergoes a variety of enzymatic modifications. UDP-glucuronic acid 4-epimerase (EC 5.1.3.6), UDP-xylose synthase (EC 4.1.1.35), and UDP-apiose/xylose synthase (EC 4.1.1.-) modify UDP-GlcA through NAD^+-dependent redox chemistry, producing enzyme-specific sugar products (8–10). These structurally and functionally related enzymes belong to the family of the short-chain dehydrogenase/reductases (SDRs) (11). SDRs are characterized by a strictly conserved catalytic triad, Ser/Thr-Tyr-Lys. The tyrosine residue functions as the base that abstracts a proton from the substrate 4′-OH group and promotes C4′ oxidation by NAD^+ (12–18). The generated 4-keto-hexose-uronic acid intermediate is unstable and converted into different products, depending on the enzyme (Scheme 1). Because of their catalytic versatility, sugar-modifying SDR enzymes are increasingly recognized as valuable targets for many industrial biocatalytic applications.

As can be seen from Scheme 1, the UDP-glucuronic acid 4-epimerase stands out for its ability to prevent decarboxylation at the C5′ position of the 4-keto-hexose-uronic acid intermediate. This enzyme thereby efficiently interconverts UDP-GlcA into UDP-galacturonic acid (UDP-GalA) by inverting the configuration of the 4′-carbon. The strategies used by epimerases to invert the stereochemistry of UDP-sugar carbons have been subject of in-depth investigations (12). Among these, the structural features underlying the selective C4′ epimerization by UDP-galactose 4-epimerase were extensively studied in the past few years (13, 18, 19). This enzyme is part of the Leloir pathway and interconverts UDP-galactose into UDP-glucose (20). It belongs to the SDR family, featuring the same Ser/Thr-Tyr-Lys catalytic triad as UDP-glucuronic acid 4-epimerase. The substrate is first oxidized at the C4′, and the resulting 4-keto-hexose intermediate is thought to undergo a rotational movement within the active site. The intermediate is then reduced by NADH, leading to the inversion of the C4′ configuration (18, 21). The same catalytic strategy has been hypothesized also for the epimerases acting on UDP-GlcA (22). As demonstrated by recent work, these enzymes fine-tune the rates of the individual redox steps to prevent the accumulation of the 4-keto-hexose-uronic acid, minimizing the undesired decarboxylation and/or release of this reactive intermediate (23).

Whereas the catalytic mechanisms of UDP-xylose synthase and UDP-apiose/xylose synthase have been thoroughly elucidated (13, 16, 24), the epimerization reaction by UDP-glucuronic acid 4-epimerase remains partly unexplored. In this work, we carried out a comprehensive structural analysis of UDP-glucuronic acid 4-epimerase from *Bacillus cereus*

This article contains supporting information.

*For correspondence: Bernd Nidetzky, bernd.nidetzky@tugraz.at; Andrea Mattevi, andrea.mattevi@unipv.it.

Present address for Simone Savino: Faculty of Science and Engineering Biotechnology, Groningen Biomolecular Sciences and Biotechnology Institute, Groningen, The Netherlands.

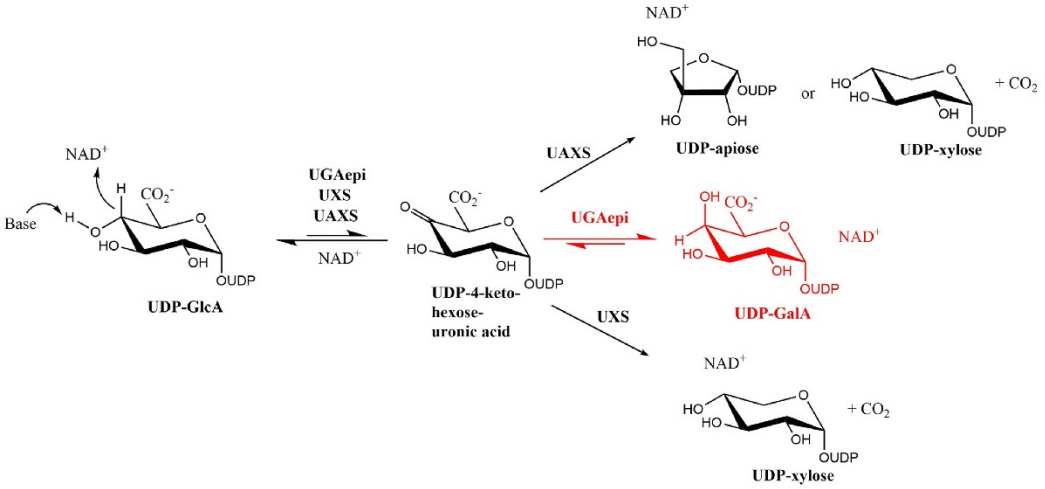

Scheme 1. Reactions carried out by UDP-glucuronic acid epimerase (*UGAepi*), UDP-xylose synthase (*UXS*) and UDP-apiose/xylose synthase (*UAXS*) using UDP-GlcA as substrate. The same 4-keto-hexose-uronic acid intermediate yields different products that are specific for every enzyme.

(BcUGAepi) by solving six high-resolution crystal structures that elucidate different steps along the reaction. The main aspects of these structures were compared with other SDR epimerases and decarboxylases. We also isolated a remarkable complex showing an equilibrium mixture of both substrate and product in approximately 1:1 ratio. We further used structural, kinetic isotope effect and site-directed mutagenesis experiments to inspect the fine roles of catalytic residues. Our studies provide an overview of catalysis with critical insight into the mechanism of 4-ketose-uronic acid intermediate rotation and protection against intermediate decarboxylation. They further demonstrate that the UDP moiety is not only an accessory part of the molecule, but it is fundamental for substrate recognition and active-site configuration.

Results and discussion

Overall structure

The crystal structure of BcUGAepi co-purified with NAD^+ was initially solved at 2.2 Å resolution by molecular replacement (Table 1). The enzyme is composed of nine β-strands and eight α-helices assembled in two domains (13, 27, 28) (Fig. 1). The N-terminal domain is characterized by a Rossmann fold motif comprising a core of seven β-strands surrounded by six α-helices. The NAD^+ cofactor is fully embedded within this domain, whereas the smaller C-terminal domain provides the binding site for the UDP-GlcA substrate. The crevice between the two domains encloses the active site (29–31). As for other SDR family enzymes, two protein chains are arranged to form a tight homodimer (11, 32, 33) where each subunit (37 kDa) interacts with two adjacent α-helices, generating an extensively intermolecular hydrophobic core of four α-helices (14, 16) (Fig. 1). Structural comparisons using the Dali server (34) indicate that the overall structure of BcUGAepi is similar to the structures of UDP-galactose 4-epimerase from *Escherichia coli* (PDB entry 1UDA) (29–31) and MoeE5 (a UDP-glucuronic acid epimerase from *Streptomyces viridosporus*; PDB entry 6KV9) (22) with Z scores of 37.2 and 42.8 and sequence identities of 30 and 38%, respectively.

NAD^+ remains tightly associated to the enzyme during the entire purification process (Fig. 2*A*) (11, 13, 35). It is bound in an elongated conformation as typically observed in other SDR enzymes (21, 28, 36). Its binding is extensively stabilized through several interactions with residues of the Rossmann fold domain. The amine group of the adenine ring hydrogen-bonds to Asn-101 and Asp-62, the adenine-ribose hydroxyl groups interact with Asp-32 and Lys-43, the β-phosphate is ionically bound to Arg-185, and the nicotinamide ribose is hydrogen-bonded to Tyr-149 and Lys-153. These last two residues belong to the Tyr-*X*-*X*-*X*-Lys motif of the Ser/Thr-Tyr-Lys triad, the typical hallmark of SDR enzymes (32, 37–39). This binding mode orients the *si*-face on the nicotinamide ring toward the substrate-binding site to cope with the sugar moiety and mediate hydride transfer.

On the structural roles of UDP

In the NAD^+ complex, two loops around the catalytic site (residues 86–91 and 269–276) are disordered as gathered from the absence of well-defined electron density around them (Fig. 2*B*). The crystal structure of the enzyme bound to UDP (1.7 Å resolution; Table 1) reveals that these two loops become ordered in the presence of the nucleotide diphosphate. In particular, Glu-276 anchors the hydroxyl groups of the nucleotide ribose, whereas loop 86–91 lends more rigidity to the part of the cavity hosting the pyrophosphate (Fig. 2, *B* and *C*). UDP binding affects the conformation of a third loop, formed by residues 204–214. This loop moves closer to the UDP-binding site so that Gln-211 and Arg-213 can hydrogen-bond to the UDP's ribose hydroxy groups and the β-phosphate, respectively.

Table 1
Data collection and refinement statistics for the UGAepi crystal structures

	NAD$^+$	NAD$^+$/UDP	NAD$^+$/UDP-GlcA	NAD$^+$/UDP-GlcA/UDP-GalA	NAD$^+$/4F-UDP-GlcA	NAD$^+$/UDP-GalA
Space group	C2	P1	P1	$P2_1$	P1	P1
Unit cell axes (Å)	214.5, 78.5, 87.9	42.5, 58.6, 64.9	42.4, 58.4, 64.7	53.7, 124.3, 98.4	42.2, 58.2, 64.4	56.8, 62.7, 105.8
Unit cell angles (degrees)	90.0, 91.0, 90.0	96.8, 98.4, 110.3	96.8, 98.4, 110.6	90.0, 90.6, 90.0	97.2, 98.2, 109.9	91.9, 99.9, 92.0
No. of chains/ asymmetrical unit	4	2	2	4	2	4
Resolution (Å)	45.6–2.20 (2.25–2.20)[a]	45.3–1.70 (1.74–1.70)	45.2–1.80 (1.84–1.80)	49.4–1.50 (1.53–1.50)	45.2–1.70 (1.74–1.70)	46.1–1.85 (1.89–1.85)
PDB code	6ZLA	6ZL6	6ZLD	6ZLK	6ZLJ	6ZLL
R_{sym}[b] (%)	4.6 (20.8)	6.5 (55.7)	8.4 (25.9)	8.3 (157)	13.7 (239)	11.6 (228)
$CC_{1/2}$[c] (%)	99.9 (92.6)	99.7 (88.1)	99.7 (78.0)	99.5 (18.8)	99.6 (68.0)	99.7 (46.6)
Completeness (%)	98 (92.6)	93 (91)	93.7 (92)	97.5 (97.5)	92.4 (90.8)	92.6 (83.6)
Unique reflections	72,646	58,368	49,095	190,286	57,074	113,316
Redundancy	4.2 (3.2)	1.7 (1.7)	1.6 (1.7)	3.8 (3.9)	9.1 (9.5)	6.9 (6.4)
I/σ	16.9 (4.6)	10.2 (1.2)	9.3 (2.5)	7.0 (1.0)	8.4 (1.5)	8.7 (1.1)
No. of nonhydrogen atoms						
Protein	9714	4932	4934	9869	4930	9988
Ligands	176	138	160	470	160	320
Waters	243	251	298	695	170	242
Average *B* value for protein/ligand atoms (Å^2)	34.2/25.4	25.59/25.8	22.4/18.7	23.6/22.8	29.3/26.4	37.14/ 38.12
R_{cryst} (%)	17.8 (21.5)	17.0 (28.6)	16.8 (24.8)	17.2 (32.2)	17.2 (29.7)	18.7 (32.2)
R_{free} (%)	22.7 (26.5)	20.0 (30.7)	20.7 (27.1)	20.3 (30.9)	21.6 (30.7)	22.2 (34.0)
Root mean square deviations from standard values						
Bond lengths (Å)	0.087	0.010	0.009	0.011	0.009	0.008
Bond angles (degrees)	1.58	1.68	1.57	1.73	1.60	1.58
Ramachandran plot						
Preferred (%)	97.5	98.0	98.0	97.7	98.0	97.3
Allowed (%)	2.3	1.7	1.7	2.0	1.7	2.2
Outliers (%)	0.2	0.3	0.3	0.3	0.3	0.4

[a]Values in parentheses are for reflections in the highest-resolution shell.
[b]$R_{sym} = \sum|I_i - \langle I\rangle| / \sum I_i$, where I_i is the intensity of the *i*th observation and is the mean intensity of the reflection.
[c]The resolution cut-off was set to $CC_{1/2} > 0.3$, where $CC_{1/2}$ is the Pearson correlation coefficient of two "half" data sets, each derived by averaging half of the observations for a given reflection. The data set for the equilibrium structure features some mild anisotropy. Following the resolution estimation given by the program Aimless (25) and based on the visual inspection of the electron density maps, only for this data set we included data with a somewhat lower $CC_{1/2}$ value (26).

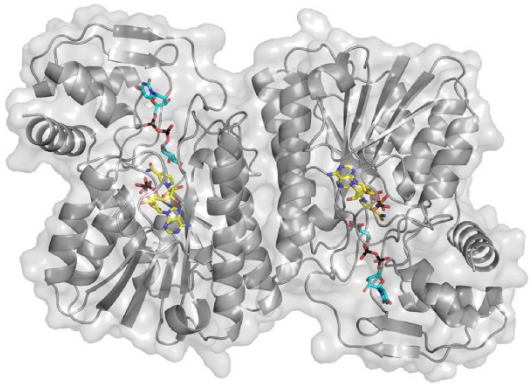

Figure 1. The overall structure of the dimeric UDP-glucuronic acid 4-epimerase from *B. cereus*. The NAD$^+$ and UDP-GlcA carbons are shown in *yellow* and *cyan*, respectively. The backbone trace is shown as a *gray ribbon* and *semitransparent protein surface*.

Moreover, Phe-206 is implicated in π-stacking with the uracil ring, whereas Thr-204 is hydrogen-bonded to the NH group of the base. This complex network of UDP-protein interactions is completed by loop 187–196. Here, Arg-192 is engaged in a hydrogen bond with the uracil, whereas the backbone N atom of Ala-189 is hydrogen-bonded to the UDP pyrophosphate (Fig. 2*D*). Unlike residues 86–91, 204–214, and 269–276, the conformation of loop 187–196 remains unaltered upon UDP ligation, being the only element of the apoenzyme that is already preorganized for nucleotide binding. These findings highlight the role of the UDP moiety of the sugar nucleotide substrate. In the apoenzyme, the binding site is open and can be readily accessed. With its many hydrogen-binding groups, UDP triggers a few localized structural changes that collectively create the cavity where the sugar group binds and is modified (Fig. 2*B*). The nucleotide group of the substrate is therefore necessary to attain the catalytically competent conformation of the active site.

Structure of the Michaelis complex

The active site is located at the interface between the NAD$^+$ and the UDP domains (29–31). To visualize the mode of the sugar binding in this cavity, BcUGAepi was co-crystallized in the presence of an excess of UDP-GlcA, and the structure was solved at 1.8 Å resolution (Table 1). The electron density map shows the conformations of the sugar and nearby nicotinamide

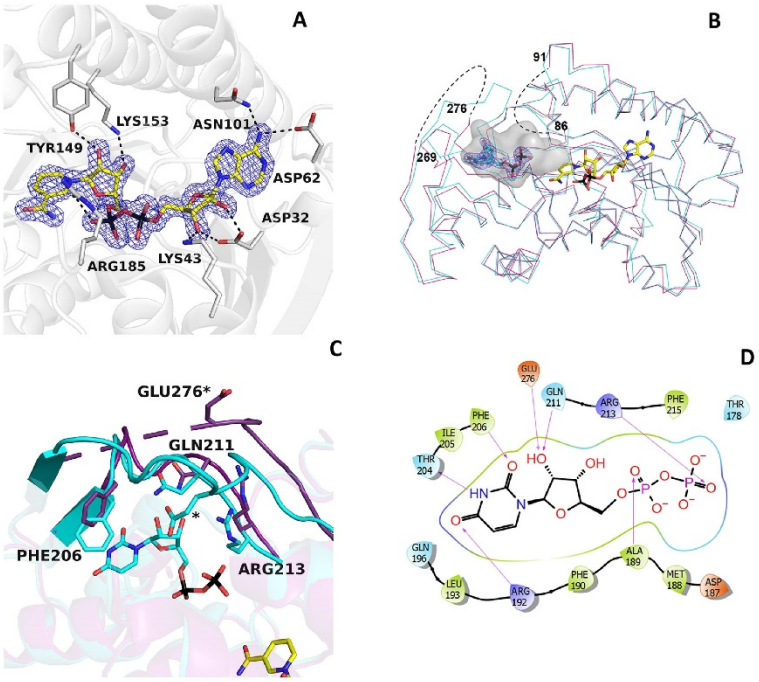

Figure 2. NAD$^+$ and UDP binding in BcUGAepi. *A*, weighted $2F_o - F_c$ electron density of NAD$^+$ in the epimerase/NAD$^+$ binary complex (subunit A). The contour level is 1.4σ. Side chains involved in hydrogen-bonding and electrostatic interactions are shown (*light gray carbons*). Together with Thr-126 (Fig. 3), Tyr-149, and Lys-153 are part of the fingerprint catalytic triad of the SDR family. *B*, superposition between the Cα traces of the epimerase structures bound to NAD$^+$ (*purple*) and NAD$^+$/UDP (*cyan*). NAD$^+$ carbons are shown in *yellow*, and UDP carbons are shown in *cyan*. The electron density of UDP is shown with a contour level of 1.4σ. The loops 86–91 and 269–276 are disordered in the NAD$^+$ complex (*dashed lines*). Upon UDP binding, both loops adopt an ordered conformation that defines a large cavity where the mononucleotide ligand binds. The large cavity space between the UDP pyrophosphate and the nicotinamide forms the sugar-binding site. *C*, *ribbon diagram* of the NAD$^-$ structure (*purple*) superposed onto the complex with NAD$^+$/UDP (*cyan*). In the absence of UDP, loop 269–276 is disordered. UDP binding reorganizes this loop that, together with residues 204–214, wraps the UDP molecule. *D*, two-dimensional schematic diagram of the extensive interactions between UDP and the protein residues.

conformation with excellent clarity (Fig. 3, *A* and *B*). In solution, the equilibrium of the reaction [UDP-GalA]/[UDP-GlcA] is 2.0 as measured using 1 mM UDP-GlcA at pH 7.6 (23). We hypothesize that crystal packing and the higher viscosity of the crystallization solutions, due to the relatively high PEG3350 concentrations (~20%, w/v), may shift the equilibrium toward the substrate, UDP-GlcA. The glucuronic acid faces the nicotinamide ring of NAD$^+$ with a geometry that is perfectly suited for the hydride transfer and 4-keto-hexose-uronic acid intermediate generation (Scheme 1). As observed in MoeE5 (22), the sugar adopts the chair conformation to position its 4′-carbon at 3.2 Å from the C4 atom of the NAD$^+$. The substrate 4′-H atom is thereby predicted to point exactly toward the C4 of the nicotinamide ring (Fig. 3*A*). Moreover, Tyr-149 properly interacts with the substrate to afford the deprotonation of the 4′-OH group (11). In essence, the co-crystallization experiment allowed us to capture the fine geometry of substrate binding in the Michaelis complex.

The sugar-binding cavity features a constellation of polar groups that are precisely positioned for hydrogen bonding to the hydroxy and carboxylate groups of the substrate (Fig. 3*B*). The 4′-OH engages two residues of the SDR catalytic triad (Thr-126 and Tyr-149), whereas the 2′-OH and 3′-OH are hydrogen-bonded to Arg-185 and Pro-85 (backbone oxygen). The 5′-carboxylate interacts with Thr-126, Ser-127, Ser-128, and Thr-178. Interestingly, Thr-178 is the only residue in a disallowed region of the Ramachandran plot in all substrate/product-bound structures. Strained conformations have been often observed in enzyme active sites (40). In BcUGAepi, this strained backbone conformation is involved in the binding of the substrate carboxylate group whose negative charge is critical for recognition specificity. Indeed, UDP-glucose, UDP-galactose, UDP-GlcNAc, and UDP-xylose are poorly active substrates or inactive against UDP-glucuronic acid 4-epimerases (19, 23, 41–43).

The comparison between the structures of the enzyme bound to UDP and UDP-GlcA shows an interesting feature that further highlights this perfect complementarity between the sugar and its binding site. In the UDP complex, the sugar cavity is occupied by three ordered water molecules whose positions exactly overlap the 3′-OH, 4′-OH, and 5′-carboxylate groups of the substrate (Fig. 3*C*). Thus, the polar groups that decorate the cavity surface define a set of polar niches whose spacing matches the geometry of the polar

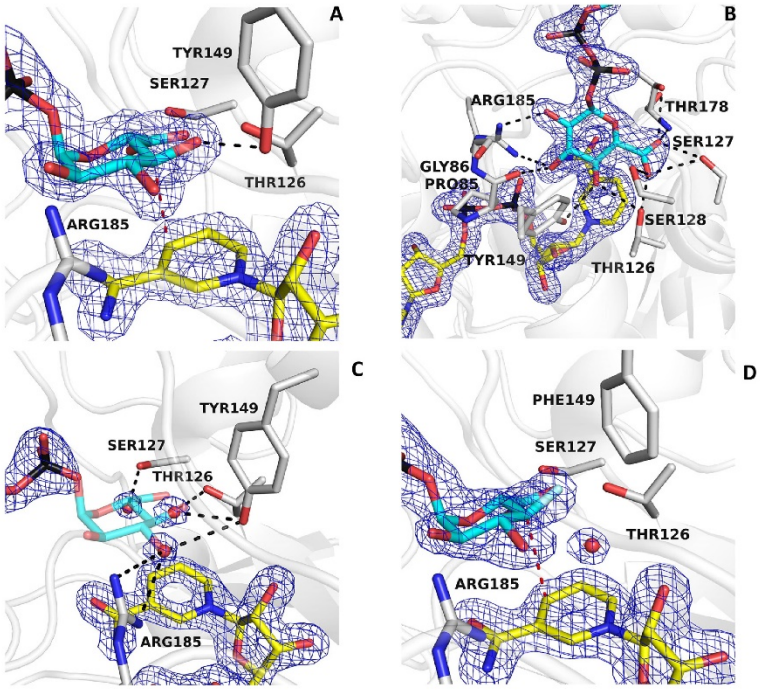

Figure 3. Binding of UDP-glucuronic acid. *A* and *B*, binding of the sugar moiety of the substrate (*cyan carbons*) in two orientations. The weighted $2F_o - F_c$ electron density for the NAD^- (*yellow carbons*) and substrate is contoured at 1.4σ (subunit A). The orientation of *A* outlines the binding of the substrate C4′ at 3.2 Å from C4 of the nicotinamide (*red dashed line*) and the hydrogen bond between the sugar O4′ and Tyr-149 (*black dashed line*). All hydroxyl groups and the carboxylate of the glucuronic acid are engaged in hydrogen-bonding interactions as shown in *B*. *C*, a cluster of ordered water molecules are bound in the sugar-binding site of the UDP/NAD^+ complex. The positions of these waters exactly superpose onto the 3′-OH, 4′-OH, and 5′-carboxylate of the substrate sugar. The orientation is the same as in the *left panel* of *A*, and the contour level of the density is 1.4σ (subunit A). *D*, binding of UDP-4-deoxy-4-fluoro-α-D-glucuronic acid (fluorine in *light cyan*) to the Y149F mutant (subunit A). The structure is virtually identical to that of the ternary NAD^-/UDP-glucuronic acid complex (Fig. 3*A*). The hydroxyl group of Tyr-149 is replaced by an ordered water molecule in contact with the fluorinated C4′ atom.

substituents on the chair conformation of the glucuronic acid substrate.

These structural features were further explored in an experiment that probed the interactions at the 4′-OH locus of the substrate. The low-activity Y149F mutant (23) was co-crystallized with UDP-4-deoxy-4-fluoro-α-D-glucuronic acid, an inert substrate analog where the 4′-OH is replaced by a fluorine atom. The structure (1.7 Å resolution; Table 1) shows the sugar ring with the same orientation and interactions as described previously with the UDP-GlcA structure (Fig. 3*D*). The 4′-carbon is at a slightly longer distance from the C4 of the nicotinamide (3.5 Å *versus* 3.2 Å observed in the substrate complex). Interestingly, the Y149F replacement gives room for the binding of an ordered water molecule that is absent in the structure of the WT protein. Possibly, this water molecule may take over the role of the Tyr-149 hydroxyl group, explaining the residual, yet significant, activity of this mutant (23). Besides this variation in the water structure, the conformation of the active site, including the side chain at position 149, is essentially identical to that observed in the WT and remains unaffected by the mutation. These observations validate the conclusions inferred from the analysis of the UDP-GlcA complex and confirm that the OH group of the strictly conserved Tyr-149 is above all critical for its role in acid-base catalysis (44, 45), whereas it has little impact on the active-site and sugar conformation.

Capturing the rotation of the 4-keto-hexose-uronic acid intermediate

After the UDP-GlcA substrate is oxidized by NAD^+ (which is reduced to NADH), the 4-keto-hexose-uronic acid is thought to rotate inside the active site to favor the hydride transfer from NADH to the opposite face of the intermediate, therefore inverting the configuration of the C4′ (see Scheme 1). To obtain evidence of this rotation mechanism, we co-crystallized BcUGAepi with an excess of the UDP-GalA product (1.5 Å resolution; Table 1). The multiple X-ray diffraction data sets collected on several crystals grown in these conditions consistently led to electron density maps that were distinctly different from that observed in the substrate-bound enzyme. The maps could not be satisfactorily explained by the presence of a bound UDP-GalA, as both modeling and crystallographic refinement systematically suggested the presence of residual density that could not be accounted for by the ligand. After various

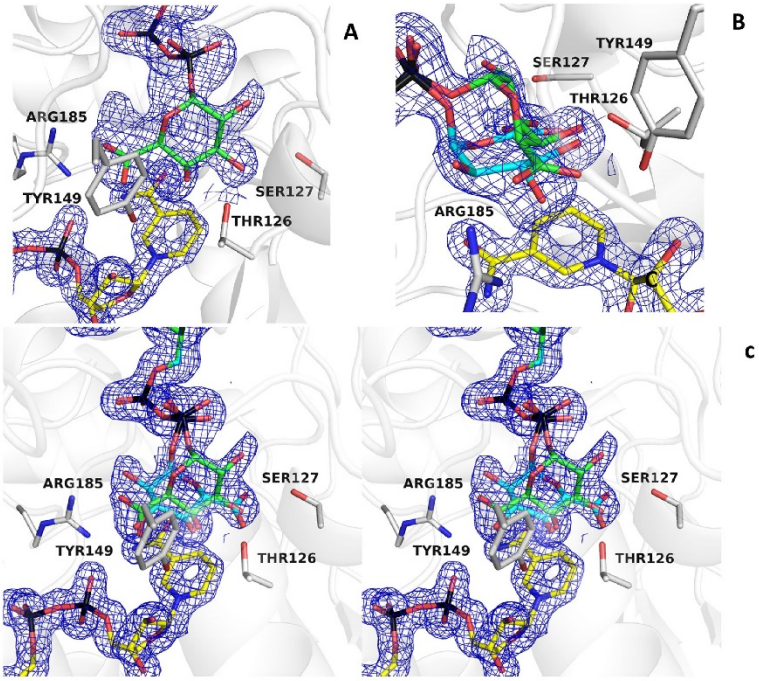

Figure 4. The equilibrium structure shows how the same active-site conformation accommodates substrate and product with their opposed chirality. *A*, the weighted $2F_o - F_c$ map obtained from crystals grown in the presence of UDP-GalA can be nicely fit by this sugar (*green carbons*), but a significant portion of the density remains unoccupied (contour level 1.4σ; subunit A). *B* and *C*, fitting of galacturonic (*green carbons*) and glucuronic (*cyan carbons*) moieties (0.5/0.5 occupancies) into the electron density shown with the same orientation as in Fig. 3 (*A* and *B*). *C* is shown in *stereoview*.

modeling experiments, we came to the conclusion that this extra density must be ascribed to a glucuronic acid molecule. In the course of crystallization, UDP-GalA is partly converted to UDP-GlcA so that the crystals contain an approximately equimolar content of GalA- and GlcA-bound crystalline enzymes (refined occupancies 0.5/0.5; Fig. 4 (*A* and *B*)). This observation is line with the above-discussed idea that the crystallization conditions likely favor substrate accumulation. We define this complex as an "equilibrium" structure that is extremely interesting to visualize the start and end points of the reaction. Above all, this structure immediately suggests that the sugar rings of substrate and product bind with opposite orientations within the active site. Moreover, it reveals that ligand flipping can take place with almost no changes in the active site because the conformation of the equilibrium structure turned out to be virtually identical to that of the UDP-GlcA complex.

To confirm these findings and obtain further insight into the geometry of product-binding orientation, we performed another crystallographic experiment to obtain the structure in complex with UDP-GalA alone. We reasoned that the ionizable group of Tyr-149 and its function as active-site base could be highly sensitive to pH. Moreover, lowering of the temperature could further modulate the enzyme reactivity. Therefore, we performed the co-crystallization experiments with UDP-GalA at a lower pH (6.5 instead of 8.0) and temperature (4 °C instead of 20 °C). This strategy proved to be successful in that the crystal structure (1.85 Å resolution; Table 1) reveals very clear and unambiguous density for the GalA product bound to the active site (Fig. 5). Moreover, the GalA-binding mode exactly matches that observed in the equilibrium structure, whose interpretation was thereby further validated by this experiment. The sugar of the UDP-GalA is flipped with respect to the orientation of the sugar of UDP-GlcA and is implicated in an intricate network of interactions. The three hydroxy groups in positions 1′, 2′, and 3′ are hydrogen-bonded to Ser-127, Thr-126, and Tyr-149, whereas the 5′-carboxylate is hydrogen-bonded to Tyr-149, Gly-86 (backbone N atom), and Arg-185. Clearly, the BcUGAepi active site can satisfy the hydrogen-bonding propensity of all polar (OH and carboxylate) groups of the sugar product despite its flipped orientation with respect to the substrate.

The superposition of BcUGAepi/NAD^-/substrate and BcUGAepi/NAD^+/product complexes is particularly helpful in delving into these findings. The two complexes are nearly identical with a root mean square deviation of 0.33 Å for their α-carbons. Likewise, the binding of the UMP moiety of UDP-GalA is identical to that observed in the UDP-GlcA complex. Critical differences are instead observed for the β-phosphate and the sugar rings (Fig. 6, *A* and *B*). Small 20–30° torsional rotations about the pyrophosphate's P–O–P bonds shift by 0.2 Å the position of the O1′ atom bound to the β-phosphorus. This movement is coupled to a 160° rotation about the O1′–

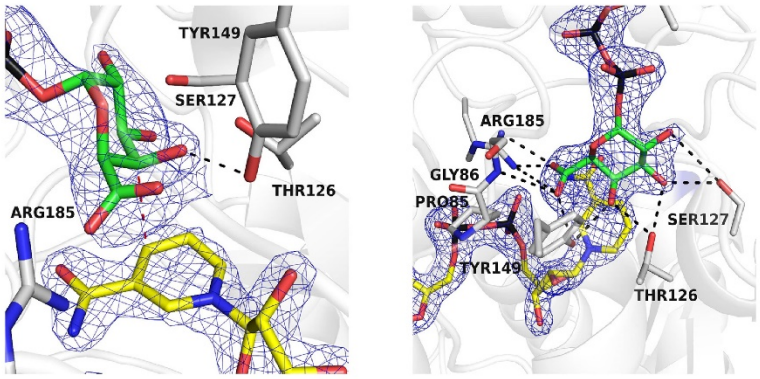

Figure 5. The crystal structure of BcUGAepi in complex with NAD^+ and UDP-galacturonic acid at pH 6.5 and 4 °C shown in two different orientations. The *left panel* highlights the position of the C4′ in proximity of the nicotinamide (*red dashed line*) and the hydrogen bond between the sugar O4′ and Tyr-149 (*black dashed line*). As shown in the *right panel*, all hydroxyl groups and the carboxylate of the glucuronic acid are engaged in hydrogen-bonding interactions with the protein. The orientations are the same as in Fig. 3 (*A* and *B*). The contour level of the weighted $2F_o - F_c$ density is 1.4σ (subunit A).

C1′ bond that flips the sugar ring. Such a "swing and flip" movement reorients and repositions the sugar within the large active-site cavity (Video S1). Despite such a drastic alteration, both product and substrate sugars retain the same chair conformation. The positions of the 3′-OH, 4′-OH, and 5′-carboxylate substituents of the glucuronic acid substrate overlap with those of the 5′-carboxylate, 4′-OH, and 3′-OH substituents of the galacturonic acid product (Fig. 6, *B–D*). Strikingly, the C4′ atom of UDP-GlcA and UDP-GalA holds exactly the same position at 3.2 Å from NAD^+ with the $C4_{nicotinamide}$–$C4'_{sugar}$–$O4'_{sugar}$ angle measuring 106–107° in both structures (Fig. 6*E*). The only protein conformational change affects the peptide bond between Pro-85 and Gly-86 that has flipped orientation in the two structures; Pro-85 oxygen (main chain) interacts with the 3′-OH of the substrate, whereas Gly-86 (main chain) interacts with the 5′-carboxylate of the product (Fig. 6*C*). Based on these observations, we surmise that after UDP-GlcA oxidation, the suboptimal interactions of the more rigid and distorted structure of the 4-keto-hexose-uronic intermediate promotes the swing and flip movement that is coupled to the flipping of the 85-86 peptide bond. The salt bridge between Arg-185 and the flipped 5′-carboxylate may be critical for holding the rotated intermediate and prevent its decarboxylation (Fig. 6, *B* and *D*). With a firm grip on the flipped sugar, NADH can transfer its 4-hydride to the C4′ of the keto intermediate affording the chirally inverted product.

A flexible UDP-binding arginine promotes catalysis

Besides the highly ordered conformation of the active site as revealed by the crystal structure of the substrate and product complexes, the epimerization mechanism inherently entails a considerable degree of malleability of the active site to allow both UDP-GlcA binding and rotation of the keto intermediate. In this context, we were intrigued by the role of Arg-88 at the entrance of the active site. This arginine residue is present only in BcUGAepi and MoeE5 (Arg-94) (22). Other epimerases, such as UDP-galactose 4-epimerase (21, 29–31, 36), have a glycine residue, whereas other SDR decarboxylases (*e.g.* UAXS in Scheme 1 (16)) show an alanine in the same position. Arg-88 belongs to one of the above-described loops that become ordered only upon UDP binding (loop 86–91; see Fig. 2*B*). In the presence of glucuronic acid, the loop moves even closer to the UDP, and the side chain swings into the active site, interacting with the pyrophosphate and optimizing the shape of the substrate cavity (Fig. 7*A*). We hypothesized that this loop, with its multiple discrete conformations, could be instrumental to substrate binding and intermediate rotation occurring during catalysis. We therefore studied the R88A mutation that removes the long and flexible side chain at this position. The mutant enzyme was found to retain the capacity to generate UDP-GalA but with an 8-fold lower catalytic rate (0.032 ± 0.002 s^{-1}; Fig. 7*B*) compared with 0.25 ± 0.01 s^{-1} of the WT enzyme (23). We then turned to the kinetic isotope effect (k_{cat}^{H}/k_{cat}^{D}) to probe the effects of the mutation using a C4′-deuterated substrate. We have previously shown that WT BcUGAepi shows a relatively low k_{cat}^{H}/k_{cat}^{D} of 2.0 ± 0.1, due to a slow catalytically relevant conformational change that partially masks the kinetic isotope effect (23). Conversely, we found that the R88A protein displays a more pronounced k_{cat}^{H}/k_{cat}^{D} of 4.2 ± 0.3, a typical value for hydride transfer reactions. These data hint at a combination of factors affecting the properties of R88A. In the mutant, the suboptimal position of the glucuronic acid substrate may impair hydride transfer, whereas the more spacious and flexible active site can be less limiting for catalysis. As a result, the kinetic isotope effect appears to be largely unmasked in the mutant protein.

Conclusion

Our work illuminates many aspects of the epimerization reaction catalyzed by UDP-GlcA epimerases. NAD^+ is fully embedded within the protein, functioning as nondissociable prosthetic group. Conversely, the substrate-binding site is lined by a set of flexible loops and side chains. Only upon UDP binding, these loops become ordered to create a cavity in front of

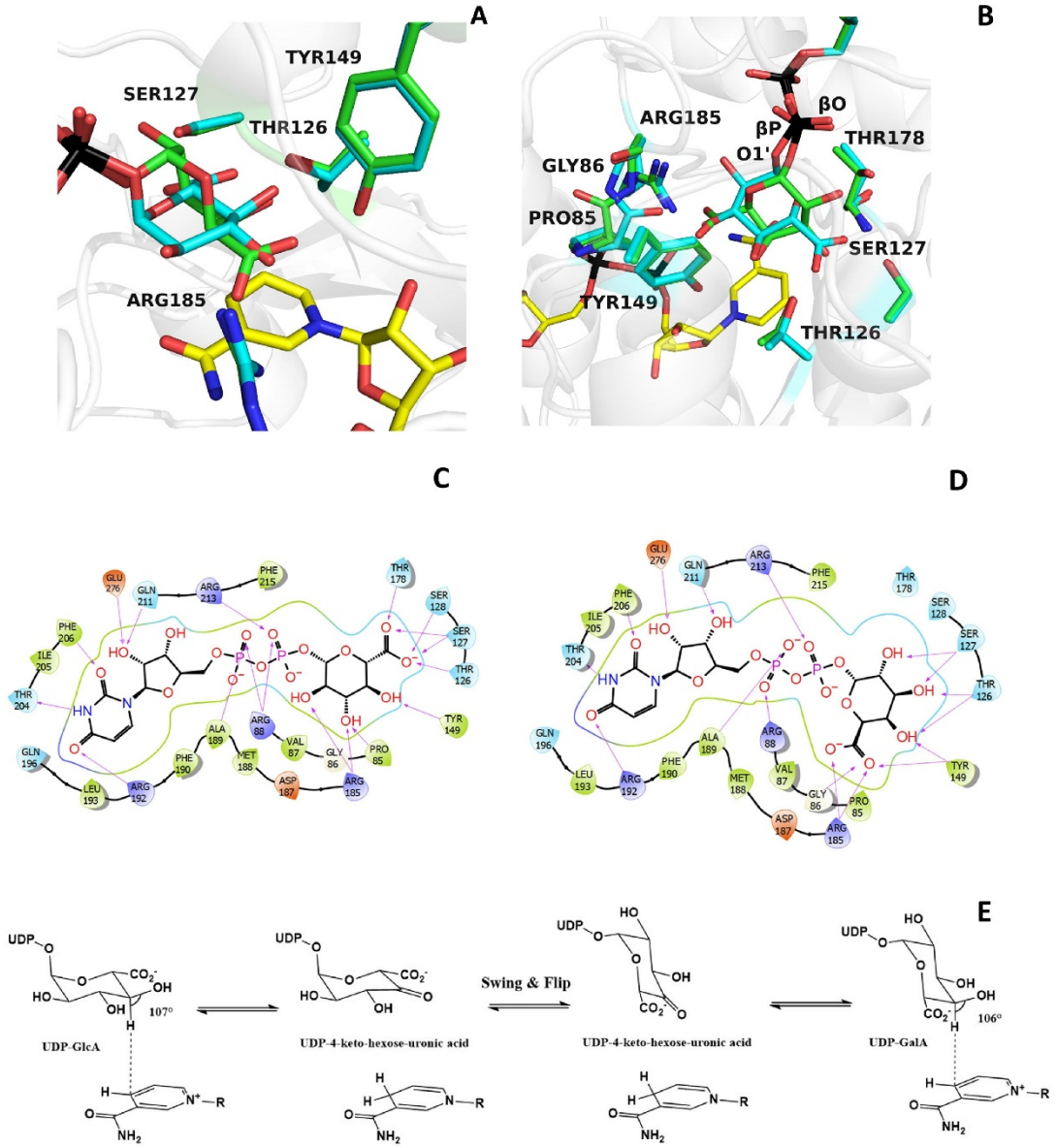

Figure 6. A detailed comparison of UDP-glucuronic and UDP-galacturonic acid binding. *A* and *B*, the galacturonic acid (*green* carbons) can be moved on top of the glucuronic acid (cyan carbons) through a rotation of about 160° around the bond between the β-phosphorus (*βP*) of UDP and O1′ of the sugar combined with a smaller "swinging" 30° rotation around the bond between the β-phosphorus and the pyrophosphate oxygen (*βO*) of UDP. These movements can be best-appreciated in the orientation of the *right panel*. The orientations are the same as in Fig. 3 (*A* and *B*). *C* and *D*, schematic two-dimensional overviews of the protein-ligand interactions. Despite their differing swing-rotated orientations, both sugars engage their polar groups in multiple hydrogen bonds with protein side chains. Only the 2′-carbon of glucuronic acid (*B*) is not hydrogen-bonded to the protein as it interacts with ordered waters. Moreover, the conformations of all active-site side chains remain virtually unaltered in the two complexes. *E*, scheme of the BcUGAepi reaction. The fine geometry of the $C4'_{sugar}$–$C4_{nicotinamide}$ contact allows C4′ oxidation of glucuronate (forward reaction) and galacturonate (reverse reaction) acid.

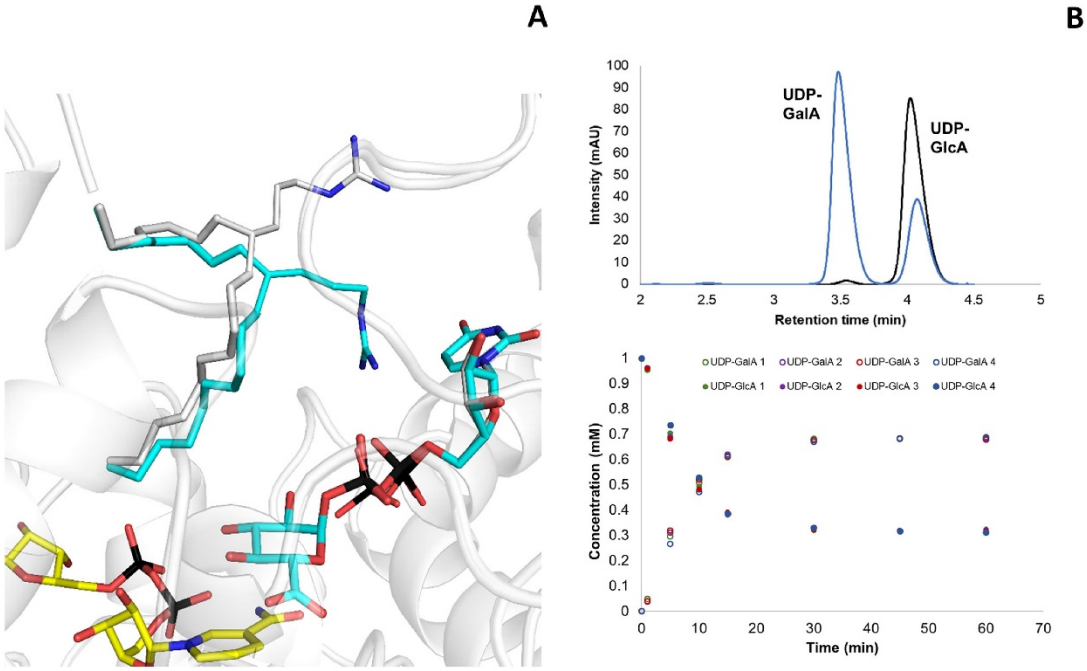

Figure 7. The role of Arg-88. *A*, in the presence of UDP-GlcA, loop 85–90 (shown as Cα trace; subunit A) closes over the substrate (*cyan carbons*), shifting its position as compared with the structure of the UDP-bound enzyme (*gray carbons*; subunit A). In particular, Arg-88 changes its conformation to interact with the UDP pyrophosphate. *B*, BcUGAepi R88A reaction with UDP-GlcA as substrate. The reaction mixture contained 1 mM UDP-GlcA, 1 mM NAD^+, and 27 μM (1 mg/ml) purified recombinant BcUGAepi R88A in sodium phosphate buffer (50 mM Na_2HPO_4, 100 mM NaCl, pH 7.6) in a final volume of 200 μl. The HPLC chromatograms after 1 min (*black*) and 60 min (*blue*) from the start of the reaction are shown in the *top panel*. The *bottom panel* depicts the time course of the depletion of UDP-GlcA (*filled circles*) and formation of UDP-GalA (*open circles*). Reactions were performed in quadruplicate, and all of the individual data points are shown.

the nicotinamide ring. The nucleotide component of the substrate is therefore necessary for attaining the catalytically competent conformation. The active-site geometry features an exquisite complementarity to the sugar substrate. All of the hydrogen-bonding groups of the glucuronic acid find a polar counterpart. Moreover, the 4′-carbon undergoing epimerization is precisely oriented for transferring a hydride to the nicotinamide. With its trigonal carbon, the resulting 4-keto-hexose-uronic acid intermediate may experience suboptimal fitting and interactions inside the cavity. Through a swing and flip movement, the intermediate eventually rotates in the active site (Video S1 and Fig. 6*E*). The spacious cavity of the enzyme is instrumental to this process. Consistently, its volume measures 990 $Å^3$ which is almost double that of the UDP-xylose and UDP-apiose/xylose synthases (500–600 $Å^3$; Fig. 8). Moreover, the very same loops that allow UDP-GlcA binding and active-site closure are likely to confer the malleability required for the intermediate rotation. The experiments on Arg-88 support this notion. The flipped orientation positions the carbonyl group of the intermediate exactly as needed for the efficient hydride transfer from NADH, which ultimately generates the chirally inverted UDP-galacturonic acid product. Strikingly, the same active-site configuration of the substrate complex (with only the exception of a peptide flip) is retained in the product complex. All polar groups of the galacturonic acid are indeed engaged in hydrogen-bond interactions with the protein. This feature explains why the enzyme can also catalyze the reverse reaction, namely the epimerization of UDP-galacturonic acid to UDP-glucuronic acid. Moreover, these precisely arranged hydrogen bond interactions guarantee that the reactive keto intermediate is protected from the facile decarboxylation, differently from similar enzymes that modify UDP-GlcA through its decarboxylation.

Experimental procedures

Materials

All chemical reagents were purchased from Sigma–Aldrich, unless otherwise stated. The synthetic gene encoding for BcUGAepi was ordered in pET17b-expression vector (pET17b_BcUGAepi) from GenScript as a codon-optimized gene for optimal expression in *E. coli* and with C-terminal Strep-tag for protein purification. For plasmid DNA isolation, the GeneJET Plasmid Miniprep Kit (Thermo Scientific, Waltham, MA, USA) was used. DpnI and Q5® High-Fidelity DNA polymerase were from New England Biolabs (Frankfurt am Main, Germany). Oligonucleotide primers were from Sigma–Aldrich. *E. coli* NEB5α competent cells were from New England Biolabs. *E. coli*

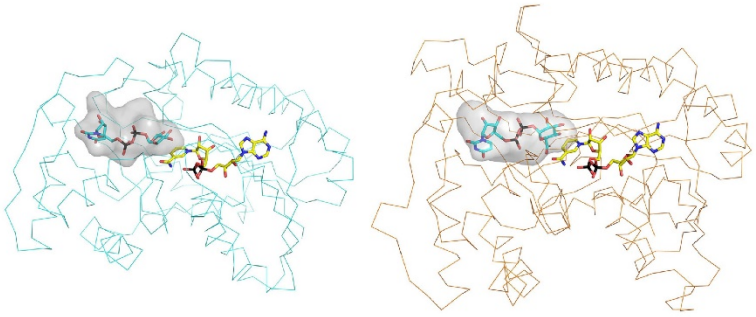

Figure 8. Comparison between the UGP-glucuronic binding sites of *B. cereus* epimerase (*left*) and *A. thaliana* UDP-apiose/UDP-xylose synthase (*right*, PDB entry 6H0N). The two enzymes share the same short-chain alcohol dehydrogenase site and catalytic (Ser/Thr-Tyr-Lys) triad. However, their sugar cavities have different shapes. The more spacious site of the epimerase is instrumental to a swing-rotation conformational change that the sugar undergoes after oxidation by NAD^+.

Lemo21(DE3) cells were prepared in-house. DNA sequencing was performed by GATC (Konstanz, Germany). UTP (98% purity) and ATP (98% purity) were purchased from Carbosynth (Compton, UK). Deuterium oxide (99.96% 2H) was from Eurisо-Top (Saint-Aubin Cedex, France). Calf intestinal alkaline phosphatase was from New England Biolabs, and D-lactate dehydrogenase was from Megazyme (Vienna, Austria). Albumin Fraktion V (BSA) was from Roth (Karlsruhe, Germany). UDP-glucose pyrophosphorylase, inorganic pyrophosphatase and human UDP-glucose 6-dehydrogenase were expressed and purified according to previously described protocols (23). GalKSpe4 was expressed following a protocol from the literature (46) and purified utilizing Strep-tag. UDP-galacturonic acid and UDP-4-[^{2}H]glucuronic acid were synthesized as described previously (23). The synthesis of UDP-4-deoxy-4-fluoro-α-D-glucuronic acid (4F-UDP-glucuronic acid) is described in the supporting information (see Scheme S1 and Figs. S1–S4).

Site-directed mutagenesis

BcUGAepi_R88A and BcUGAepi_Y149F variants were prepared using a modified QuikChange protocol as described previously (23). PCRs were carried out in a reaction volume of 50 μl using 20 ng of plasmid DNA as template and 0.2 μM forward or reverse primer. Q5 DNA polymerase was used for DNA amplification.

Protein expression and purification

E. coli cells harboring pET17b_BcUGAepi (or pET17b_BcUGAepi_Y149F/pET17b_BcUGAepi_R88A) were grown in 10 ml of lysogeny broth medium (50 μg/ml ampicillin and 35 μg/ml chloramphenicol) at 37 °C for 16 h. 2 ml of preculture were used to inoculate fresh lysogeny broth medium (250 ml) supplemented with ampicillin (50 μg/ml) and chloramphenicol (35 μg/ml), and the cells were grown at 37 °C and 120 rpm. When the cell density (A_{600}) reached a value of 0.8, isopropyl β-D-thiogalactoside (0.2 mM) was added to the culture media to induce gene expression. The cells were incubated at 18 °C and 120 rpm for 20 h. The cells were harvested by centrifugation (2800 × *g*, 4 °C, 20 min), the pellet was resuspended in 10 ml of Strep-tag loading buffer (100 mM Tris, 150 mM NaCl, pH 8), and the suspension was stored overnight at −20 °C prior to cell lysis. The cells were disrupted by sonication (pulse 2 s on, 5 s off, 70% amplitude, 5 min) and centrifuged (16,100 × *g*) at 4 °C for 45 min. The supernatant was collected and filtered (0.45 μm) prior to loading onto the StrepTrap^{TM} HP column (5 ml of resin, GE Healthcare) pre-equilibrated with the loading buffer (100 mM Tris, 150 mM NaCl, pH 8). The Strep-tagged protein was eluted with elution buffer (100 mM Tris, 150 mM NaCl, 2.5 mM D-desthiobiotin, pH 8) and rebuffered against the reaction buffer (50 mM Na_2HPO_4, 100 mM NaCl, pH 7.6) containing 10% glycerol using Amicon filter tubes (30-kDa cut-off). After buffer exchange, the protein was divided into aliquots, flash-frozen in liquid nitrogen, and stored at −20 °C. Protein concentration was determined based on the absorption at 280 nm on a NanoDrop spectrophotometer. Size and purity of the protein were confirmed by SDS-PAGE.

X-ray crystallography

Purified BcUGAepi was concentrated at 11 mg ml^{-1} in 20 mM Tris-HCl buffer at pH 8, 50 mM NaCl. Crystallization screenings were performed by the vapor-diffusion sitting-drop technique using commercial kits (Jena Bioscience and Hampton Research) and an Oryx 8 crystallization robot (Douglas Instruments, East Garston, UK). Crystallization hits were optimized manually using the sitting-drop protocol. After optimization, the best-diffracting crystals were found in a condition containing 200 mM potassium acetate and 14–24% PEG 3350, and the protein was co-crystallized in the presence of 2 mM NAD^+ and a 2 mM concentration of different UDP ligands (Table 1). Crystals grew in 48 h from drops prepared in a ratio of 1:1 BcUGAepi (11 mg ml^{-1}) and reservoir at 20 °C. Crystals grown in the presence of NAD^+/UDP-GalA were obtained at 4 °C using a BcUGAepi sample concentrated to 11 mg ml^{-1} in 20 mM Tris-HCl buffer at pH 6.5, 50 mM NaCl. Crystals were harvested from the mother liquor using nylon cryoloops (Hampton Research) and flash-cooled in liquid nitrogen after a short soak in a solution containing 26% (v/v) PEG 3350, 200 mM potassium acetate, 20% (w/v) glycerol, 2 mM NAD^+, and 2 mM ligand. X-ray diffraction data used for structure

determination and refinement were collected at the PX beamline of the Swiss Light Source in Villigen, Switzerland. Data were scaled using the XDS (47) program and CCP4 (25) package for indexing and processing of the data. The space group symmetry together with final data collection and processing statistics are listed in Table 1. The initial structure (NAD^+ complex) was solved with MOLREP (48) using the coordinates of NAD-dependent epimerase from *Klebsiella pneumoniae* (PDB entry 5U4Q) as a search model. Manual building, the addition of water molecules, and crystallographic refinement were performed with COOT (49), REFMAC5 (50), and other programs of the CCP4 suite. Hydrogen atoms were added in the riding position following REFMAC5 protocols. Structure quality and validation were assessed using the wwPDB validation server. Figures were created with PyMOL (51) and Maestro (release 2020-1) of the Schrödinger suite of programs, whereas cavity size was measured with Caver (52). Hydrogen bonds were inferred with Maestro using the default parameters (Schrödinger).

Activity assays

The reaction mixture (200-μl final volume) contained 1 mM UDP-GlcA, 1 mM NAD^+, and 27 μM (1 mg/ml) purified recombinant BcUGAepi R88A in sodium phosphate buffer (50 mM Na_2HPO_4, 100 mM NaCl, pH 7.6). The reaction was incubated at 23 °C and quenched with methanol (50% (v/v) final concentration) at desired time points, and the precipitated enzyme was removed by centrifugation (16,100 × *g*, 4 °C, 30 min) prior to HPLC analysis. The initial rate was determined from the linear part of the time course by dividing the slope of the linear regression (mM/min) by the enzyme concentration (mg ml^{-1}), giving the initial rate in μmol/(min mg protein). The apparent k_{cat} value (s^{-1}) was calculated as an average of four independent experiments from the initial rate with the molecular mass of the functional enzyme monomer (BcUGAepi R88A: 36,918 g/mol).

Kinetic isotope effect measurement

The sugar nucleotides UDP-GlcA and UDP-GalA were separated with the Shimadzu Prominence HPLC-UV system (Shimadzu, Korneuburg, Austria) on a Kinetex C18 column (5 μM, 100 Å, 50 × 4.6 mm) using an isocratic method with 5% acetonitrile and 95% tetrabutylammonium bromide buffer (40 mM tetrabutylammonium bromide, 20 mM K_2HPO_4/KH_2PO_4, pH 5.9) as mobile phase. UDP-sugars were detected by UV at 262-nm wavelength. For kinetic isotope effect measurements, a BcUGAepi concentration of 0.1 mg ml^{-1} (2.7 μM) was used, and the reactions (30-μl final volume) were performed in quintuplicates for both UDP-GlcA and 4-^{2}H-UDP-GlcA (1 mM). The reaction mixtures were quenched (incubation in 50% (v/v) methanol) after 5 min and analyzed on HPLC. Initial reaction rates (*V*) were calculated from the linear dependence of the product formed and time used. The kinetic isotope effect was calculated from the ratio of the reaction rates (effectively k_{cat}) for the unlabeled and deuterium-labeled substrate ($KIE = V_{unlabeled}/V_{labeled}$).

Data availability

The structures presented in this paper have all been deposited in the Protein Data Bank (PDB) with the codes 6ZLA, 6ZL6, 6ZLD, 6ZLK, 6ZLJ, and 6ZLL. All remaining data are contained within the article.

Author contributions—L. G. I., A. J. B., B. N., and A. M. conceptualization; L. G. I., S. S., and A. J. B. investigation; L. G. I., S. S., A. J. B., and B. N. methodology; L. G. I. and A. M. writing-original draft; A. J. B., C. B., and A. M. validation; A. J. B., B. N., and A. M. writing-review and editing; C. B., B. N., and A. M. supervision; B. N. and A. M. funding acquisition.

Funding and additional information—This work was supported by the Federal Ministry of Science, Research and Economy (BMWFW), the Federal Ministry of Traffic, Innovation, and Technology (bmvit), the Styrian Business Promotion Agency SFG, the Standortagentur Tirol, and the Government of Lower Austrian and Business Agency Vienna through the COMET-Funding Program managed by the Austrian Research Promotion Agency FFG. This work was also supported by Austrian Science Funds (FWF) Grant I-3247 (to B. N. and A. J. E. B.) and by the Italian Ministry of Education, University, and Research (MIUR): Dipartimenti di Eccellenza Program (2018–2022)–Department of Biology and Biotechnology "L. Spallanzani" University of Pavia.

Conflict of interest—The authors declare that they have no conflicts of interest with the contents of this article.

Abbreviations—The abbreviations used are: SDR, short-chain dehydrogenase/reductase; BcUGAepi, UDP-glucuronic acid 4-epimerase from *Bacillus cereus*; UDP-GlcA, UDP-glucuronic acid; UDP-GalA, UDP-galacturonic acid; PDB, Protein Data Bank.

References

1. Bethke, G., Thao, A., Xiong, G., Li, B., Soltis, N. E., Hatsugai, N., Hillmer, R. A., Katagiri, F., Kliebenstein, D. J., Pauly, M., and Glazebrook, J. (2016) Pectin biosynthesis is critical for cell wall integrity and immunity in *Arabidopsis thaliana*. *Plant Cell* **28,** 537–556 CrossRef Medline
2. Reboul, R., Geserick, C., Pabst, M., Frey, B., Wittmann, D., Lütz-Meindl, U., Leonard, R., and Tenhaken, R. (2011) Down-regulation of UDP-glucuronic acid biosynthesis leads to swollen plant cell walls and severe developmental defects associated with changes in pectic polysaccharides. *J. Biol. Chem.* **286,** 39982–39992 CrossRef Medline
3. Reiter, W. D. (2008) Biochemical genetics of nucleotide sugar interconversion reactions. *Curr. Opin. Plant Biol.* **11,** 236–243 CrossRef Medline
4. Bowles, D., Lim, E. K., Poppenberger, B., and Vaistij, F. E. (2006) Glycosyltransferases of lipophilic small molecules. *Annu. Rev. Plant Biol.* **57,** 567–597 CrossRef Medline
5. Radominska-Pandya, A., Little, J. M., and Czernik, P. J. (2001) Human UDP-glucuronosyltransferase 2B7. *Current drug metabolism* **2,** 283–298 CrossRef
6. Ritter, J. K. (2000) Roles of glucuronidation and UDP-glucuronosyltransferases in xenobiotic bioactivation reactions. *Chem. Biol. Interact.* **129,** 171–193 CrossRef Medline
7. Creuzenet, C., Belanger, M., Wakarchuk, W. W., and Lam, J. S. (2000) Expression, purification, and biochemical characterization of WbpP, a new UDP-GlcNAc C4 epimerase from *Pseudomonas aeruginosa* serotype O6. *J. Biol. Chem.* **275,** 19060–19067 CrossRef Medline
8. Kelleher, W. J., and Grisebach, H. (1971) Hydride transfer in the biosynthesis of uridine diphospho-apiose from uridine diphospho-D-glucuronic

acid with an enzyme preparation of *Lemna minor*. *Eur. J. Biochem.* **23,** 136–142 CrossRef Medline
9. Moriarity, J. L., Hurt, K. J., Resnick, A. C., Storm, P. B., Laroy, W., Schnaar, R. L., and Snyder, S. H. (2002) UDP-glucuronate decarboxylase, a key enzyme in proteoglycan synthesis: cloning, characterization, and localization. *J. Biol. Chem.* **277,** 16968–16975 CrossRef Medline
10. Neufeld, E. F., Feingold, D. S., and Hassid, W. Z. (1958) Enzymatic conversion of uridine diphosphate D-glucuronic acid to uridine diphosphate galacturonic acid, uridine diphosphate xylose, and uridine diphosphate arabinose1,2. *J. Am. Chem. Soc.* **80,** 4430–4431 CrossRef
11. Kavanagh, K. L., Jörnvall, H., Persson, B., and Oppermann, U. (2008) Medium- and short-chain dehydrogenase/reductase gene and protein families: the SDR superfamily: functional and structural diversity within a family of metabolic and regulatory enzymes. *Cell Mol. Life Sci.* **65,** 3895–3906 CrossRef Medline
12. Allard, S. T., Giraud, M. F., and Naismith, J. H. (2001) Epimerases: structure, function and mechanism. *Cell Mol. Life Sci.* **58,** 1650–1665 CrossRef Medline
13. Eixelsberger, T., Sykora, S., Egger, S., Brunsteiner, M., Kavanagh, K. L., Oppermann, U., Brecker, L., and Nidetzky, B. (2012) Structure and mechanism of human UDP-xylose synthase: evidence for a promoting role of sugar ring distortion in a three-step catalytic conversion of UDP-glucuronic acid. *J. Biol. Chem.* **287,** 31349–31358 CrossRef Medline
14. Gatzeva-Topalova, P. Z., May, A. P., and Sousa, M. C. (2005) Structure and mechanism of ArnA: conformational change implies ordered dehydrogenase mechanism in key enzyme for polymyxin resistance. *Structure* **13,** 929–942 CrossRef Medline
15. Samuel, J., and Tanner, M. E. (2002) Mechanistic aspects of enzymatic carbohydrate epimerization. *Nat. Prod. Rep.* **19,** 261–277 CrossRef Medline
16. Savino, S., Borg, A. J. E., Dennig, A., Pfeiffer, M., de Giorgi, F., Weber, H., Dubey, K. D., Rovira, C., Mattevi, A., and Nidetzky, B. (2019) Deciphering the enzymatic mechanism of sugar ring contraction in UDP-apiose biosynthesis. *Nat. Catal.* **2,** 1115–1123 CrossRef Medline
17. Thibodeaux, C. J., Melançon, C. E., and Liu, H. W. (2007) Unusual sugar biosynthesis and natural product glycodiversification. *Nature* **446,** 1008–1016 CrossRef Medline
18. Thoden, J. B., Henderson, J. M., Fridovich-Keil, J. L., and Holden, H. M. (2002) Structural analysis of the Y299C mutant of *Escherichia coli* UDP-galactose 4-epimerase: teaching an old dog new tricks. *J. Biol. Chem.* **277,** 27528–27534 CrossRef Medline
19. Frirdich, E., and Whitfield, C. (2005) Characterization of Gla(KP), a UDP-galacturonic acid C4-epimerase from *Klebsiella pneumoniae* with extended substrate specificity. *J. Bacteriol.* **187,** 4104–4115 CrossRef Medline
20. Holden, H. M., Rayment, I., and Thoden, J. B. (2003) Structure and function of enzymes of the Leloir pathway for galactose metabolism. *J. Biol. Chem.* **278,** 43885–43888 CrossRef Medline
21. Thoden, J. B., Wohlers, T. M., Fridovich-Keil, J. L., and Holden, H. M. (2001) Human UDP-galactose 4-epimerase: accommodation of UDP-*N*-acetylglucosamine within the active site. *J. Biol. Chem.* **276,** 15131–15136 CrossRef Medline
22. Sun, H., Ko, T. P., Liu, W., Liu, W., Zheng, Y., Chen, C. C., and Guo, R. T. (2020) Structure of an antibiotic-synthesizing UDP-glucuronate 4-epimerase MoeE5 in complex with substrate. *Biochem. Biophys. Res. Commun.* **521,** 31–36 CrossRef Medline
23. Annika, J. E., Borg, A. D., Weber, H., and Nidetzky, B. (2020) Mechanistic characterization of UDP-glucuronic acid 4-epimerase. *FEBS J.* CrossRef CrossRef Medline
24. Eixelsberger, T., Horvat, D., Gutmann, A., Weber, H., and Nidetzky, B. (2017) Isotope probing of the UDP-apiose/UDP-xylose synthase reaction: evidence of a mechanism via a coupled oxidation and aldol cleavage. *Angew. Chem. Int. Ed. Engl.* **56,** 2503–2507 CrossRef Medline
25. Collaborative Computational Project, Number 4 (1994) The CCP4 suite: programs for protein crystallography. *Acta Crystallogr. D Biol. Crystallogr.* **50,** 760–763 CrossRef Medline
26. Karplus, P. A., and Diederichs, K. (2012) Linking crystallographic model and data quality. *Science* **336,** 1030–1033 CrossRef Medline
27. Gatzeva-Topalova, P. Z., May, A. P., and Sousa, M. C. (2004) Crystal structure of *Escherichia coli* ArnA (PmrI) decarboxylase domain: a key enzyme for lipid A modification with 4-amino-4-deoxy-L-arabinose and polymyxin resistance. *Biochemistry* **43,** 13370–13379 CrossRef Medline
28. Polizzi, S. J., Walsh, R. M., Jr., Peeples, W. B., Lim, J. M., Wells, L., and Wood, Z. A. (2012) Human UDP-α-D-xylose synthase and *Escherichia coli* ArnA conserve a conformational shunt that controls whether xylose or 4-keto-xylose is produced. *Biochemistry* **51,** 8844–8855 CrossRef Medline
29. Thoden, J., Frey, P., and Holden, H. (1996) High-resolution X-ray structure of UDP-galactose 4-epimerase complexed with UDP-phenol. *Protein Sci.* **5,** 2149–2161 CrossRef Medline
30. Thoden, J., Frey, P., and Holden, H. (1996) Molecular structure of the NADH/UDP-glucose abortive complex of UDP-galactose 4-epimerase from *Escherichia coli*: implications for the catalytic mechanism. *Biochemistry* **35,** 5137–5144 CrossRef Medline
31. Thoden, J., Frey, P., and Holden, H. (1996) Crystal structures of the oxidized and reduced forms of UDP-galactose 4-epimerase isolated from *Escherichia coli*. *Biochemistry* **35,** 2557–2566 CrossRef Medline
32. Jörnvall, H., Persson, B., Krook, M., Atrian, S., Gonzàlez-Duarte, R., Jeffery, J., and Ghosh, D. (1995) Short-chain dehydrogenases/reductases (SDR). *Biochemistry* **34,** 6003–6013 CrossRef Medline
33. Persson, B., Kallberg, Y., Bray, J. E., Bruford, E., Dellaporta, S. L., Favia, A. D., Duarte, R. G., Jörnvall, H., Kavanagh, K. L., Kedishvili, N., Kisiela, M., Maser, E., Mindnich, R., Orchard, S., Penning, T. M., *et al.* (2009) The SDR (short-chain dehydrogenase/reductase and related enzymes) nomenclature initiative. *Chem. Biol. Interact.* **178,** 94–98 CrossRef Medline
34. Holm, L. (2019) Benchmarking fold detection by DaliLite v.5. *Bioinformatics* **35,** 5326–5327 CrossRef Medline
35. Liu, Y., Vanhooke, J. L., and Frey, P. A. (1996) UDP-galactose 4-epimerase: NAD^+ content and a charge-transfer band associated with the substrate-induced conformational transition. *Biochemistry* **35,** 7615–7620 CrossRef Medline
36. Thoden, J. B., and Holden, H. M. (1998) Dramatic differences in the binding of UDP-galactose and UDP-glucose to UDP-galactose 4-epimerase from *Escherichia coli*. *Biochemistry* **37,** 11469–11477 CrossRef Medline
37. Jörnvall, H. (1999) Multiplicity and complexity of SDR and MDR enzymes. *Adv. Exp. Med. Biol.* **463,** 359–364 CrossRef Medline
38. Jörnvall, H., Höög, J.-O., and Persson, B. (1999) SDR and MDR: completed genome sequences show these protein families to be large, of old origin, and of complex nature. *FEBS Lett.* **445,** 261–264 CrossRef Medline
39. Rossman, M. G., Liljas, A., Brändén, C.-I., and Banaszak, L. J. (1975) 2 Evolutionary and structural relationships among dehydrogenases. in *The Enzymes* (Boyer, P. D., ed) pp. 61–102, Academic Press, New York
40. Herzberg, O., and Moult, J. (1991) Analysis of the steric strain in the polypeptide backbone of protein molecules. *Proteins* **11,** 223–229 CrossRef Medline
41. Broach, B., Gu, X., and Bar-Peled, M. (2012) Biosynthesis of UDP-glucuronic acid and UDP-galacturonic acid in *Bacillus cereus* subsp. cytotoxis NVH 391-98. *FEBS J.* **279,** 100–112 CrossRef Medline
42. Gu, X., and Bar-Peled, M. (2004) The biosynthesis of UDP-galacturonic acid in plants: functional cloning and characterization of *Arabidopsis* UDP-D-glucuronic acid 4-epimerase. *Plant Physiol.* **136,** 4256–4264 CrossRef Medline
43. Muñoz, R., López, R., de Frutos, M., and García, E. (1999) First molecular characterization of a uridine diphosphate galacturonate 4-epimerase: an enzyme required for capsular biosynthesis in *Streptococcus pneumoniae* type 1. *Mol. Microbiol.* **31,** 703–713 CrossRef Medline
44. Berger, E., Arabshahi, A., Wei, Y., Schilling, J. F., and Frey, P. A. (2001) Acid-base catalysis by UDP-galactose 4-epimerase: correlations of kinetically measured acid dissociation constants with thermodynamic values for tyrosine 149. *Biochemistry* **40,** 6699–6705 CrossRef Medline
45. Liu, Y., Thoden, J. B., Kim, J., Berger, E., Gulick, A. M., Ruzicka, F. J., Holden, H. M., and Frey, P. A. (1997) Mechanistic roles of tyrosine 149 and serine 124 in UDP-galactose 4-epimerase from *Escherichia coli*. *Biochemistry* **36,** 10675–10684 CrossRef Medline
46. Chen, M., Chen, L. L., Zou, Y., Xue, M., Liang, M., Jin, L., Guan, W. Y., Shen, J., Wang, W., Wang, L., Liu, J., and Wang, P. G. (2011) Wide sugar substrate specificity of galactokinase from *Streptococcus pneumoniae* TIGR4. *Carbohydr. Res.* **346,** 2421–2425 CrossRef Medline

47. Kabsch, W. (2010) XDS. *Acta Crystallogr. D Biol. Crystallogr.* **66,** 125–132 CrossRef Medline
48. Vagin, A., and Teplyakov, A. (1997) MOLREP: an automated program for molecular replacement. *J. Appl. Crystallogr.* **30,** 1022–1025 CrossRef
49. Emsley, P., Lohkamp, B., Scott, W. G., and Cowtan, K. (2010) Features and development of Coot. *Acta Crystallogr. D Biol. Crystallogr.* **66,** 486–501 CrossRef Medline
50. Murshudov, G. N., Skubák, P., Lebedev, A. A., Pannu, N. S., Steiner, R. A., Nicholls, R. A., Winn, M. D., Long, F., and Vagin, A. A. (2011) REFMAC5 for the refinement of macromolecular crystal structures. *Acta Crystallogr. D Biol. Crystallogr.* **67,** 355–367 CrossRef Medline
51. DeLano, W. L. (2012) *The PyMOL Molecular Graphics System*, version 1.5.0.1, Schrödinger, LLC, New York
52. Chovancova, E., Pavelka, A., Benes, P., Strnad, O., Brezovsky, J., Kozlikova, B., Gora, A., Sustr, V., Klvana, M., Medek, P., Biedermannova, L., Sochor, J., and Damborsky, J. (2012) CAVER 3.0: a tool for the analysis of transport pathways in dynamic protein structures. *PLoS Comput. Biol.* **8,** e1002708 CrossRef Medline

Supplementary Information

Crystallographic snapshots of UDP-glucuronic acid 4-epimerase ligand binding, rotation and reduction

Luca Giacinto Iacovino[1], Simone Savino[2,4], Annika J.E. Borg[2], Claudia Binda[1], Bernd Nidetzky[2,3*], and Andrea Mattevi[1*]

[1]Department of Biology and Biotechnology "Lazzaro Spallanzani", University of Pavia, Via Ferrata 9, 27100, Pavia, Italy

[2]Institute of Biotechnology and Biochemical Engineering, Graz University of Technology, NAWI Graz, Petersgasse 12, 8010 Graz, Austria

[3]Austrian Centre of Industrial Biotechnology, Petersgasse 14, 8010 Graz, Austria

[4]Current address: Faculty of Science and Engineering Biotechnology, Gron Inst Biomolecular Sciences & Biotechnology, Nijenborgh 4, 9747 AG Groningen, The Netherlands

*Correspondence to bernd.nidetzky@tugraz.at and andrea.mattevi@unipv.it

Supplementary Video S1

The "swing & flip" movement as inferred from the structures of the enzyme bound to the substrate (UDP-glucuronic acid) and product (UDP-galacturonic acid). The orientations shown in videos S1A and S1B are the same as in Figures 3A and 5A and Figures 3B and 5B, respectively.

Synthesis of UDP-4-deoxy-4-fluoro-α-D-glucuronic acid

The synthesis strategy is indicated in **Scheme S1**. The reaction mixture (10 ml) contained 50 mM 4-deoxy-4-fluoro-α-D-glucose (91 mg, 0.5 mmol), 50 mM ATP (275.5 mg, 0.5 mmol) and 6 mM $MgCl_2$ (12.3 mg, 0.06 mmol) dissolved in 50 mM Tris/HCl buffer (pH 8). 4 mg/ml (86 μM) GalKSpe4 was added and the reaction mixture was incubated at 37 °C for 20 h. The progress of the phosphorylation reaction was analyzed on TLC (**Figure S1a**) by using a mixture of butanol, acetic acid and H_2O (2:1:1, respectively) as an eluent. The phosphorylated product was visualized by staining with a mixture consisting of thymol (0.5 w/v), ethanol (95 v/v) and concentrated H_2SO_4 (5 v/v). The nucleotidyl transfer reaction was initiated by adding 40 mM UTP (220 mg, 0.4 mmol), 1.3% (w/v) BSA, 0.42 mg/ml UGPase (6.4 mg) and 0.17 mg/ml iPPase (2.6 mg) and the reaction mixture was incubated at 30 °C for 4.5 h, until all the sugar 1-phosphate was converted to the corresponding UDP-sugar. The reaction mixture was analyzed on HPLC (**Figure S1b**). After confirming the completeness of the reaction on HPLC, the final oxidation step towards UDP-4-deoxy-4-fluoro-GlcA was initiated by the addition of 2 mM NAD^+ (13.2 mg, 0.02 mmol), 40 mM sodium pyruvate (44 mg, 0.4 mmol), 20 U/ml LDH (200 U) and 9 mg/ml hUGDH (90 mg), and the reaction was incubated at 37 °C for 24 h until no further conversion to UDP-4-deoxy-4-fluoro-GlcA was observed (followed on HPLC, **Figure S1c**). The enzymes were removed with Vivaspin Turbo centrifugal filter tubes (10 kDa cut-off, Sartorius) prior to column purification of the nucleotide sugar.

UDP-4-deoxy-4-fluoro-GlcA was separated from the other components by one enzymatic and four chromatographic purification steps. The first chromatographic purification was performed using ÄKTA FPLC system (GE Healthcare) connected to a 125 ml TOYOPEARL SuperQ-650M anion exchange column (GE Healthcare) and a 10 ml sample loop. 20 mM sodium acetate solution (pH 4.3) was used as

binding buffer. Compounds bound to the column were eluted with a step-wise gradient of 1 M sodium acetate buffer at pH 4.3. The steps were: 270 ml of 20 mM NaOAc, 200 ml of 300 mM NaOAc and 720 ml of NaOAc from 300 to 1000 mM with gradient for 240 min. Fractions containing the desired product were detected via UV absorption (λ = 254 nm), identified by HPLC and combined prior to concentrating under reduced pressure on a Laborota 4000 rotary evaporator (Heidolph, Schwabach, Germany) at 40 °C to a final volume of approximately 10 ml. UDP-4-deoxy-4-fluoro-GlcA was co-eluted with UTP and therefore further purification steps were needed. NaOAc was removed from the concentrated product mixture using an ÄKTA FPLC connected to Superdex G-10 size-exclusion column (GE Healthcare) and 5 ml sample loop. The product was detected based on its UV absorption at 254 nm and eluted with deionized water. The product-containing fractions were combined and concentrated under reduced pressure at 40 °C to a final volume of 6 ml. The pH of the product mixture was adjusted to 7.0 with NaOH and 10 U/ml CIP (60 U) was added to degrade the terminal phosphates (UTP) while leaving the nucleotide sugar intact. The dephosphorylation was performed at 30 °C and followed on HPLC every 2 h for 24 h, until all the UTP was degraded (**Figure S2**). The product mixture was subjected to a second round of anion exchange chromatographic purification (**Figure S3a**) with step-wise gradient: 20 mM NaOAc (until uridine eluted), 150 mM NaOAc (until UMP eluted) and 550 mM NaOAc (until UDP-4-deoxy-4-fluoro-GlcA eluted). The fractions containing the desired product were collected, concentrated in rotary evaporator and loaded into the size-exclusion column (for acetate removal, **Figure S3b**) as described above. Residual H_2O was removed by lyophilization (Christ Alpha 1-4 lyophilizer, B. Braun Biotech International, Melsungen, Germany), and the pure nucleotide sugar obtained as white powder. The purity and identity of UDP-4-deoxy-4-fluoro-GlcA were confirmed on HPLC (**Figure S4a**) and NMR (**Figure S4b,c**). The product was obtained in 66.2 mg (23%) yield and >95% purity.

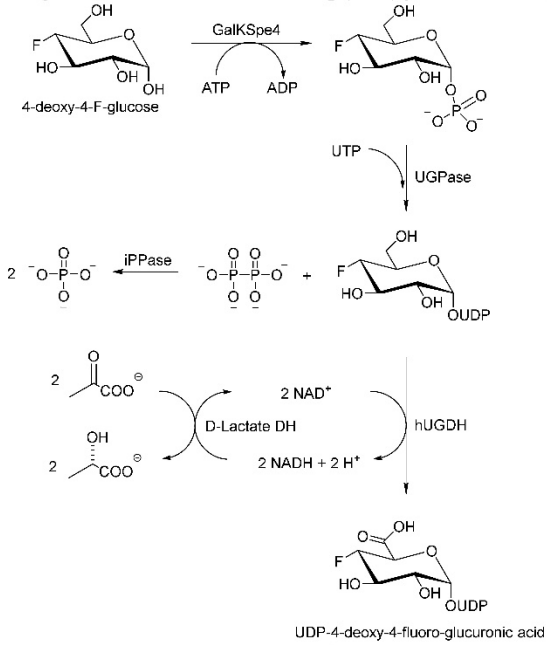

Scheme S1. Schematic representation of the one-pot synthesis of UDP-4-deoxy-4-fluoro-α-D-glucuronic acid starting from 4-deoxy-4-fluoro-α-D-glucose. ATP = adenosine-5'-triphosphate, ADP = adenosine-5'-diphosphate, UTP = uridine-5'-triphosphate, UGPase = UDP-glucose pyrophosphorylase, iPPase =

inorganic pyrophosphatase, hUGDH = human UDP-glucose 6-dehydrogenase, D-lactate DH = D-lactate dehydrogenase.

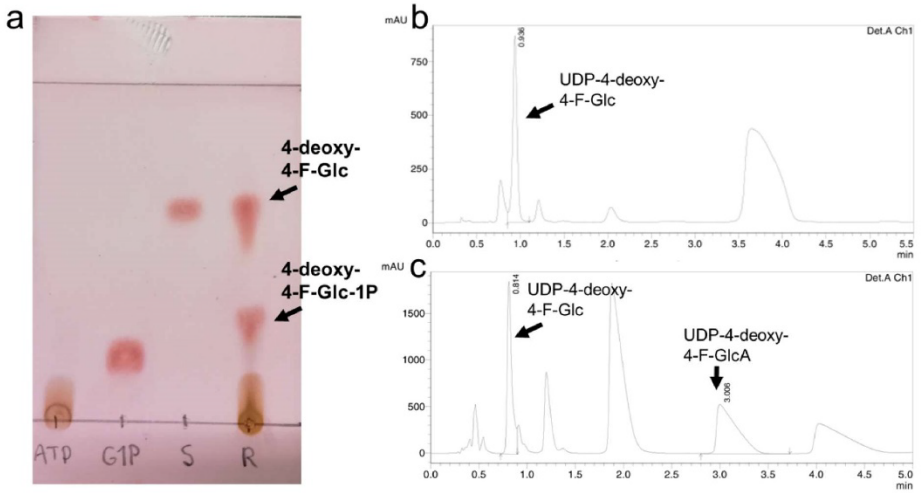

Figure S1. Three-step synthesis of UDP-4-deoxy-4-fluoro-α-D-glucuronic acid. **a**. TLC of the phosphorylation reaction of 4-deoxy-4-fluoro-Glc yielding 4-deoxy-4-fluoro-Glc-1-phosphate catalyzed by anomeric kinase GalKSpe4. **b**. HPLC chromatogram of the nucleotidyl transfer reaction forming UDP-4-deoxy-4-fluoro-Glc as a product. **c**. HPLC chromatogram of the oxidation of UDP-4-deoxy-4-fluoro-Glc to UDP-4-deoxy-4-fluoro-GlcA catalyzed by hUGDH.

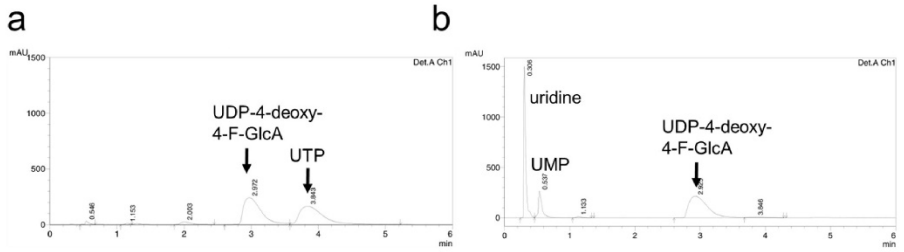

Figure S2. CIP digestion for UTP removal from the product mixture of UDP-4-deoxy-4-fluoro-GlcA. **a**. HPLC chromatogram after 1 min of CIP digestion. **b**. HPLC chromatogram after 24 h of CIP digestion.

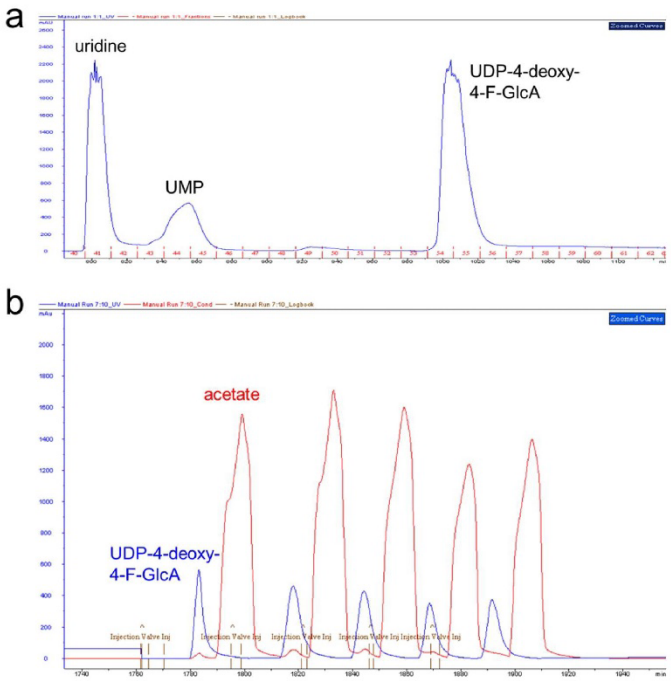

Figure S3. ÄKTA chromatograms of the column chromatographic purification steps of UDP-4-deoxy-4-fluoro-GlcA. **a**. Anion exchange chromatogram recorded during the purification of UDP-4-deoxy-4-fluoro-GlcA. The blue line corresponds to the UV signal at 280 nm. **b**. Chromatogram recorded during the desalting step of UDP-4-deoxy-4-fluoro-GlcA. The blue line corresponds to the UV-signal of the desired product (at 280 nm), the red line corresponds to the conductivity signal of acetate.

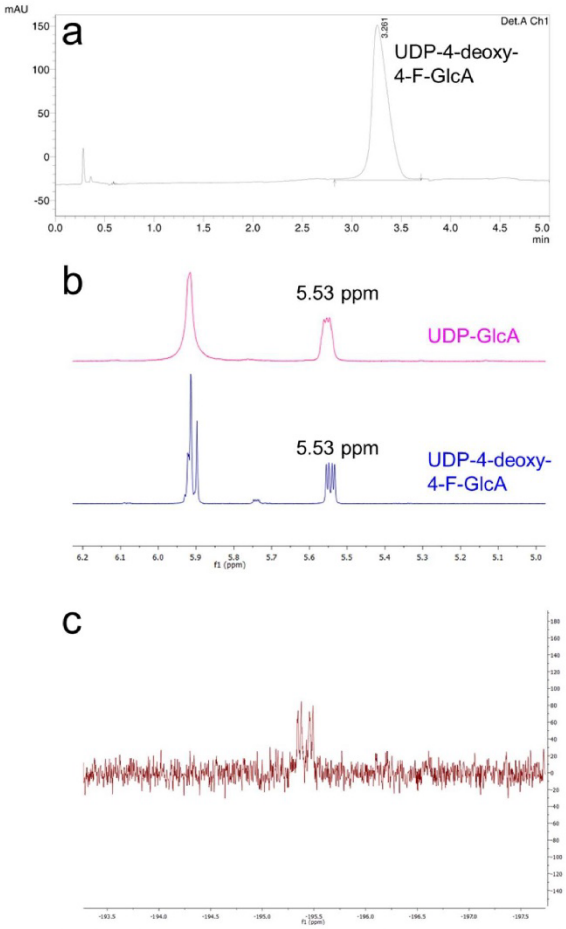

Figure S4. Analysis of the identity and purity of isolated UDP-4-deoxy-4-fluoro-GlcA. **a**. HPLC chromatogram of purified UDP-4-deoxy-4-fluoro-GlcA. **b**. Snapshot of the anomeric region of ^{1}H-NMR spectrum (D_2O, Varian INOVA 500-MHz NMR spectrometer) of UDP-4-deoxy-4-fluoro-GlcA (blue). UDP-GlcA is shown as a reference (pink). **c**. ^{19}F-NMR spectrum of UDP-4-deoxy-4-fluoro-GlcA confirming the attachment of fluorine at C4'.

Stereo-Electronic Control of Reaction Selectivity in Short-Chain Dehydrogenases: Decarboxylation, Epimerization, and Dehydration

Available online at www.sciencedirect.com

ScienceDirect

Current Opinion in Chemical Biology

Stereo-electronic control of reaction selectivity in short-chain dehydrogenases: Decarboxylation, epimerization, and dehydration

Annika J. E. Borg[1], Koen Beerens[2], Martin Pfeiffer[1,3], Tom Desmet[2,3] and Bernd Nidetzky[1,3]

Abstract

Sugar nucleotide–modifying enzymes of the short-chain dehydrogenase/reductase type use transient oxidation–reduction by a tightly bound nicotinamide cofactor as a common strategy of catalysis to promote a diverse set of reactions, including decarboxylation, single- or double-site epimerization, and dehydration. Although the basic mechanistic principles have been worked out decades ago, the finely tuned control of reactivity and selectivity in several of these enzymes remains enigmatic. Recent evidence on uridine 5′-diphosphate (UDP)-glucuronic acid decarboxylases (UDP-xylose synthase, UDP-apiose/UDP-xylose synthase) and UDP-glucuronic acid-4-epimerase suggests that stereo-electronic constraints established at the enzyme's active site control the selectivity, and the timing of the catalytic reaction steps, in the conversion of the common substrate toward different products. The mechanistic idea of stereo-electronic control is extended to epimerases and dehydratases that deprotonate the Cα of the transient keto-hexose intermediate. The human guanosine 5′-diphosphate (GDP)-mannose 4,6-dehydratase was recently shown to use a minimal catalytic machinery, exactly as predicted earlier from theoretical considerations, for the β-elimination of water from the keto-hexose species.

Addresses

[1] Institute of Biotechnology and Biochemical Engineering, Graz University of Technology, NAWI Graz, 8010, Graz, Austria

[2] Centre for Synthetic Biology, Department of Biotechnology, Ghent University, 9000, Ghent, Belgium

[3] Austrian Centre of Industrial Biotechnology (acib), 8010, Graz, Austria

Corresponding author: Nidetzky, Bernd (bernd.nidetzky@tugraz.at)

Current Opinion in Chemical Biology 2021, **61**:43–52

This review comes from a themed issue on **Biocatalysis and Biotransformation**

Edited by **Bernd Nidetzky** and **Tom Desmet**

For a complete overview see the Issue and the Editorial

https://doi.org/10.1016/j.cbpa.2020.09.010

Keywords

SDR, Short-chain dehydrogenase/reductase, Decarboxylase, Epimerase, Dehydratase, Transient oxidation-reduction, Stereo-electronic effect.

Introduction

Transient oxidation–reduction is a central mechanistic principle of sugar nucleotide–modifying enzymes to achieve a variety of biosynthetically important transformations [1–5]. These transformations notably involve epimerization, decarboxylation, and dehydration (Figure 1) [3,4,6]. The enzymes catalyzing these reactions share common membership to the short-chain dehydrogenase/reductase (SDR) protein superfamily [4]. They are often referred to as 'extended SDRs' for the additional features of structure and function they involve compared with the prototypical SDR oxidoreductase [4]. They generally use a tightly bound NAD^+ or $NADP^+$ cofactor and are equipped with the basic SDR catalytic machinery (a highly conserved Asn/Ser/Tyr/Lys tetrad of residues) to facilitate oxidation–reduction [4]. The active sites of extended SDRs are often expanded by residues fulfilling deprotonation–protonation types of catalytic function [4]. Thus, the extended SDRs integrate unique reactivities (e.g., epimerization [2,7–10,11*,12,13**], β-elimination of water [14**,15*,16–18], aldol cleavage for ring opening [19*,20**], decarboxylation [20**,21,22**]) into a cycle of hydride transfer to and from the nicotinamide cofactor. Oxidation of the sugar nucleotide serves the essential role of activating the substrate for further transformations. Except in hexose nucleotide 4,6-dehydratases as discussed later, the hydride is delivered back to the same substrate carbon from which it was abstracted. The reduction is usually stereospecific, except in C2- and C4-epimerases (Figure 1, UGAepi reaction) that require nonstereospecific reduction of the corresponding 2- or 4-keto-hexose intermediate. The C2/C4-epimerases must add the feature of free rotation of the transient intermediate to enable delivery of the hydride from either face of the carbonyl group [2,5,7,10,12,13**,23,24*]. Mechanistic proposals have been worked out in considerable detail for catalytic

Figure 1

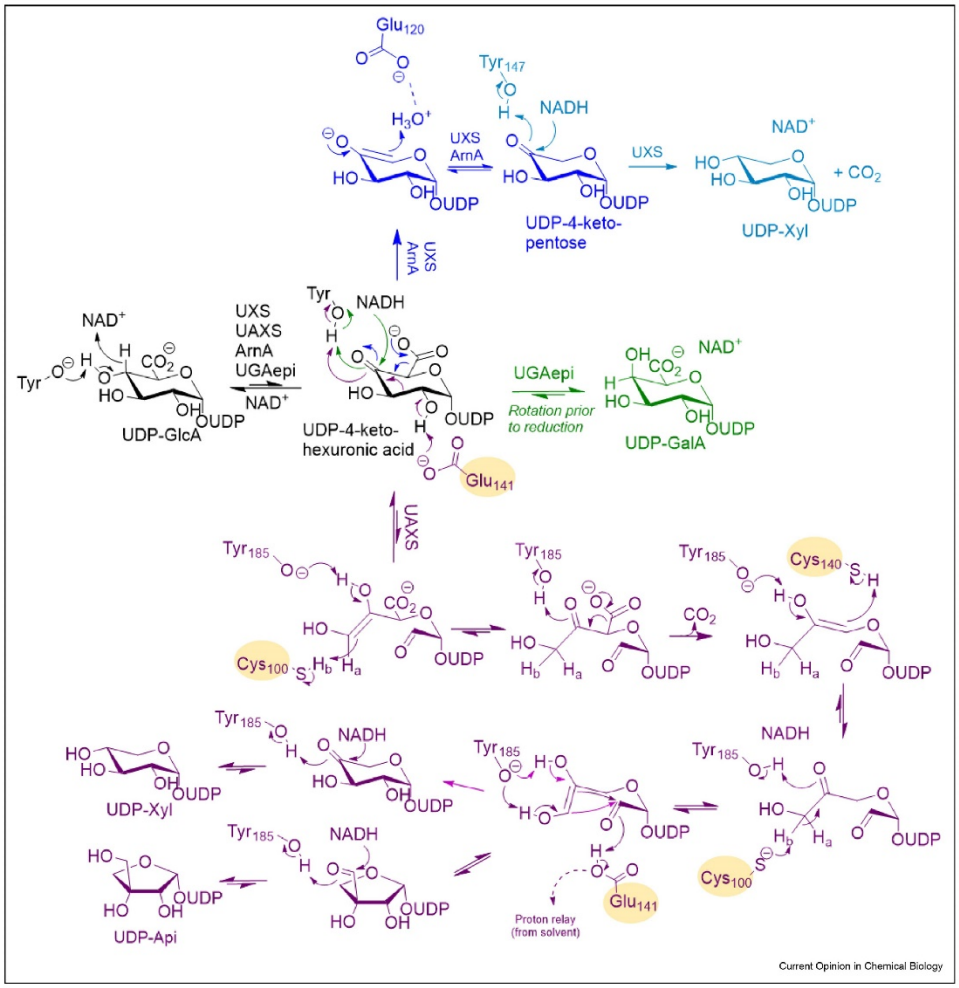

Schematic representation of the reaction mechanisms of UAXS (black/purple) [20**], UXS (black/dark blue/light blue) [22**], UGAepi (black/green) [13**], and ArnA (black/dark blue) [21]. The key residues responsible for the acid/base catalysis on the active site of UAXS are highlighted with yellow circles. UDP, uridine 5'-diphosphate; UAXS, UDP-xylose synthase; UGAepi, UDP-GlcA 4-epimerase; UXS, UDP-xylose synthase.

epimerization [2,10,13**,23,24*,25,26,27**], decarboxylation [19*,20**,21,22**], and dehydration [14**,15*,18] based on structural and biochemical studies performed on different enzymes over decades.

Despite this, the finely tuned control of reactivity and selectivity in several of these enzymes still remains a mystery. A biologically important and mechanistically striking example is represented by uridine 5'-diphosphate-glucuronic acid (UDP-GlcA), which is the common substrate for epimerase and decarboxylase types of extended SDRs (Figure 1) [19*,20**,21,22**]. The UDP-GlcA 4-epimerase (UGAepi) (EC 5.1.3.6) catalyzes the reversible interconversion of UDP-GlcA

and UDP-galacturonic acid (UDP-GalA) [7,13**,27**,28–31]. The UDP-GlcA decarboxylases (UDP-xylose synthase [UXS] EC 4.1.1.35 [22**,32]; UDP-apiose/UDP-xylose synthase [UAXS], EC 4.1.1 [19*,20**,33]; UDP-GlcA decarboxylase ArnA, EC 1.1.1.305 [21,34]) convert UDP-GlcA into different UDP-pentose products (Figure 1).

Recent studies suggest an important role for stereo-electronic control by the enzymes to steer a perfectly selective transformation of UDP-GlcA, leading to different products from the same substrate [13**,20**,22**]. The studies also indicate that stereo-electronic constraints at the active site enable the decarboxylase enzymes to achieve a unique timing of their catalytic reaction steps [20**]. The mechanistic idea of stereo-electronic control is extended to epimerases and dehydratases that deprotonate the Cα of the transient keto-hexose intermediate. In addition, the human guanosine 5'-diphosphate (GDP)-mannose 4,6-dehydratase is discussed here for the recent mechanistic insight it has provided into the elimination mechanism. Based on structure snapshots from the reaction coordinate, the enzyme was shown to use a minimal catalytic machinery comprised of just two active-site groups, exactly as predicted earlier from theoretical considerations, for the β-elimination of water from the keto-hexose species [14**].

Extended SDR enzymes for conversion of UDP-GlcA and their proposed catalytic mechanisms

The proposed reaction paths and the basic catalytic mechanisms of UGAepi, UXS, ArnA, and UAXS for the conversion of UDP-GlcA are shown in Figure 1. Each reaction is initiated by transient oxidation at substrate C4. Hydride abstraction to NAD^- is facilitated by tyrosine (from the conserved SDR catalytic tetrad) functioning as the general base [13**,20**,21,22**,27**].

UXS and ArnA promote decarboxylation of the UDP-4-keto-hexuronic acid intermediate [21,22**]. UXS reduces the resulting UDP-4-keto-pentose stereospecifically to UDP-xylose [22**]. Contrary to UXS, ArnA lacks a tightly bound nicotinamide cofactor and must bind NAD^- from solution [21]. Interestingly, ArnA reaction with UDP-GlcA stops at the UDP-4-keto-pentose, which is then used by a different enzyme (ArnB) in a transamination reaction with L-glutamic acid to form UDP-4-amino-4-deoxy-L-arabinose [35,36]. ArnA releases the NADH formed [21]. In UXS and ArnA, a conserved glutamic acid residue is involved in proton transfer to C5 during decarboxylation and/or fixing the substrate in place for the enzymatic conversion (Figure 2a) [21,22**]. The Glu is also conserved in hexose nucleotide 4,6-dehydratases, in which it plays the mechanistically comparable role of deprotonation-protonation at C5 [14**,15*,18,37], as discussed later.

The Glu is lacking in UGAepi (Figure 2a). Structurally, UGAepi resembles the well-characterized UDP-galactose 4-epimerase in that it provides fully formed binding pockets for NAD^- and UDP [27**]. From the perspective of molecular structure, therefore, any repositioning of the two molecules in the course of the UGAepi catalytic cycle is highly unlikely. To perform a nonstereospecific reduction of the C4 carbonyl group, UGAepi must therefore enable free rotation of the 4-keto-hexuronic acid moiety. An interesting mechanistic challenge for UGAepi is to combine this free rotation requirement with proper protection of the chemically labile β-keto-acid intermediate against decarboxylation [13**].

The reaction of UAXS leading to UDP-apiose is unusually complex to be carried out by a single active site. The proposed mechanism involves a retro-aldol reaction for ring opening of the 4-keto-hexuronic acid intermediate [19*,20**]. The conserved Glu (Figure 2a) adopts a unique role to facilitate deprotonation of the 2-OH during aldol cleavage, as shown in Figure 1 [20**]. Two cysteine residues participate in the subsequent decarboxylation and ring-closure steps (Figure 1) [20**]. The cysteines of UAXS are not conserved in UXS and ArnA. However, cysteine residues are involved in deprotonation–protonation steps at sugar carbon in reactions of GDP-mannose 3,5-epimerase [38*] and GDP-L-fucose synthetase [39*]. Both enzymes also belong to the extended SDRs. The UAXS (from *Arabidopsis thaliana*) was shown to not catalyze ring opening on an isolated UDP-4-keto-pentopyranose intermediate [20**]. Therefore, timing of the catalytic steps, such that the ring opening occurs before the decarboxylation, appears to be essential. Ring closure establishes the ring contraction in a reversible aldol reaction. Ring closure without ring contraction appears to be effectively irreversible. Reduction leads to UDP-apiose and UDP-xylose in a ratio that seems to depend on both the enzyme and the reaction conditions used [20**].

Evidence for stereo-electronic control in reactions of UXS, UGAepi, and UAXS

As shown in Figure 1, the catalytic paths of UAXS, UXS, ArnA, and UGAepi diverge at the UDP-4-keto-hexuronic acid intermediate. To appreciate the enzymes' individual ways of handling the intermediate (a labile β-keto acid species), it is relevant to consider chemical requirements for decarboxylation in the context of a six-membered ring system. Generally, decarboxylation is stereo-electronically favored when the dihedral angle between the C=O bond and the cleaved C–C bond is ~90° (Figure 2b) [40,41]. In the

Current Opinion in Chemical Biology 2021, 61:43–52

www.sciencedirect.com

Figure 2

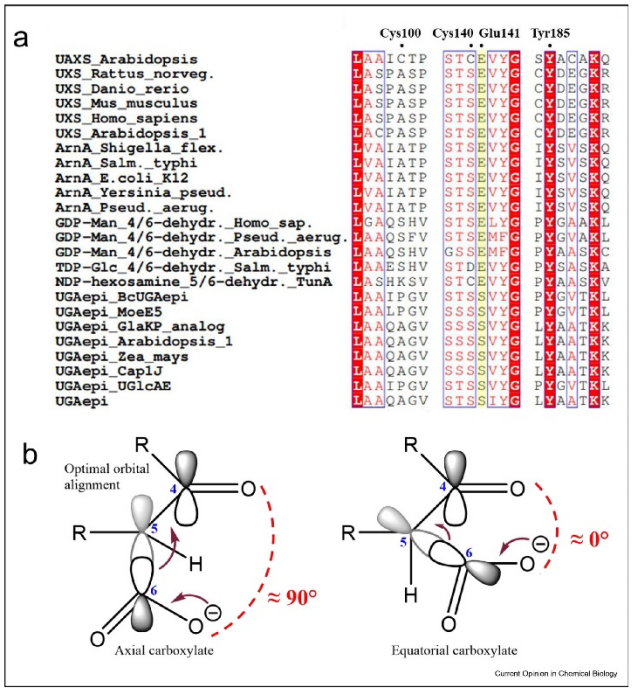

Sequence comparison of SDR epimerases, decarboxylases and dehydratases (a) and illustration of orbital alignment for decarboxylation of a β-keto acid (b). **(a)** A partial multiple sequence alignment of UAXS, UXS, ArnA, UGAepi, and NDP-sugar dehydratases. The key amino acids for the catalysis in UAXS are labeled on the top of the alignment. The conserved Glu residue in decarboxylases and dehydratases (Ser in UGAepis) is highlighted in yellow. **(b)** Orbital alignment in decarboxylation of a β-keto acid with the axial (left) and equatorial (right) carboxylate moiety. The C5 p-orbital on the incipient 4,5-enolate is shown in light gray. GDP-Man, guanosine 5′-diphosphate-mannose; TDP-Glc, thymidine 5′-diphosphate glucose; UAXS, UDP-xylose synthase; UGAepi, UDP-GlcA 4-epimerase; UXS, UDP-xylose synthase.

UDP-4-keto-hexuronic acid intermediate, a dihedral of ~90° requires the carboxylate group to be positioned axially. Chemical studies show that optimal orbital alignment for decarboxylation involves a continuous overlap, via hyperconjugation and resonance, from the breaking C–C bond and the π-orbital of the carbonyl (C4=O) group [41–43]. In the stereo-electronically optimal case for the enzymatic decarboxylation (axial carboxylate), the breaking C5–C6 bond is roughly orthogonal to the plane of the C5–C4=O system, allowing for productive σ–π delocalization [43] to enable good overlap of the π-orbital system of the carbonyl carbon (C4) with the developing C5 p-orbital in the incipient 4,5-enolate [41,43] (Figure 2b). To bring the carboxylate into an axial position at the enzyme's active site, a binding energy–driven distortion from the pyranose chair conformation may be necessary. The relaxed chair conformation of the 4-keto-hexuronic acid features an equatorial carboxylate with a dihedral angle of ~0°. The equatorial carboxylate thus provides stereo-electronic constraints nonoptimal for decarboxylation. For an enzymatic path to exclude (UGAepi), or to delay (UAXS), the decarboxylation, therefore, a stereo-electronic rational to maintain an equatorial carboxylate is thus provided. The mechanistic idea of differential stereo-electronic control in epimerase and decarboxylase reactions of UDP-GlcA is supported by a comparison of UXS and UGAepi. Binding of UDP-GlcA by UAXS is also consistent with the overall stereo-electronic argument. The importance of proper orbital alignment for promoting or preventing decarboxylation has been recognized over decades in studies of pyridoxal 5'-phosphate (PLP)-dependent enzymes, where the enzyme applies stereo-electronic constraints to 'choose' between decarboxylation and transamination/racemization [42,44–46].

Figure 3

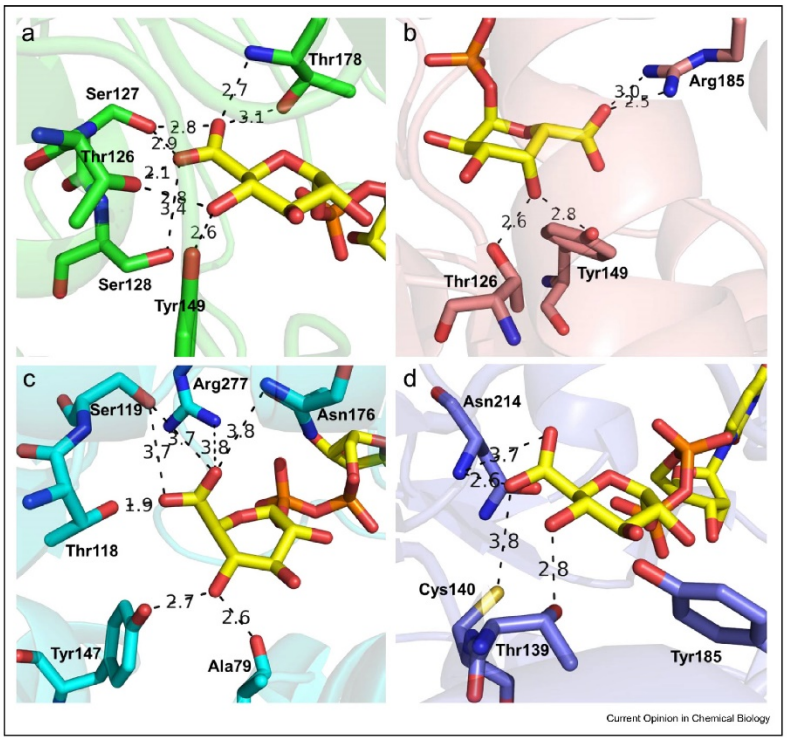

Active site close-ups of BcUGAepi **(a,b)**, UXS **(c)**, and UAXS **(d)** showing the interactions with the carboxylate and C4–OH of the substrate (yellow carbons). **(a)** The substrate complex of BcUGAepi (green; PDB: 6Z73, [27**]) with UDP-GlcA. The carboxylate moiety is positioned equatorially. **(b)** The product complex of BcUGAepi (salmon; PDB: 6Z75, [27**]) with UDP-GalA showing the equatorial carboxylate. Structure of UXS (cyan; PDB: 2B69, [22**]) highlighting the perfectly axial carboxylate moiety of UDP-GlcA. **(c)** The substrate complex of UAXS (blue; PDB: 6H0P, [20**]) showing the equatorial carboxylate of UDP-GlcA.

Structures of UGAepi bound with UDP-GlcA (Figure 3a) and UDP-GalA (Figure 3b) show the pyranose ring in an undistorted $^4C_1$ conformation, which places the carboxylate group equatorially [27**]. In each structure, the carboxylate is accommodated within a tight network of hydrogen bonds. The reactive 4-OH of the substrate/product is well aligned with the catalytic residues of the enzyme. Threonine from the SDR catalytic triad orients the 4-OH for proton abstraction by tyrosine. Interestingly, the threonine is also close to the substrate/product carboxylate. Besides establishing stereo-electronic conditions to disfavor decarboxylation, binding of the carboxylate group could arguably contribute to precise positioning of the substrate for catalysis. Binding constraints from the active site pose a conundrum for UGAepi given the requirement for free rotation of the 4-keto-hexuronic acid intermediate for epimerization. Computational analysis will be important to elucidate dynamic features of the catalytic reaction. The conformational rearrangements associated with the rotation have now been captured at high resolution in the crystal [27**].

For UXS, the conformation of the Michaelis complex was derived from a high-resolution crystal structure of the human enzyme bound with NAD^+ and UDP. The UDP-GlcA was modeled into the active site [22**]. Molecular dynamics computational studies revealed that to achieve a plausible positioning of GlcA for catalysis the pyranose $^4C_1$ chair had to be distorted. A $B_{O,3}$ boat conformation, placing the carboxylate in an almost perfect axial position 'ready for decarboxylation', was found to yield a seemingly proper alignment between the reactive groups on the substrate (UDP-GlcA), cofactor (NAD^+), and the catalytic groups on the enzyme (Figure 3c) [22**]. UXS provides fewer interactions with the substrate carboxylate than UGAepi, and binding of the carboxylate lacks the direct connection to the immediate catalytic machinery. The crystal structure of ArnA bound with UDP-GlcA shows an undistorted chair conformation for the pyranose ring with the carboxylate in the equatorial position. However, the substrate is not positioned for catalytic oxidation at C4 to occur via the canonical SDR mechanism, and, therefore, a nonproductive enzyme–substrate complex appears to have been captured in the ArnA crystal [21].

The special case of UAXS: precise timing of decarboxylation in multistep SDR catalysis

Similar as in UXS, molecular dynamics simulations had to be done on the experimental enzyme crystal structure (the C100A variant of *A. thaliana* UAXS bound with NADH and UDP-GlcA) to identify the plausible conformation of the Michaelis complex [20**]. The substrate-bound conformation of the enzyme's active site is unusually flexible, with the pyranose ring pucker changing substantially along simulated trajectories. The enzyme complex conformations featuring a plausible positioning of UDP-GlcA for the initial catalytic step (oxidation at C4) all have the carboxylate group in a closely equatorial position, as shown in Figure 3d. This supports the particular timing of UAXS catalytic steps that delays the decarboxylation of the β-keto-acid until after the ring opening between C2 and C3 has happened. The ring-opened intermediate can then position the carboxylate moiety for suitable orbital alignment to meet the stereo-electronic requirements for efficient decarboxylation [20**].

Stereo-electronic considerations extended to other epimerases and dehydratases

In pyranose ring systems, the α-proton of a ketone is more easily abstracted (i.e., becomes more acidic) when it is positioned axially [38*,47]. Concerning the orbital alignment optimal for deprotonation, effectively the same considerations (σ–π delocalization) apply as for decarboxylation [41,43,47]. Structural and mechanistic studies of hexose nucleotide 4,6-dehydratases (e.g., thymidine 5'-diphosphate (dTDP)-glucose 4,6-dehydratase; cytidine 5'-diphosphate (CDP)-glucose 4,6-dehydratase; GDP-mannose 4,6-dehydratases) [14**,37,48–54] and epimerases acting on the α-carbon(s) (e.g., GDP-mannose 3,5-epimerase [38*]; GDP-L-fucose synthetase [39*,55]) suggest that each enzyme applies stereo-electronic control. Changes in sugar ring pucker can be important to meet the stereo-electronic requirements for efficient deprotonation/protonation, as shown for GDP-mannose 3,5-epimerase [38*,39*].

Recent study of the human GDP-mannose 4,6-dehydratase has rekindled mechanistic considerations of Gerlt and Gassman [56*] for the enzymatic β-elimination of a ketone [14**,56*]. Their suggestion was that the lowest energy pathway for the reaction is a stepwise general acid/general base–catalyzed formation of an enol intermediate followed by 1,4-(E2-like)-elimination from the enol (not an E1cB mechanism via an enolate) [56*]. They also considered that, given suitable geometry of the enzyme–substrate complex, as shown in Figure 4a, the conjugate acid of the base catalyzing the enol formation could also catalyze expulsion of the β-substituent [56*]. The proposed mechanism implies a *syn* stereochemical course for the β-elimination reaction and suggests two as the minimal number of functional groups required for efficient catalysis [56*]. However, precatalytic and postcatalytic complex structures of the human GDP-mannose 4,6-dehydratase (hGMD) suggest that the enzyme represents a perfect realization of the chemical principle in its most parsimonious form [14**]. The proposed enzymatic mechanism is shown in Figure 4b. Concerted catalysis by Tyr179 and Glu157 is involved in the formation of the enol intermediate. Molecular dynamics simulations revealed the essential side chain

Figure 4

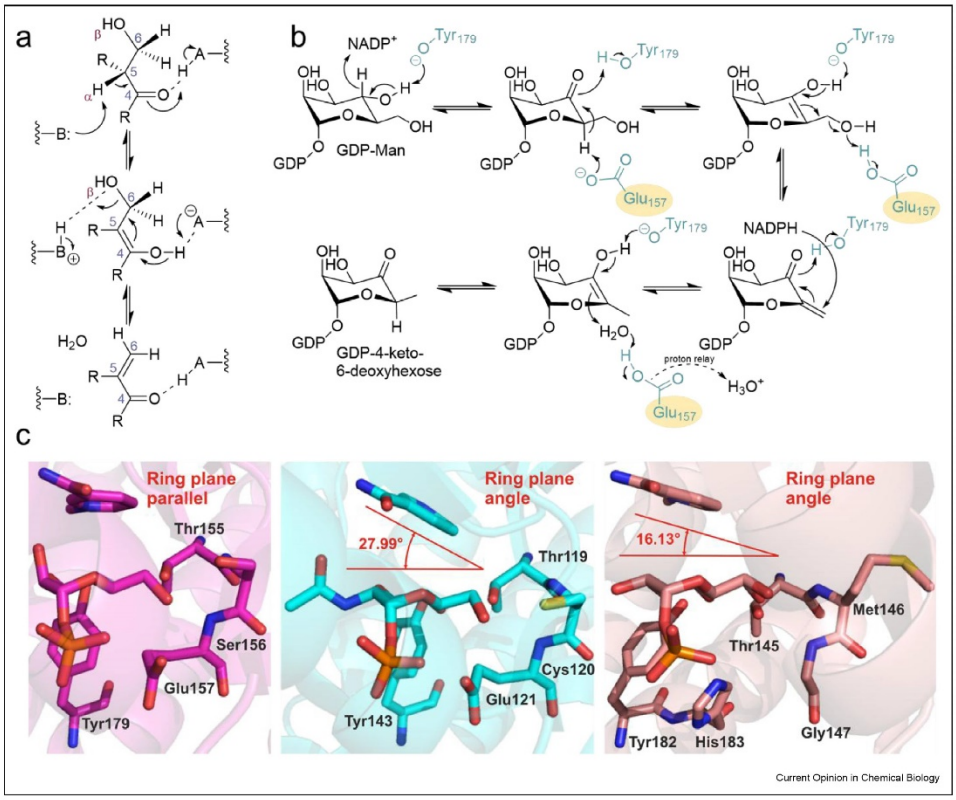

The proposed catalytic mechanism of dehydration by hGMD (a, b) and active site close ups of hGMD, TunA and SQD1 (c). **(a)** The **stepwise** mechanism **of β-el**imination of water from a ketone as implemented into the hGMD active site. **(b)** The mechanism of guanosine 5'-diphosphate-mannose (GDP-Man) 4,6-dehydration catalyzed by hGMD [14**]. **(c)** Relative positions and angles of substrates and cofactors in the active sites of hGMD (purple, PDB: 6GPJ, [14**]), TunA (cyan, PDB: 3VPS, [15*]), and SQD1 (salmon, PDB: 1QRR, [16]).

conformational flexibility for Glu157, so that it could function as a catalytic base during the enol formation and, in conjugate acid form, as a catalytic acid during the expulsion of water [14**]. Further reaction to product proceeds in two steps, representing in opposite order the reversal of the previous catalytic steps of oxidation and enolization [14**]. In the UDP-GlcNAc 5,6-dehydratase (TunA) [15*] and in the UDP-sulfoquinose synthase (SQD1, Agl3) [16–18], the initial oxidation and β-elimination are catalyzed analogously as described for the 4,6-dehydratases, whereas SQDs utilize His instead of Asp as the general acid/base catalyst. However, reduction of the C4-carbonyl, instead of the 5,6-ene, results in the formation of a 5,6-ene product or reaction intermediate in case of TunA and SQDs, respectively [15*–18]. The regioselectivity of the reduction is controlled by a fine-tuned alignment of nicotinamide ring of the NAD^+ cofactor relative to the sugar ring plane. In 4,6-dehydratases a parallel alignment is observed, allowing hydride abstraction from C4 and re-donation to C6. In contrast, a nonparallel alignment is observed in TunA and SQD1 with an angle of around 15–30° to each other, favoring re-donation of the hydride to C4 (Figure 4c) [14**,15*].

Conclusion

Constraining substrates into optimal conformations is an essential aspect of enzymatic catalysis [57]. Enzymes promote proper orientation of the orbitals to facilitate the desired biochemical transformation [42,57–59].

The contribution of stereo-electronic effects into enzyme-catalyzed reactions has been appreciated for decades, especially in context where enzymes apply stereo-electronic control to either allow or exclude certain reaction pathways [42,57,58,60,61]. Recent studies on SDR decarboxylases (UAXS, UXS, ArnA) [19*,20**,21,22**] and epimerases (UGAepi) [13**,27**] demonstrate how structurally closely related enzymes can utilize effectively the same substrate (UDP-GlcA) to catalyze different reaction pathways (decarboxylation, epimerization, aldol cleavage for ring opening) assisted by stereo-electronic control. This fascinating concept can be expanded to NDP-sugar dehydratases (hGMD, TunA, SQD) [14**,15*,18] from the SDR superfamily, where stereo-electronic constraints contribute to the regioselectivity of the reaction. In addition, the studies from the last few years highlight how essentially the same active site of the SDR epimerases, decarboxylases, and dehydratases is fine-tuned to perform different catalytic pathways. Realizing the importance of proper orbital alignment in (bio)chemical reactions is crucial for mechanistic enzymology and will be helpful in understanding the enzymatic mechanisms in future.

Declaration of competing interest

Nothing declared.

Acknowledgement

Financial support through the EpiSwitch and DeoxyBioCat projects, both jointly funded by the Austrian Science Fund (FWF; projects I 3247 and I 4516-B, respectively; B.N.) and the Fund for Scientific Research Flanders, Belgium (FWO-Vlaanderen, grant n° G0F3417N and G0A7520N, respectively; T.D.), are gratefully acknowledged.

References

Papers of particular interest, published within the period of review, have been highlighted as:

* of special interest
** of outstanding interest

1. Field RA, Naismith JH: **Structural and mechanistic basis of bacterial sugar nucleotide-modifying enzymes**. *Biochemistry* 2003, **42**:7637–7647.

2. Allard STM, Giraud M-F, Naismith JH: **Epimerases: structure, function and mechanism**. *Cell Mol Life Sci* 2001, **58**: 1650–1665.

3. Thibodeaux CJ, Melançon CE, Liu HW: **Unusual sugar biosynthesis and natural product glycodiversification**. *Nature* 2007, **446**:1008–1016.

4. Kavanagh KL, Jörnvall H, Persson B, Oppermann U: **Medium- and short-chain dehydrogenase/reductase gene and protein families: the SDR superfamily: functional and structural diversity within a family of metabolic and regulatory enzymes**. *Cell Mol Life Sci* 2008, **65**:3895–3906.

5. Samuel J, Tanner ME: **Mechanistic aspects of enzymatic carbohydrate epimerization**. *Nat Prod Rep* 2002, **19**:261–277.

6. Reiter W-D: **Biochemical genetics of nucleotide sugar interconversion reactions**. *Curr Opin Plant Biol* 2008, **11**:236–243.

7. Sun H, Ko TP, Liu W, Liu W, Zheng Y, Chen CC, Guo RT: **Structure of an antibiotic-synthesizing UDP-glucuronate 4-epimerase MoeE5 in complex with substrate**. *Biochem Biophys Res Commun* 2020, **521**:31–36.

8. Van Overtveldt S, Gevaert O, Cherlet M, Beerens K, Desmet T: **Converting galactose into the rare sugar talose with cellobiose 2-epimerase as biocatalyst**. *Molecules* 2018, **23**.

9. Gevaert O, Van Overtveldt S, Beerens K, Desmet T: **Characterization of the first bacterial and thermostable GDP-mannose 3,5-epimerase**. *Int J Mol Sci* 2019, **20**.

10. Van Overtveldt S, Verhaeghe T, Joosten HJ, van den Bergh T, Beerens K, Desmet T: **A structural classification of carbohydrate epimerases: from mechanistic insights to practical applications**. *Biotechnol Adv* 2015, **33**:1814–1828.

11. * Nam YW, Nishimoto M, Arakawa T, Kitaoka M, Fushinobu S: **Structural basis for broad substrate specificity of UDP-glucose 4-epimerase in the human milk oligosaccharide catabolic pathway of *Bifidobacterium longum***. *Sci Rep* 2019, **9**:11081.
This article provides an excellent discussion and overview for the substrate specificity determinants in UDP-glucose 4-epimerases.

12. Hallis TM, Zhao Z, Liu HW: **New insights into the mechanism of CDP-D-tyvelose 2-epimerase: an enzyme-catalyzing epimerization at an unactivated stereocenter**. *J Am Chem Soc* 2000, **122**:10493–10503.

13. ** Borg AJE, Dennig A, Weber H, Nidetzky B: **Mechanistic characterization of UDP-glucuronic acid 4-epimerase**. *FEBS J* 2020, https://doi.org/10.1111/febs.15478.
This article discusses and explains the impact of stereo-electronic control on the UDP-glucuronic acid 4-epimerase reaction.

14. ** Pfeiffer M, Johansson C, Krojer T, Kavanagh KL, Oppermann U, Nidetzky B: **A parsimonious mechanism of sugar dehydration by human GDP-mannose-4,6-dehydratase**. *ACS Catal* 2019, **9**: 2962–2968.
An important research paper deciphering the reaction mechanism of GDP-mannose 4,6-dehydration catalyzed by the minimal catalytic machinery of GDP-mannose 4,6-dehydratase.

15. * Wyszynski FJ, Lee SS, Yabe T, Wang H, Gomez-Escribano JP, Bibb MJ, Lee SJ, Davies GJ, Davis BG: **Biosynthesis of the tunicamycin antibiotics proceeds via unique exo-glycal intermediates**. *Nat Chem* 2012, **4**:539–546.
The authors describe the crystal structure and decipher the reaction mechanism of UDP-GlcNAc 5,6-dehydratase while discovering the determinants for the regioselectivity of the final reduction step.

16. Mulichak AM, Theisen MJ, Essigmann B, Benning C, Garavito RM: **Crystal structure of SQD1, an enzyme involved in the biosynthesis of the plant sulfolipid headgroup donor UDP-sulfoquinovose**. *Proc Natl Acad Sci U S A* 1999, **96**: 13097–13102.

17. Sanda S, Leustek T, Theisen MJ, Garavito RM, Benning C: **Recombinant *Arabidopsis* SQD1 converts UDP-glucose and sulfite to the sulfolipid head group precursor UDP-sulfoquinovose in vitro**. *J Biol Chem* 2001, **276**:3941–3946.

18. Zolghadr B, Gasselhuber B, Windwarder M, Pabst M, Kracher D, Kerndl M, Zayni S, Hofinger-Horvath A, Ludwig R, Haltrich D, *et al.*: **UDP-sulfoquinovose formation by *Sulfolobus acidocaldarius***. *Extremophiles* 2015, **19**:451–467.

19. * Eixelsberger T, Horvat D, Gutmann A, Weber H, Nidetzky B: **Isotope probing of the UDP-apiose/UDP-xylose synthase reaction: evidence of a mechanism via a coupled oxidation and aldol cleavage**. *Angew Chem Int Ed* 2017, **56**:2503–2507.
This article discusses the first direct evidence for the pyranoside-to-furanoside ring contraction in the catalytic pathway of UDP-apiose/UDP-xylose synthase.

20. ** Savino S, Borg AJE, Dennig A, Pfeiffer M, De Giorgi F, Weber H, Dubey KD, Rovira C, Mattevi A, Nidetzky B: **Deciphering the enzymatic mechanism of sugar ring contraction in UDP-apiose biosynthesis**. *Nat Catal* 2019, **2**:1115–1123.
This work reveals the detailed enzymatic mechanism of UDP-apiose/UDP-xylose synthase and illustrates how the timing of the catalytic steps is supported by stereo-electronic control applied by the enzyme.

21. Gatzeva-Topalova PZ, May AP, Sousa MC: **Structure and mechanism of ArnA: conformational change implies ordered**

dehydrogenase mechanism in key enzyme for polymyxin resistance. *Structure* 2005, **13**:929–942.

22. ** Eixelsberger T, Sykora S, Egger S, Brunsteiner M, Kavanagh KL, Oppermann U, Brecker L, Nidetzky B: **Structure and mechanism of human UDP-xylose synthase: evidence for a promoting role of sugar ring distortion in a three-step catalytic conversion of UDP-glucuronic acid**. *J Biol Chem* 2012, **287**: 31349–31358.
Here the authors describe how UDP-xylose synthase utilizes stereoelectronic control, i.e. promotes a change in its substrate's ring pucker, to facilitate the catalyzed reaction.

23. Beerens K, Soetaert W, Desmet T: **UDP-hexose 4-epimerases: a view on structure, mechanism and substrate specificity**. *Carbohydr Res* 2015, **414**:8–14.

24. * Frey PA, Hegeman AD: **Chemical and stereochemical actions of UDP–galactose 4-epimerase**. *Acc Chem Res* 2013, **46**: 1417–1426.
This review gives an excellent overview of the catalytic mechanism of UDP-galactose 4-epimerase.

25. Ishiyama N, Creuzenet C, Lam JS, Berghuis AM: **Crystal structure of WbpP, a genuine UDP-N-acetylglucosamine 4-epimerase from *Pseudomonas aeruginosa*: substrate specificity in UDP-hexose 4-epimerases**. *J Biol Chem* 2004, **279**: 22635–22642.

26. Berger E, Arabshahi A, Wei Y, Schilling JF, Frey PA: **Acid - base catalysis by UDP-galactose 4-epimerase: correlations of kinetically measured acid dissociation constants with thermodynamic values for tyrosine 149**. *Biochemistry* 2001, **40**: 6699–6705.

27. ** Iacovino LG, Savino S, Borg AJE, Binda C, Nidetzky B, Mattevi A: **Crystallographic snapshots of UDP-glucuronic acid 4-epimerase ligand binding, rotation and reduction**. *J Biol Chem* 2020 [Manucript accepted for publication].
Here the authors have captured several high resolution crystal structures of UDP-glucuronic acid 4-epimerase, including a unique structure where the substrate- and product-bound enzymes coexist within the same crystal.

28. Feingold DS, Neufeld EF, Hassid WZ: **The 4-epimerization and decarboxylation of uridine diphosphate D-glucuronic acid by extracts from *Phaseolus aureus* seedlings**. *J Biol Chem* 1960, **235**:910–913.

29. Munoz R, Lopez R, de Frutos M, Garcia E: **First molecular characterization of a uridine diphosphate galacturonate 4-epimerase: an enzyme required for capsular biosynthesis in Streptococcus pneumoniae type 1**. *Mol Microbiol* 1999, **31**: 703–713.

30. Broach B, Gu X, Bar-Peled M: **Biosynthesis of UDP-glucuronic acid and UDP-galacturonic acid in *Bacillus cereus* subsp. cytotoxis NVH 391-98**. *FEBS J* 2012, **279**:100–112.

31. Gu X, Bar-Peled M: **The biosynthesis of UDP-galacturonic acid in plants. Functional cloning and characterization of Arabidopsis UDP-d-glucuronic acid 4-epimerase**. *Plant Physiol* 2004, **136**:4256–4264.

32. Moriarity JL, Joseph Hurt K, Resnick AC, Storm PB, Laroy W, Schnaar RL, Snyder SH: **UDP-glucuronate decarboxylase, a key enzyme in proteoglycan synthesis. Cloning, characterization, and localization**. *J Biol Chem* 2002, **277**:16968–16975.

33. Sandermann H, Tisue GT, Grisebach H: **Biosynthesis of d-apiose IV. Formation of UDP-apiose from UDP- d-glucuronic acid in cell-free extracts of parsley (*Apium petroselinum L.*) and *Lemna minor***. *Biochim Biophys Acta Gen Subj* 1968, **165**: 550–552.

34. Gatzeva-Topalova PZ, May AP, Sousa MC: **Crystal structure of *Escherichia coli* ArnA (PmrI) decarboxylase domain. A key enzyme for lipid A modification with 4-amino-4-deoxy- l -arabinose and polymyxin resistance**. *Biochemistry* 2004, **43**: 13370–13379.

35. Breazeale SD, Ribeiro AA, Raetz CRH: **Origin of lipid a species modified with 4-amino-4-deoxy-l-arabinose in polymyxin-resistant mutants of *Escherichia coli*: an aminotransferase (ArnB) that generates UDP-4-amino-4-deoxy-L-arabinose**. *J Biol Chem* 2003, **278**:24731–24739.

36. Noland BW, Newman JM, Hendle J, Badger J, Christopher JA, Tresser J, Buchanan MD, Wright TA, Rutter ME, Sanderson WE, *et al.*: **Structural studies of *Salmonella typhimurium* ArnB (PmrH) aminotransferase: a 4-amino-4-deoxy-l-arabinose lipopolysaccharide-modifying enzyme**. *Structure* 2002, **10**: 1569–1580.

37. Allard STM, Beis K, Giraud MF, Hegeman AD, Gross JW, Wilmouth RC, Whitfield C, Graninger M, Messner P, Allen AG, *et al.*: **Toward a structural understanding of the dehydratase mechanism**. *Structure* 2002, **10**:81–92.

38. * Major LL, Wolucka BA, Naismith JH: **Structure and function of GDP-mannose-3′,5′-epimerase: an enzyme which performs three chemical reactions at the same active site**. *J Am Chem Soc* 2005, **127**:18309–18320.
This work illustrates how GDP-mannose 3,5-epimerase applies stereoelectronic control by the means of ring flip and pucker change to direct the regioselectivity of the catalyzed reaction.

39. * Lau STB, Tanner ME: **Mechanism and active site residues of GDP-fucose synthase**. *J Am Chem Soc* 2008, **130**: 17593–17602.
Here the authors elucidate the unusually complex sequence of two epimerizations and a reduction catalyzed by a single active site of GDP-fucose synthase.

40. Pollack RM: **Stereoelectronic control in the reactions of ketones and their enol(ate)s**. *Tetrahedron* 1989, **45**:4913–4938.

41. Kayser RH, Brault M, Pollack RM, Bantia S, Sadoff SF: **Kinetics of decarboxylation of the two epimers of 5-ieri-butyl-l-methyl-2-oxocyclohexanecarboxylic acid: lack of stereoelectronic control in β-keto acid decarboxylation**. *J Org Chem* 1983, **48**: 4497–4502.

42. Toney MD: **Controlling reaction specificity in pyridoxal phosphate enzymes**. *Biochim Biophys Acta Protein Proteonomics* 2011, **1814**:1407–1418.

43. Behnam SM, Behnam SE, Ando K, Green NS, Houk KN: **Stereoelectronic, torsional, and steric effects on rates of enolization of ketones**. *J Org Chem* 2000, **65**:8970–8978.

44. Dunathan HC: **Conformation and reaction specificity in pyridoxal phosphate enzymes**. *Proc Natl Acad Sci U S A* 1966, **55**: 712–716.

45. Fogle EJ, Liu W, Woon S-T, Keller JW, Toney MD: **Role of Q52 in catalysis of decarboxylation and transamination in dialkylglycine decarboxylase**. *Biochemistry* 2005, **44**:16392–16404.

46. Walsh CT: **Biologically generated carbon dioxide: nature's versatile chemical strategies for carboxy lyases**. *Nat Prod Rep* 2020, **37**:100–135.

47. Corey EJ: **The stereochemistry of α-haloketones. V. Prediction of the stereochemistry of α-brominated ketosteroids**. *J Am Chem Soc* 1954, **76**:175–179.

48. Koropatkin NM, Holden HM: **Structure of CDP-D-glucose 4,6-dehydratase from Salmonella typhi complexed with CDP-D-xylose**. *Acta Crystallogr Sect D Biol Crystallogr* 2005, **61**: 365–373.

49. Beis K, Allard STM, Hegeman AD, Murshudov G, Philp D, Naismith JH: **The structure of NADH in the enzyme dTDP-D-glucose dehydratase (RmlB)**. *J Am Chem Soc* 2003, **125**: 11872–11878.

50. Vogan EM, Bellamacina C, He X, Liu HW, Ringe D, Petsko GA: **Crystal structure at 1.8 Å resolution of CDP-D-glucose 4,6-dehydratase from Yersinia pseudotuberculosis**. *Biochemistry* 2004, **43**:3057–3067.

51. Mulichak AM, Bonin CP, Reiter WD, Garavito RM: **Structure of the MUR1 GDP-mannose 4,6-dehydratase from Arabidopsis thaliana: implications for ligand binding and specificity**. *Biochemistry* 2002, **41**:15578–15589.

52. Ferek JD, Thoden JB, Holden HM: **Biochemical analysis of a sugar 4,6-dehydratase from Acanthamoeba polyphaga Mimivirus**. *Protein Sci* 2020, **29**:1148–1159.

53. Riegert AS, Thoden JB, Schoenhofen IC, Watson DC, Young NM, Tipton PA, Holden HM: **Structural and biochemical investigation of PglF from Campylobacter jejuni reveals a new**

mechanism for a member of the short chain dehydrogenase/reductase superfamily. *Biochemistry* 2017, **56**:6030–6040.

54. Allard STM, Cleland WW, Holden HM: **High resolution X-ray structure of dTDP-glucose 4,6-dehydratase from streptomyces venezuelae**. *J Biol Chem* 2004, **279**:2211–2220.

55. Menon S, Stahl M, Kumar R, Xu GY, Sullivan F: **Stereochemical course and steady state mechanism of the reaction catalyzed by the GDP-fucose synthetase from Escherichia coli**. *J Biol Chem* 1999, **274**:26743–26750.

56. * Gerlt JA, Gassman PG: **Understanding enzyme-catalyzed proton abstraction from carbon acids: details of stepwise mechanisms for β-elimination reactions**. *J Am Chem Soc* 1992, **114**:5928–5934.
This article deciphers the pre-requisites and detailed mechanism of enzyme-catalyzed β-elimination reactions.

57. Gorenstein DG: **Stereoelectronic effects in biomolecules**. *Chem Rev* 1987, **87**:1047–1077.

58. Kirby AJ: *Stereoelectronic effects on reactivity: the kinetic anomeric effect*. 1983:78–135.

59. Mesecar AD, Stoddard BL, Koshland DE: **Orbital steering in the catalytic power of enzymes: small structural changes with large catalytic consequences**. *Science (80-)* 1997, **277**:202–206.

60. Fortner KC, Shair MD: **Stereoelectronic effects dictate mechanistic dichotomy between Cu(II)-catalyzed and enzyme-catalyzed reactions of malonic acid half thioesters**. *J Am Chem Soc* 2007, **129**:1032–1033.

61. Gorenstein DG, Findlay JB, Luxon BA, Kar D: **Stereoelectronic control in carbon-oxygen and phosphorus-oxygen bond breaking processes. Ab initio calculations and speculations on the mechanism of action of ribonuclease A, staphylococcal nuclease, and lysozyme**. *J Am Chem Soc* 1977, **99**:3473–3479.

Enzymatic C4 Epimerization of UDP-Glucuronic Acid: Precisely Steered Rotation of Transient 4-Keto Intermediate for Inverting Reaction without Decarboxylation

Enzymatic C4 Epimerization of UDP-Glucuronic Acid: Precisely Steered Rotation of Transient 4-Keto Intermediate for Inverting Reaction without Decarboxylation

Annika J. E. Borg[a] and Bernd Nidetzky[a,b]*

[a] Institute of Biotechnology and Biochemical Engineering, Graz University of Technology, NAWI Graz, Petersgasse 12, 8010 Graz, Austria
[b] Austrian Centre of Industrial Biotechnology, Petersgasse 14, 8010 Graz, Austria

* Corresponding author (B.N., bernd.nidetzky@tugraz.at)

Keywords: SDR, short-chain dehydrogenase/reductase, epimerase, decarboxylase, UDP-glucuronic acid, UDP-galacturonic acid, UDP-xylose, UDP-4-keto-pentose

Abbreviations: SDR, short-chain dehydrogenase/reductase; UGAepi; UDP-glucuronic acid 4-epimerase

Abstract

The biosynthetically important stereo-inversion at the hexose/pentose C4 of common sugar nucleotides is catalyzed by a class of epimerases that use tightly bound NAD^+ for transient oxidation. Non-stereospecific reduction of the 4-keto-intermediate by enzyme-NADH equilibrates the C4 epimers. Applied to C4 epimerization of uridine 5'-diphosphate (UDP)-α-D-glucuronic acid (UDP-GlcA) and UDP-α-D-galacturonic acid (UDP-GalA), the enzyme catalysis must confront decarboxylation of the unstable UDP-4-keto-hexose-uronic acid species enabled to free rotation in the active site. We show with a UDP-glucuronic acid 4-epimerase (UGAepi) from *Bacillus cereus* (BcUGAepi) how finely tuned carboxylate binding interactions from the enzyme's active site contribute to defining the chemoselectivity of the reaction. The substrate (UDP-GlcA) and product (UDP-GalA) complexes of BcUGAepi present the sugar in relaxed $^4C_1$ chair conformation, where the carboxylate moiety of the substrate is held in equatorial position by ionic interactions (UDP-GalA) or by a tight hydrogen bonding network (UDP-GlcA). With the carboxylate group locked in equatorial position, stereo-electronic constraints are set to disfavor decarboxylation for a perfectly chemo-selective epimerization in the wild-type enzyme. We performed a comprehensive mutagenesis study on the carboxylate binding interactions on both rotational isomers. Epimerase variants give decarboxylation in the extent that they remove binding interactions with the carboxylate group in the opposite rotational isomer of the substrate used in the reaction. Substitutions R185A and R185D convert the original epimerase into low-activity UDP-xylose synthases (UXS; EC 4.1.1.35) that decarboxylate UDP-GlcA in completely stereospecific reactions, while R185H and R185K variants show characteristics of both UXS and UGAepi. Our study shines light into the evolutionary connection between SDR epimerases and decarboxylases.

Introduction

Stereochemical inversion at the glycosyl carbons of sugar nucleotide substrates is catalyzed by a class of epimerases essential to carbohydrate biosynthesis.[1–4] Epimerization enables new monosaccharide building blocks to be generated from the chiral pool of basic sugar nucleotides.[1,3,5,6] Sugar nucleotide epimerases are unusual among carbohydrate-active enzymes in their requirement to be non-stereospecific.[7] Their catalysis involves stabilization of two stereoisomeric transition states for reversible cleavage of C-H bonds at carbon stereocenters. The enzymes employ transient oxidation, via hydride abstraction by a tightly bound NAD^+ cofactor, as common strategy in catalysis.[2,3,5,8,9] The epimerization often consists of deprotonation/protonation at the carbon adjacent to the intermediate's carbonyl group.[3] An alternative approach, exemplified by UDP-galactose 4-epimerase (GALE), is direct oxidation of the hydroxyl group at the targeted stereocenter. Redelivery of the abstracted hydride from enzyme-NADH to the opposite face of the carbonyl in a suitably repositioned keto-intermediate gives the stereo-inverted product.[7,10–12] Sugar nucleotide epimerases form a distinct group within the short-chain dehydrogenase/reductase (SDR) protein superfamily. They employ the basic catalytic machinery of SDR enzymes for oxidation-reduction.[8]

Hallmark of the GALE mechanism is free rotation of the 4-keto-intermediate for non-stereospecific reduction.[7] GALE-NADH binds the intermediate's 4-keto-pyranosyl moiety more loosely than the corresponding UDP moiety ($\Delta\Delta G$ = -5 kcal/mol).[7] Enzyme structures show UDP-sugar binding driven by the rigidly bound "UDP anchor" and torsional mobility left to the sugar moiety.[13] Rotation around the O1-P_β bond, as shown in Figure 1a, causes the pyranosyl moiety of UDP-galactose to revolve as a rigid body around its C1-C4 axis compared to UDP-glucose. The UMP moiety remains immobile in the process.[13] Both sugar epimers have their reactive C4 effectively in the same position, suitable for hydride transfer with the nicotinamide C4 of NAD. Like GALE, UDP-*N*-acetyl-D-glucosamine 4-epimerase enables torsional mobility for the (4-keto)-pyranosyl moiety, with the notable difference that rotation occurs around the O1-C1 bond and largely in plane of the glycopyranosyl ring (Figure 1b).[14,15]

UDP-glucuronic acid 4-epimerase (UGAepi; EC 5.1.3.6) catalyzes the interconversion of UDP-glucuronic acid and UDP-galacturonic acid[16]. The enzyme uses a GALE-like "out of plane" rotation of the glycopyranosyl moiety, with the O1-P_β bond serving as the rotating hinge (Figure 1c).[17]

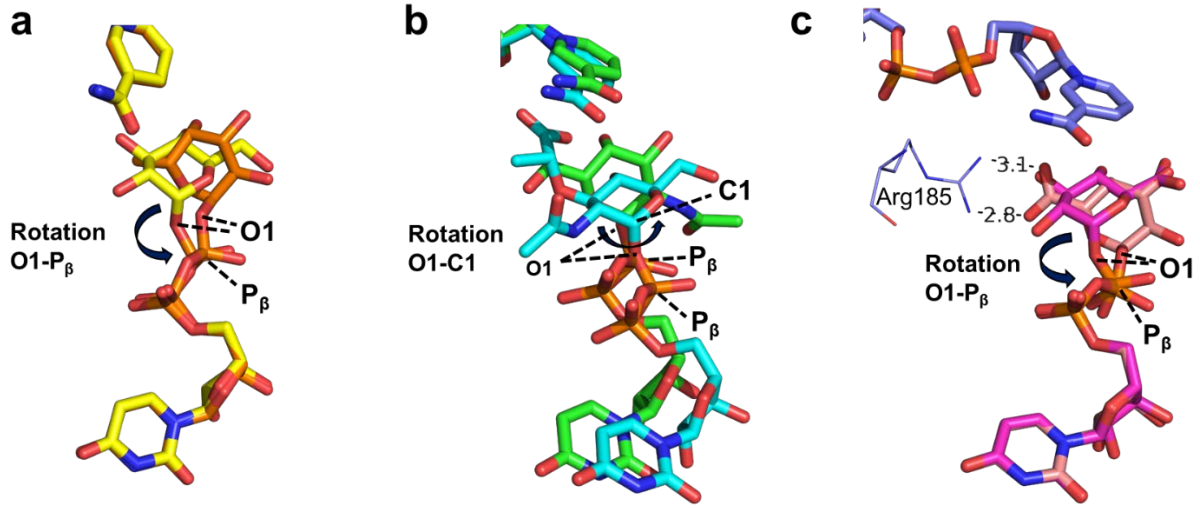

Figure 1. Overlayed active site close-ups of substrate and product complexes of GALE, UDP-GlcNAc 4-epimerase and UGAepi. **a.** Top-view on the overlay of *E. coli* GALE complexed with UDP-Glc (yellow carbons, PDB: 1XEL)[10] and UDP-Gal (orange, PDB: 1A9Z)[13] illustrating the rotational movement around the bond of β-phosphate (P_β) and O1. **b.** Structures of UDP-GlcNAc 4-epimerases MrWbpP in complex with a substrate analog UDP-MurNAc (cyan, PDB: 6DNT)[14] and PaWbpP complexed with UDP-GalNAc (green, PDB: 1SB8)[15] illustrating the rotational movement from the bond of anomeric carbon and O1. **c.** Top-view on the equilibrium complex of BcUGAepi (PDB: 6ZLK)[17] with UDP-GlcA (pink) and UDP-GalA (salmon) showing the rotation from the bond of β-phosphate and O1. The Arg185 residue important for binding the carboxylate moiety of UDP-GalA is highlighted with lines.

Despite these similarities, UGAepi poses unique challenges of fundamental importance for enzymatic epimerization via transient oxidation. To perform its reaction chemo-selectively, the UGAepi must confront decarboxylation of the UDP-4-keto-hexose-uronic acid intermediate (a highly unstable β-keto-acid species) enabled to torsional mobility in the active site. The strategy adopted by the enzyme revolves around stereo-electronic control.[18] UGAepi structures reveal both UDP-glucuronic acid and UDP-galacturonic acid accommodated with their pyranosyl moiety in a relaxed $^4C_1$ chair conformation.[17] Due to binding pocket interactions, the carboxylate group of each substrate epimer is held tightly in an equatorial position (Figure 2a).[17] Generally, β-keto-acid decarboxylation is favored by optimal orbital overlap when the C=O bond of the ketone is roughly orthogonal to the Cα-CO_2^- bond. It is disfavored when the two bonds are in plane.[18–20] For the

UDP-4-keto-hexose-uronic acid intermediate, stereo-electronic considerations imply decarboxylation to be minimized when in the undistorted $^4C_1$ sugar ring the carboxylate group is placed equatorially (Figure 2a).[18] Conundrum for UGAepi catalysis arises from the requirement to integrate stereo-electronic control with the mechanistic feature of 4-keto-intermediate rotation. High-resolution UGAepi structures suggest significant constraints from the binding pocket on the rotational itinerary between the stereo-isomeric enzyme-substrate complexes.[17] The implication, that efficient UGAepi catalysis necessitates a precisely steered (rather than free) rotation of the 4-keto-intermediate bound to enzyme-NADH, places immediate importance on mutagenesis experiments to gain deeper understanding on the function of the active site residues in the process. Our current mutagenesis study on *Bacillus cereus* UGAepi (BcUGAepi) delineates the rotational itinerary of the UDP-4-keto-hexose-uronic acid intermediate coordinated to the catalytic steps of oxidation-reduction.

The UGAepi way of handling the UDP-4-keto-hexose uronic acid receives significant mechanistic interest beyond epimerization, considering the existence of a distinct SDR family of decarboxylase enzymes.[8] Reaction of these decarboxylases, exemplified by UDP-xylose synthase (EC 4.1.1.35; UXS), involves the very same UDP-4-keto-hexose-uronic acid species formed from enzyme-NAD^+ as the UGAepi reaction, but proceeds from the intermediate via decarboxylation (Figure 2b).[21] Evidence for sugar ring distortion ($^4C_1$ chair $\rightarrow$ $B_{3,O}$ boat $\rightarrow$ ^2S_O skew-boat) concomitant with position change of the carboxylate group from equatorial to axial in the UXS-bound UDP-glucuronic acid suggests stereo-electronic control from the enzyme to promote the decarboxylation optimally (Figure 2b).[18,21] The post-decarboxylation intermediate UDP-4-keto-pentose is reduced stereo-specifically, with retention of configuration at the C4, to give UDP-xylose as the product.[21] Mutagenesis data from the current study show that BcUGAepi variants acquire the ability to decarboxylate UDP-glucuronic acid in the extent that they weaken binding interactions with the carboxylate group in the opposite rotational isomer of the substrate, UDP-glucuronic acid or UDP-galacturonic acid, used in the reaction. Strikingly, site-directed substitutions R185A and R185D convert the original epimerase into a primitive UDP-glucuronic acid decarboxylase that shows reactivity and stereochemical features of the native UXS.

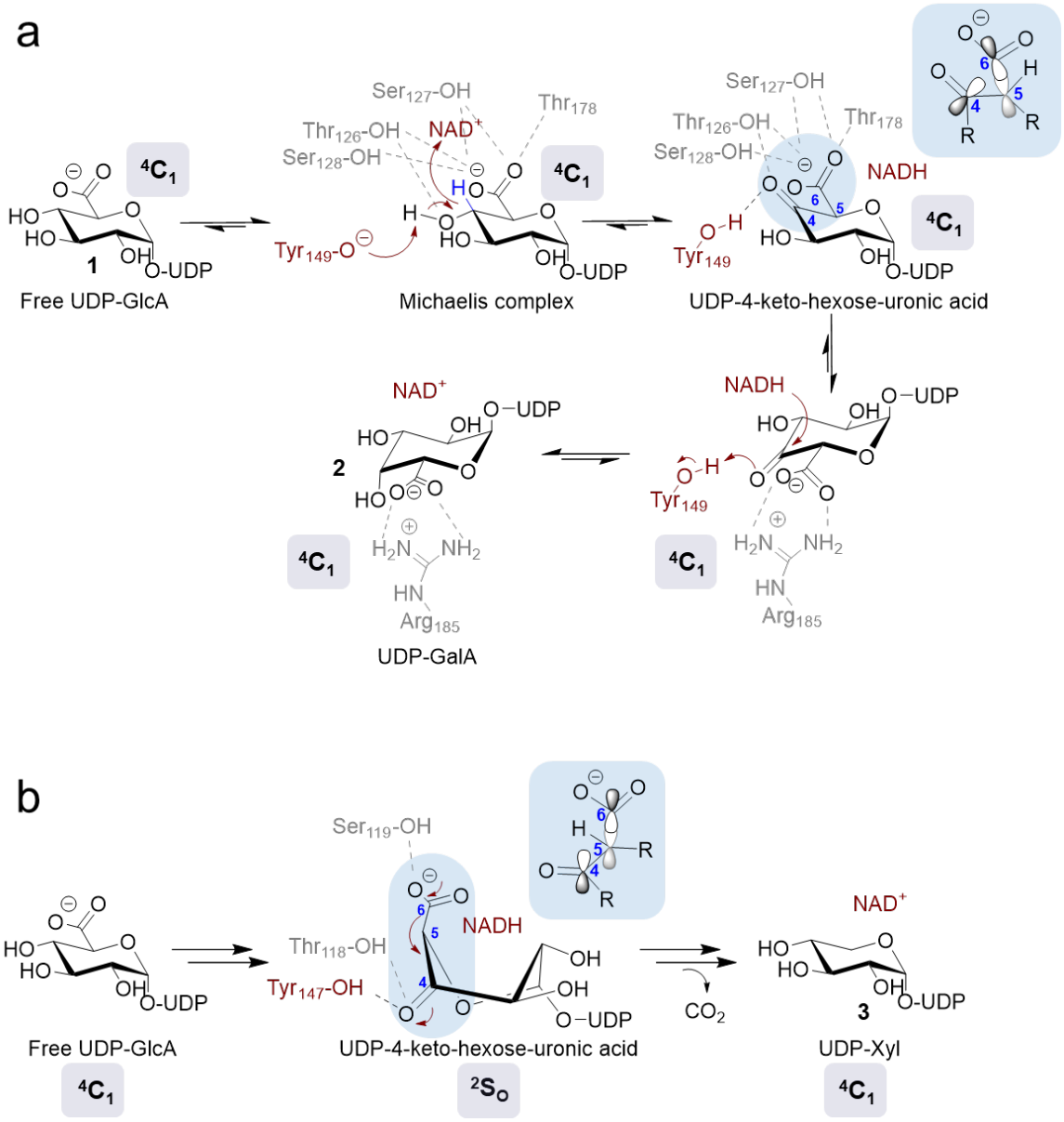

Figure 2. The reaction mechanisms of BcUGAepi and UXS highlighting the ring puckers observed during the reaction coordinate. **a**. Mechanistic overview of BcUGAepi catalyzed interconversion of UDP-GlcA (**1**) and UDP-GalA (**2**). The equatorial carboxylate moiety of the UDP-4-keto-hexose-uronic acid intermediate results in the orbital alignment disfavored for decarboxylation. **b**. Simplified reaction mechanism of UXS reacted with UDP-GlcA (**1**) and yielding UDP-Xyl (**3**). The ring pucker change from initial $^4C_1$ chair in UDP-GlcA to ^2S_O skew-boat in UDP-4-keto-hexose-uronic acid results in axial carboxylate moiety in the intermediate, which presents the optimal orbital alignment for rapid decarboxylation.

Results

Mutagenesis of the carboxylate binding pockets

We used mutagenesis to probe binding pocket interactions with the 4-keto-intermediate's carboxylate group in the two stereo-isomeric end points of the rotational itinerary. In the intermediate positioned for conversion into UDP-GalA, referred to as pro-*S* complex (Figure 3a), the carboxylate is coordinated by the side chains of Thr126, Ser127 and Ser128 as well as by the main-chain NH of Thr178. In the stereo-isomeric pro-*R* complex (Figure 3b), the carboxylate is coordinated by the side chain of Arg185. Residues were individually substituted by alanine to remove the side chain interactions and to possibly weaken the main chain interaction. Sequence comparison (Figure 3c) shows that Ser128, Thr178 and Arg185 are unique to the UGAepi subclass of SDRs.

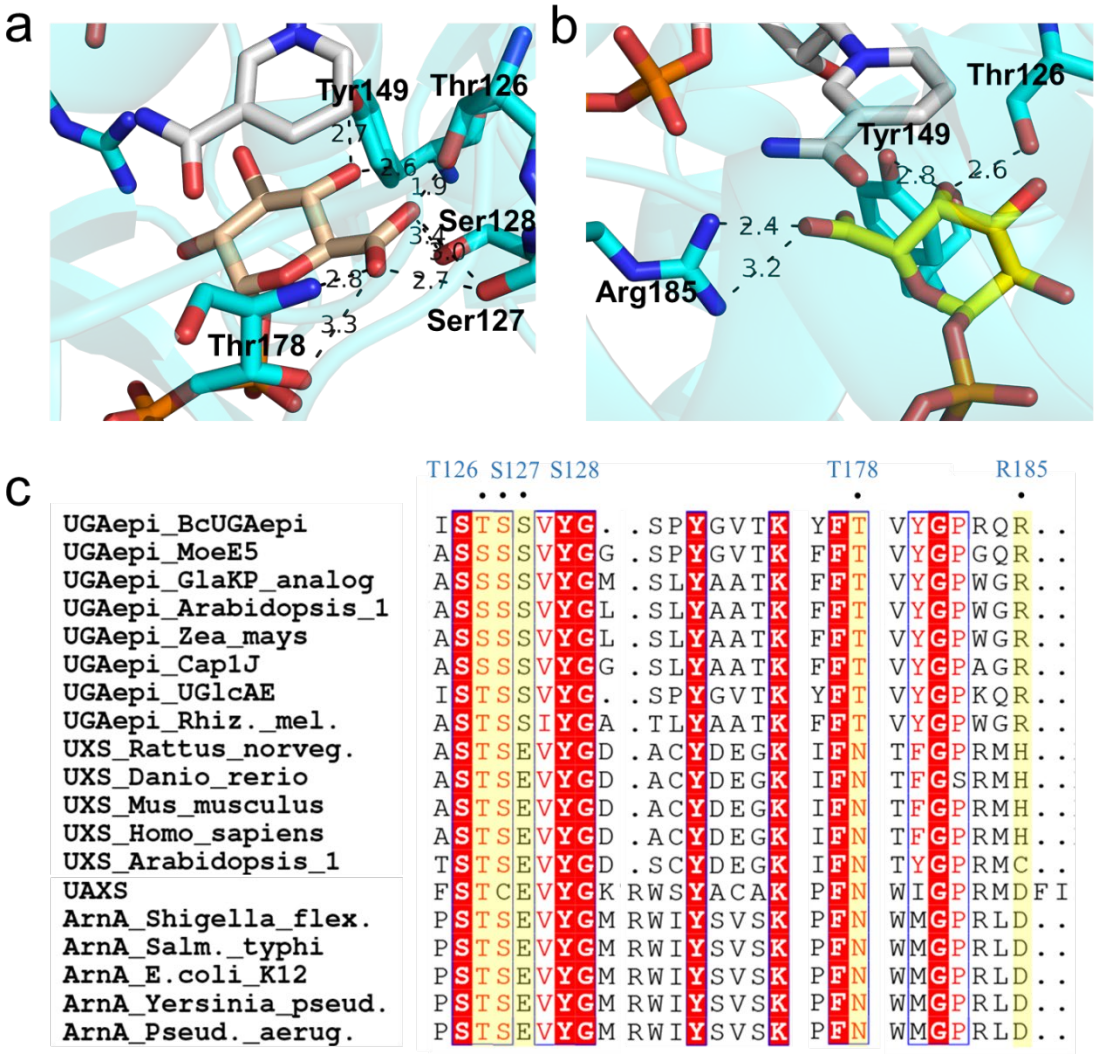

Figure 3. Crystal structures of the rotational end-points of BcUGAepi reaction and partial sequence alignment of UDP-GlcA-active SDR enzymes. **a**. Close-up into the active site of BcUGAepi complexed with UDP-GlcA and NAD^+ (PDB: 6Z73)[17] showing the SDR catalytic dyad (Thr126, Tyr149) and the residues coordinating the carboxylate moiety of UDP-GlcA (Thr126, Ser127, Ser128, Thr178). **c**. An active site close-up of BcUGAepi complexed with UDP-GalA and NAD^+ (PDB: 6Z75)[17] highlighting the catalytic dyad and the interactions of the Arg185 residue with the carboxylate group of UDP-GalA.

Thr126 is from the conserved catalytic motif (Tyr-Thr/Ser-Lys) of the SDRs.[3,5,8,11] Carboxylate coordination by Thr126 was of interest for the implied suggestion that by way of precise positioning (Figure 3a), BcUGAepi connects the element of stereo-electronic control to the immediate act of catalysis at the C4 of UDP-GlcA. The UGAepi residue Ser128 is changed to a glutamic acid in the sequences of UDP-GlcA decarboxylases. The S128E variant was constructed with the notion that the "decarboxylase" feature of sequence would strongly destabilize binding pocket interactions with the carboxylate in the pro-*S* complex. Arg185 was substituted by lysine, histidine and aspartic acid in addition to alanine. The series of variants should represent a graduated change from stabilization (wild-type > R185K > R185H) to destabilization (R185D > R185A) of the carboxylate in the pro-*R* complex.

The BcUGAepi variants were isolated from *E. coli* overexpression culture similarly as reported for the wild type enzyme. Production of the Arg185 variants gave soluble enzyme in tiny amount; the functional enzyme was obtained at ~1 mg/L of bacterial culture. Purified variants showed the ~37 kDa subunit mass of the full-length protein (Figure S1, S2) and contained nicotinamide cofactor in the oxidized state. BcUGAepi variants were assessed in reactions with UDP-GlcA analyzed by HPLC (Figure 4). Products identified with authentic standards in HPLC were additionally confirmed by NMR. Table 1 summarizes the results along with reference data for the wild type enzyme. The full reaction time course for each enzyme is shown in the Supplementary Information (Figures S3-S11).

Table 1. Activities and product ratios of BcUGAepi variants reacted with UDP-GlcA (**1**) and UDP-GalA (**2**). Unless stated otherwise, the ratios are reported after 24 h of reaction time.

Enzyme	Substrate	Activity (mU/mg)	UDP-GlcA (**1**, %)	UDP-GalA (**2**, %)	UDP-Xyl (**3**, %)	UDP-4-keto-pentose (**4**, %)
Wild type	**1**	500	33	67	0	0
T126A	**1**	0.08	33[a]	67[a]	0[a]	0[a]
S127A	**1**	24.3	33	67	0	0
S128A	**1**	11.8	33	67	0	0
S128E	**1**	0.2	85.4[b]	12.1[b]	1.7[b]	0.8[b]
T178A	**1**	0.09	33[a]	67[a]	0[a]	0[a]
R185A	**1**	0.05	90.7[c]	0[c]	0[c]	9.3[c]
R185D	**1**	0.05	92.5[c]	0[c]	5.1[c]	2.4[c]
R185H	**1**	0.05	81.3[c]	8.1[c]	9.0[c]	1.6[c]
R185K	**1**	0.3	51.1[c]	21.8[c]	26.8[c]	0.3[c]
Wild type	**2**	500	33	67	0	0
T126A	**2**	0.09	24.8	74.8	0	0.4
S127A	**2**	218	29.1	70.5	0.4[d]	0
R185H	**2**	0.1	18.3	70.7	5.0[d]	6.0

[a]Product ratios are after 48 h reaction. [b]Product ratios are after 2 h reaction. [c]Product ratios are after 2 h 30 min reaction. [d]Product is UDP-pentose (UDP-Xyl and/or UDP-Ara).

The specific activity of UDP-GlcA consumption at apparent steady-state was strongly ($\geq 10^3$-fold) decreased in all variants, except in the S127A and S128A enzymes that were, respectively, ~25- and ~50-fold less active than wild type UGAepi. Product analysis revealed distinct difference between substitutions affecting the pro-*S* as compared to the pro-*R* binding pocket. Variants featuring change in the pro-*S* binding pocket converted UDP-GlcA cleanly into UDP-GalA, except S128E variant which, additionally, showed a trace amount of decarboxylation (Figure 4a,b). Strikingly, however, Arg185 variants affecting the pro-*R* binding pocket gave predominantly decarboxylation on about half (R185K, R185H) or all (R185A, R185D) of the UDP-GlcA used (Table 1; Figure 4c). The portion of substrate escaping decarboxylation in the R185K and R185H reactions was converted with C4 stereo-inversion into UDP-GalA. The decarboxylated product was comprised of UDP-4-keto-pentose and UDP-xylose in relative amounts that varied among the enzymes (Table 1). The R185A variant produced UDP-4-keto-pentose only while the R185K variant produced UDP-xylose with traces of UDP-4-keto-pentose. The R185H and R185D variants produced mixtures of UDP-xylose/UDP-4-keto-pentose in ratio of 5.6 and 2.1, respectively. NMR data showed the identity of UDP-xylose and ruled out UDP-L-arabinose (Figure S12). Reduction

of the UDP-4-keto-pentose was therefore stereospecific and retained the configuration at C4 from the UDP-GlcA substrate.

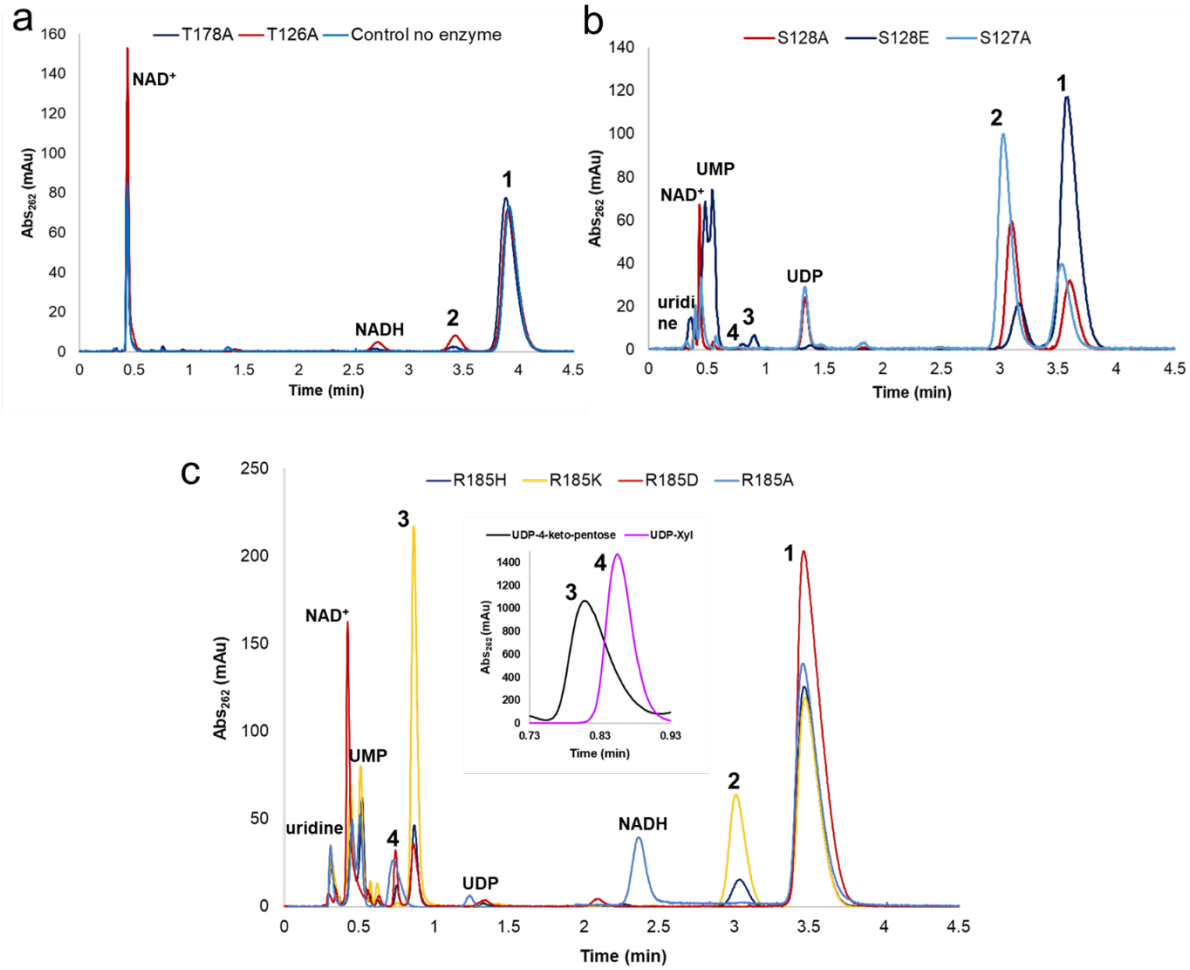

Figure 4. HPLC traces of the reaction mixtures of BcUGAepi variants reacted with UDP-GlcA. **a**. Overlay of the HPLC chromatograms of T178A (dark blue), T126A (red) and control (without enzyme, light blue) reactions after 120 min reaction time. **b**. Overlay of the HPLC chromatograms of S128A (red), S128E (dark blue) and S127A (light blue) reactions after 120 min reaction time. The release of tiny amount of decarboxylated products UDP-Xyl (**3**) and UDP-4-keto-pentose (**4**) can be seen for the S128E reaction. **c**. Overlay of the HPLC chromatograms of R185 variants' reactions after 150 min reaction time: R185H (dark blue), R185K (yellow), R185D (red) and R185A (light blue). The formation of UDP-GalA (**2**) in addition to the decarboxylated products **3** and **4** is only observed with R185K and R185H variants. An overlay of the HPLC chromatograms of the standards of isolated **3** (black) and **4** (pink) is shown to confirm the retention times.[17]

We then examined reaction of selected variants (T126A, S127A, R185H) with UDP-GalA. The enzymes showed similar (T126A) or higher (R185H, 2-fold increase; S127A, ~9-fold increase) activity than with UDP-GlcA (Table 1, Figure S13-S15). The T126A and S127A variants released mainly UDP-GlcA, however, small amounts of decarboxylation product were formed additionally (Figure 5). Reaction via decarboxylation stopped at the oxidized UDP-4-keto-pentose (T126A) or proceeded almost fully to the reduced UDP-pentose (S127A). From the HPLC analysis used, the C4 stereo-configuration of the UDP-pentose was not assignable. The R185H variant produced decarboxylated product in substantial amount (~11%) of the UDP-GalA converted.. UDP-pentose and UDP-4-keto-pentose were present in a ratio of about 2:1. Interestingly, the R185H reaction mixture showed an unidentified compound whose elution in the HPLC would be consistent with the UDP-4-keto-hexose-uronic acid intermediate before decarboxylation (Figure 5).

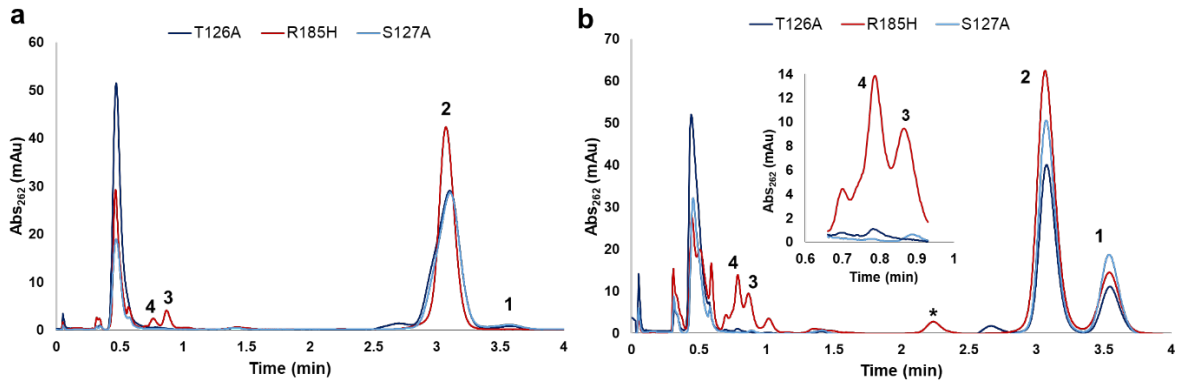

Figure 5. HPLC chromatograms from the reactions of BcUGAepi variants T126A (dark blue), S127A (light blue) and R185H (red) reacted with UDP-galacturonic acid (**2**). **a**. Overlay of the chromatograms after 1 min of reaction. **b**. Overlay of the chromatograms after 16 h reaction time. Zoom-in into the region of 0.6-1 min shows a trace amount of decarboxylated products in the T126A (UDP-4-keto-pentose, **4**) and S127A (UDP-xylose/UDP-arabinose, **3**) reactions after 16 h. UDP-glucuronic acid, **1**; UDP-galacturonic acid, **2**; UDP-xylose/UDP-arabinose, **3**; UDP-4-keto-pentose, **4**. The peak predicted to correspond to UDP-4-keto-hexose-uronic acid is labelled with an asterisk.

Discussion

Our study provides evidence for the importance of stereo-electronic control in UGAepi catalysis. The rotational end-points show UDP-GlcA and UDP-GalA in $^4C_1$ conformation where the carboxylate is held tightly in perfectly equatorial orientation by the surrounding amino acids in the active site. Single site-directed substitutions by alanine in the carboxylate binding pocket of the pro-*S* complex (T126A, S127A, S128A, T178A) result in significant activity loss in the enzyme variant, without influencing the product pattern. UDP-GalA was obtained as a sole product of the T126A, S127A, S128A and T178A variants' reactions. The replacement of Ser128 by glutamic acid (S128E) created an enzyme variant which, in addition to UDP-GalA, formed a trace amount of decarboxylated products from UDP-GlcA. The behavior of S128E variant is fascinating since the glutamic acid in that position is highly conserved in SDR-decarboxylases active on UDP-GlcA.[18] The carboxylate binding pocket in the pro-*R* complex involves only the residue Arg185, where the site-directed substitutions led to a significant amount of decarboxylation. R185A and R185D variants adopted the behavior of UXS, forming UDP-4-keto-pentose and UDP-xylose as sole products of the reaction. Enzyme variants carrying a positive charge in the position 185 (R185H and R185K) were able to catalyze epimerization to UDP-GalA in addition to decarboxylation. The predominant presence of decarboxylated products in the Arg185 variants' reactions indicate that the sugar ring must undergo a ring-pucker change during the rotational itinerary to facilitate decarboxylation. We hypothesize that the ring adopts a boat-like conformation (similar to UXS mechanism) during the rotation to re-orient the carboxylate group axially. A boat-like rotational intermediate would provide a complex which is activated for decarboxylation, if the carboxylate moiety is not tightly bound to immediately restore the equatorial orientation in the receiving rotational end-point. This would explain why the R185A and R185D variants show exclusively decarboxylase activity (rotational end-point unstabilized) while the R185H and R185K can partially restore the natural enzymatic activity (rotational end-point stabilized, although weaker than with Arg). To further support our theory, we tested the reactivity of the T126A, S127A and R185H variants with UDP-GalA. Strikingly, the T126A and S127A enzymes showed a trace amount of decarboxylation in addition to the UDP-GlcA formation. Removing either Thr126 or Ser127 from the rotational end-point leads to partial destabilization of the carboxylate-binding pocket, therefore providing a longer life-time for the predicted boat-like reaction intermediate and leakage of the decarboxylated products. R185H

variant produced a substantial amount of decarboxylated products from UDP-GalA, presumably due to poor stabilization of the carboxylate moiety in the substrate complex. Our study highlights how minimalistic changes in the enzyme's active site can effectively convert an SDR epimerase to a primitive decarboxylase.

Materials and methods

Materials

The synthetic gene of BcUGAepi was ordered in pET17b-expression vector (pET17b_BcUGAepi) from GenScript (USA). UDP-D-glucuronic acid (UDP-GlcA; >98% purity) and sodium pyruvate were from Sigma-Aldrich (Vienna, Austria). NAD^+ (>98% purity) was from Roth (Karlsruhe, Germany). Deuterium oxide (99.96% ^2H) was from Euriso-Top (Saint-Aubin Cedex, France). All other reagents and chemicals were of highest available purity. For plasmid DNA isolation, the GeneJET Plasmid Miniprep Kit (Thermo Scientific; Waltham, MA, USA) was used. DpnI and Q5® High-Fidelity DNA polymerase were from New England Biolabs (Frankfurt am Main, Germany) and D-lactate dehydrogenase from Megazyme (Vienna, Austria). All other enzymes were prepared in-house. Oligonucleotide primers were from Sigma-Aldrich (Vienna, Austria). *E. coli* NEB5α competent cells were from New England Biolabs (Frankfurt, Germany). *E. coli* Lemo21(DE3) cells were prepared in-house.

Preparation of the BcUGAepi variants

The site-directed amino acid substitutions were introduced by a modified QuikChange protocol (see SI for details) and the successful mutagenesis confirmed by DNA sequencing (LGC Genomics, Berlin, Germany). All BcUGAepi variants were produced by expression in *E. coli* Lemo21 (DE3) cells that harbored the pET17b-expression vector containing the gene of interest. The proteins were purified utilizing the C-terminal Strep-tag, and the size and purity of the proteins were confirmed by SDS-PAGE. The Strep-tag columns were washed thoroughly with extreme caution after each purification, to eliminate any chance of cross-contamination in between the mutants. Full details of the expression and purification conditions are reported elsewhere.[16]

Activity assays of BcUGAepi variants

The reaction mixtures (250 µl final volume) of the BcUGAepi variants contained 1 mM UDP-GlcA (or UDP-GalA) and 100 µM NAD^+ in sodium phosphate buffer (50 mM Na_2HPO_4, 100 mM NaCl, pH 7.6). The enzyme concentrations were variant-dependent: 0.07 mg/ml (1.9 µM, wild type), 5 mg/ml (135 µM, S128E), 10 mg/ml (270 µM, T126A; R185A), 1.6 mg/ml (43 µM, T178A), 0.2 mg/ml (5.4 µM, S127A; S128A), 4.7 mg/ml (127 µM, R185K), 15 mg/ml (405 µM, R185D; R185H). The reactions were incubated at 23 °C, quenched with methanol (50% (v/v) final concentration) at desired time points and the precipitated enzyme removed by centrifugation (16100 g, 4 °C, 30 min) prior to HPLC analysis. The initial rates were determined from the linear part of the time-course by dividing the slope of the linear regression (mM/min) by the enzyme concentration (mg/ml) giving the initial rate in µmol/(min mg protein).

HPLC

The sugar nucleotides and NAD^+/NADH were separated with Shimadzu Prominence HPLC-UV system (Shimadzu, Korneuburg, Austria) on a Kinetex C18 column (5 µm, 100 Å, 50 x 4.6 mm) using an isocratic method with 5% acetonitrile and 95% tetrabutylammonium bromide buffer (40 mM TBAB, 20 mM K_2HPO_4/KH_2PO_4, pH 5.9) as mobile phase. UDP-sugars, NAD^+ and NADH were detected by UV at 262 nm wavelength. The amount of UDP-GlcA/UDP-GalA/UDP-Xyl/UDP-4-keto-pentose formed was determined based on the relative integrated peak areas. Due to the close proximity of the peaks of UDP-Xyl and UDP-4-keto-pentose, standards of isolated compounds were used as reference for the retention times.[17]

Product identification by ^{1}H-NMR

The absence of UDP-arabinose in R185 variants' reactions was confirmed by NMR. Due to the poor activity of these variants, standard sample preparation for the measurements was not possible (except for the R185A variant). The enzymatic activity in D_2O was too low to detect any product formation on NMR. Performing the reactions in H_2O, freeze-drying the samples and re-dissolving in D_2O prior to the NMR measurements was also tried, but the signals from the excess of the remaining substrate (UDP-GlcA) were overlapping with the signals of the products. To improve the resolution of the NMR spectra and to make the product signals detectable in R185H, R185K and R185D reactions, half of the remaining substrate was enzymatically converted to UDP-4-keto-

pentose by ArnA (expression and purification of ArnA are reported elsewhere[16]) prior to the measurements. The reaction mixtures contained 2 mM UDP-GlcA and 100 μM NAD^+ in sodium phosphate buffer (50 mM Na_2HPO_4, 100 mM NaCl, pH 7.6). The enzyme concentrations were 6 mg/ml (162 μM, R185A), 0.9 mg/ml (24.3 μM, R185D), 14.7 mg/ml (397 μM, R185H) and 7.7 mg/ml (208 μM, R185K). After 24 h at 23 °C, the progress of the reaction was confirmed on HPLC and the following components were added: 1 mg/ml ArnA, 10 mM sodium pyruvate, 20 U/ml D-lactate dehydrogenase. The reaction was run for 30 min and followed on HPLC, and the enzymes removed with Vivaspin Turbo centrifugal filter tubes (10 kDa cut-off, Sartorius) when ~50% of UDP-GlcA was converted to UDP-4-keto-pentose. The addition of ArnA into the R185A reaction was not necessary due to the better conversion of UDP-GlcA in this reaction (higher stability of R185A variant allowed to use 30 °C instead of 23 °C reaction temperature, resulting in more substantial substrate depletion). The reaction mixtures were lyophilized (Christ Alpha 1-4 lyophilizer, B. Braun Biotech International, Melsungen, Germany) and the obtained solid material re-dissolved in 600 μl of D_2O for the NMR measurements. The acquisition was carried out on a Varian INOVA 500-MHz NMR spectrometer (Agilent Technologies, Santa Clara, California, USA). The VNMRJ 2.2D software was used for the measurements. ^{1}H-NMR spectra (499.98 MHz) were recorded on a 5 mm indirect detection PFG-probe with pre-saturation of the water signal by a shaped pulse. The spectra were analyzed using MestReNova 16.0 (Mestrelab Research, S.L.). The products were identified based on their chemical shifts, by using reference values from literature.[17]

References

1. Thibodeaux, C. J., Melançon, C. E. & Liu, H. W. Unusual sugar biosynthesis and natural product glycodiversification. *Nature* **446**, 1008–1016 (2007).

2. Samuel, J. & Tanner, M. E. Mechanistic aspects of enzymatic carbohydrate epimerization. *Nat. Prod. Rep.* **19**, 261–277 (2002).

3. Allard, S. T. M., Giraud, M.-F. & Naismith, J. H. Epimerases: structure, function and mechanism. *Cell. Mol. Life Sci.* **58**, 1650–1665 (2001).

4. Van Overtveldt, S. *et al.* A structural classification of carbohydrate epimerases: From mechanistic insights to practical applications. *Biotechnol. Adv.* **33**, 1814–1828 (2015).

5. Beerens, K., Soetaert, W. & Desmet, T. UDP-hexose 4-epimerases: a view on structure, mechanism and substrate specificity. *Carbohydr. Res.* **414**, 8–14 (2015).

6. Beerens, K., Van Overtveldt, S. & Desmet, T. The "epimerring" highlights the potential of carbohydrate epimerases for rare sugar production. *Biocatal. Biotransformation* **35**, 230–237 (2017).

7. Frey, P. A. & Hegeman, A. D. Chemical and stereochemical actions of UDP–galactose 4-epimerase. *Acc. Chem. Res.* **46**, 1417–1426 (2013).

8. Kavanagh, K. L., Jörnvall, H., Persson, B. & Oppermann, U. Medium- and short-chain dehydrogenase/reductase gene and protein families: The SDR superfamily: Functional and structural diversity within a family of metabolic and regulatory enzymes. *Cell. Mol. Life Sci.* **65**, 3895–3906 (2008).

9. Field, R. A. & Naismith, J. H. Structural and mechanistic basis of bacterial sugar nucleotide-modifying enzymes. *Biochemistry* **42**, 7637–7647 (2003).

10. Thoden, J. B., Frey, P. A. & Holden, H. M. Molecular structure of the NADH/UDP-glucose abortive complex of UDP-galactose 4-epimerase from *Escherichia coli*: Implications for the catalytic mechanism. *Biochemistry* **35**, 5137–5144 (1996).

11. Yijeng Liu *et al.* Mechanistic Roles of tyrosine 149 and serine 124 in UDP-galactose 4-epimerase from *Escherichia coli*. *Biochemistry* **36**, 10675–10684 (1997).

12. Berger, E., Arabshahi, A., Wei, Y., Schilling, J. F. & Frey, P. A. Acid-base catalysis by UDP-galactose 4-epimerase: Correlations of kinetically measured acid dissociation constants with

thermodynamic values for tyrosine 149. *Biochemistry* **40**, 6699–6705 (2001).

13. Thoden, J. B. & Holden, H. M. Dramatic differences in the binding of UDP-galactose and UDP-glucose to UDP-galactose 4-epimerase from *Escherichia coli*. *Biochemistry* **37**, 11469–11477 (1998).

14. Carbone, V., Schofield, L. R., Sang, C., Sutherland-Smith, A. J. & Ronimus, R. S. Structural determination of archaeal UDP-N-acetylglucosamine 4-epimerase from *Methanobrevibacter ruminantium* M1 in complex with the bacterial cell wall intermediate UDP-N-acetylmuramic acid. *Proteins Struct. Funct. Bioinforma.* **86**, 1306–1312 (2018).

15. Ishiyama, N., Creuzenet, C., Lam, J. S. & Berghuis, A. M. Crystal structure of WbpP, a genuine UDP-N-acetylglucosamine 4-epimerase from *Pseudomonas aeruginosa*: Substrate specificity in UDP-hexose 4-epimerases. *J. Biol. Chem.* **279**, 22635–22642 (2004).

16. Borg, A. J. E., Dennig, A., Weber, H. & Nidetzky, B. Mechanistic characterization of UDP-glucuronic acid 4-epimerase. *FEBS J.* **288**, 1163–1178 (2021).

17. Iacovino, L. G. *et al.* Crystallographic snapshots of UDP-glucuronic acid 4-epimerase ligand binding, rotation and reduction. *J. Biol. Chem.* **295**, 12461–12473 (2020).

18. Borg, A. J. E., Beerens, K., Pfeiffer, M., Desmet, T. & Nidetzky, B. Stereo-electronic control of reaction selectivity in short-chain dehydrogenases: Decarboxylation, epimerization, and dehydration. *Curr. Opin. Chem. Biol.* **61**, 43–52 (2021).

19. Kayser, R. H., Brault, M., Pollack, R. M., Bantia, S. & Sadoff, S. F. Kinetics of decarboxylation of the two epimers of 5-tert-butyl-1-methyl-2-oxocyclohexanecarboxylic acid: Lack of stereoelectronic control in β-keto acid decarboxylation. *J. Org. Chem.* **48**, 4497–4502 (1983).

20. Pollack, R. M. Stereoelectronic control in the reactions of ketones and their enol(ate)s. *Tetrahedron* **45**, 4913–4938 (1989).

21. Eixelsberger, T. *et al.* Structure and mechanism of human UDP-xylose synthase: evidence for a promoting role of sugar ring distortion in a three-step catalytic conversion of UDP-glucuronic acid. *J. Biol. Chem.* **287**, 31349–58 (2012).

SUPPLEMENTARY INFORMATION

Enzymatic C4 Epimerization of UDP-Glucuronic Acid: Precisely Steered Rotation of Transient 4-Keto Intermediate for Inverting Reaction without Decarboxylation

Annika J. E. Borg[a] and Bernd Nidetzky[a,b]*

[a] Institute of Biotechnology and Biochemical Engineering, Graz University of Technology, NAWI Graz, Petersgasse 12, 8010 Graz, Austria

[b] Austrian Centre of Industrial Biotechnology, Petersgasse 14, 8010 Graz, Austria

* Corresponding author (B.N., bernd.nidetzky@tugraz.at)

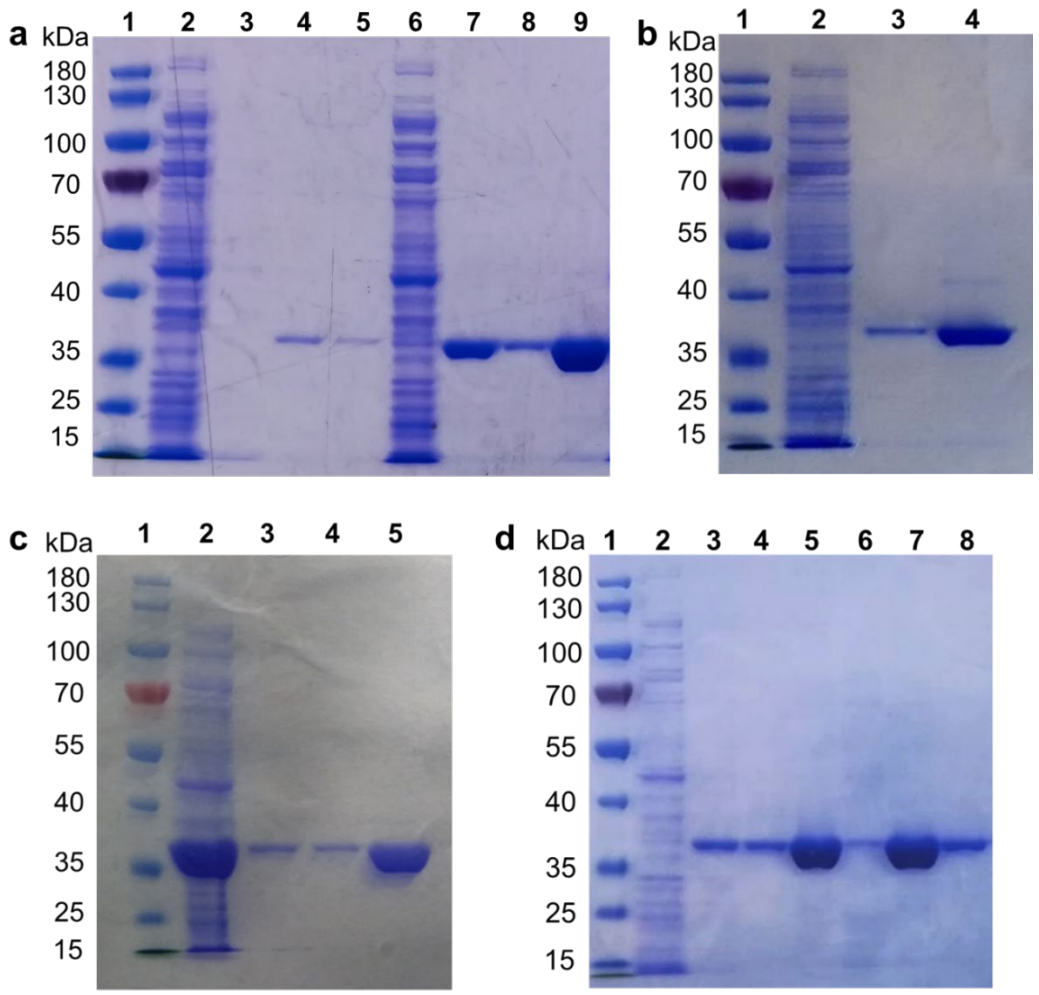

Figure S1. SDS-PAGE gels from Strep-tag purifications of BcUGAepi variants (~37 kDa). **a**. The gel from the purification of the T178A and T126A variants. Lane 1: molecular mass ladder, lane 2: flow through fraction from purification of T178A, lane 3: washing fraction from purification of T178A, lane 4 and 5: elution fractions from purification of T178A, lane 6: flow through fraction from purification of T126A, lane 7: washing fraction from purification of T126A, lane 8 and 9: elution fractions from purification of T126A. **b**. The gel from the purification of the R185A variant. Lane 1: molecular mass ladder, lane 2: flow through fraction, lane 3: washing fraction, lane 4: elution fraction. **c**. The gel from the purification of the S128E variant. Lane 1: molecular mass ladder, lane 2: flow through fraction, lane 3: washing fraction, lane 4 and 5: elution fractions. **c**. The gel from the purification of the S127A and S128A variants. Lane 1: molecular mass ladder, lane 2: flow through fraction from purification of S127A, lane 3: washing fraction from purification of S127A, lane 4 and 5: elution fractions from purification of S127A, lane 6: washing fraction from purification of S128A, lane 7 and 8: elution fractions from purification of S128A.

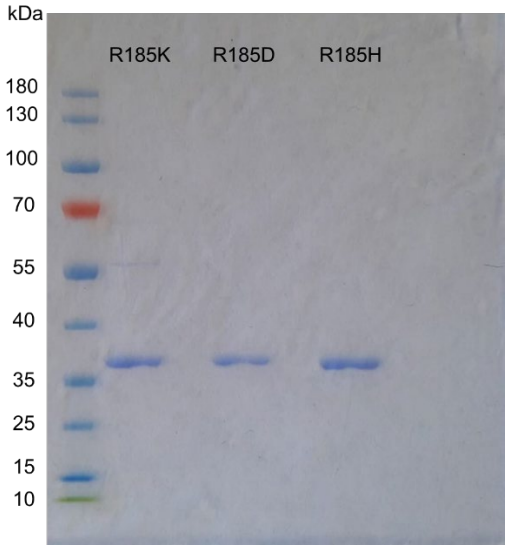

Figure S2. SDS-PAGE gel of the elution fractions from the Strep-tag purifications of BcUGAepi variants R185K, R185D and R185H (~37 kDa).

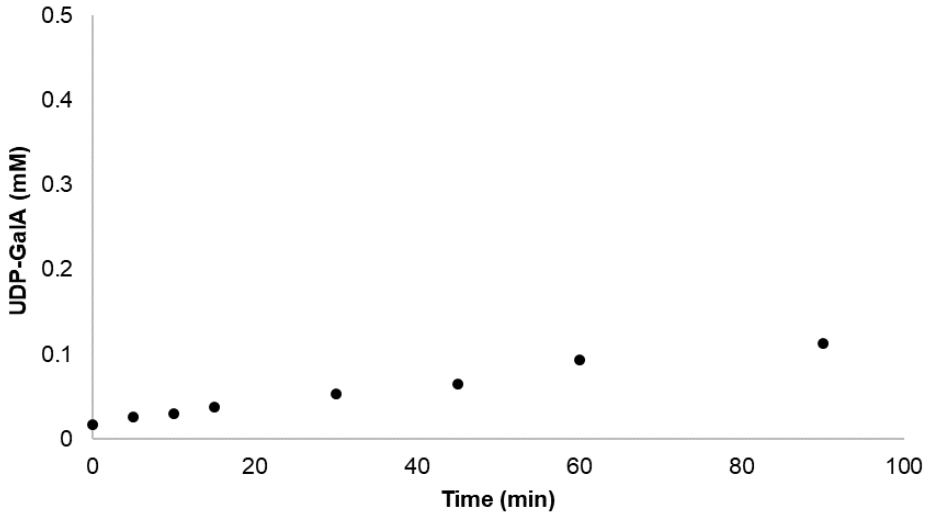

Figure S3. Time course of BcUGAepi_T126A catalyzed reaction with UDP-GlcA as a substrate. The reaction was performed with 1 mM UDP-GlcA, 100 µM NAD^+ and 270 µM (10 mg/ml) purified recombinant BcUGAepi_T126A in sodium phosphate buffer (50 mM Na_2HPO_4, 100 mM NaCl, pH 7.6) in final volume of 250 µl. The activity of T126A variant (0.08 mU/mg) was calculated from the linear part of the time course.

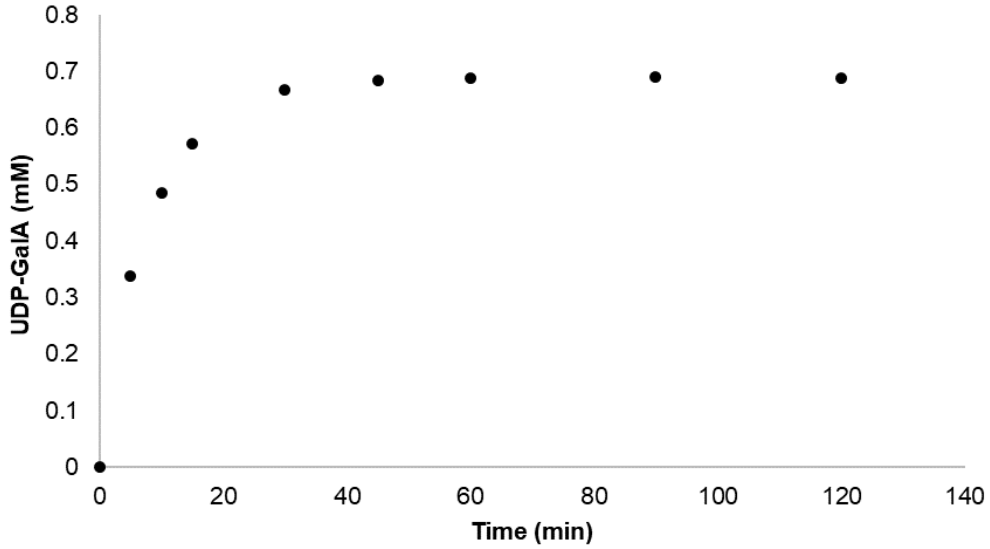

Figure S4. Time course of BcUGAepi_S127A catalyzed reaction with UDP-GlcA as a substrate. The reaction was performed with 1 mM UDP-GlcA, 100 µM NAD^+ and 5.4 µM (0.2 mg/ml) purified recombinant BcUGAepi_S127A in sodium phosphate buffer (50 mM Na_2HPO_4, 100 mM NaCl, pH 7.6) in final volume of 250 µl. The activity of S127A variant (24.3 mU/mg) was calculated from the initial velocity (linear part) of the time course.

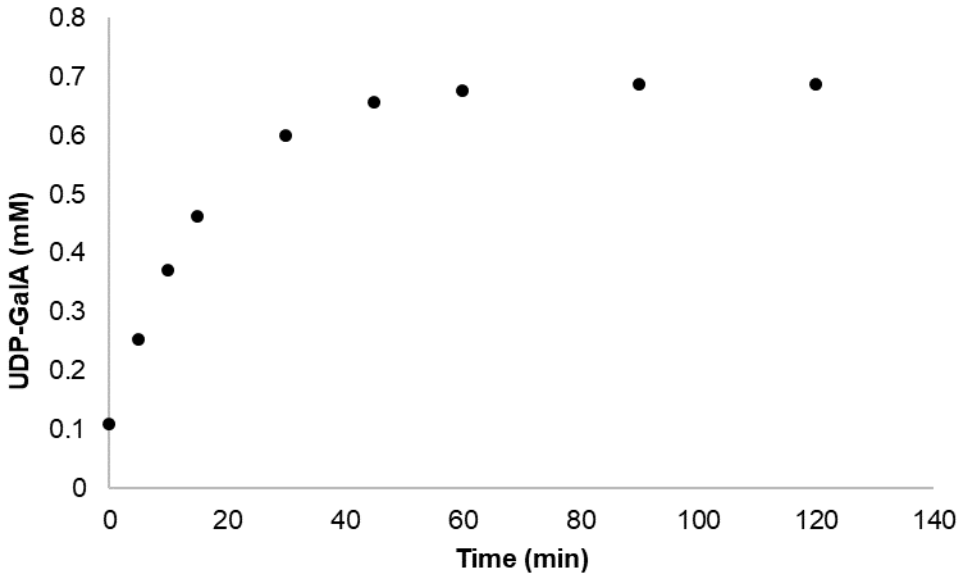

Figure S5. Time course of BcUGAepi_S128A catalyzed reaction with UDP-GlcA as a substrate. The reaction was performed with 1 mM UDP-GlcA, 100 µM NAD^+ and 5.4 µM (0.2 mg/ml) purified recombinant BcUGAepi_S128A in sodium phosphate buffer (50 mM Na_2HPO_4, 100 mM NaCl, pH 7.6) in final volume of 250 µl. The activity of S128A variant (11.8 mU/mg) was calculated from the initial velocity (linear part) of the time course.

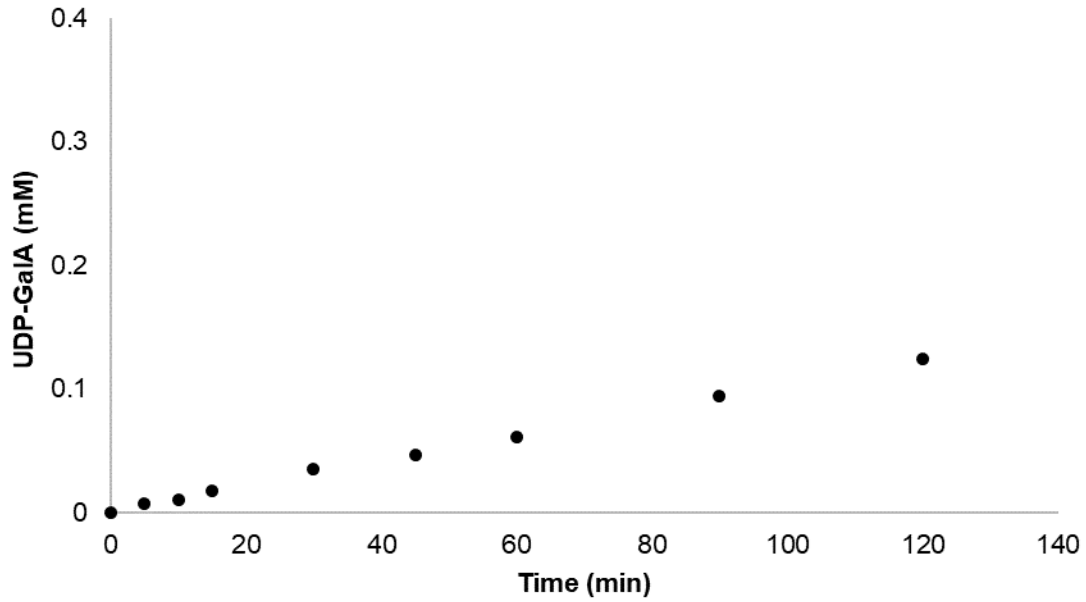

Figure S6. Time course of BcUGAepi_S128E catalyzed reaction with UDP-GlcA as a substrate. The reaction was performed with 1 mM UDP-GlcA, 100 µM NAD^+ and 135 µM (5 mg/ml) purified recombinant BcUGAepi_S128E in sodium phosphate buffer (50 mM Na_2HPO_4, 100 mM NaCl, pH 7.6) in final volume of 250 µl. The activity of S128E variant (0.2 mU/mg) was calculated from the time course.

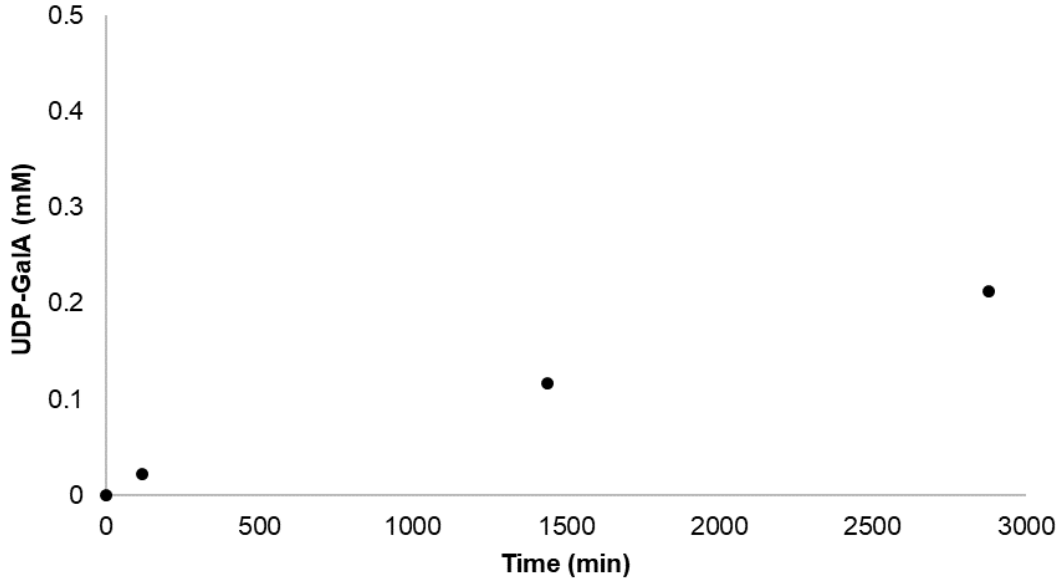

Figure S7. A brief time course of BcUGAepi_T178A catalyzed reaction with UDP-GlcA as a substrate. The reaction was performed with 1 mM UDP-GlcA, 100 µM NAD^+ and 43 µM (1.6 mg/ml) purified recombinant BcUGAepi_T178A in sodium phosphate buffer (50 mM Na_2HPO_4, 100 mM NaCl, pH 7.6) in final volume of 250 µl. The activity of T178A variant (0.09 mU/mg) was calculated from the time course.

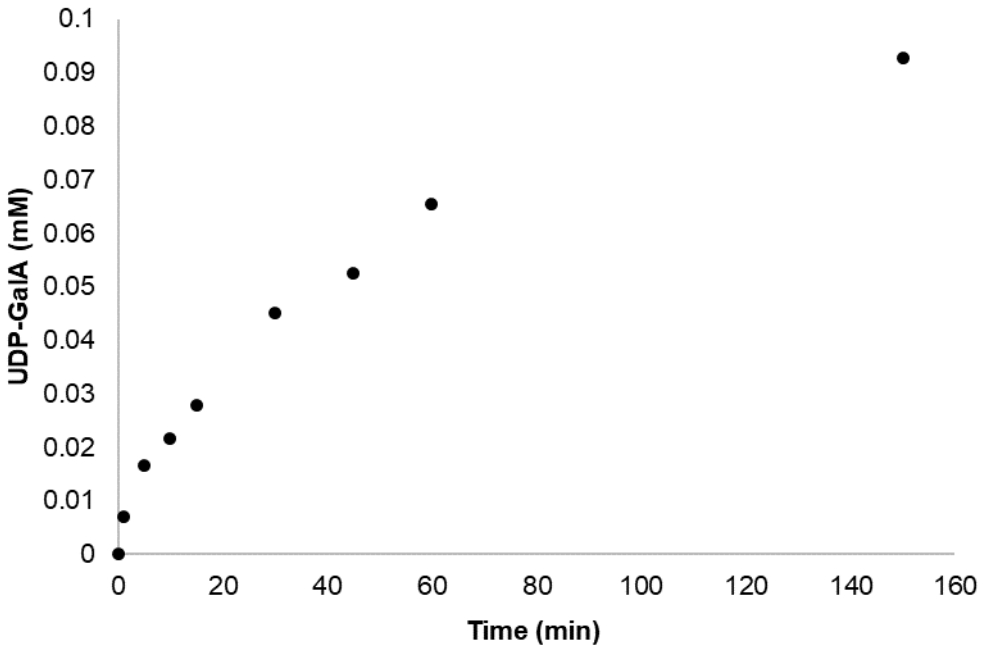

Figure S8. Time course of BcUGAepi_R185A catalyzed reaction with UDP-GlcA as a substrate. The reaction was performed with 1 mM UDP-GlcA, 100 µM NAD^+ and 270 µM (10 mg/ml) purified recombinant BcUGAepi_R185A in sodium phosphate buffer (50 mM Na_2HPO_4, 100 mM NaCl, pH 7.6) in final volume of 250 µl. The activity of R185A variant (0.05 mU/mg) was calculated from the linear part (excluding 0 and 1 min time points) of the time course.

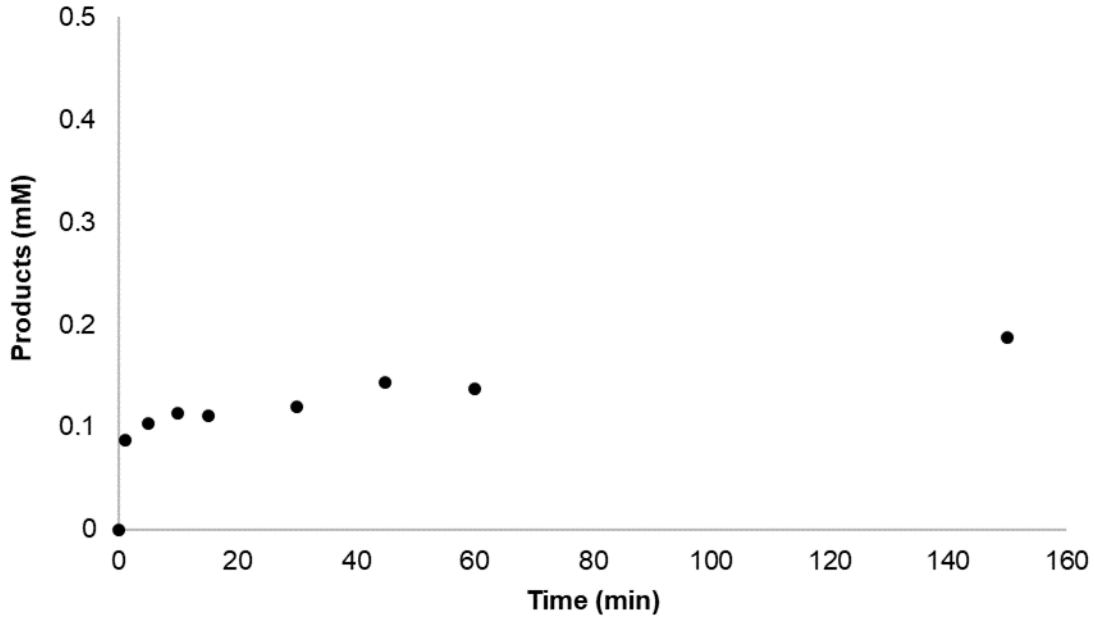

Figure S9. Time course of BcUGAepi_R185H catalyzed reaction with UDP-GlcA as a substrate. The reaction was performed with 1 mM UDP-GlcA, 100 µM NAD^+ and 405 µM (15 mg/ml) purified recombinant BcUGAepi_R185H in sodium phosphate buffer (50 mM Na_2HPO_4, 100 mM NaCl, pH 7.6) in final volume of 250 µl. The activity of R185H variant (0.05 mU/mg) was calculated from the linear part (excluding 0 and 1 min time points) of the time course.

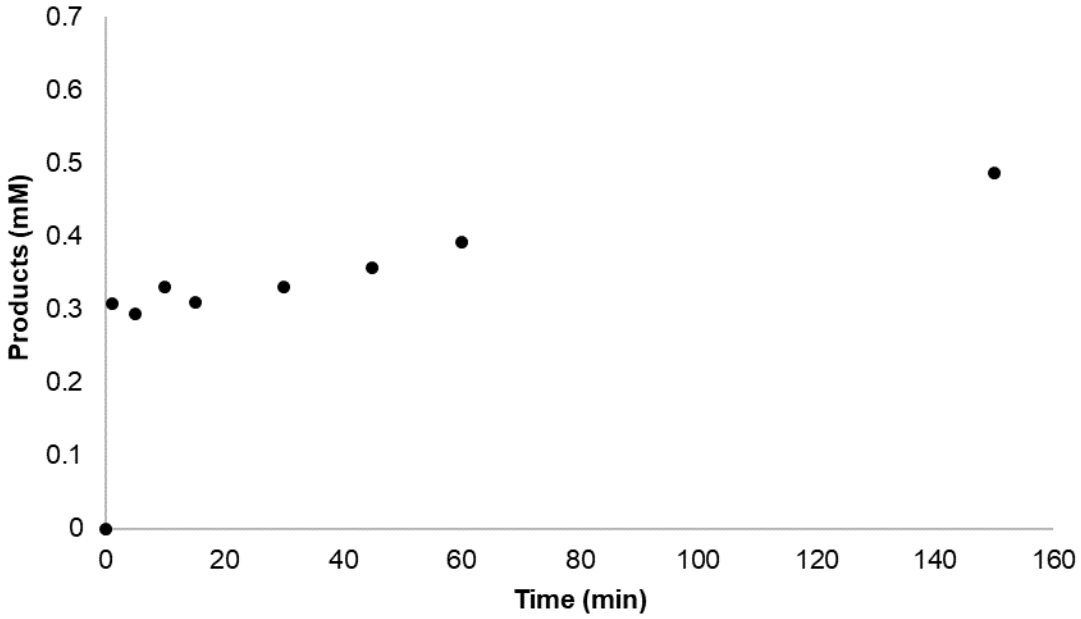

Figure S10. Time course of BcUGAepi_R185K catalyzed reaction with UDP-GlcA as a substrate. The reaction was performed with 1 mM UDP-GlcA, 100 µM NAD^+ and 127 µM (4.7 mg/ml) purified recombinant BcUGAepi_R185K in sodium phosphate buffer (50 mM Na_2HPO_4, 100 mM NaCl, pH 7.6) in final volume of 250 µl. The activity of R185K variant (0.3 mU/mg) was calculated from the linear part (excluding 0 and 1 min time points) of the time course.

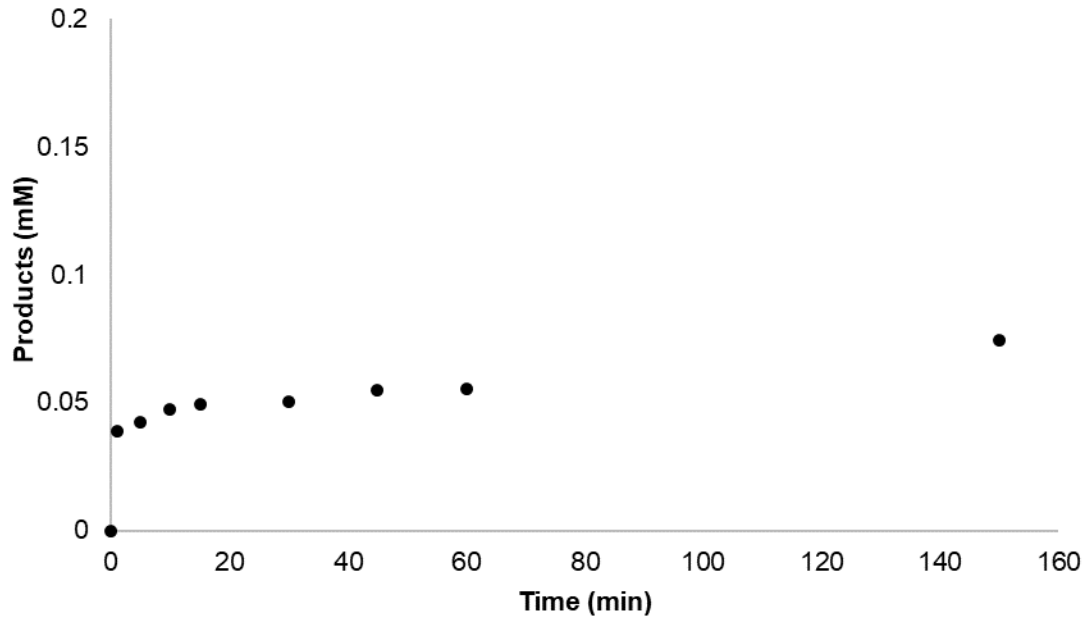

Figure S11. Time course of BcUGAepi_R185D catalyzed reaction with UDP-GlcA as a substrate. The reaction was performed with 1 mM UDP-GlcA, 100 µM NAD^+ and 405 µM (15 mg/ml) purified recombinant BcUGAepi_R185D in sodium phosphate buffer (50 mM Na_2HPO_4, 100 mM NaCl, pH 7.6) in final volume of 250 µl. The activity of R185D variant (0.05 mU/mg) was calculated from the linear part (excluding 0 and 1 min time points) of the time course.

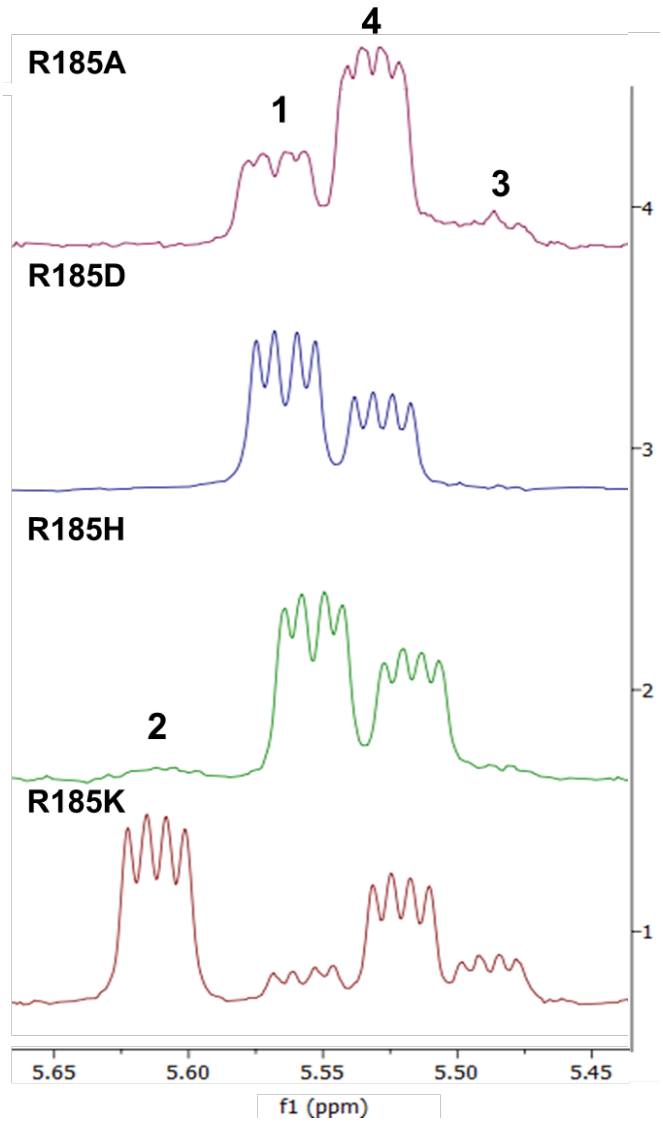

Figure S12. ^{1}H-NMR spectra of the reaction mixtures of R185 variants. Prior to NMR analysis, each reaction mixture was treated with ArnA to convert ~50% of the remaining substrate to UDP-4-keto-pentose to improve the resolution on the anomeric region. The reactions were performed in H_2O, the enzymes removed by filtration and the remaining supernatant lyophilized prior to re-dissolving the compounds in D_2O. A close-up of the anomeric region is shown. UDP-glucuronic acid, **1**, 5.48 ppm; UDP-galacturonic acid, **2**, 5.52 ppm; UDP-xylose, **3**, 5.62 ppm; UDP-4-keto-pentose, **4**, 5.56 ppm. If UDP-arabinose was present, a signal would be seen at 5.65 ppm.

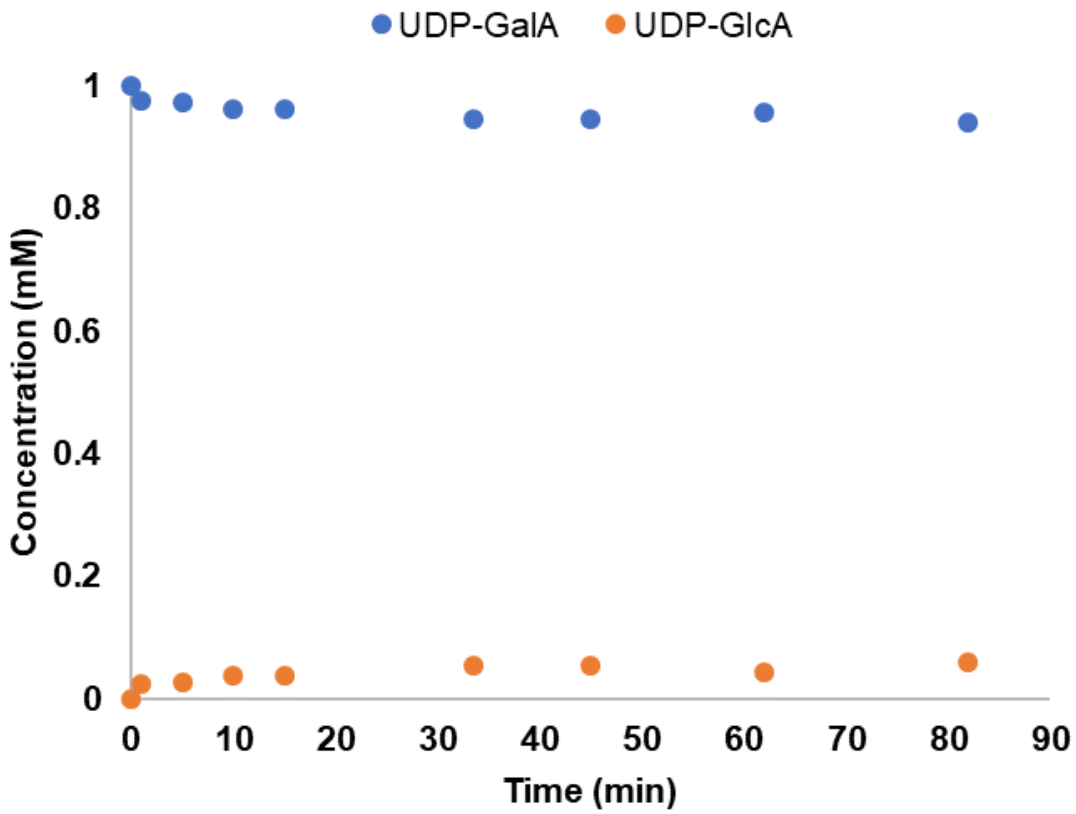

Figure S13. Time course of BcUGAepi_T126A catalyzed reaction with UDP-GalA as a substrate. The reaction was performed with 1 mM UDP-GalA, 100 µM NAD^+ and 270 µM (10 mg/ml) purified recombinant BcUGAepi_T126A in sodium phosphate buffer (50 mM Na_2HPO_4, 100 mM NaCl, pH 7.6) in final volume of 250 µl. The activity of T126A variant (0.09 mU/mg) was calculated from the linear part (excluding 0 and 1 min time points) of the time course.

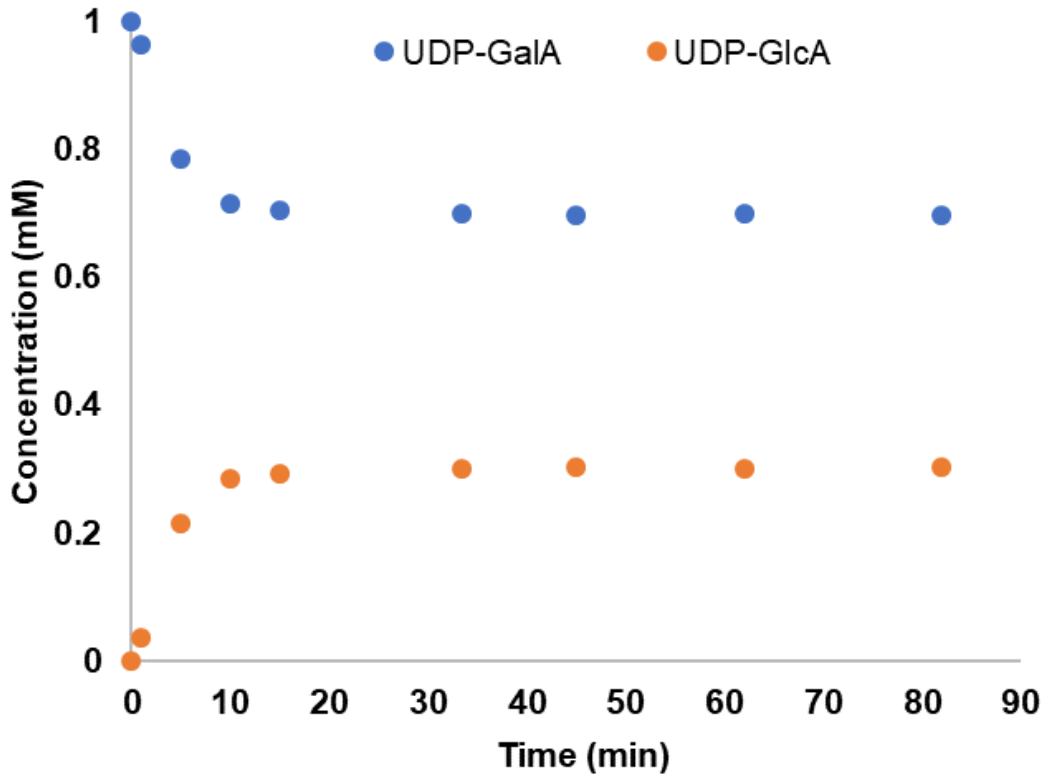

Figure S14. Time course of BcUGAepi_S127A catalyzed reaction with UDP-GalA as a substrate. The reaction was performed with 1 mM UDP-GalA, 100 µM NAD^+ and 5.4 µM (0.2 mg/ml) purified recombinant BcUGAepi_T126A in sodium phosphate buffer (50 mM Na_2HPO_4, 100 mM NaCl, pH 7.6) in final volume of 250 µl. The activity of S127A variant (218 mU/mg) was calculated from the linear part (0-5 min) of the time course.

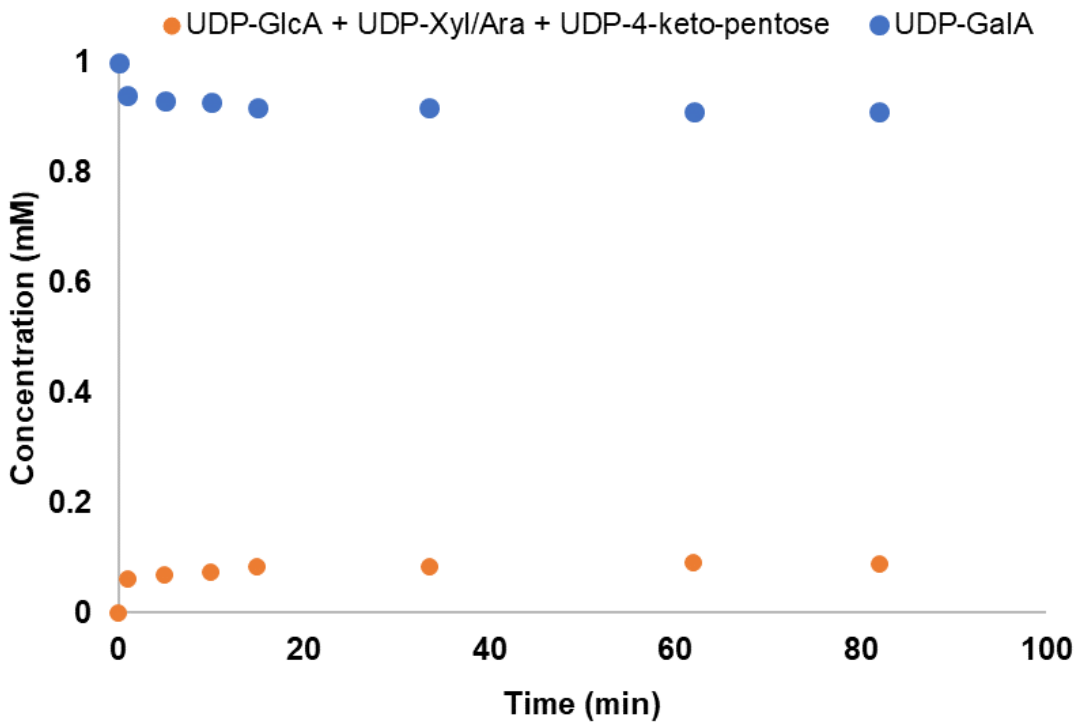

Figure S15. Time course of BcUGAepi_R185H catalyzed reaction with UDP-GalA as a substrate. The reaction was performed with 1 mM UDP-GalA, 100 µM NAD^+ and 405 µM (15 mg/ml) purified recombinant BcUGAepi_R185H in sodium phosphate buffer (50 mM Na_2HPO_4, 100 mM NaCl, pH 7.6) in final volume of 250 µl. The activity of R185H variant (0.1 mU/mg) was calculated from the time points 1-15 min.

Experimental procedures (addition to the main text)

Site-directed mutagenesis

BcUGAepi variants were prepared using a modified QuikChange protocol. PCRs were carried out in the reaction volume of 50 µl using 20 ng of plasmid DNA as template and 0.2 µM of forward or reverse primer. Q5 DNA polymerase was used for DNA amplification. The sequences of DNA oligonucleotide primers used for the mutagenesis in BcUGAepi are shown below. The underlined nucleotides highlight the mutations introduced by PCR.

Name	Mutation	DNA primer sequence (5'-3')
T126A_fw	T126A	CAAGTTTATCCACATTAGCGCAAGCAGCGTGTACGGCGAG
T126A_rv		CTCGCCGTACACGCTGCTTGCGCTAATGTGGATAAACTTG
T178A_fw	T178A	GATCCTGCGTTACTTTGCCGTTTATGGTCCG
T178A_rv		CGGACCATAAACGGCAAAGTAACGCAGGATC
S127A_fw	S127A	GTTTATCCACATTAGCACCAGCAGCGTGTACGGCGAGAAG
S127A_rv		CTTCTCGCCGTACACGCTGCTGGTGCTAATGTGGATAAAC
S128A_fw	S128A	CACATTAGCACCAGCGCAGTGTACGGCGAGAAG
S128A_rv		CTTCTCGCCGTACACTGCGCTGGTGCTAATGT
S128E_fw	S128E	CACATTAGCACCAGCGAAGTGTACGGCGAGAAG
S128E_rv		CTTCTCGCCGTACACTTCGCTGGTGCTAATGT
R185A_fw	R185A	TATGGTCCACGTCAGGCACCGGACATGGCGTTC
R185A_rv		GAACGCCATGTCCGGTGCCTGACGCGGACCATA
R185D_fw	R185D	TATGGTCCGCGTCAGGATCCAGACATGGCGTTC
R185D_rv		GAACGCCATGTCTGGATCCTGACGCGGACCATA
R185H_fw	R185H	TATGGTCCACGTCAGCACCCGGACATGGCGTTC
R185H_rv		GAACGCCATGTCCGGGTGCTGACGTGGACCATA
R185K_fw	R185K	TATGGTCCGCGTCAGAAACCGGACATGGCGTTC
R185K_rv		GAACGCCATGTCCGGTTTCTGACGCGGACCATA

First, three cycles of linear PCR amplification were performed with separate forward and reverse primers (initial denaturation: 30 sec/98 °C; 3 cycles amplification: 10 sec/98 °C for denaturation,

15 sec/55 °C for primer annealing and 6 min/72 °C extension; final extension: 5 min/72 °C). The reaction mixtures were combined to mix the forward and reverse primer solutions, divided again into two mixtures of 50 µl (for better heat transfer) and the PCR program was restarted for 15 cycles of exponential DNA amplification (initial denaturation: 30 sec/98 °C; 3 cycles amplification: 10 sec/98 °C for denaturation, 15 sec/55 °C for primer annealing and 6 min/72 °C extension; final extension: 5 min/72 °C). Residual template DNA was removed by addition of 10 U DpnI and incubation at 37 °C for 16 h. DpnI was inactivated by incubating at 80 °C for 20 min, the mixtures were centrifuged and the PCR products analyzed by agarose gel electrophoresis and visualized by DNA staining. The PCR products were directly transformed into chemically competent *E. coli* NEB5α cells (New England Biolabs). Plasmid DNA was extracted and sequenced with T7prom/T7term primers provided by LGC Genomics (Berlin, Germany) to confirm the mutations. The correct construct was transformed into *E. coli* Lemo21(DE3) cells followed by expression of BcUGAepi.

Scientific record

Publications:

Deciphering the Enzymatic Mechanism of Sugar Ring Contraction in UDP-Apiose Biosynthesis
Savino, S.*; Borg, A.J.E.*; Dennig, A.*; Pfeiffer, M.; De Giorgi, F.; Weber, H.; Dutta Dubey, K.; Rovira, C.; Mattevi, A.; Nidetzky, B., *Nat. Catal.* **2019**, *2*, 1115-1123
*Equally contributing first authors

Mechanistic Characterization of UDP-Glucuronic Acid 4-Epimerase
Borg, A.J.E.; Dennig, A.; Weber, H.; Nidetzky, B., *FEBS J.* **2020**, doi:10.1111/febs.15478

Crystallographic Snapshots of UDP-Glucuronic Acid 4-Epimerase Ligand Binding, Rotation and Reduction
Iacovino, L.G.; Savino, S.; Borg, A.J.E.; Binda, C.; Nidetzky, B.; Mattevi, A., *J. Biol. Chem.* **2020**, *295*, 12461-12473

Stereo-Electronic Control of Reaction Selectivity in Short-Chain Dehydrogenases: Decarboxylation, Epimerization, and Dehydration
Borg, A.J.E.; Beerens, K.; Pfeiffer, M.; Desmet, T.; Nidetzky, B., *Curr. Opin. Chem. Biol.* **2021**, *61*, 43-52

Conference contributions:

Synthesis of nucleotide sugars. ***Poster presentation***, ESIB – European Summit of Industrial Biotechnology – Graz, Austria, **2017**, A.J.E. Borg, M. Lemmerer, A. Dennig, B. Nidetzky.

Characterization and mechanistic analysis of UDP-glucuronic acid 4-epimerase. ***Oral communication***, Austrian Carbohydrate Workshop (22nd) – Vienna, Austria, **2018**, A.J.E. Borg, A. Dennig, S. Savino, A. Mattevi, B. Nidetzky.

Mechanistic analysis on a UDP-glucuronic acid 4-epimerase. ***Oral communication***, ICS – International Carbohydrate Symposium (29th) – Lisbon, Portugal, **2018**, A.J.E. Borg, A. Dennig, S. Savino, A. Mattevi, B. Nidetzky.

Crystallization, characterization and mechanistic analysis of a novel UDP-glucuronic acid 4-epimerase. ***Poster & poster pitch presentation***, CBM – Carbohydrate Bioengineering Meeting (13th) – Toulouse, France, **2019**, A.J.E. Borg, A. Dennig, S. Savino, A. Mattevi, B. Nidetzky.

Crystallization, characterization and mechanistic analysis of a novel UDP-glucuronic acid 4-epimerase. ***Poster presentation***, BIOTRANS – International Symposium on Biocatalysis and Biotransformations (14th) – Groningen, the Netherlands, **2019**, A.J.E. Borg, A. Dennig, S. Savino, A. Mattevi, B. Nidetzky.